Mathematical modelling for bidirectional motor-mediated motility in a fungal model system

Submitted by Congping Lin to the University of Exeter
as a thesis for the degree of
Doctor of Philosophy
in July 2012

I certify that all material in this thesis which is not my own work has been identified and that no material has previously been submitted and approved for the award of a degree by this or any other University.

Signature: ....

This page is intentionally left blank.

Abstract

In *Ustilago maydis* hyphae, bidirectional transport of early endosomes (EEs) occurs on microtubules (MTs) that have plus and minus ends. The transport is powered by kinesin-3 towards the plus ends of MTs and dynein towards the minus ends. Experiments show an accumulation of dynein at the MT plus end.

To investigate the mechanism of this accumulation, I consider two extended asymmetric simple exclusion principle (ASEP) models for the bidirectional transport of dynein in this thesis. In the simpler two-lane model, collision between opposite-directed motors is excluded whereas the more sophisticated 13-lane model takes into account that the MT usually consists of thirteen protofilaments. The presence of multi protofilaments allows dynein to avoid collision with kinesin by changing protofilaments, a behaviour that has been experimentally described. Both models are supplied by quantitative data obtained in *U. maydis* by live cell imaging and suggest that the stochastic behaviour of dynein can account for half of dynein motors in the accumulation at the MT plus end. Moreover, for the two-lane model, by using a mean field approximation, I give an analytical approximation for the accumulation size which shows linear dependence on the flux. In contrast, this dependence is nonlinear in the 13-lane model and appears to be associated with a phase transition leading to a "pulsing state".

Accompanied experimental studies have shown that *U. maydis* contains a complex MT array and that kinesin-3 moves early endosomes along antipolar MT bundles. In order to better understand the bidirectional EE motility, I extend the two-lane ASEP to model bidirectional transport along an antipolar MT bundle. In this model, the MTs are coupled at minus ends where organelles can switch MTs on which they move. By a mean-field approximation and numerical simulations, I investigate how the switching affects phases of density profiles as well as the type of motor that dominates the active transport in the bundle.

Contents

List of Figures

7

List of Tables

Acknowledgements

I would like to thank the people who helped me on my way to the completion of this PhD thesis:

First and foremost, I would like to thank my two supervisors Prof. Peter Ashwin and Prof. Gero Steinberg for introducing me the topic of molecular motor transport and for their ideas, enthusiasm, support and encouragement during my work. I am also very grateful to their generous help in writing up my work.

I am also greatly appreciative of Dr. Martin Schuster for his consistent help in explaining basic biological knowledge and experiments to me as well as fruitful discussions on this project. Particularly, I would like to thank for his assistance in the preparation of the experimental image used for publications.

I would like to thank Ms. Yvonne Roger for introducing me the mitosis in *Ustilago maydis*. Meanwhile, I would like to thank those people organizing the Friday seminar in Steinberg's lab and allowing me to take part, as well as those people who kindly explain their work to me in a more basic way during the seminar.

I am also grateful of Kong Da-li for his friendship and his support in programming problems.

Finally, I offer my deepest thanks to my husband Yiwei Zhang for being with me and for all the support during the PhD.

Nomenclature

$\alpha_\pm,\ \beta_\pm$ injection and exit rates of plus/minus-type particles

$\omega_\pm$ direction-change rates of plus/minus-type particles (Chapter 5)

$\rho(\sigma)$ densities of plus-(minus-)type particles

i site in the lattice

l lane in the lattice (Chapter 4); track in the lattice (Chapter 5)

$p_{\pm,b(u)}^{l\to l\pm 1}$ lane-change rates of plus/minus-type particles when blocked (unblocked) (Chapter 4)

p_{+-}, p_{-+} type-change rates (Chapter 4)

$p_\pm$ forward rates of plus/minus-type particles

$p_{u,d}$ direction-change rates from up (down) lane to the other (Chapter 3)

$q_{1,2}$ track switching rates

ADP adenosine diphosphate

ASEP asymmetric simple exclusion principle

ATP   adenosine triphosphate

EE   early endosome

GDP guanosine diphosphate

GFP   green fluorescent protein

GTP   guanosine triphosphate

MT   microtubule

Chapter 1

Biological background

Spatial redistribution of intracellular components organizes the cell, generates polarity and is involved in signal transduction. The process of intracellular motility is therefore of central importance to all eukaryotic cells. Spatial redistribution can be achieved via diffusion or/and active transport. Diffusion is usually considered to be inefficient to overcome long distances (larger than 200 nm) and long-distance transport requires the activity of molecular motors that hydrolyze adenosine triphosphate (ATP) to "walk" along the cytoskeleton [1]. Failure of the transport of motors is associated with various human diseases including Alzheimer disease, Huntington disease and amyotrophic lateral sclerosis [2, 3]. Understanding the mechanism of transport is thus an important task, for both fundamental cell biology and medical research. Furthermore, a full picture of intracellular transport offers a basis to design and construct new biological systems not found in nature.

1.1 Bidirectional transport

Intracellular transport along cytoskeleton is usually bidirectional [4]. Numerous different "cargos" have been reported to move bidirectionally, including lipid droplets in the fly *Drosophila melanogaster* [4] and in mammalian tissue-culture cells [5], human adenoviruses [6], and early endosomes (EEs) in *Dictyostelium discoideum* [7] and in the model fungus *Ustilago maydis* [8, 9]. In general, bidirectional motility of cargo is mediated by mechanoenzymes, so-called molecular motors, and occurs on the microtubules (MTs). It was suggested that cargo moves in a bidirectional fashion to allow the organelles to pass obstacles on tracks via sidewise stepping of moleular motors along MTs, thus to help delivering the organelles to their correct location [10, 11].

1.1.1 Microtubules

Microtubules are one of major components of the cytoskeleton in eukaryotic cells. Together with another major cytoskeletal system, the filamentous actin (F-actin), MTs mediate organelle and vesicle transport. In general, it is assumed that MTs support transport over long distances, whereas F-actin mediates short range organelle motility [12]. Besides this, MTs also play a role in maintaining cell structure, forming the spindle during mitosis as well as other cellular processes [13].

The fundamental subunits of a MT are $\alpha-$ and $\beta-$tubulin, which form a heterodimer of 8 nm length. The $\alpha\beta$ tubulin dimers polymerize end to end and form a protofilament. Thirteen of these protofilaments bundle into a hollow cylinder of about 23 nm in diameter and form a single microtubule [14] (see Figure 1.1).

An important feature of the microtubule structure is its intrinsic polarity. In each microtubule, the plus end refers to the fast-polymerizing end, which is also characterized by the exposure of β subunits, whereas the minus-end is usually embedded in a MT-organizing centre [13]. MTs are dynamic structures that elongate at the plus-end by adding tubulin dimers, or that rapidly shrink due to release of tubulin from the plus-end. MTs dynamically switch between growth (polymerization) and shrinking (depolymerization) phases [13] (see Figure 1.1 c), a process called "dynamic instability" [15]. The stability of a MT is determined by hydrolysis of guanosine triphosphate (GTP). Only GTP-bound tubulin dimers bind to the growing plus-end, which forms a GTP-cap at the end of the MT. When GTP gets hydrolysed by tubulin, the GTP-cap tuns into a guanosine diphosphat(GDP)-cap. This decreases the stability of the MT end and triggers the rapid release of tubulin dimmers. Thus, the switch between growing and shrinking of a MT depends on the GTP/GDP ratio at the MT plus-end. The phenomenon of dynamic instability was discovered in *in vitro* assays using MTs generated from purified tubulin [15]. However, in the living cells, MT dynamics are modified by MT-associated proteins, which could stabilize or destabilize MTs, resulting in considerable variations in the dynamic behaviours of MTs [16].

1.1.2 Molecular motors

Molecular motors are mechanical enzymes that move along cytoskeletal filaments by the hydrolysis of ATP into adenosine diphosphate (ADP) and inorganic phosphate. Motors convert the released chemical energy into a conformational change within the motor domain, which results in a step along the cytoskeletal element. MT-based motors include two families: kinesin and dynein. Both motors undertake steps of 8 nm along the MT [18, 19, 20], but they differ in their transport direction. Kinesins travel towards the plus end of MTs whereas dynein motors transport
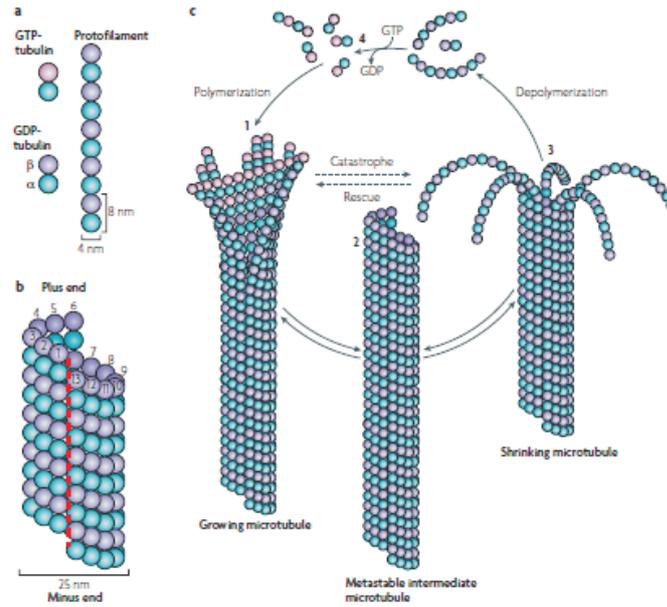
Figure 1.1: The constitution of a MT and its polarity shown in (a) and (b) while the dynamics of a MT is shown in (c). Image is taken from [17].

their cargos towards the minus end [21]. By this counteracting activity, both motors mediate bidirectional motility of their "cargo". The cargo can be diverse and includes organelles, vesicles, proteins and RNA complexes [10]. For instance, kinesins bind to mitochondria, as well as to lysosomes, receptor and adaptor proteins, and signalling-pathway interacting proteins [22]; cytoplasmic dynein transports elements of the Golgi apparatus, lysosomes, and late and recycling endosomes [23]. In *U. maydis*, kinesin and dynein are both involved in early endosome transport [24, 25].

Both kinesins and dynein walk along MTs by an alternating head or "hand-over-hand" mechanism [26, 27] and their binding sites on the microtubule surface overlap [28]. Thus opposite-directed motors compete for binding sites on the filaments and appear as "obstacles" for the competitors, which probably block each other on encounters in bidirectional transport. In vitro, quantitative data show that cytoplasmic dynein-coated beads exhibit lateral movements among MT protofilaments 5.1 times per μm on average, comparing with kinesin 0.9 times per μm on average [29]. This may offer as a possibility that motors are able to avoid collisions. However, how motors interact with obstacles is still unclear, particularly in living cells.

Most quantitative information on motor behaviour has hitherto been based on *in vitro* assays and therefore are often performed under non-physiological conditions. Thus the measured parameters of motor behaviour in vitro might not reflect the situation in a living cell and differ between different studies. An obvious example is given by the speed in intracellular traffic. *In vitro* studies have demonstrated that

the speed of a single dynein motors is measured to be $\sim 0.8\ \mu m/s$ [30, 31, 32] while the speed for conventional kinesin is measured to be $\sim 0.7\ \mu m/s$ [33, 34, 30]. Kinesin from the fungus *Neurospora crassa* shows a higher *in vitro* speed of $\sim 1.5\ \mu m/s$ [35]. Thus, variations of the measured speed occur in *in vitro* experiments, which might be due to the different kinesins used (e.g. fungal versus mammalian). However, in the *in vivo* study of peroxisome movements by localization of fluorescence imaging with one nanometer accuracy, Kural *et al* [20] show that dynein and kinesin move with average speeds of 1.7 $\mu m/s$ and 1.5 $\mu m/s$. More recently, in the *in vivo* study of early endosome motility in hyphae, both motors dynein and kinesin are moving at $\sim 2.0\ \mu m/s$ [24]. Along the same line, the difference between *in vitro* and *in vivo* experiment measurements also appears in the motor run length (i.e., the spatial length covered during consecutive motility). From *in vitro* data, the motor run length is typically 1 μm for kinesin [36, 37] and 2 μm for dynein [27]. However, *in vivo* experiments on EE motility show that kinesin and dynein motors can travel up to $\sim 10\ \mu m$ [24]. Moreover, studies have confirmed that the source of a motor has a significant impact on its biophysical properties. A good example is given by the force exerted on kinesin-3, which in *Dictyostelium discoideum* is found to be $5 - 6\ pN$ [7], whereas 0.15 pN is measured for kinesin-3 motor from mammalian neurons [38].

In conclusion, modelling using parameters from different species may be not reliable in understanding experimental results. Moreover, motility parameters measured from *in vitro* experiments do not always reflect that in living cells and can raise problems in extrapolating *in vitro* experimental studies from the results of *in vitro* work back to the biology of the intact organism. Furthermore, multiple motors can bind to cargos simultaneously *in vivo* [39], which might differ to transport with only one single motor. A simple example is that simultaneously binding of both kinesin and dynein motors to cargos allows the possibility of bidirectional transport on a single MT whereas one-motor binding scenario could not result bidirectional transport.

1.1.3   Mechanisms of bidirectional transport

Bidirectional transport is not a minor extension of unidirectional motion [10], as elements such as how often does a switch of direction occur in bidirectional transport need to be considered and these elements might strongly influence the transport. Recent technology advance, such as the use of the green fluorescent protein (GFP) for tagging organelles and proteins, and force measurements, are providing clues on the strategies employed by various organisms in bidirectional motility. Based on various experimental studies, three possible mechanisms have been put forward to explain bidirectional transport. These are summarized below (see [40, 41, 10] for

more detailed review).

1. The cargo simultaneously binds opposite-directed motors that are both active at the same time, thereby compete in a "tug-of-war". This hypothesis is consistent with a stochastic "tug-of-war" developed by Reinhard Lipowsky and co-workers [42]. This stochastic "tug-of-war" well predicts the number of motors moving the neuronal vesicles in comparison with experimental analysis [43]. Moreover, observation of slow movement segment of early endosome between fast motions in a *Dictyostelium* cell also supports the "tug-of-war" situation [7]. However, there is also evidence from *in vitro* experiment observations in contrast to the "tug-of-war" hypothesis, thus doubting this hypothesis. For example, stalling forces are balanced in each direction in *in vitro* lipid-droplet system [41] whereas from the hypothesis of "tug-of-war" one side would typically win by exerting more force than the opposition.

2. Both motors would be engaged simultaneously with a cargo but their activities would be coordinated so that competition does not occur. This concept is supported by experiments on lipid droplets in *Drosophila* embryos [44]. In that study the opposite-polarity motors are shown to be coordinated as a severe impairment of plus-end motion is observed due to alterations of minus-end motor activity. Moreover, using *Drosophila melanogaster* S2 cells, Ally *et al* in [11] demonstrate that mechanical interactions between opposite-polarity motors are shown to be necessary and sufficient for bidirectional organelle transport in living cells and suggest that any pair of opposite-polarity motors, provided they move along MTs, can activate each other.

3. The cargo would selectively and sequentially bind and/or release either retrograde or anterograde motors. Until recently, this mechanism has been ruled out in several systems as it has been shown in *in vivo* experiments on mitochondria or pigment granules that opposing motors are simultaneously and stably attached to the cargos; see review [10]. However, a recent study in the model fungus *Ustilago maydis* visualizes both motors (kinesin-3 and dynein) and their cargo - early endosomes in the living cells and demonstrates that dynein motors only bind to EEs in retrograde transport, whereas kinesin-3 constantly bound to the organelle [24]. Interestingly, the binding of dynein reverses the direction of the transport indicating that dynein either turns off the activity of kinesin-3 or overcomes kinesin-3 in a "tug-of-war" [24].

In the investigation of the stochastic "tug-of-war" model proposed by Lipowsky *et al* [42], they show that at most of the time there is only one type of motors bound to the filament [45]; in other words, the motors of other type are inactive. Thus the "tug-of-war" hypothesis, in some sense, agrees with that of coordination
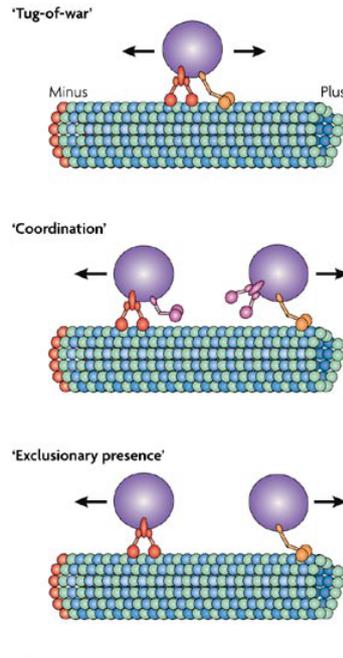
Figure 1.2: Description of three hypotheses for bidirectional transport. 'Tug-of-war' hypothesis: the cargo simultaneously engages retrograde and anterograde motors that compete in a "tug-of-war" manner. 'Coordination' hypothesis: both motors would be engaged simultaneously but their activities would be coordinated such that competition does not occur. 'Exclusionary presence' hypothesis: the cargo would selectively and sequentially bind and/or release either retrograde or anterograde motors. Image is taken from [46].

mechanism. In addition, in the bidirectional motility of EEs in *U. maydis* hyphae, both opposite-directed motors simultaneously bind to the cargo in the anterograde travelling whereas only dynein bind for retrograde travelling [24]. Thus different hypotheses do not exclude each other in the bidirectional motility of cargos in one system; instead, they may complement with each other in travelling.

1.2 Endosome motility in the fungal model system - *Ustilago maydis*

Ustilago maydis is a pathogenic plant fungus that causes smut disease on maize. It induces the formation of tumours at the stem, the leaves and in the corncob of the plants. *U. maydis* has a long history of being an attractive system for studying concepts and mechanisms of pathogenesis [47, 48, 49]. This fungus undergoes a number of morphological transitions throughout its life cycle. Particularly, it can exist as a non-pathogenic budding yeast cell as well as a hyphal cell; see Figure 1.3. Pathogenic development is initiated by two compatible cells that recognize each other, switch to hyphal growth and form the infectious hyphae, which can reach a

length of more than 100 μm. In recent years, numerous studies have demonstrated that MT-based long-distance transport of vesicles, organelles and most likely RNA is essential for filamentous growth and therefore pathogenic development of *U. maydis* [50]. Moreover, it emerges that the fundamental principles of long-distance transport and microtubule organization are conserved between *U. maydis* and humans (see Figure 1.4 (a)) [51]. This is reflected by the fact that the predicted proteome of *U. maydis* shares remarkably high sequence similarity with mammalian cells (see Figure 1.4 (b)) [52]. Thus, the fungus -*U. maydis*- offers a highly feasible system for the study of certain mammalian processes such as long-distance transport of early endosomes.

Bidirectional motility of early endosomes in *U. maydis* hyphae is thought to support recycling processes at the hyphal tip [9], which is related to the hyphal growth. The motility of early endosomes is microtubule based and occurs along antipolar MT bundles [16]. Most plus ends of MTs extend towards the growing tip and septum of the hyphae [53, 9] and the dynamics of long MTs in *U. maydis* is low comparing to the velocity of motors [16].

Organelle transport along MTs is supported by molecular motors that belong to kinesins and dyneins [21]. The genome of *U. maydis* encodes for 10 kinesins [53] and one dynein [54]. Surprisingly, only a small subset of kinesins is involved in tip growth, which includes a homologue of kinesin-1 and kinesin-3 [53]. The reported MT organization, with the plus-ends being directed towards the cell tip [53, 9] suggests that kinesin-3 mediates anterograde transport whereas retrograde trafficking of early endosomes depends on dynein [9]. To support retrograde transport of early endosomes, dynein accumulates at MT plus ends [9]. This concentration of dynein at MT plus ends requires kinesin-1, suggesting that dynein and kinesin-1 oppose each other on an unknown vesicle or organelles. When kinesin-3 delivers an early endosome to the dynein comet at MT plus-ends, dynein can capture this organelle and takes both the EEs and the associated kinesin-3 back towards sub-apical regions [9, 46]. This process is highly processive and organelles are not frequently diffusing into the cytoplasma [24]. Interestingly, *in vivo* experiments on early endosome motility in [25] indicates that dynein transports the organelles through the unipolar MT array near the cell ends and kinesin-3 takes over at the beginning of the medial antipolar MT array. This suggests that EEs switches MTs on which the active motors attached in the bipolar MTs. The cooperation of both motors mediates EE movements over the length of the entire cell.

In short, long-distance transport of organelles including early endosomes is essential in hyphal growth of *U. maydis* [53]. The motors that support EEs are minus-end kinesin-3 and plus-end dynein, and dynein is delivered to microtubule plus-ends by the motor kinesin-1.
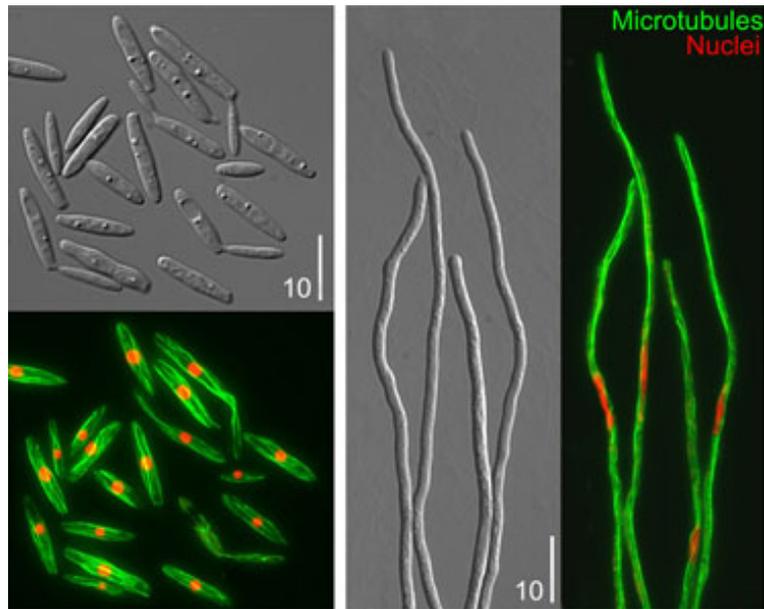
Figure 1.3: Image shows two different morphological states: yeast-like (left) and hyphal (right) cell; bar: $10\mu m$. Image is taken from [51].
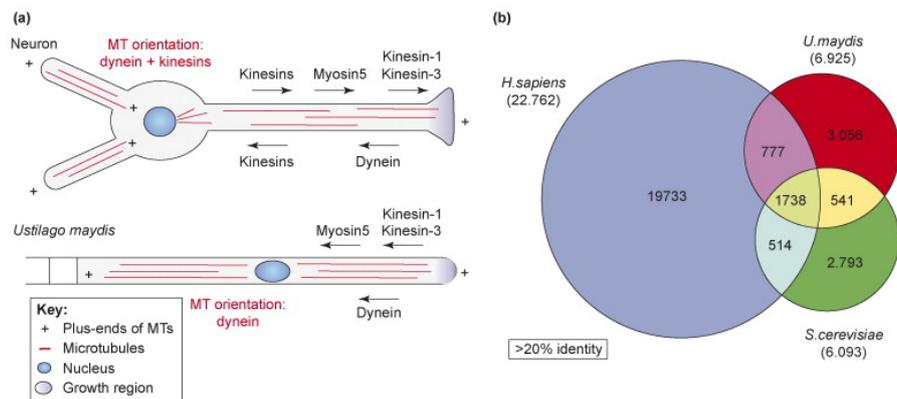
Figure 1.4: Similarities between *Ustilago maydis* and *Homo sapiens*. (a) The mammalian neuron and the fungal hypha are both elongated and expanded at cell poles. In addition, long-distance transport of organelles is based on MTs as well as a similar set of motors. (b) Sequence comparison of predicted proteins in *U. maydis*, *Saccharomyces cerevisiae* and *H. sapiens*, indicates that *U. maydis* shares a larger number of genes that are ($> 20\%$) identical to human. Image is taken from [51].

1.3   Summary of biological background

In intracellular transport, molecular motors are the key players that carry cargos along filaments. The detailed mechanisms of the active transport are still unclear. It is widely thought that the transport is controlled by specific molecules (e.g., kinase or phosphatase), however, theoretical modelling approaches in comparison with experimental analysis suggest stochastic "tug-of-war" [42, 7, 43]. When employing stochastic modelling to study the mechanisms of motor-based transport, most motility parameters are obtained from *in vitro* experiments and vary in different systems. These *in vitro* data may differ from those in living cells. Thus modelling using *in vitro* data has flaws. For instance, it is likely that attachment rates and detachment rates of motors to MTs depends on additional microtubule-associated proteins [55, 56], that motor run-length can be limited by obstacles along the track [57, 58] and that it depends on associated factors that we are just beginning to understand [59, 56]. To have reliable quantitative information in living cells, it faces great challenges. Fortunately, because of recent technology advances in living cell imaging, motors can be visualised in living cells [60, 61, 62]. This raises the possibility that mathematical models can be built on quantitative descriptions of motor behaviour in living cells. In particular, the model system *Ustilago maydis* not only shows similarities with humans but also offers as a system for real-time analysis of transport. In *U. maydis*, live observations of motors in long-range microtubule (MT) dependent transport have reported bidirectional motion of dynein and an accumulation of the motor at the polymerization-active (the plus-end) of the microtubule [9]; more recently, *in vivo* experiments show that early endosomes can move along the entire antipolar MT array with unipolar MTs at the cell ends, which suggests EEs switch MTs [25].

1.4   Thesis overview

This thesis aims to investigate mechanisms of motor cooperation for long-distance bidirectional transport along MTs in *U. maydis* by mathematical modelling, particularly using lattice models. Some known results and methods for lattice models are reviewed in Chapter 2. In Chapter 3, we use a two-lane lattice model (assuming no collisions between opposite-directed motors) and theoretically study the queuing properties induced by the bidirectional motion. This model together with a more sophisticated 13-lane lattice model (considering that a MT consists of 13 protofilaments) is used to investigate the mechanisms of dynein accumulation at MT plus ends, based on *in vivo* experiments and quantitative data. A complete description of this investigation is given in a paper reproduced in Appendix A. In Chapter 4, we generalize the 13-lane model and study the influence on the transport

properties from the lateral motion of motors on the multifilaments by mean-field approximations and numerical simulations. Detailed mean-field approximations are given in Appendix B and an example of C++ code used for the numerical simulations is given in Appendix C. In Chapter 5 we extend the two-lane model discussed in Chapter 3 to describe the bidirectional transport along an antipolar microtubule bundle and study the influence from MT switching behaviour. Finally, we conclude with a summary and outlook in Chapter 6.

Chapter 3 is devoted to developing a two-lane ASEP model that describes the coordinated motion of anterograde and retrograde motors sharing a single oriented microtubule. We assume that there is no collision between opposite-directed motors in the model. Using mean-field analysis we give approximate expressions for the size and distribution of the accumulation of dynein at the MT tip (tip size), and discuss queueing properties for motors entering this accumulation.

With quantitative data derived from *in vivo* observation of dynein in *U. maydis*, the two-lane ASEP model gives half of the experimentally measured tip size. We extend this model by including the information that each MT consists of 13 protofilaments [14] and dynein motors "dance" along MTs [63] to introduce a 13-lane ASEP model in Appendix A. Again with the same quantitative *in vivo* data, this more sophisticated 13-lane model also gives a similar number as that in the two-lane model. This deviation in tip size from experimentally measured size motivates to test the possibility of other processes at work in dynein accumulation. In Appendix A, by overexpressing peptides which block the interaction of the EB1 and dynactin and thus inhibit capturing dynein, it is shown that there is a reduction of about 60% in the dynein accumulation. The reduced number agrees well with the predicted number from both stochastic ASEP models. Thus, these *in vivo* experiments together with mathematical modelling suggest half of ∼55 dynein motors concentrated in a single comet is kept by an active retention mechanism involving an interaction between dynactin and EB1 and the other half is achieved by stochastic motion of dynein motors. This dual mechanism ensures that an excess of dynein motors offers a sufficiently large possibility that an arriving early endosome gets captured by the retrograde transport process.

The 13-lane ASEP model in Appendix A is further studied in Chapter 4 where we generalize the model to a multi-lane ASEP-like transport model for bidirectional motion of motors. We show that the ability of motors to change protofilaments can affect the transport efficiency. Particularly, the particle-direction change rate obtained from experiments is close to optimal in order to achieve efficient motor and organelle transport in a living cell, in that they balance efficient transport to the tip against the average delay at the tip. Moreover, we find a nonlinear scaling of the tip size with injection rate and an associated phase transition leading to pulsing states

characterized by periodic filling and emptying of the system.

Chapter 5 is devoted to extending the two-lane ASEP-like model in Chapter 3 to model bidirectional motility of early endosomes along an antipolar microtubule bundle. In our model, the MTs are linked to each other at the minus ends in the middle of the bundle and it is assumed that particles can switch between MTs. We find various types of distribution of organelles along the bundle depending on the model parameters. In particular, we show that even in an overall dilute situation, the organelles can exhibit accumulations near plus and minus ends depending on the MT switching rates. We also discuss how the switching rates influence the type of motor that dominates the active transport in the bundle.

The results presented in Chapter 3 have been published in *Phys. Rev. E* [64] by myself and my supervisors and the experimental image used in Figure 3.2 is produced by Dr. Martin Schuster. I did most of the analytical and numerical analysis and wrote part of the manuscript and Prof. Peter Ashwin wrote the rest of the manuscript. The Appendix A has been published in *EMBO J.* [65]. In this manuscript, Prof. Peter Ashwin and I conduct the mathematical modelling and non-linear regression while all the corresponding biological experiments and data analysis were provided by other coauthors. Prof. Gero Steinberg provided the overall project management and wrote the manuscript. The results presented in this chapter have been published in *J. Stat. Mech.* [66] by myself and my supervisors. I constructed the model, did most of the analytical and numerical analysis and wrote most of the manuscript. The results presented in Chapter 5 have been submitted [67] by myself and my supervisors. I constructed the model, did most of the analytical and numerical analysis and wrote most of the manuscript.

Chapter 2

Stochastic lattice models for intracellular transport

This thesis mainly concerns the bidirectional transport of molecular motors or organelles along MTs and constructs different stochastic processes (models) based on *in vivo* experiments in order to understand the bidirectional transport. By process, we mean the time evolution of the state for some real or hypothetical system. The state might be the velocity of a molecule, or the number of molecules at the MT plus end. The term *stochastic* is used to mean systems whose behaviour is non-deterministic. We say that a process is *deterministic* if a knowledge of its states to and including time t allows us to unambiguously predict its value at any infinitesimally later time $t + dt$ while a process is *stochastic* if a knowledge of its states up to and including time t allows us to probabilistically predict its value at any infinitesimally later time $t + dt$.

An important subclass of stochastic processes is memorlyess stochastic process which is termed as a *Markov process*. For them, the state of the system in the future only depends on the current state and independent of its history (in other words, the process is memoryless). When there are only finite or countable number of states in the system, the Markov process is called a *Markov chain*.

One of the important notions for stochastic processes is a *stationary distribution*. By *stationary distribution*, we mean a distribution of the states which remains the same under the time evolution. For a Markov chain, which can be described via a Markov transition matrix [68], the stationary distribution is the eigenvector of transition matrix corresponding to the eigenvalue 1 [68]. The uniqueness of the stationary distribution can be ensured by *ergodicity* which means that any state can be reached from any other state under a common constant step size for a (discrete-time) Markov chain with finite states. Moreover, the ergodicity also ensures that the stationary distribution can be evaluated by time average independent of initial conditions [68].

In modelling complex systems, stochastic approaches have proven to be a powerful tool, e.g., Brownian motion well describes the motion of particles suspended in a fluid. Particularly, in modelling intracellular transport, stochastic lattice models (Markov chains) have been widely employed to understand the intrinsic of the transport in a qualitative way [69, 70, 71, 72, 73, 74]. Besides applications on intracellular transport, stochastic lattice models have also been used to model a wide range of other transports, such as vehicle traffic [75, 76, 77, 74].

Two basic elements of a lattice model are particles and a lattice which serves as "tracks" for particles. For intracellular transport, particles can be motors while a lattice can be a MT where motors move. The lattice is usually discretized into discrete sites corresponding to a step space of particles. In the lattice, the interaction among particles and lattice during the transport is characterized by the transition of particles between sites during the evolution of the system, which are quantified into transition rates. If the transition rates only depend on the current state itself and independent of history of the system, then the process is a Markov chain and the corresponding Markov transition matrix is composed of transition rates. More generally, the time evolution of the probability of finding a state $\mathcal{C}$ in a continuous-time Markov chain is governed by a master equation [78]:

$$\frac{\partial P(\mathcal{C}, t)}{\partial t} = \sum_{\mathcal{C}' \neq \mathcal{C}} P(\mathcal{C}', t) W(\mathcal{C}' \to \mathcal{C}) - \sum_{\mathcal{C}' \neq \mathcal{C}} P(\mathcal{C}, t) W(\mathcal{C} \to \mathcal{C}')$$

with some initial condition $P(\mathcal{C}, 0)$. Here $P(\mathcal{C}, t)$ denotes the probability of finding the state $\mathcal{C}$ in the system at time t, and $W(\mathcal{C}' \to \mathcal{C})$ represents the transition rate from state $\mathcal{C}'$ to state $\mathcal{C}$ which is independent of time t. If some power of the transition matrix W has only positive elements (which indicates the ergodicity), then in the time limit $P(\mathcal{C}) = \lim_{t \to \infty} P(\mathcal{C}, t)$ gives the stationary distribution which is invariant under the time evolution and can be evaluated by time average independent of initial conditions.

Intracellular transport in living cells is usually considered to be in statistically stationary states (i.e., statistical equilibrium). In this thesis, we investigate lattice models for particular intracellular transport in living cells. For convenience, all the stochastic processes we are considering are assumed to be Markov chains and they are in most cases further assumed to be ergodic to ensure a unique stationary distribution independent of initial conditions.

2.1 Asymmetric simple exclusion process

One of the simplest and well studied examples of lattice models is the asymmetric simple exclusion process (ASEP). The ASEP has been developed into one of the

standard models for investigating non-equilibrium systems in statistical physics. In the mathematical literature, the terminology *simple exclusion* is first given by Spitzer [79] and many rigorous mathematical statements on ASEP have been demonstrated (see e.g., [80, 81]).

ASEP was first introduced in 1968 as a model for transport of ribosomes along the mRNA in the process of translation [82]. The translation proceeds in four separate stages: activation; initiation, where ribosomes bind to a start codon at one end of an open reading frame of an mRNA; elongation, where amino acids are provided to the ribosome via transfer RNA molecules, and are added to the growing polypeptide; and finally termination, where ribosomes detach from the mRNA at a stop codon, and the polypeptide chain is released. In this ASEP model, particles are ribosomes while left and right open boundaries are the stop and start codons respectively. In general several ribosomes can elongate at the same mRNA at once; the hard-core interaction between ribosomes is described by the exclusion principle in the model. More recently, based on certain modifications of the ASEP model, different factors such as limited resources of ribosomes [83] or dynamic resources of tRNA [84] have been investigated in the process for mRNA translation.

In the following, we give a formal description of the ASEP model and review some results on certain statistical quantities in the stationary (steady) state of this model.

2.1.1 Model definition

The ASEP model is defined on a one-dimensional lattice discretized into finite sites, say N. Particles hop to the nearest-right site with rate p if the target site is empty. Each site can be occupied by at most one particle, subject to the exclusion principle. This also refers to *totally asymmetric simple exclusion process* as hopping direction of particles are totally biased. Let $\tau_i(t)$ denote the occupancy of any site $i \in \{1, 2, \cdots, N\}$ at time t in the system, then $\tau_i(t)$ can only have values 0 or 1. Any state of the system can be described by a configuration $\mathcal{C} = (\tau_1, \tau_2, \cdots, \tau_N)$.

At the boundary sites $i = 1, N$, there are two typical considerations. One is the periodic boundary condition where the lattice is closed by connecting the sites N and 1 with the same constant hopping rate p. In this case, the total number of particles is conserved under the time evolution and a uniform distribution over all the possible states forms in the steady state as time tends to infinity. The other is the open boundary condition where particles are interacted with environment in such a way that they are injected into site 1 with rate α, subject to the exclusion principle, and exit at site N with rate β; see Figure 2.1. In this boundary condition, the total number of particles in the system is no longer conserved, in contrast to the periodic boundary condition and the system shows rich behaviours in the steady
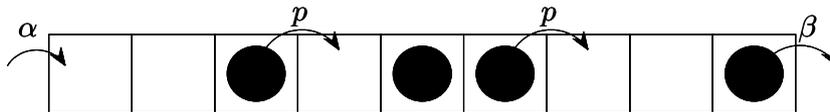
Figure 2.1: Schematic diagram showing the ASEP with open boundary conditions. Particles hop to the next site on the right with rate p if it is empty; a particle injects into the first site with rate α if it is empty while exits from the last site with rate β.

state.

2.1.2 Properties of ASEP in steady state

For investigating properties of transport systems in the steady state, among the research interests are the density (mean occupancy) at each site $\rho_i := \langle \tau_i \rangle$ and the mean flux (current) cross each site J_i, where $\langle \cdot \rangle$ denotes the mean (expectation). Particularly, the current J_i is usually considered as a characterization of efficiency in the transport.

For the above continuous-time discrete-state ASEP model, the current can be expressed as $J_i = p \langle \tau_i(1 - \tau_{i+1}) \rangle$. Using mean-field approximation (which neglects the correlation of two consecutive sites), this current is approximated as $J_i \approx p\rho_i(1 - \rho_{i+1})$. Under the periodic boundary condition, each state is known to have equal probability in the steady state, which follows a constant density ρ for all sites and so for the current, i.e., $J \approx p\rho(1 - \rho)$, with a conserved particle number ρN. This approximation is actually exact in the limit where $N \to \infty$ through a combinatorial calculation [85]. In the open boundary conditions, the current-density relation $J = p\rho(1 - \rho)$ also holds in the continuum limit [86]. In contrast to periodic boundary condition, the ASEP with open boundary conditions shows rich behaviours. For the two boundary rates α, β, we can think of two virtual sites $i = 0, N+1$ with densities α/p and $1 - \beta/p$ respectively where $\alpha, \beta < p$ are assumed. Depending on these two parameters, three different phases can be reached [85]:

Low-density phase (LD). In the parameter region $\alpha < \beta$ and $\alpha/p < 1/2$, the injection rate dominates the system's behaviour and determines the current and density profile far away from the boundaries as:

$$J = \alpha(1 - \alpha/p), \quad \rho = \alpha/p.$$

High-density phase (HD). In the region $\alpha > \beta$ and $\beta/p < 1/2$, the system's behaviour is dominated by the exit rate:

$$J = \beta(1 - \beta/p), \quad \rho = 1 - \beta/p.$$

Maximum-current phase (MC). In the parameter region $\alpha/p > 1/2$ and $\beta/p > 1/2$, a maximum current is reached, which is independent of the parameter values.

$$J = p/4, \quad \rho = 1/2$$

It is clear to see that transitions in the density between (LD/HD) and (MC) are continuous while the transition between (LD) and (HD) is discontinuous. The corresponding phase diagram is shown in Figure 2.2. The mechanisms under which this phase diagram is governed have been investigated following the obtained exact solutions of density and current. One mechanism is the *extreme current principle* first proposed by Krug [87] and later developed into a more general description for driven systems [88, 89]. It argues that in systems where the density profile is monotonic in space and bounded due to finite values of the left and right boundary densities $\rho_{L,R}$ and in the limit of an infinite system, there is a bulk region in which the density is constant, the current of particles J is governed by the extreme principle

$$J = \begin{cases} \max_{\rho \in [\rho_R, \rho_L]} J(\rho), & \rho_R < \rho_L \\ \min_{\rho \in [\rho_L, \rho_R]} J(\rho), & \rho_L < \rho_R \end{cases}$$

Another mechanism is called *domain wall theory* first proposed by Kolomeisky [90], which is able to make general predictions even for multi-species problems in steady state as well as in transient states [91, 92, 93]. The dynamics of domain wall (shock) can be viewed as a random walk at rates $V_{\pm} = \frac{J_{\pm}}{\rho_+ - \rho_-}$ to the left and right respectively with a net rate $V = V_+ - V_-$. Here, the parameters $J_{\pm}$ and $\rho_{\pm}$ are the fluxes and densities respectively in the right (left) domains separated by the shock. A zero net rate indicates the existence of a localized shock. This occurs when $\alpha = \beta < p/2$ in the ASEP model. Moreover, with this choice of parameters, the shock can appear at any site in the space domain, leading to the linear density profile [90].

An important property of the ASEP is its particle-hole-symmetry, i.e., the identical behaviour of the model under the symmetry operations: $\alpha \leftrightarrow \beta$ and $\tau_i \leftrightarrow 1 - \tau_i$ for every site i. This also helps to obtain the phase diagram.

2.2 Generalizations of ASEP

The ASEP introduced in the above section is the simplest lattice model describing unidirectional transport with hard-core interaction[1] between particles. Various modifications have been made to include some realistic details even for unidirec-

---

[1] "Hard-core interaction" is used to describe the interaction between particles to compete for a single binding site, resulting that each site can be occupied by one particle at most.
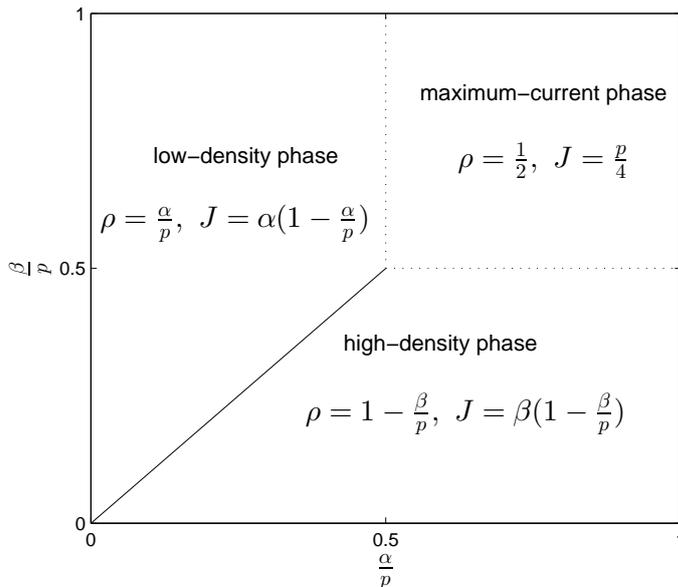
Figure 2.2: Phase diagram of the ASEP with open boundary conditions described in Section 2.1.1. The solid line shows a first order transition between low-density and high-density phase while dashed lines show continuous transitions between low-/high-density and maximum-current phase.

tional transport. For instance, ASEP with quenched disorder in hopping rates has been employed to understand the effects from inhomogeneous transition rates in intracellular transport, e.g., due to permanent obstacles on the track [94, 95] or dynamical obstacles (or defects) on the track [96]. Similarly, ASEP with finite resources which modify the injection and exit rates to be dependent on the sources available in the environment, has also been discussed [97, 98, 84, 99]. Additionally, to include scenarios such as active motors are likely to detach from MTs (due to their limited run length) and diffusive motors also have the ability to bind to MTs, the detachments and attachments have been included in the ASEP [100]. This extended model with detachments/attachments has been used to compare with *in vitro* experiments in investigating molecular crowding [74]. The detached motors are further modelled via diffusion process in [101, 102]. In addition, dynamics of MTs have also been included in ASEP [103]. Moreover, to include a complex network structure of MTs leads to a consideration of coupled multiple tracks with ASEP on each track [104, 105, 63, 106, 107]. Particularly in [104], an ASEP on parallel tracks coupled via junctions is first introduced to model traffic flow on a road network. This simple coupling allows particles on a single track to step into either of the parallel tracks in the unidirectional ASEP and thus modifies the phase diagram as well as the density-current relation. This junction mechanism offers an approach to model complex network structures such as in [107] where they argue that the disorder in the topology of vertices of the network crucially modifies the transport features.

Combination of these details can exhibit additional effects on the transport; see e.g. [108, 109, 110, 111].

Intracellular transport is usually bidirectional and driven by opposite-directed motor proteins (e.g., kinesin and dynein). Similar to the detachement/attachement in unidirectional ASEP models, there are bidirectional ASEP models where two opposite-directed motors move on a single MT and they may detach into a diffusive phase [112, 113]. Particularly in [113], the authors find clusters formed by motors moving in opposite directions, forming stationary blockages on a single MT filament. The authors in [114] note that the former models may be "unrealistically inefficient due to jam formation" and propose possible solutions to this problem by modifying the dynamics of the MT. Lui *et al* [115] consider another model where exclusion only applies to motors moving in the same direction; the presence of a motor in the opposite direction modifies the rate at which motors can enter the site. Muhuri *et al* study another bidirectional ASEP model where particles on a single lane can switch directions [116, 117]. Another ASEP-like modelling approach for bidirectional transport is using so-called bridge models introduced in [118] where two opposite-directed species can exchange on a single lane. This bridge model has been further studied [119, 120] and extended [121, 122]. In particular, in [121] the bridge model is extended with two junctions between one and two lanes; the one-lane section in the middle supporting both species is considered as a bridge with specie exchange and the opposite-directed species move on different lanes in the two-lane sections. Similarly, Jelić *et al* [123] introduce another bidirectional model with junctions where the bottleneck (the one-lane section in the middle) only supports one direction in contrast to the bridge model in [121]. In another approach for bidirectional transport, Juhász introduces a two-lane ASEP [124] with opposite-directed particles moving in separate lanes to avoid collisions similar to the two-lane section in [121, 123] and particles can change directions by changing lanes which couples the transport on the two lanes. The details such as quenched disorder are also applicable and discussed in the bidirectional transport models; see e.g., [125]. In the following, we give a more detailed review of the two-lane bidirectional ASEP introduced by Juhász [124], which is similar to the model we discuss in Chapter 3.

The two-lane ASEP introduced in [124] is a continuous-time stochastic process where transitions occur independently and randomly after an exponentially distributed waiting time and is confined to a lattice with two parallel lanes, one for each direction of motility; see Figure 2.3. Each lane consists of N sites and supports predefined unidirectional transport, say the up lane serves for right-directed motility while the down lane serves for the left-directed. Particles in each lane hop with rate p which is set to be 1 and other rates are scaled by p, and can change lanes with rate $p_d(p_u)$ inversely proportional to the length of lattice N from up lane to down

lane (from down lane to up lane). The dynamics of the process on the two lanes are coupled via these lane change events. In addition, injection at the first (last) site of up (down) lane occurs with rate α while exit occurs with rate β at last (first) site of the up (down) lane. All the transitions can occur only when the target site is empty. From the symmetric injection and exit rates in the two lanes, one can see that this stochastic process possesses the particle-hole symmetry as the ASEP in Section 2.1.

In the two-lane ASEP model with weakly coupling where $p_{u,d}$ are in the order of $O(1/N)$ (i.e., $\Omega_{u,d} = p_{u,d}N$ is in order of $O(1)$), by scaling $x = i/N$, in the continuum limit $N \to \infty$, the system is described by the partial differential equation for the local density [124], say $\rho(x,t)$ for the up lane (similarly for the density on the down lane σ),

$$\frac{\partial \rho(x,t)}{\partial t} + \frac{\partial J_u(\rho(x,t))}{\partial x} = S_u(\rho(x,t)).$$

Here $S_u(\rho(x,t))$ is the source term written as $S_u = \Omega_u \sigma(1-\rho) - \Omega_d \rho(1-\sigma)$ and $J_u(\rho)$ is the current as a function of the density in the steady state in the corresponding system without non-conserving processes (i.e., $S_u(\rho(x,t)) = 0$), which is simply as $J_u = \rho(1-\rho)$. In the steady state where $\partial_t(\rho(x,t)) = \partial_t(\sigma(x,t)) = 0$, the density profiles $\rho(x)$ and $\sigma(x)$ satisfy the coupled differential equations:

$$(2\rho - 1)\frac{d\rho}{dx} + \Omega_u(1-\rho)\sigma - \Omega_d\rho(1-\sigma) = 0; \tag{2.1}$$

$$(2\sigma - 1)\frac{d\sigma}{dx} + \Omega_u(1-\rho)\sigma - \Omega_d\rho(1-\sigma) = 0. \tag{2.2}$$

Subtracting the two differential equations yields the obvious result that the total net current $J = \rho(1-\rho) - \sigma(1-\sigma)$ is constant. A simple case is of symmetric coupling where $\Omega_u = \Omega_d = \Omega$. In this case the total net current is zero and hence there will be either $\rho = \sigma$ ("equal density") or $\rho = 1 - \sigma$ ("complementary density"). Moreover, for $\alpha \neq \beta$ the density profiles in the bulk are identical to that of the standard ASEP in these phases and for $\alpha = \beta$ the density profile might be polynomial in contrast to the linear density profiles in the standard ASEP. For asymmetric coupling where $\Omega_u \neq \Omega_d$, the system shows a variety of phases including localized shocks; see Figure 2.4 as an example of SH phase. In general, besides this SH phase, there are also LL, HH, LS and LH phases and we refer to [124] for a detailed analysis of phase diagrams in this model.

Note that this two-lane ASEP model introduced by Juhász is accompanied by symmetry boundary conditions. In general, we can have four general boundary conditions $\alpha_\pm, \beta_\pm$, not necessarily symmetric. We discuss the two-lane ASEP with boundary condition $\alpha_- = \beta_+ = 0$ in Chapter 3 and with certain inner-related four boundary conditions in Chapter 5. It remains to study the transport properties for four general boundary conditions. Clearly, symmetry is lost and extra parameters
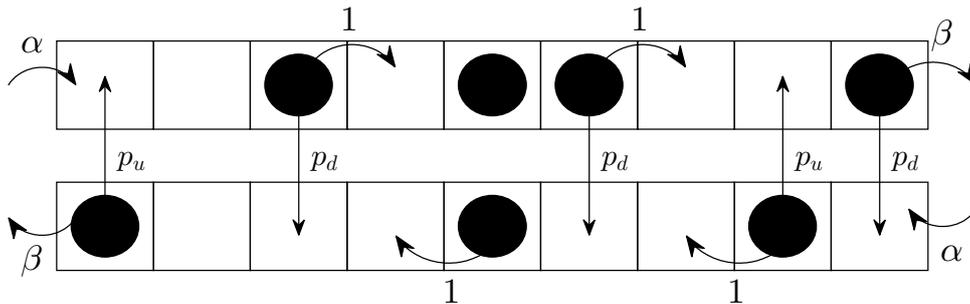
Figure 2.3: Schematic diagram showing a two-lane ASEP with opposite hopping directions and symmetric open boundary conditions. Particles on the up (down) lane hop to the next site on the right (left) with rate $p = 1$ subject to the exclusion principle; a particle injects at rate α if it is empty while exits at rate β.

increase the difficulty in characterizing the general model.

2.3 Numerical methods

In this section, we review two numerical algorithms used to simulate stochastic lattice models such as those mentioned in the above sections. One is the Monte Carlo method, which approximates the continuous-time stochastic process by updating with small fixed time step h_t. The other is the Gillespie algorithm.

For the Monte Carlo method, there are different schemes in the update for each time step. For example, in so-called *random sequential update*, every single transition of one particle is chosen randomly and sequentially; in this scheme, on average, every particle is updated once during each time step. Another scheme is called *parallel update* where every particle is updated in one time step. In addition, the so-called *sub-parallel update* divides the whole lattice into several subunits and particles within each subunit are updated at the same time step. One more choice for the update is the *ordered sequential update* in which all particles are updated in the each time step but in a predefined order. In all the above update schemes for the Monte Carlo method, the time step keeps unchanged in the time evolution and in each time step the chosen particles may be not allowed to take steps due to the occupancy of the target sites.

In contrast to the Monte Carlo method, the Gillespie algorithm gives random time steps and one allowable transition in each time step. This Gillespie algorithm is firstly introduced by Gillespie for simulating chemical reactions [126] and is reviewed in [127] with further improvements. The procedure of the original Gillespie algorithm for a stochastic process $X(t)$ is stated as follows [126]:

1. Initialize the time $t = t_0$ and system state $X(t_0) = \mathcal{C}$;
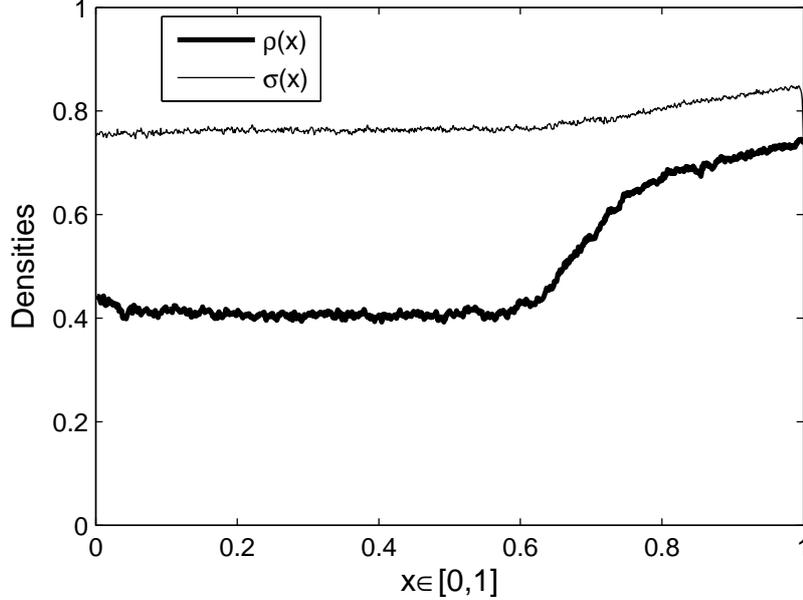
Figure 2.4: Numerical illustration of a localized shock phase near continuum limit. Parameters are given as $\Omega_d = 2$, $\Omega_u = 0.4$, $\alpha = 0.45$ and $\beta = 0.25$ with a lattice size of $N = 1000$. The x-axis is a scaled variable $x = i/N$. The bold line shows the density profile for the up lane, i.e., $\rho(x)$ while the thin line shows for the down lane $\sigma(x)$.

2. For the system in state $\mathcal{C}$ at time t, evaluate all allowable transition rates $a_j(\mathcal{C})$ and their sum $a_0(\mathcal{C}) := \sum_j a_j(\mathcal{C})$;

3. Generate two random values $r_{1,2}$ from a uniform distribution on $[0, 1]$ and calculate

$$h_t = \frac{1}{a_0(\mathcal{C})} \ln \left(\frac{1}{r_1} \right), \quad j = \min \left\{ j_2 : \sum_{j_1=1}^{j_2} a_{j_1}(\mathcal{C}) > r_2 a_0(\mathcal{C}) \right\}.$$

4. Update time with $t = t + h_t$ and the jth transition to give the new state;

5. Record $X(t)$; return to step 2 or end the simulation if t is larger than a given maximum time t_{max}.

The Gillespie algorithm is efficient and accurate in taking "real" transitions in each time step, however we remark here that the cost is paid by spending time in step 3 for the calculations in simulations. The Monte Carlo method is also accurate with sufficient small time step h_t and is expected to converge to the Gillespie algorithm as the fixed time step $h_t \to 0$. However, for small h_t, it takes relatively long iterations to reach statistically stationary state. A large time step in Monte Carlo method can speed up the simulations; however, different update schemes might produce different results. In addition, the time step h_t in Monte Carlo methods is predefined and it might be difficult to find out how small a time step can be

sufficient to produce accurate results. In this thesis, we use both Gillespie algorithm and Monte Carlo method to check our results, except for some scenarios where the time cost for Gillespie algorithm is too long and we use Monte Carlo method only.

Chapter 3

Queueing induced by bidirectional motor motion near the end of a microtubule

Recent live observations of motors in long-range microtubule (MT) dependent transport in the fungus *Ustilago maydis* have reported bidirectional motion of dynein and an accumulation of the motor at the polymerization-active (the plus-end) of the microtubule. Using quantitative data derived from *in vivo* observation of dynein has enabled us to develop an accurate, quantitatively-valid ASEP model that describes the coordinated motion of anterograde and retrograde motors sharing a single oriented microtubule. We give approximate expressions for the size and distribution of the accumulation, and discuss queueing properties for motors entering this accumulation. We show for this ASEP model, that the mean accumulation can be modelled as an $M/M/\infty$ queue (i.e., a queue where arrive and leave with memoryless property and there are infinite "servers") and the queue is Poisson distributed with mean F_{arr}/p_d. Here F_{arr} is the flux of motors that arrives at the tip and p_d is the rate at which individual motors change direction from anterograde to retrograde motion. Deviations from this can in principle be used to gain information about other processes at work in the accumulation. Furthermore, this work is a significant step towards a mathematical description of the complex interactions of motors in cellular long-range transport of organelles.

The chapter is organized as follows: in Section 3.1 we introduce a stochastic exclusion model for bidirectional motion of dynein. In Section 3.2 we analyse the equilibrium distributions of the model using mean-field approximations. This is used to perform quantitative estimates of the size of the accumulation at the tip in Section 3.3. Finally, in Section 3.4 we discuss predicted queueing properties of motors in the tip. Few authors have explicitly considered queueing properties of motors (Arita [128] is an exception) and we suggest that precise measurements of

queueing properties will in future be an important way to test models and to gain a better understanding of the intracellular transport processes.

3.1 Modelling bidirectional motor motion

The model we consider here is closest to the one introduced by Juhász [124] among the models for bidirectional transport reviewed in Section 2.2 of Chapter 2. In that model, he considers a system where indistinguishable particles are transported in to the right on one lane (say A) and to the left on a second (say B), and where particles can switch lanes at a certain rate. This in principle permits much larger fluxes of motors in both directions than observed in [113] as the motions in each direction are separated from collision. As molecular motors only perform unidirectional motion on an oriented MT, this model poses the question of how one can use the model to understand the coordination of real *in vivo* transport processes unless one interprets the two lanes A and B as being an antiparallel arrangement of microtubules.

Nonetheless, recent experiments suggest that head-on collisions of kinesin and dynein on a single microtubule are rare and, at least away from any build-ups of motors, we can interpret the lanes of [124] as independent bidirectional motion of the motors; the switching of lanes simply correspond to dynein moving from active retrograde to passive anterograde transport. Because of this, we interpret the ASEP process of [124] as modelling a coordinated bidirectional motion of individual dynein motors on a single MT. Although [124] only considers one species of motor that moves in antiparallel lanes, we interpret this as motion on a single MT in the following way: We assume that dynein moves under their own power in one direction, but they are carried by kinesin-1 bound to the dynein while moving in the other direction. The entire motion is assumed to take place on a single MT.

3.1.1 Assumptions for the model

Consider an oriented MT aligned from left (minus end) to right (plus end) parametrized by a spatial variable x. There are typically several populations of motors that may use a single MT *in vivo*, and in this model we concentrate on one of these; a dynein that moves to the minus end when bound to a MT, but which can be carried as a cargo of a kinesin to the plus end. We assume:

H1 All motors are one of two types- moving either to the right or to the left.

H2 Right and left moving motors pass without interaction, but there is an "exclusion principle" that means a motor can only move forwards if the site ahead is free of motors of the same type.

v_+	velocity to right	1.66	$\mu m s^{-1}$
v_-	velocity to left	1.76	$\mu m s^{-1}$
M_a	mean anterograde run-length	41.89	μm
M_r	mean retrograde run-length	62.37	μm
F_{in}	flux of anterograde dynein at a distance L from tip	1.06	s^{-1}
h_s	space step	8	nm
L	length of microtubules in simulation	10	μm

Table 3.1: Parameters using in the simulations. The values for $v_\pm$, $M_a = v_+/p_d$, $M_r = v_-/p_u$ and F_{in} are from *in vivo* experiments on *Ustilago maydis*; see [65]. The space step h_s corresponds to the size of the monomers making up the MT and is taken from [129]. The length L of the simulation corresponds to the field of view used for the kymographs.

H3 In the dilute state, the motors move at a mean velocity v_+ and v_- to the right/left respectively.

H4 There is a random switching of direction where right-moving motors change to left-moving at a rate p_d, and left-moving motors change to right-moving at a rate p_u, where $p_{d,u}$ can be expressed by velocities and $M_{a,r}$, the mean free run length of left (right) moving motors before turning as $p_d = v_+/M_a$ ($p_u = v_-/M_r$).

We are particularly interested in the boundary conditions inferred from these experiments for a single MT at the hyphal tip of the fungus *Ustilago maydis* [65]. For this reason we assume

H5 The right boundary of the MT has no-flux boundary conditions.

H6 The right-moving motors appear at the left boundary with flux rate $\alpha_+ = F_{in}$ while left-moving motors exit without impediment.

Finally we assume:

H7 The system is in statistical equilibrium.

This suggests an ASEP model with two lanes; assumptions (H1-H4) are essentially the same as considered by Juhász [125], though we consider different boundary conditions (H5-H7). In that paper right moving motors exit without impediment, while here they cannot exit. The effect of this is that the predictions in [125] on net flux rates is not applicable here; assumptions (H5-H7) imply that the net flux must be zero. Table 3.1 gives measured or estimated values for the parameters discussed.

3.1.2 A discrete model for bidirectional coordinated motor motion

We discretize the single MT into two notional tracks; one for motors (dynein carried by kinesin-1) going towards the plus-end, and one for motors (dynein) going towards the minus-end. On each track we assume there are sites separated by steps of length h_s; we refer to a "site" as an adjacent location on both tracks; this is illustrated in Figure 3.1. Let $\tau_i^\pm$ represent the state of the system for $i = 1, \cdots N$. The model updates this as time progresses to give $\tau_i^\pm(t)$; in the rightwards direction, $\tau_i^+ = 0$ if the site is empty and $\tau_i^+ = 1$ if it is occupied; similarly $\tau_i^-(t)$ encodes the motion of leftwards-moving motors; see Figure 3.1.
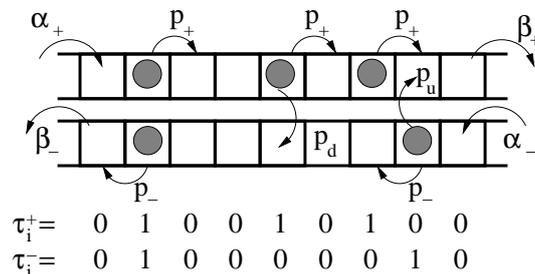
Figure 3.1: Schematic diagram of the states and transition rates for the ASEP approximating bidirectional motion of the particles representing motors. The "plus-end" of the MT is on the right, and each track has dynein motors (represented as filled disks) moving in only one direction, carried to the right by kinesin-1 on the upper track, and moving to the left under their own power on the lower track. The motors move as shown with rates p_+, p_-. They change direction with rate p_d (down to the left moving track) or p_u (up to the right moving track). Motors are injected into the $+/-$ tracks at rate $\alpha_\pm$ and leave at rate $\beta_\pm$ as shown.

We formulate a model using H1-H4 by assuming the following occur at given rates: occupants of $+$ sites move one step to the right with rate p_+ if the site is empty (an exclusion principle) while occupants of the $-$ sites move one step to the left with rate p_- subject to a similar exclusion principle. We assume that changes in direction from right-going to left-going occurs with rate p_d while from left-going to right-going occur with rate p_u, with the obvious exclusion principles blocking the possibility of more than one particle at any site. In the dilute situation, the rates, in terms of H1-H4 and h_s can be written

$$p_+ = \frac{v_+}{h_s}, \quad p_- = \frac{v_-}{h_s}, \quad p_d = \frac{v_+}{M_a}, \quad p_u = \frac{v_-}{M_r} \tag{3.1}$$

Figure 3.2 shows a comparison from [65] of an experimentally measured kymograph (a time-distance graph) showing the motion of photo-activated dynein moving on a single MT near a hyphal tip of *Ustilago maydis*, and a simulated kymograph using the model illustrated in Figure 3.1 with parameters in Table 3.1. The param-

eters for the simulation are obtained from experimental images such as Figure 3.2 by measurement of the slopes of the observed kymograph traces (to give $v_{\pm}$), the frequency of turning of left- or right-going traces (to give $p_{u,d}$ and hence from (3.1) M_a and M_r) and the flux rates (to give the boundary conditions for the simulation). In [65], the turning rate is extracted by measuring the fraction of motors passing a fixed reference point that have travelled less than a given distance past this point before turning; this is fitted to an exponential distribution with mean distance M_a (resp. M_r) and then (3.1) is used to give $p_{u,d}$. For more details of experimental measurement of the parameters see [65]. We note here that :

- From Table 3.1, the two velocities $v_{\pm}$ are of similar magnitudes and individual motors are visible as they are relatively dilute on MT away from the end of the MT.

- The motors moving in opposite directions seem to pass each other with no measurable interaction, suggesting that the two-lane model is reasonable.

- The turning rates are small, meaning that the majority of motors move from one end of the MT and enter an accumulation that is at the plus-end of the MT; the mean free run-length is longer than the illustrated section of MT.

- Individual motors can be observed to enter the tip, remain there for some time and then leave. We will be concerned with estimating the *tip size*, i.e. the average number of motors that are queued at the tip at any one time.

3.2 Mean field analysis of equilibrium states

The ASEP model in Figure 3.1 is not amenable to explicit analytic solution and so we use a mean field approximation as in [125] to reduce the system to an approximating PDE. If we define

$$\rho_i = \langle \tau_i^+ \rangle, \quad \sigma_i = \langle \tau_i^- \rangle$$

to be the average occupancy of site i where the average is over an ensemble of initial states, then a mean field approximation assumes that occupancy properties of the adjacent sites are independent of each other. This gives the approximation

$$
\begin{aligned}
\frac{d\rho_i}{dt} &= p_+\rho_{i-1}(1-\rho_i) - p_+\rho_i(1-\rho_{i+1}) - p_d\rho_i(1-\sigma_i) + p_u\sigma_i(1-\rho_i) \quad (3.2) \\
\frac{d\sigma_i}{dt} &= p_-\sigma_{i+1}(1-\sigma_i) - p_-\sigma_i(1-\sigma_{i-1}) - p_u\sigma_i(1-\rho_i) + p_d\rho_i(1-\sigma_i).
\end{aligned}
$$

Simulation

Experiment

1.5s

1μm
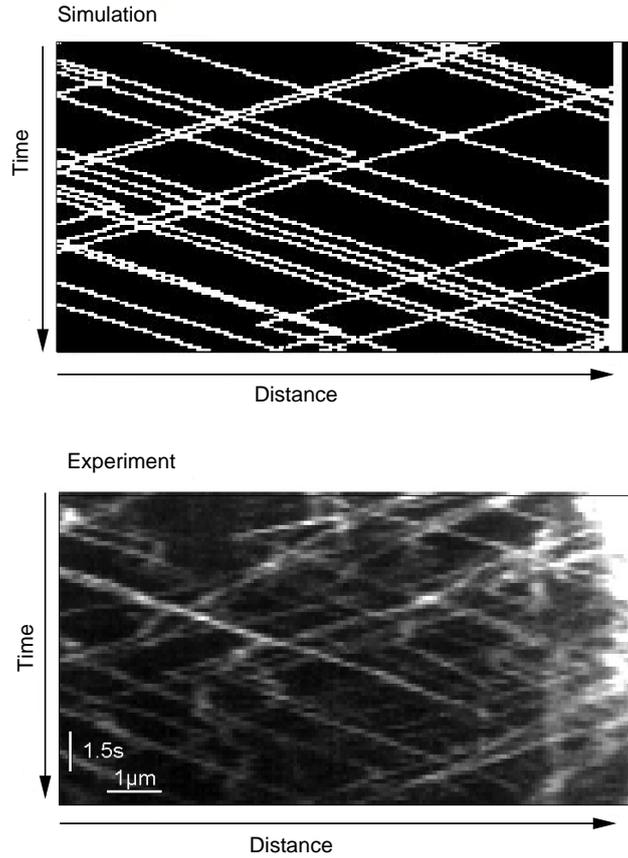
Figure 3.2: Top: a simulated kymograph using the model in Figure 3.1 and parameters in Table 3.1. Bottom: an experimentally measured kymograph showing dynein motion over $10\mu m$ near the hyphal tip of the fungus *Ustilago maydis*, obtained using methods described in [65]. Dynein moves away from the tip under its own power, and is carried by kinesin-1 towards the tip; it is visualised by fluorescent GFP attached to endogenous copies of the dynein. Observe (a) the presence of an accumulation of dynein on the right hand side in both cases, (b) the apparent absence of any significant interaction between counter-moving motors (c) the occasional change in direction away from the tip and (d) the velocities (represented by the slopes in either direction) are consistent along the microtubule.

We approximate this further to a PDE by considering a spatial variable $x \in [0,1]$ and noting that if $x = i\delta$ where $\delta = h_s/L = 1/N$ is a small parameter, then

$$\rho_{i\pm1} = \rho_i \pm \delta\frac{\partial \rho_i}{\partial x} + \frac{\delta^2}{2}\frac{\partial^2 \rho_i}{\partial x^2} + O(\delta^3)$$

$$\sigma_{i\pm1} = \sigma_i \pm \delta\frac{\partial \sigma_i}{\partial x} + \frac{\delta^2}{2}\frac{\partial^2 \sigma_i}{\partial x^2} + O(\delta^3)$$

where all derivatives are evaluated at x. Ignoring terms of order $O(\delta^2)$, (3.2) can be written as

$$
\begin{aligned}
\frac{\partial \rho}{\partial t} &= -p_d \rho(1-\sigma) + p_u \sigma(1-\rho) + \frac{v_+}{L}(2\rho-1)\frac{\partial \rho}{\partial x} + \delta \frac{v_+}{2L}\frac{\partial^2 \rho}{\partial^2 x} \qquad (3.3) \\
\frac{\partial \sigma}{\partial t} &= p_d \rho(1-\sigma) - p_u \sigma(1-\rho) + \frac{v_-}{L}(1-2\sigma)\frac{\partial \rho}{\partial x} + \delta \frac{v_-}{2L}\frac{\partial^2 \sigma}{\partial^2 x}
\end{aligned}
$$

Adding these two equations gives

$$
\begin{aligned}
\frac{\partial (\rho+\sigma)}{\partial t} &= \frac{\partial}{\partial x}\left(\frac{v_+}{L}(\rho^2-\rho) - \frac{v_-}{L}(\sigma^2-\sigma)\right) + \delta\left(\frac{v_+}{2L}\frac{\partial^2 \rho}{\partial x^2} + \frac{v_-}{2L}\frac{\partial^2 \sigma}{\partial x^2}\right) \quad (3.4) \\
&= \frac{\partial}{\partial x}J(\rho(x,t),\sigma(x,t))
\end{aligned}
$$

where

$$
J(x,t) = \frac{v_+}{L}(\rho^2-\rho) - \frac{v_-}{L}(\sigma^2-\sigma) + \delta\left(\frac{v_+}{2L}\frac{\partial \rho}{\partial x} + \frac{v_-}{2L}\frac{\partial \sigma}{\partial x}\right). \qquad (3.5)
$$

Any stationary state will satisfy $\frac{\partial J}{\partial x} = 0$ meaning that the steady-state net flux along the domain is constant independent of x. To first order in δ the steady-state satisfies

$$
\begin{aligned}
0 &= -p_d \rho(1-\sigma) + p_u \sigma(1-\rho) + \frac{v_+}{L}(2\rho-1)\frac{d\rho}{dx} \qquad (3.6) \\
0 &= -p_u \sigma(1-\rho) + p_d \rho(1-\sigma) + \frac{v_-}{L}(1-2\sigma)\frac{d\sigma}{dx}.
\end{aligned}
$$

Note that $\frac{v_\pm}{L}$ has units of s^{-1}. The net flux can be written in this case as

$$
j_+(x) - j_-(x) = J_0. \qquad (3.7)
$$

The quantities $j_+(x) = \frac{v_+}{L}(\rho - \rho^2)$ and $j_-(x) = \frac{v_-}{L}(\sigma - \sigma^2)$ are the fluxes of the left and right-going particles. The mean field equations are well-known to have solutions with shock formation; the second derivative (diffusion) terms of (3.3) act as a singular perturbation that permits shocks or boundary layers to form between regions where (3.6) is a valid approximation.

3.2.1 Asymptotic form of the shock solution

Consider the mean field model (3.3) on the spatial domain x in the interval $[0,1]$ with boundary conditions as illustrated in Figure 3.1. As described in [124] the equilibrium state may have boundary layers depending on the phase and the boundary conditions. General boundary conditions $\alpha_\pm$ and $\beta_\pm$ for the mean field model (3.3) on a spatial domain $x \in [0,1]$ may be replaced by *effective boundary conditions* that will depend on the phase induced within the system; for example an effective boundary condition $\alpha_{+,\text{eff}} = \min(\alpha_+, p_+/2)$ recognizes that an injection rate larger

than half cannot induce more than a maximal current.

The symmetric case $\alpha = \alpha_+ = \alpha_-$, $\beta = \beta_+ = \beta_-$ together with $p_+ = p_- = 1$ is discussed in [124], while [125] examines the case $\alpha_- = 0$ and $\beta_+ > 0$. Here, we consider the case of the plus end blocked, i.e., $\alpha_- = \beta_+ = 0$ so that the balanced total flux J_0 is zero and a boundary layer may develop on one (or both) of the left-hand lanes.

We concentrate on the case of injection and escape at $x = 0$ (α_+/p_+ small, $\beta_- = p_-$) and no-flux at $x = 1$: ($\alpha_- = 0$, $\beta_+ = 0$). This can be expressed as boundary conditions on the densities:

$$\rho(0) = \frac{\alpha_+}{p_+} = \delta \frac{F_{in}L}{v_+}, \quad \sigma(0) = 0,$$
$$\rho(1) = 1, \quad \sigma(1) = 0$$

where a boundary layer will appear in $\sigma(x)$ at $x = 0$; we can remove this by replacing this boundary condition with an effective boundary condition, solving the identical equation $\rho - \rho^2 = \sigma - \sigma^2$ to give $\sigma(0)$ in terms of $\rho(0)$. Note that both fluxes at the right are zero, meaning that the net flux is zero.

In the case where $v = v_+ = v_-$ we can solve $J_0 = 0$ in (3.7) to give

$$\rho = \sigma, \quad \text{or} \quad \rho = 1 - \sigma. \tag{3.8}$$

These states are termed *equal-density* and *complementary-density* respectively in [124]. For *equal-density* states we have

$$0 = \frac{v}{L}(2\rho - 1)\frac{d\rho}{dx} + (p_u - p_d)\rho(1 - \rho)$$

so that

$$\rho(x) = \frac{1 \pm \sqrt{1 - 4C_e \exp\left((p_u - p_d)xL/v\right)}}{2} \tag{3.9}$$

where C_e is a constant. Similarly, for the *complementary-density* states we have

$$0 = \frac{v}{L}(2\rho - 1)\frac{d\rho}{dx} + p_u(1 - \rho)^2 - p_d\rho^2 \tag{3.10}$$

which can in principle be integrated to give an implicit expression for the complementary-density states.

As in [124], we classify the equilibrium state as H (high density) or L (low density) in each lane. For the case of $v_+ = v_-$ and the boundary conditions considered here, in the statistically stationary state, a localized shock may form in the system that join regions of equal density to those with complementary density. I.e., the system will be in a state where there is a stable shock from a LL state to a HL state; the

shock corresponds to a change from equal density to complementary density. If we assume that there is a shock at $x = x_s \in (0, 1)$ and write the densities

$$\rho(x) = \begin{cases} \rho_l(x) & \text{for } x < x_s \\ \rho_r(x) & \text{for } x > x_s \end{cases}$$

$$\sigma(x) = \begin{cases} \sigma_l(x) & \text{for } x < x_s \\ \sigma_r(x) & \text{for } x > x_s, \end{cases}$$

where $\rho_{l,r}$ ($\sigma_{l,r}$) are the solutions from left and right boundary for ρ (σ), then the fluxes in each direction will match across the shock

$$\lim_{x \to x_s-} j_+(x) = \lim_{x \to x_s+} j_+(x),$$
$$\lim_{x \to x_s-} j_-(x) = \lim_{x \to x_s+} j_-(x).$$

This matching implies $\rho_l(x_s) = 1 - \rho_r(x_s)$ or $\sigma_l(x_s) = \sigma_r(x_s)$. Section 3.3 extends this analysis to the more general case of unequal velocities in retrograde and anterograde directions.

3.3 Quantitative estimates for queue size

We assume that the flux F_{in} rate is small and accords with the *in vivo* experimental observations of [65]. In such a case there will be an equilibrium state where $\rho(x)$ and $\sigma(x)$ are approximately equal density from the left boundary up to a point close to the right boundary. At this "shock" there is a rapid transition to a region where the total density is almost full - a queue at the plus-end tip.

We will estimate the densities and tip size (the mean size of the motor accumulation at the plus-end) using simulations and analytical approximations of the model. We will be interesting in properties of solutions where v_+ and v_- are

$$v_\pm = v(1 \pm \epsilon)$$

with v is the mean of the average velocity of motors in either direction and a small parameter ϵ. From the boundary conditions $\alpha_- = \beta_+ = 0$, the net flux must be zero ($J_0 = 0$), so that

$$\frac{\sigma^2 - \sigma}{\rho^2 - \rho} = \frac{1 + \epsilon}{1 - \epsilon}, \tag{3.11}$$

and hence

$$\sigma = \frac{1}{2} \left(1 \pm \sqrt{1 + 4 \left(1 + \frac{2\epsilon}{1 - \epsilon} \right) (\rho^2 - \rho)} \right).$$

We make the hypothesis that there is a solution such that

$$\begin{aligned}
\min(\rho(x), 1 - \rho(x)) &< K\delta, \\
\min(\sigma(x), 1 - \sigma(x)) &< K\delta
\end{aligned} \tag{3.12}$$

for small enough δ and seek a solution that satisfies this away from any shocks. Solving (3.11) with this hypothesis gives a perturbed *equal-density* state

$$\sigma = \rho + \frac{2\epsilon}{1 - \epsilon}\left[\frac{\rho^2 - \rho}{2\rho - 1}\right] + O(\delta^2) \tag{3.13}$$

and a perturbed *complementary-density* state

$$\sigma = 1 - \rho - \frac{2\epsilon}{1 - \epsilon}\left[\frac{\rho^2 - \rho}{2\rho - 1}\right] + O(\delta^2). \tag{3.14}$$

For δ small, the inflowing boundary condition at $x = 0$, $\rho(0) = \delta L F_{in}/v_+$, and a shock appears at $x_s = 1 - y \in (0, 1)$ where

$$y = \delta n_{tip} + O(\delta^2).$$

This shock is a transition from LL to HL as described above and n_{tip} is the number of occupied sites at the tip and we refer to as the queue or tip size. In the equal density (LL) region $x \in (0, x_s)$ we have

$$0 = \frac{v_+}{L}(2\rho - 1)\frac{d\rho}{dx} + p_u\sigma(1 - \rho) - p_d\rho(1 - \sigma) + O(\delta^2).$$

Using the ansatz (3.12), noting that when $\frac{d\rho}{dx}$ and $\frac{d\sigma}{dx}$ are of order δ, and taking leading order terms we have

$$\frac{d\rho}{dx} = \frac{L}{v(1 + \epsilon)}\left(\left(1 + \frac{2\epsilon}{1 - \epsilon}\right)p_u - p_d\right)\rho$$

and so, using $v_+ = (1 + \epsilon)v$ and the boundary condition $\rho_l(0) = F_{in}h_s/v_+$ we have

$$\rho_l(x) = \delta\frac{F_{in}L}{v_+}\exp\left[x\left(\frac{L}{M_r} - \frac{L}{M_a}\right)\right] + O(\delta^2)$$

when $x \in (0, x_s)$. In the complementary density region (HL) $x \in (x_s, 1)$ we have

$$\begin{aligned}
\frac{v_+(2\rho - 1)}{L}\frac{d\rho}{dx} &= -p_u(1 - \rho)\left(1 - \rho - \frac{2\epsilon}{1 - \epsilon}\frac{\rho^2 - \rho}{2\rho - 1}\right) \\
&\quad + p_d\rho\left(\rho + \frac{2\epsilon}{1 - \epsilon}\frac{\rho^2 - \rho}{2\rho - 1}\right) + O(\delta^2)
\end{aligned}$$
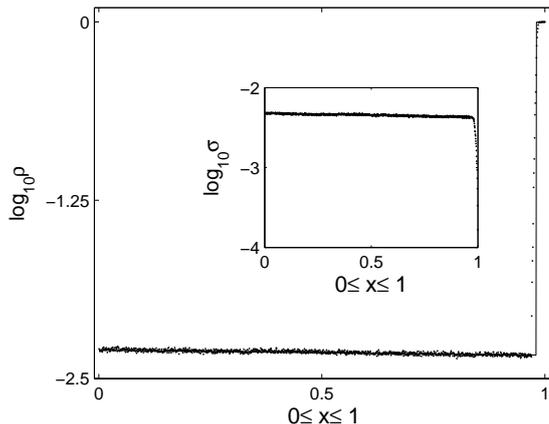
Figure 3.3: A comparison of the mean field approximation of the densities ρ and σ from equations (3.13) and (3.14) (lines), with densities obtained from numerical simulations using a Monte Carlo algorithm (points). Parameters are as in Table 3.1.

so that to leading order we have $\frac{v_+}{p_d L}\frac{d\rho}{dx} = 1$. Applying the boundary condition $\rho(1) = 1$, we have

$$\rho_r(x) = 1 + \frac{p_d L}{v_+}(x - 1) + O(\delta^2).$$

Balancing the flux on the right-moving track at the shock $x = x_s = 1 - \delta n_{tip} + O(\delta^2)$ allows us to find a solution that satisfies the ansatz (3.12). For n_{tip} large this will give a solution with a shock of width approximately 2δ from (3.5) and a boundary layer if n_{tip} is small. From $\rho_l(x_s) = 1 - \rho_r(x_s)$, we take the first order in δ, leading to

$$\delta n_{tip} L\frac{p_d}{v_+} \approx \delta\frac{F_{in}L}{v_+}\exp\left(\frac{L}{M_r} - \frac{L}{M_a}\right)$$

which means that the average number of motors at the tip is

$$n_{tip} \approx \frac{F_{in}}{p_d}\exp\left(\frac{L}{M_r} - \frac{L}{M_a}\right) \tag{3.15}$$

where $p_d = \frac{v_+}{M_a}$.

Denoting by F_{arr} the leading order flux of arrivals at the tip of the MT, to leading order $F_{arr} = F_{in}\exp\left(\frac{L}{M_r} - \frac{L}{M_a}\right)$, meaning that we can express the leading order mean tip size as

$$n_{tip} \approx \frac{F_{arr}}{p_d}. \tag{3.16}$$

3.3.1 Tip size from simulations

To confirm the results in the previous section, we have performed stochastic simulations using both Gillespie and parallel update Monte Carlo algorithms. The Gillespie algorithm [126] produces quantitatively correct statistics for events that
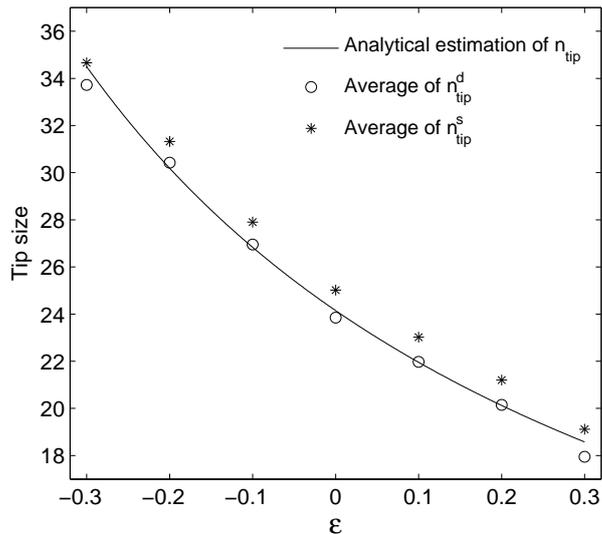
Figure 3.4: Comparison of tip size predictions between simulation and analytical approximation from equation (3.15) for a range of unequal velocities parameterized by ϵ: parameters as in Table 3.1 except for $v_\pm = v(1 \pm \epsilon)$ and $v = 1.7 \mu s^{-1}$.

are instantaneous and independently distributed in an exponential manner. We use a small enough time step ($h_t = 4.2 \times 10^{-3}s$) to resolve the fastest process at each site in a Monte Carlo simulation. The sequence of updates may affect the outcome, so we specify that we update first the anterograde lane and then the retrograde lane. For both Gillespie and Monte Carlo schemes we use simulation time of at least order $t = 160s$, taking care to ensure that the system has reached a statistically stationary state before measuring tip size. There is no unique way to determine exactly where the queue for the tip starts - here we consider the following two definitions which agree well with a number of other definitions of tip size (not shown):

- We define n_{tip}^d to be the tip size as the total number of sites where the average density is over half, i.e., plus-direct current reaches its maximal, similar to the tip size definition in [130].

- We define n_{tip}^s to be the total sites that are occupied in an arbitrarily chosen "tip region" (in our case, the last $1\mu m$ of the MT).

The quantity n_{tip}^s corresponds to the definition of tip size used in simulations in [65]. Using the measured parameters from [65] as in Table 3.1, long simulations show that there is little difference in tip size between the two simulation algorithms: we find $n_{tip}^d = 25$, $n_{tip}^s = 25.4 \pm 0.22$ using the Monte Carlo and $n_{tip}^d = 24$, $n_{tip}^s = 25.3 \pm 0.29$ using the Gillespie algorithm. The explicit expressions (3.14) and (3.13) for the motor density ρ and σ are in good agreement with Gillespie and Monte Carlo simulations of the process as illustrated in Figure 3.3; tip size for general
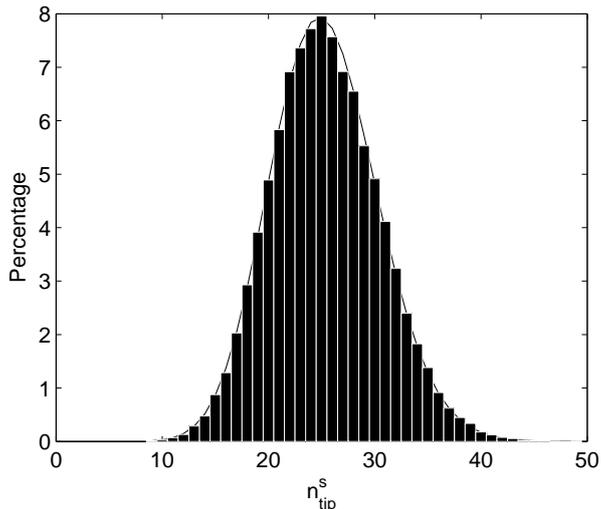
Figure 3.5: The bar-graph shows the distribution of instantaneous tip size n^s_{tip} for parameters as in Table 3.1. This was obtained using a Monte Carlo simulation with a very long sample length $(2.1 \times 10^5 s)$. The smooth curve shows a fit to a Poisson distribution with mean 25.3.

velocity from analytical expression (3.15) is also in good agreement with simulation as illustrated in Figure 3.4.

3.4   Queueing models at the tip

3.4.1   Queueing at the tip as an $M/M/\infty$-process

The motors that reach the tip for the ASEP model can be thought of as joining a queue that has approximately $M/M/\infty$ type - motors arrive at and leave from the tip with exponential (memoryless $= M$) distributions, and there is no limit in the number (∞) of identical "servers" at which a single motor can queue [131]. In our case, the arrival rate is F_{arr} while the leaving rate from each server is p_d.

   This allows us to conceptually understand the queueing process at the tip as a quantitative process without worrying about detailed motion within the tip. Let $X(t)$ be the number of motors at the tip. In the stationary state, the mean tip size is simply the mean queue size [132]:

$$\lim_{t \to \infty} E[X(t)] = F_{arr}E[M_1] = \frac{F_{arr}}{p_d}$$

where M_n is a random variable that gives the time spent by nth motor in the queue before it leaves; and $E[M_n] = 1/p_d$. We write the distribution of tip sizes at time t as $Q_n(t) = P[X(t) = n]$. Assuming that a flux F_{arr} of motors arrive at the tip per second, and that loss of motors is at a rate np_d for n motors at the tip, Q_n evolves

according to the master equation:

$$\begin{aligned}
\frac{dQ_0}{dt} &= p_d Q_1 - F_{arr} Q_0 \\
\frac{dQ_n}{dt} &= F_{arr} Q_{n-1} + (n+1) p_d Q_{n+1} - F_{arr} Q_n - n p_d Q_n.
\end{aligned} \tag{3.17}$$

Solving for the steady (equilibrium) distribution $Q_n(t) = \tilde{Q}_n$ and normalizing so that $\sum_n Q_n = 1$ gives the Poisson distribution:

$$\tilde{Q}_n = \frac{\xi^n}{n!} \exp(-\xi)$$

with parameter $\xi = F_{arr}/p_d$ as observed in simulations (see figure 3.5). The mean size of tip for this model is given by $\sum_n n\tilde{Q}_n$ which is precisely $\xi = F_{arr}/p_d$ in agreement with (3.16).

More generally, using equation (3.17) and $E(X(t)) = \sum_{n=0}^{\infty} nQ_n$, there is a closed form differential equation for $E(X(t))$

$$\frac{d}{dt}[E(X(t))] = F_{arr} - p_d E(X(t)).$$

with solution (for initial condition $X(0) = 0$)

$$E(X(t)) = \frac{F_{arr}}{p_d}(1 - \exp(-p_d t)). \tag{3.18}$$

From the above equation (3.18), we can also see that starting from an empty tip, it will take a time approximately $O\left(\frac{1}{p_d}\right)$ seconds for the tip size to approach the stationary state. This approximation of $E(X(t))$ agrees well with simulations - Figure 3.6 illustrates this, along with typical fluctuations of tip size for a single simulation.

More generally, the rate of slowest convergence to the equilibrium distribution of (3.17) (assuming rapidly decaying distributions) is $-p_d$, with corresponding eigenvector

$$R_n = \frac{\xi^n}{n!}(\xi - n).$$

Note that the eigenvector changes sign at the maximum of the distribution, the slowest decaying mode being associated with long-range fluctuations, and the rate coincides with the convergence rate in (3.18). As a consequence, transients in the mean size of the tip are expected to settle on a timescale of $1/p_d$. The agreement of the convergence rates suggests that, if this is a good model for the experiment of [65], then we expect fluctuations in tip size to settle on this timescale.
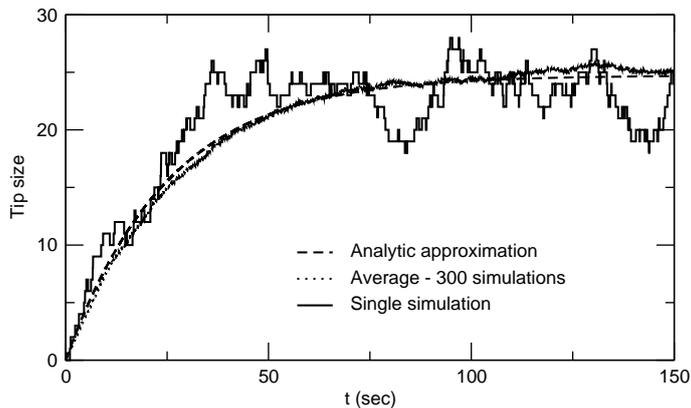
Figure 3.6: Tip size as a function of time, starting from no motors at the tip, comparing the analytic approximation (3.18) with stochastic simulations using a Gillespie algorithm. The ensemble average over 300 simulations (parameters as in Table 3.1) and a single simulation are shown.

3.4.2 Other queueing models at the tip

Further generalizations of this model could consider more complex queueing models such as those with non-memoryless distributions of incoming and outgoing motors; queues with a finite number of "servers"; reducing the number of servers should not make a significant difference as long as the mean queue for each server is small. In addition, it would be interested to include a more realistic geometry for the queue, though it will still be a great challenge to discover the processes that governs the queue *in vivo*.

3.5 Discussion

For the first time, we have been able to present a model of a complete system of bi-directional motor transport using *in vivo* parameters and to predict the observed appearance of a fluctuating concentration of motors at the tip of a microtubule. In this chapter we have focused on queueing effects induced by the exclusion dynamics of a stochastic transport model. We use a development of a model of Juhász [125] as a qualitative model of the bi-directional transport process observed in hyphal growth of *Ustilago maydis*.

The homogeneous stochastic model for motion on the MT predicts the dependence of the size of this concentration on measurable transport parameters- the crucial parameters being the flux rate of arrival at the tip F_{arr} and the mean rate of turning of motors p_d - the latter can be obtained by estimating (as in [65]) the mean free path of motors away from the tip.

In principle, many predictions from the model, such as queuing properties, average densities and accumulation sizes might potentially be experimentally measurable

in vivo. Validation of the model from the queuing properties might require a detailed biological analysis on the motility of dynein motors in the accumulation, which may be difficult under the current limited microscopic resolutions. In addition, to verify the linear increase on the tip size with the injection rate, requires changes in flux while keeping other motility parameters constant in experiments; this raises some difficulties for designing experiments in living cells.

The accumulation size predicted from the model with quantitative data is validated by estimating the number when overexpressing a specific peptide in living cells as shown in a paper reproduced in Appendix A. Actually, the number of motors experimentally observed at the tip in the normal condition is in fact underestimated by this model by a factor of about two; the observed average number of dynein at the tip is approximately 55. Moreover, the model here predicts the turnover with a half-life $T_{1/2} = \ln 2/p_d \approx 16\ s$, while the experiment observes two populations in the accumulation; one with a fast turnover ($T_{1/2} \approx 10\ s$) in the order of $\ln 2/p_d$, and one with a slower turnover ($T_{1/2} \approx 90\ s$); these observations suggests that there are (at least) two dynamical processes keeping dynein at the tip and the ASEP model discussed here is only one of these. In fact, an additional control mechanism has been observed to capture a subpopulation of dynein at the plus-end; the capture mechanism involves plus-end binding proteins, such as EB1 and its interactor dynactin, that anchors the dynein complex to the MT tip [17]. High expression of the peptide that inhibits the interaction of EB1 and dynactin, is found surprisingly to be only able to remove $\approx 60\%$ of dynein from the MT plus ends; the remaining $\approx 40\%$ of dynein in the accumulation is found to turnover of $\approx 20\ s$, which represents the more dynamic population in the accumulation. These agree with our ASEP model predictions. The biological function of the accumulation is studied in Appendix A which suggests that the accumulation of dynein ensures a high rate of capture of arriving organelles by preventing them from "falling off" the end of the track.

Chapter 4

Bidirectional transport and pulsing states in a multi-lane ASEP model

In this chapter, we introduce an ASEP-like transport model for bidirectional motion of particles on a multi-lane lattice. The model is motivated by *in vivo* experiments on organelle motility along a microtubule (MT), consisting of thirteen protofilaments [14], where particles are propelled by molecular motors (dynein and kinesin). In the model, organelles (particles) can switch directions of motion due to "tug-of-war" events between counteracting motors. Collisions of particles on the same lane can be cleared by switching to adjacent protofilaments (lane changes).

We analyze transport properties of the model with no-flux boundary conditions at one end of a MT ("plus-end" or tip). We show that the ability of lane changes can affect the transport efficiency and the particle-direction change rate obtained from experiments is close to optimal in order to achieve efficient motor and organelle transport in a living cell. In particular, we find a nonlinear scaling of the mean *tip size* (the number of particles accumulated at the tip) with injection rate and an associated phase transition leading to *pulsing states* characterized by periodic filling and emptying of the system.

4.1 Introduction

Various lattice models have been proposed to understand the role of cooperation and competition between motors involved in such bi-directional transport. These are typically generalizations of asymmetric simple exclusion processes (ASEP) in one dimension [86, 90] where motors are represented by particles that move on a lattice; see a short review in Chapter 2. Already for unidirectional motor transport models [130, 100, 93] there are nontrivial effects such as traffic jams due to the

mutual exclusion of particles on sites of the MT [130, 101].

Bidirectional transport has previously been modelled by an exclusion process with binding and unbinding events [112, 116, 113, 114] or a lattice model with site sharing [115]. Change in direction of individual cargos may be due to "tug-of-war"[1] events [42, 45, 43, 7] and this can be incorporated into ASEP models by assuming that motion of a single type of particle in different directions takes place on different lanes (and change of direction is modelled simply by change of lane) [124, 125, 64] or that particles may change type [65]. In the latter case, counter-moving particles approaching on the same lane can only pass if at least one of them can change lane. The lane-change rules in the latter model are based on experimental observations that (a) dynein can switch between lanes on the MT at a certain rate [29], whereas (b) kinesin remains on a single lane [133], and (c) no long-lasting traffic jam is observed between particles away from the tip. However, recent reports show that kinesin can change lanes to overcome obstacles on the MT [134]. Thus the situation in the living cell is less clear and one aim of this chapter is to investigate the impact of different lane-change rules on bidirectional transport.

We study a generalization of the models from [64, 65] for bidirectional motion motivated by *in vivo* experimental observations of bidirectional motion of dynein particles near the hyphal tip of *Ustilago maydis*. The particles represent dynein that is transported towards the plus-end of a MT by kinesin-1 and towards the minus-end under its own power. As the dynamics of the MT in this system are comparatively stable [16] and binding/unbinding events are rare in this system [24], we focus on modelling bidirectional transport of particles that remain bound at all times to a fixed section of MT where one end is a plus-end (with no-flux boundary conditions are applied) while at the other end we inject particles at a given *injection rate*. In particular we explore the behaviour of the tip accumulation (or *tip size*) as a function of this injection rate.

This chapter is organized as follows: In Section 4.2 we introduce a general multi-lane model for bidirectional motion and demonstrate that it includes, as special cases, the models of [64, 65]. Section 4.3 examines the influence of collisions and lane changes on bidirectional transport in this model. In particular we find cross-lane diffusion due to lane changes, and for low injection rates we find an approximately linear scaling of the tip size with injection rate as discussed in [64]. However, for higher injection rates we find there is a nonlinear growth in the tip size (depending on the lane-change rules) due to trapping of particles near the plus-end, and a singularity at a finite critical injection rate. We suggest that is associated with a phase transition of the system. We also study how the lane change rules influence the tip structure and discuss measures of efficiency for the bidirectional transport.

---

[1]"tug-of-war" events refer to simultaneous and competitive activity of counteracting motors on the same organelle.

Interestingly, we find that the *in vivo* parameters obtained from living cell images [65] are close to optimal for effective bidirectional transport, in that they balance efficient transport to the tip against the average delay at the tip. In Section 4.4 we describe novel *pulsing states* (with whole-system approximately periodic filling and emptying) and *filled states* that can both appear at injection rates beyond the critical value. We finish with a discussion of biological relevance, implications and generalizations of these results in Section 4.5.

4.2 A multi-lane model for bidirectional transport

Consider a bidirectional transport model where particles move on a lattice of spatial locations consisting of M adjacent lanes around the circumference of a cylinder.[1] Each oriented lane is discretized into N *sites* between a *plus-end* and *minus-end*, as illustrated in Figure 4.1. Particles are of two types; *plus-type* particles move towards the plus-end, while *minus-type* particles move towards the minus-end; a single particle represents a bound pair of opposite-directed motor proteins that is pulled along the lane by one of the motors being bound to the MT and the type of the particle corresponds to which of the motors is currently bound to the MT.

We identify each location along the cylinder by a pair (l, i) where $l \in \{1, \cdots, M\}$ denotes the lane and $i \in \{1, \cdots, N\}$ the site along the lane and let $\tau_{\pm,i}^l = 1$ or 0 represent the presence or absence of a plus-type (minus-type) particle at location (l, i). Each location is occupied by at most one particle (i.e. $\tau_{+,i}^1 + \tau_{-,i}^l$ can only be 0 or 1) and particles move from one location to another at given rates. We also allow the possibility that each particle can change from one type to the other at rates representing the resolution of brief "tug-of-war" events [42, 45, 43, 7] between opposite oriented motor proteins bound to the particle. This change of type may or may not be associated with a change of lane.

The plus- and minus- type particles may have transition rates that describe *motion* and *particle-type change* and both of these may depend on site; however, here we will assume that they are independent of site, though they may depend on lane. We say a model is *lane-inhomogeneous* (or simply *inhomogeneous*) if the transition rates and/or boundary conditions are not uniform between lanes; otherwise we say the model is (lane) *homogeneous*. A particle is *blocked* if there is another particle that prevents it from undergoing the *forward motion* below, otherwise it is *unblocked*. Transition rates may depend on whether a particle is blocked or not as illustrated in Figure 4.1 and the possible transitions we consider are defined below:

---

[1] We identify lane $M + 1$ with lane 1 to represent this cylinder.

- **Motion:** Plus-type particles move from (l, i) to $(k, i+1)$ with a change of lane l to k when unblocked (resp. blocked) at rate $p_{+,u}^{l \to k}$ (resp. $p_{+,b}^{l \to k}$). Similarly, minus-type particles move from (l, i) to $(k, i-1)$ at rate $p_{-,u(b)}^{l \to k}$. Motion is subject to an exclusion principle - a change can only occur if the target location to move into is vacant. **Forward motion** is used to mean the motion on a single lane (i.e., $k = l$) in either direction; this can occur only to a particle that is unblocked. If this forward motion is lane-homogeneous then we write

$$p_+ := p_{+,u}^{l \to l}, \quad p_- := p_{-,u}^{l \to l}.$$

- **Particle type/direction change:** Plus-type particles can change to minus-type particles with a change of lane l to lane k at rate $p_{+-}^{l \to k}$. Minus-type particles can change to plus-type particles with a similar change in lane at rate $p_{-+}^{l \to k}$ (we assume that the site i is preserved for a change in type). For lane-homogeneous direction changes on the same lane, we write

$$p_{+-} := p_{+-}^{l \to l}, \quad p_{-+} := p_{-+}^{l \to l}.$$

Boundary conditions for the model are assumed as follows:

- **Inflow:** Plus-type (resp. minus-type) particles are injected at rate α_+^l (resp. α_-^l) into the minus end (reps. plus end) of the $l-$th lane. Both cases are subject to an exclusion principle.

- **Outflow:** Plus-type (resp. minus-type) particles exit from the plus end (resp. minus end) of the $l-$th lane at rate β_+^l (resp. β_-^l).

The state of the model $\{\tau_{\pm,i}^l(t)\}$ at time t changes according to the above events (assumed to take place independently and instantaneously) from an initial state $\{\tau_{\pm,i}^l(0)\}$. In summary, the model for a given lattice (fixed M and N) has a number of parameters

$$p_{\pm,b}^{l \to k}, \quad p_{\pm,u}^{l \to k}, \quad p_{+-}^{l \to k}, \quad p_{-+}^{l \to k}, \quad \alpha_\pm^l \quad \text{and} \quad \beta_\pm^l$$

for $k, l = 1, \cdots M$ that collectively determine the bidirectional transport behaviour. We write $\alpha_+ = \sum_{l=1}^{l=M} \alpha_+^l$ to denote the total inflow of plus-type particles. In practice, many of these rates will be zero - for example, here we only permit a type change of a particle that remains on the same lane or moves to an adjacent lane. As in other ASEP models, we assume that the dynamics for typical choices of parameters converges to a unique statistical equilibrium independent of initial conditions, though possibly after a long transient. Exceptions occur if there is a degeneracy of the parameters, for example if no lane-changes are permitted, i.e., $p_{\pm,b(u)}^{l \to k} = 0$ for $k, l = 1, \cdots M$, then accumulations can be created at arbitrary locations that are
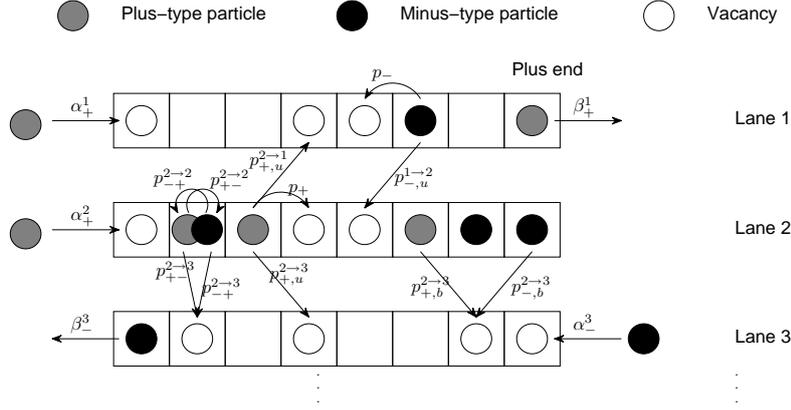
Figure 4.1: Schematic diagram showing transition rates for the multi-lane bidirectional ASEP model; we consider M lanes on the surface of a cylinder. The plus end (resp. minus end) of the MT is at the right (resp. left). Plus-type (resp. minus-type) particles move step forward with rate p_+ (resp. p_-) while they move forward associated with a change of lane with rates $p_{+,b(u)}^{l \to l \pm 1}$ (resp. $p_{\pm,b(u)}^{l \to l \pm 1}$) when blocked (resp. unblocked). Plus-type (resp. minus-type) particles are injected into the left (resp. right) boundary of the system at rate α_+^l (resp. α_-^l) and exit at rate β_+^l (resp. β_-^l) in the l-th lane. Particles can also change from plus-type to minus-type (resp. from minus-type to plus-type) with rate $p_{+-}^{l \to k}$ (resp. $p_{-+}^{l \to k}$) associated with a possible change of lane l to k (if $l \neq k$); we assume the site is preserved during a change of type.

never cleared. The system exhibits various different dynamical regimes depending on parameters. We have not attempted to characterize the phase diagram of these states in full, but do discuss this further in Section 4.4.1.

The equilibrium densities of plus- and minus-type particles are defined to be the mean occupancy of the particles:

$$\rho_i^l := \langle \tau_{+,i}^l(t) \rangle, \quad \sigma_i^l := \langle \tau_{-,i}^l(t) \rangle \tag{4.1}$$

where $\langle \cdot \rangle$ denotes the ensemble average; assuming ergodicity this can be evaluated using a time average. In particular, if there is an accumulation at the tip then we denote the *lane tip length* $\lambda_{tip}^l(t)$ as the number of particles in the accumulation within lane l at time t, and the *tip size* $n_{tip}(t)$ is

$$n_{tip}(t) = \sum_{l=1}^{M} \lambda_{tip}^l(t).$$

with mean tip size as $\langle n_{tip} \rangle$ at a steady state.

There are few methods giving exact analytical solutions of the equilibrium state for ASEP models (we refer to [85] for a review of ASEP models and their analytical solutions). Therefore, we numerically simulate this discrete event, continuous time

(a) Transport rates

$p_{-+}^{l \to l} = p_{+-}^{l \to l} = 0, \quad p_{\pm,u(b)}^{l \to l \pm 1} = 0 \ (l = 1, 2), \quad p_d := p_{+-}^{1 \to 2} \quad \text{and,} \quad p_u := p_{-+}^{2 \to 1}, \quad p_\pm := p_{\pm,u}^{l \to l}$

(b) Boundary conditions I	Boundary conditions II
$\alpha_+^2 = \alpha_-^1 = 0,$	$\beta_+^1 = \alpha_-^2 = 0$

Table 4.1: The transition rates (a) with boundary conditions I in (b) for a two-lane model ($M = 2$) that gives bidirectional transport where each lane supports transport in one direction only and allows lane changes only together with a type change; if also associated with boundary Conditions II, the model corresponds to no-flux boundary at the plus end.

model using both Gillespie [126] and fixed time-step (h_t) Monte Carlo methods. The latter method converges to the Gillespie method and gives outcomes that are independent of update methods in the limit $h_t \to 0$. This general multi-lane model can reduce to previously studied ASEP models in special cases. For instance, restricting to $M = 1$ and one particle-type gives the simplest unidirectional ASEP model. In particular of bidirectional transport, this multi-lane model limits the two models recalled in the following sections.

4.2.1 A simple two-lane model

A lattice model for bidirectional transport needs to either segregate, or deal with collisions between, opposite-directed particles. Works such as [112, 114] include the possibility of binding/unbinding from/to a reservoir in their model. In our multi-lane model, for $M = 2$ one can segregate the particles into two lanes of unidirectional motion by setting the parameters in Table 4.1 (a) with boundary conditions I as in Table 4.1 (b). This particular choice of parameters corresponds to the two-lane model of [124, 125] and segregates the particles into two lanes- one lane will have no particles of minus-type, while the other lane will have no particles of plus-type, i.e., the equilibrium densities $\rho^2 = \sigma^1 = 0$. If, in addition, boundary conditions II in Table 4.1 (b) are satisfied then there is no flux at the right boundary and the model corresponds to the special case studied in [64]. We recall from [64] that in these circumstances, if the minus-end boundary condition $\alpha_+^1 = \alpha_+$ small enough (that the density profile in 4.2 away from the tip is low) on the first lane and $\beta_-^2 = p_-$ on the second lane then a shock forms near the tip that traps a number of particles there. Using a mean-field approximation and denoting $x = i\delta$ where $\delta = 1/N$, one can find an asymptotic profile for the equilibrium densities of ρ and σ for plus- and minus-type particles along the domain as follows (assuming σ^2 and $\min\{\rho^1, (1-\rho^1)\}$

are of order δ):

$$\rho^1(x) \approx \begin{cases} \frac{\alpha_+}{p_+} \exp\left[x\left(\frac{Np_u}{p_-} - \frac{Np_d}{p_+}\right)\right], & x \in [0, x_s] \\ 1 + \frac{p_d N}{p_+}(x-1), & x \in [x_s, 1] \end{cases}, \qquad (4.2)$$

$$\sigma^2(x) = \begin{cases} \rho^1(x), & x \in [0, x_s] \\ 1 - \rho^1(x), & x \in [x_s, 1] \end{cases}, \qquad (4.3)$$

where x_s represents the shock position. Continuity of the flux [64] then implies that the *mean tip size* can be approximated as:

$$\langle n_{tip} \rangle \approx (1 - x_s)N \approx \frac{\alpha_+}{p_d} \exp\left(\frac{Np_u}{p_-} - \frac{Np_d}{p_+}\right). \qquad (4.4)$$

4.2.2   A homogeneous thirteen-lane model

Taking $M = 13$ and considering lane-homogeneous transition rates as in Table 4.2 (a,b), the multi-lane model reduces to the thirteen-lane model of [65]. If we consider boundary conditions

$$\alpha_+^l = \alpha_+/M, \quad \alpha_-^l = 0, \quad \beta_+^l = 0 \quad \text{and} \quad \beta_-^l = p_+ \qquad (4.5)$$

for all $l \in \{1, \cdots, M\}$, this corresponds to homogeneous injection of plus-type particles into the minus-end and no flux at the plus-end of the domain, while minus-type particles exit without impediment. Experiments and other information reported in [65] suggest that the rates listed in Table 4.2 (a) are appropriate for this system. Rates in Table 4.2 and boundary conditions in (4.5) are considered as default parameters for simulations unless otherwise specified.

(a) Transition rates

p_+	p_-	p_{+-}	p_{-+}	$p_{+,u}^{l \to l \pm 1}$	$p_{+,b}^{l \to l \pm 1}$	$p_{-,u}^{l \to l \pm 1}$	$p_{-,b}^{l \to l \pm 1}$	α_+	β_-^l
212.5	203.83	0.0406	0.0273	0	0	4.335	106.25	1.06	212.5

(b) Only adjacent lane-changes permitted	type changes occur on the same lane
$p_{\pm,b(u)}^{l \to k} = 0 \ (k \neq l, l \pm 1)$	$p_{-+}^{l \to k} = p_{+-}^{l \to k} = 0 \ (k \neq l)$

Table 4.2: Transition rates for the thirteen-lane model based on *in vivo* experiment measurements or estimations of velocities, mean run length and fluxes on a MT for the *Ustilago maydis* hyphal tip as detailed in [65]. Note that α_+ represents the total injection rate, i.e., $\alpha_+ = \sum_{l=1}^{M} \alpha_+^l$. Simulations use $N = 1250$ sites (i.e., $L = 10$ μm in length discretised with spatial step $h_s = 8 \ nm$) and a sequential Monte-Carlo update with time step $h_t = 0.0042$ s unless otherwise specified.

For the rest of this chapter, we vary certain rates (particularly the lane-change

rates, injection rate and direction change rates) from Table 4.2 to see their influences on the transport properties.

4.3 Influence of collisions and lane-changes on transport properties

In this section, we consider the multi-lane model with lane-homogeneous transition rates satisfying Table 4.2 (b) and boundary conditions as in (4.5) except for possibly inhomogeneous injection rates. For lane-homogeneous and symmetric lane-change rates, we remove the superscript and write

$$p_{+,u(b)} := p^{l \to l \pm 1}_{+,u(b)}; \quad p_{-,u(b)} := p^{l \to l \pm 1}_{-,u(b)}$$

independent of lane l.

4.3.1 Mean field approximation and cross-lane diffusion

In cases of inhomogeneous boundary conditions, the densities of plus- or minus-type particles can be homogenized by lane changes of particles, and lane changes are necessary for this to happen. Depending on which particles change lanes under which circumstances (blocked or unblocked), this homogenization can occur to one or both types of particle.

For example, if only minus-type particles can change lanes when unblocked in a dilute situation, then the density of minus-type becomes lane-homogeneous by cross-lane diffusion (see Figure 4.2 (c)), while the density of plus-type particles (not shown) may still be inhomogeneous due to the inhomogeneous injection rates and there being no lane changes of this type. If plus-type particles changes lanes when unblocked, the density of both types of particles will be smoothed as shown in Figure 4.2 (b) for the density of plus-type particles (minus-type particles are driven from tip where they are homogeneously distributed along the lanes due to homogeneous density for plus-type particles). Exceptions to this are shown in Figure 4.2 (a1,a2) when lane change only occurs after collision - in this case the plus-type particles injected into the middle lane "sweep" that lane clear of minus-type particles.

These effects can be understood in terms of cross-lane diffusion of particles induced by lane changes in a dilute region. If we apply the mean field description of Appendix B to a dilute region and assume small variation of density with site $x = i\delta$ ($x \in [0,1]$ and $\delta = 1/N$), in the case of $p_{-,u} = p_{+,u} = 0$, the solutions (B.1) in Appendix B indicate the non-homogeneity of densities in both types of particles if given non-homogeneous injection rates α^l_+. If we allow lane changes when unblocked and assume that a change of type occurs more slowly than a change
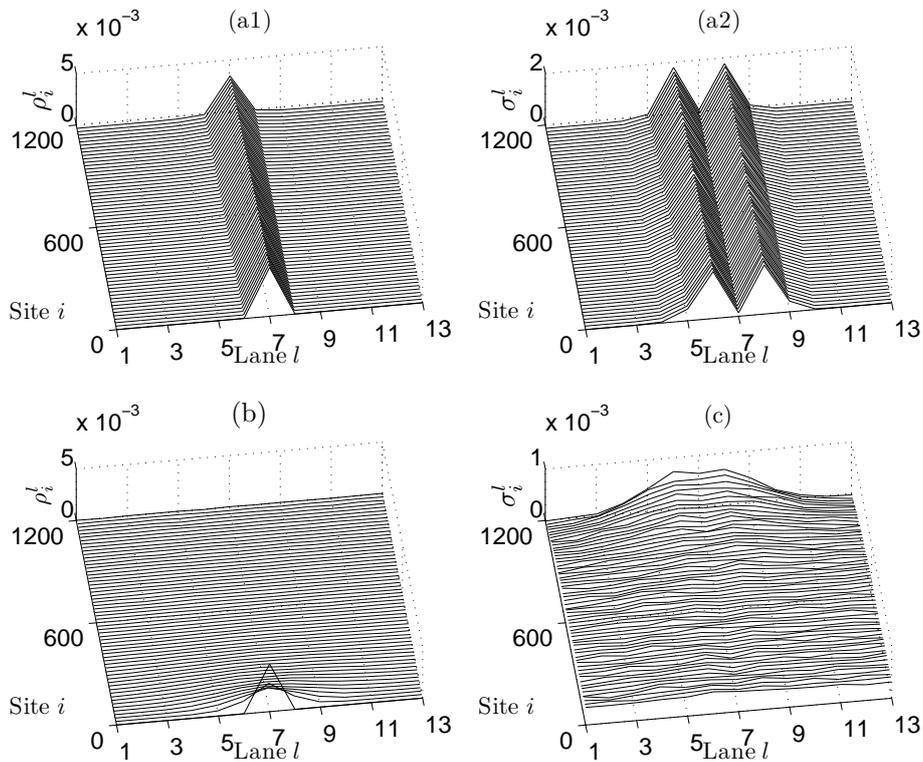
Figure 4.2: Densities of plus- or minus-type particles corresponding to default parameters in Table 4.2 and boundary conditions in (4.5) except that the lane-change rates when unblocked are varied and there is injection only in one lane (namely $\alpha_+^7 = 1 \; s^{-1}$ and $\alpha_+^l = 0$ for $l \neq 7$). (a1) and (a2) show the inhomogeneous densities of plus- and minus-type particles respectively, when $p_{\pm,u} = 0$, i.e., particles only change lanes after collisions; (b) (resp. (c)) shows cross-lane diffusion leading to a more homogeneous density of plus-type (resp. minus-type) particles away from the boundaries with lane-change rates when unblocked as $p_{-,u} = 0$, $p_{+,u} = 4.335 \; s^{-1}$ (resp. $p_{-,u} = 0.4335 \; s^{-1}$, $p_{+,u} = 0$). In all cases the densities near the tip (not shown) are high.

of lane, i.e., $p_{-+}, p_{+-} \ll p_{\pm,u}$, then the stationary state distribution $\rho^l(x)$ satisfies (see Appendix B for details):

$$0 = -\delta p_+ \frac{d\rho^l}{dx} + p_{+,u}\left[\rho^{l-1} + \rho^{l+1} - 2\rho^l - \delta\frac{d\rho^{l-1}}{dx} - \delta\frac{d\rho^{l+1}}{dx}\right], \quad l = 1, 2, \cdots, M$$

to leading order in δ. Solving this differential-difference equation for M lanes gives

$$\rho^l(x) = \sum_{k=0}^{\lfloor M/2 \rfloor}\left[A_k \cos\frac{2\pi kl}{M} + B_k \sin\frac{2\pi kl}{M}\right]\exp\left[-\kappa_+(k)x\right] \qquad (4.6)$$

where

$$\kappa_+(k) = \frac{2p_{+,u}\left[1 - \cos\frac{2\pi k}{M}\right]}{\delta p_+ + 2p_{+,u}\delta \cos\frac{2\pi k}{M}},$$

and A_k, B_k are constants determined by the density at $\rho^l(x_0)$. Similarly, the density for the minus-type particles can be approximated as

$$\sigma^l(x) = \sum_{k=0}^{\lfloor M/2 \rfloor}\left[A'_k \cos\frac{2\pi kl}{M} + B'_k \sin\frac{2\pi kl}{M}\right]\exp\left[\kappa_-(k)x\right]$$

where

$$\kappa_-(k) = \frac{2p_{-,u}\left[1 - \cos\frac{2\pi k}{M}\right]}{\delta p_- + 2p_{-,u}\delta \cos\frac{2\pi k}{M}},$$

and A'_k, B'_k are constants determined by $\sigma^l(x_0)$. This suggests, not surprisingly, that the main effect of the lane-change in dilute cases is simply a diffusion of the density across the lanes in the direction of travel. Figure 4.3 shows an example of this mean-field approximation which agrees well with the numerical simulation - parameters are used as in Figure 4.2 (b).

Assuming there is a unique equilibrium state, the density for plus- and minus-type particles in the multi-lane model with homogeneous rates will have lane homogeneity though it will depend on site. For small injection rate α_+, the system tends to a stationary state that is dilute near the minus end and in a high density near the plus end. Using a similar method as in Chapter 3, which is detailed in Appendix B to the lane-homogeneous case, for small injection rate, under the conditions that $\rho, \sigma = O(\delta)$ far away from the tip and ignoring $O(\delta^2)$, we find similar approximate expressions as (4.2) for the stationary state in dilute regions; see (B.2). For large enough α_+, dynamically *pulsing states* or *filled states* as discussed in Section 4.4.1 will appear.
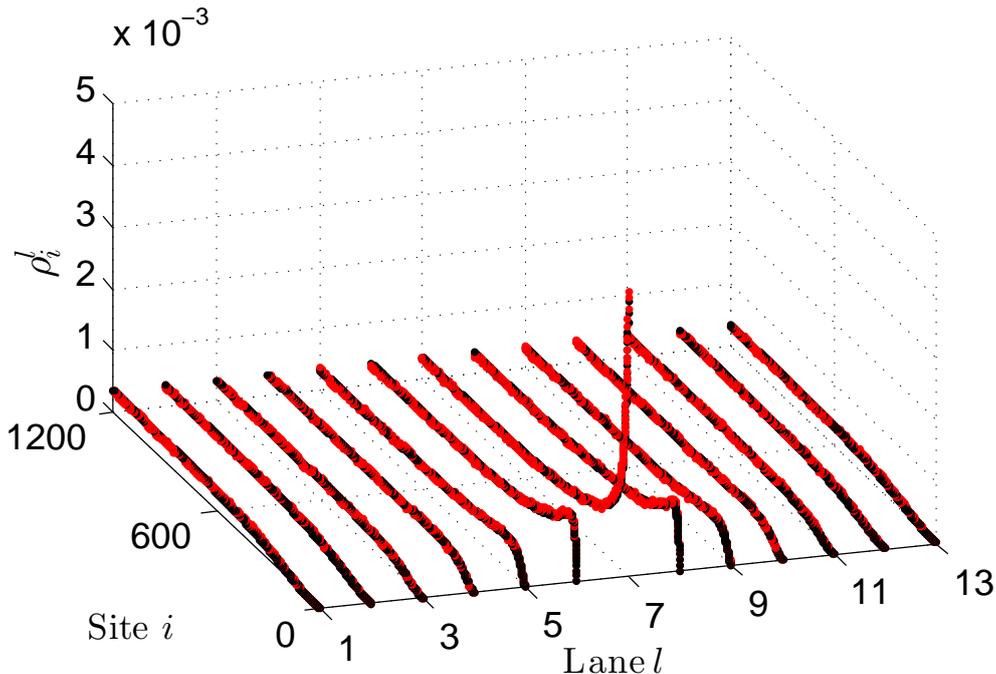
Figure 4.3: Comparison of mean-field approximation (red) from (4.6) to the numerical simulation (black) in Figure 4.2 (b).

4.3.2 A phase transition in the tip accumulation

For the half-closed system (i.e. closed at the plus end) in both the two-lane [64] and thirteen-lane models [65], it is clear that for typical particle-type change rates (e.g., $p_{+-} \ll p_+$), particles accumulate at the tip. On the other hand, from the mean tip size approximation (4.4) for the two-lane model, we see that $\langle n_{tip} \rangle$ increases linearly with injection rate α_+. However, this is not necessarily the case for the multi-lane (say, $M = 13$) model. In the following, we investigate the size of the tip accumulation and its dependence on the total injection rate α_+ for the thirteen-lane model with otherwise default parameters as in Table 4.2 and boundary conditions as in (4.5).

We compare two lane-change protocols: PI motivated from experiment observations in [29] and PII motivated from the study [134] (further protocols are considered in the next section). The protocol PI only allows minus-type particles to change lanes when blocked while protocol PII allows both type to change lanes when blocked; lane-change rates are assumed homogeneous and symmetric (see details in Section 4.3.3). Simulations gave a mean tip size that depends on α_+, fitting to a rational function with three fitting parameters A, B and C

$$\langle n_{tip}(\alpha_+) \rangle = \frac{\alpha_+ A(1 + \alpha_+ C)}{1 - \alpha_+ B};$$

see Figure 4.4 (a) and Table 4.3. Note that there is a singularity in this rational
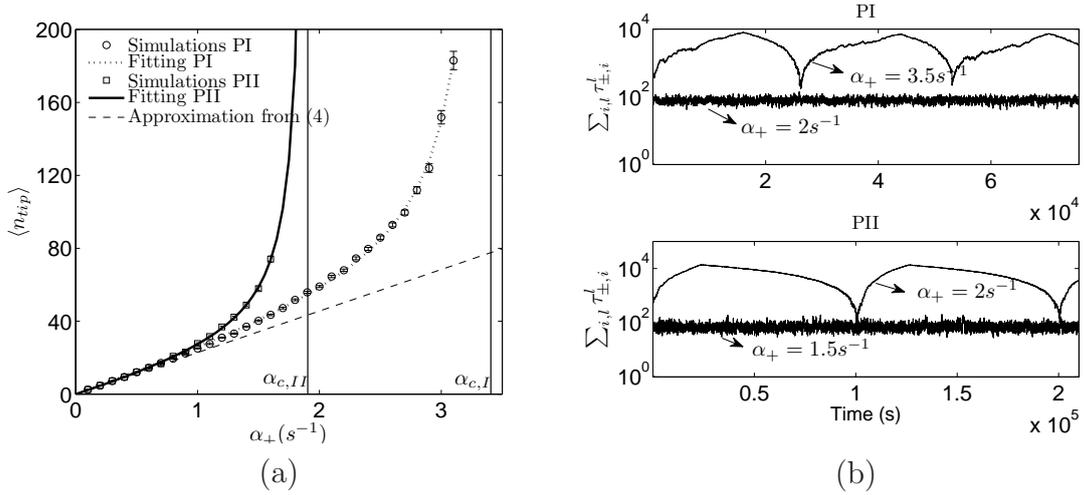
Figure 4.4: (a) shows mean tip size as a function of total injection rate α_+ for the multi-lane (M=13) model. Simulations PI refers to lane-change protocol PI where $p_{-,b} = p_+/2$ and $p_{+,b} = 0$ while simulations PII is for protocol PII where $p_{\pm,b} = p_+/2$. In both protocols we find a good fit to a rational function of α_+ with a singularity at a critical value $\alpha_{c,I} \approx 3.406$ s^{-1} (fitting PI) or $\alpha_{c,II} \approx 1.947$ s^{-1} (fitting PII). For comparison, the straight dash line shows the linear dependence (4.4) of α_+ in the two-lane model recalled in Section 4.2.1; other parameters use the values of corresponding rates in Table 4.2; see [64] for details. (b) shows the total occupancy $\sum_{l,i} \tau_{\pm,i}^l$ as a function of time for two typical injection rates as indicated, beyond and below the critical value for each of the lane-change protocols PI and PII. Other parameters used in the multi-lane model are default as in Table 4.2 and boundary conditions as in (4.5).

fitting function at $\alpha_+ = 1/B$. For the simulated system, these critical values are $\alpha_{c,I} = 3.406$ s^{-1} and $\alpha_{c,II} = 1.947$ s^{-1} respectively for lane-change protocol PI and protocol PII. Moreover, by comparing the change of the total occupancy of particles in the system in time between injection rates below and beyond the critical value, Figure 4.4 (b) indicates the existence of a transition between a *shock state* (where there is an approximately steady accumulation at the tip) and a new phase of motion, an unsteady *pulsing state* which is further examined in Section 4.4.1.

Additionally, by comparison with approximation (4.4) of the mean tip size from the two-lane model, we note that the mean tip size in the multi-lane model increases initially linearly but then nonlinearly for both lane-change protocols. This nonlinear increase is due to trapped minus-type particles at the tip and is investigated in the following section.

4.3.3 Influence of lane-changes on the tip accumulation

The size of accumulation at the tip clearly depends on the lane-change rules; see Figure 4.4 (a). Recall from Section 4.3.1 that lane changes can homogenize the densities so we expect the homogeneity of $\lambda_{tip}^l(t)$ among the lanes will depend on

A	B	C
PI	24.45 ± 0.329	0.2936 ± 0.00139	-0.2525 ± 0.00388
PII	22.18 ± 0.509	0.5136 ± 0.00908	-0.3978 ± 0.002219

Table 4.3: Best fit of the data from simulations in Figure 4.4 (a) to a rational function $\langle n_{tip}(\alpha_+)\rangle = \frac{\alpha_+ A(1+\alpha_+ C)}{1-\alpha_+ B}$ with parameters A, B, C. The values indicate best fit values and standard errors.

the lane-change rules when blocked. To confirm this, we examine the maximum difference among the $\lambda_{tip}^l(t)$ defined as

$$\Delta\lambda_{tip}(t) = \max\{\lambda_{tip}^l(t) - \lambda_{tip}^k(t) : k, l = 1, \cdots, M\}.$$

The distribution of this quantity gives a measure that characterizes how "smooth" ($\Delta\lambda_{tip}$ small) or "ragged" ($\Delta\lambda_{tip}$ large) the tip is. In particular, the larger the mean value $\langle\Delta\lambda_{tip}\rangle$, the easier it is for minus-type particles to be released from the tip.

We consider four different lane-change (when blocked) protocols with homogeneous lane-change rates in an attempt to better understand their influence on the structure of tip accumulation via the distribution of $\Delta\lambda(t)$ at stationary state. These are:

(PI) $p_{-,b} = p_+/2$, $p_{+,b} = 0$ – only minus-type particles are allowed to change lanes with a rate (homogeneous and symmetric) that preserves the velocity; this corresponds to the assumption used in [65];

(PII) $p_{\pm,b} = p_+/2$ – both minus- and plus-type particles are allowed to change lanes;

(PIII) $p_{-,b} = 0$, $p_{+,b} = p_+/2$ – only plus-type particles are allowed to change lanes;

(PIV) $p_{-,b}^{l \to l-1} = p_+/2$, $p_{-,b}^{l \to l+1} = 0 = p_{+,b}$ – only minus-type particles are allowed to change and to only one of the adjacent lanes with lane-homogeneous rate.

We ignore the influence from lane changes in the unblocked case as these are clearly not significant for escape from the tip. The distributions of the length differences $\Delta\lambda_{tip}$ at a fixed stationary time are shown in Figure 4.5 for above four different lane-change protocols; other rates are as default ones. Note that allowing plus-type particles to undertake lane changes "smooths" the structure of the tip. The results for lane-change protocols PI and PII agree with the homogenized density of both type of particles on the effect of lane changes (see Figure 4.2). Note the similar distribution of Δ_{tip} between PI and PIV (PII and PIII) from Figure 4.5, it is then reasonable to consider protocols PI and PII as typical lane-change protocols.

For both lane-change protocols PI and PII, particles can be trapped under several layers in the tip accumulation. Shown in Figure 4.4 (a) that the mean tip size increases more rapidly with injection rates for protocol PII, we suggest this is due

to there being more minus-type particles "trapped" in the tip which in turn lead to larger increase on the tip size. We say a particle is "trapped" if its motion (including forward motion and lane changes) is obstructed by occupation of other particles and loss the ability to take the motion due to the exclusion principle. We define two fractions: the *trapped minus-type fraction* $F_{-,trap}$ and the *minus-type fraction* F_- within the tip in the steady state as

$$F_{-,trap} = \frac{\text{mean number of "trapped" minus-type particles at the tip}}{\text{mean number of total minus-type particles at the tip}},$$

$$F_- = \frac{\text{mean number of total minus-type particles at the tip}}{\langle n_{tip} \rangle}.$$

In the two-lane model discussed in Section 4.2.1 where two types of particles move on different lanes, the density profile of minus-type particles is dilute, which indicates $F_{-,trap} \approx 0$. Additionally, from expressions (4.2) and (4.3),

$$F_- \approx \int_{x_s}^1 \sigma(x) dx / \int_{x_s}^1 (\rho(x) + \sigma(x)) dx \approx \frac{p_d}{2p_+} \langle n_{tip} \rangle$$

For the particular parameters in Table 4.2 with $p_d = p_{+-}$, the minus-type fraction $F_- \approx 0.2\%$ associated with a mean tip size $\langle n_{tip} \rangle \approx 20$. However, in the thirteen lane model, from Table 4.4, for low $\alpha_+ = 0.8 \ s^{-1}$ in lane-change protocol PI, $F_- \approx 4\%$ associated with $\langle n_{tip} \rangle \approx 20$ and $F_{-,trap} \approx 40\%$. This shows a difference between the two-lane model and the thirteen-lane model even for low injection rates, though with a similar mean tip size. Moreover, in the two-lane model, viewed as a queueing process, the expected delay for particles at the tip is $1/p_{+-}$, while in the multi-lane model, the positive fraction of trapped minus-type indicates that the average time spent at the tip is larger than $1/p_{+-}$. This *average tip delay* will be discussed later on in Section 4.3.4.

Comparing between the two lane-change protocols from Table 4.4, protocol PI gives lower $F_{-,trap}$ and F_- than those in protocol PII, with the same α_+ or the same mean tip size. This agrees with that a smoother structure of the tip accumulation is more likely to trap minus-type particles at the tip and indicates that the tip size and the (trapped) minus-type fraction are affected by each other.

4.3.4 Measures of bidirectional transport efficiency

The previous subsections indicate that allowing only minus-type particles to change lanes as a result of collisions is more effective (with less trapped minus-type particles) than allowing both types of particles to change lanes. To understand more on the bidirectional transport observed in living cells, it is interesting to speculate on the implications of the *in vivo* experiment data, particularly in Table 4.2, in terms of
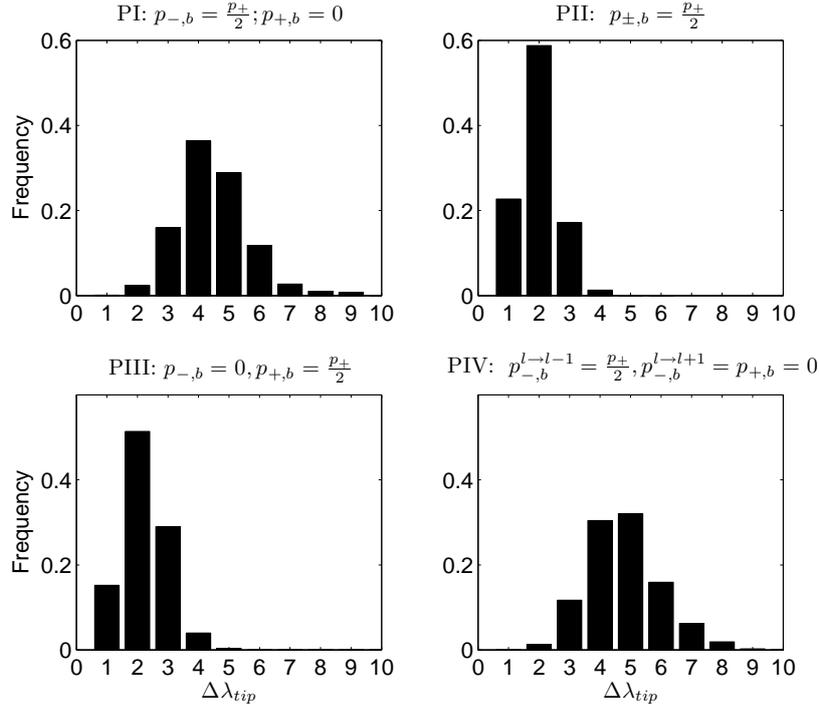
Figure 4.5: Distribution of maximum length difference $\Delta\lambda_{tip}$ for lane-change protocols PI-IV; other parameters are default as in Table 4.2 and boundary conditions as in (4.5). Note that the structure of the tip accumulation in PI or PII is clearly smoother than that in PI and PIV.

some non-trivial quantifiable efficiency.

There are many possible ways to quantify efficiency of bidirectional transport, depending on what sort of behaviour is important. For example, in some circumstances it could be that maximum speed is required while in other circumstances it could be that the maximum flux is required - for a practical system of bidirectional transport on a MT, different notions may be needed for different purposes. In a fungal model system, the particles accumulate at the MT plus end are thought to prevent endosome falling off the MT and to support their backward transport [65]. Therefore, efficiency transport of dynein requires a certain proportion of dynein reaching the tip to form an accumulation and a short duration at the tip. Therefore, we consider *particle arrival efficiency* and *average tip delay* defined as following.

Suppose that the n-th particle injected at the minus end is at location $(l, i) = (L_n(t), I_n(t))$ at time t, and suppose that:

- it enters the system at time $t_{n,1}$ and leaves the system at time $t_{n,4}$;

- the farthest point it reaches in the system is d_n, i.e. $d_n = \max_t I_n(t)$;

- it enters the "tip" at time $t_{n,2}$, i.e. this is the smallest t such that $I_n(t) > L_{tip}$;

- it leaves the "tip" at time $t_{n,3}$, i.e. this is the largest t such that $I_n(t) > L_{tip}$;

	$\alpha_+(s^{-1})$	0.8	1	1.2	1.4	1.6	1.8	2.0	4
	$F_{-,trap}$	37.8%	49.0%	66.7%	72.5%	79.6%	85.7%	88.2%	99.7%
PI	F_-	3.7%	4.5%	5.7%	7.6%	9.4%	12.1%	14.3%	51.3%
	$\langle n_{tip} \rangle$	19.7	24.9	31.0	36.8	43.7	52.1	59.9	$--$
	$F_{-,trap}$	59.7%	83.3%	89.8%	92.6%	95.8%	98.5%	99.6%	100%
PII	F_-	5.4%	9.9%	14.3%	20.2%	28.6%	42.7%	50.4%	57.6%
	$\langle n_{tip} \rangle$	20.3	28.1	36.5	48.3	70.1	$--$	$--$	$--$

Table 4.4: Comparison of trapped minus-type fraction $F_{-,trap}$ and minus-type fraction F_- at the tip between lane-change protocols PI and PII. This shows for protocol PI that there are lower F_- and $F_{-,trap}$ even for a similar mean tip size. When $\alpha_+ > \alpha_c$ in both protocols, $F_{-,trap} \approx 100\%$ and mean tip size does not convergent with time; marked as "$-$". Other parameters are default as in Table 4.2 and boundary conditions as in (4.5).

where L_{tip} refers to the farthest site away from the plus end at the tip, typically we set $L_{tip} \approx 90\%N$ for simulations. These times are illustrated in Figure 4.6 (left panel) with a comparison of endosome motility *in vivo* in Figure 4.6 (right panel). If the particle does not reach the tip then we have only $t_{n,1} < t_{n,4}$ defined, while if $d_n \geq L_{tip}$ then we have $t_{n,1} < t_{n,2} < t_{n,3} < t_{n,4}$ defined. Based on these notations, we define the *particle arrival efficiency* to be [1]

$$E_1 = \lim_{T \to \infty} E_1(T) = \lim_{T \to \infty} \frac{\#\{n \; : \; d_n \geq L_{tip}, \; t_{n,4} < T\}}{\#\{n \; : \; T_0 < t_{n,1} < t_{n,4} < T\}}.$$

Note that $0 \leq E_1 \leq 1$ is a dimensionless measurement of efficiency that is close to zero if few of particles arrive at the tip before leaving the system while it is close to one if most of particles arrive at the tip before leaving the system. The quantity E_1 is independent of how long it takes to arrive at the tip or leave the system. Meanwhile, we define the *average tip delay* to be

$$E_2 = \lim_{T \to \infty} E_2(T) = \lim_{T \to \infty} \frac{\sum_{\{n \; : \; ||d_n|| \geq L_{tip}, t_{n,4} < T\}}(t_{n,3} - t_{n,2})}{\#\{n \; : \; d_n \geq L_{tip}, \; t_{n,4} < T\}}.$$

The average tip delay E_2 has unit of time, and measures the average time spent at the tip for all particles that get there: larger values indicate that particles are trapped at the tip for a long time while small values indicate that the particles wait only a short time before leaving the tip. Note that the quantity E_2 is independent of E_1, the proportion of particles that arrive at the tip. Note also that if we assume homogeneous particle-type change rates then $E_2 \geq 1/p_{+-}$.

One can derive approximated upper and lower bounds of E_1 for the lane homogeneous multi-lane model. Considering the density of plus-type particles in dilute

---

[1] T_0 is assumed to be large enough that any transients have decayed, i.e., $t_{1,1} \geq T_0$.
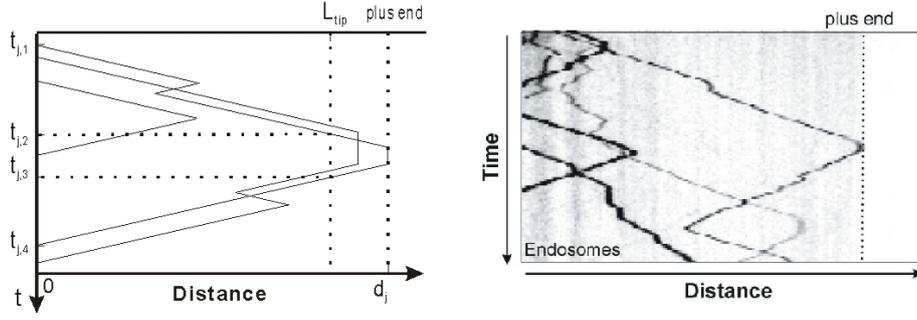
Figure 4.6: Typical motion of three particles injected into the system (left panel). We show the times $t_{j,m}$ $m = 1, \ldots, 4$ for the j−th particle. Particles that exceed L_{tip} are said to have entered the tip region. Kymograph (right panel) shows motility of early endosomes that were visualized by photo-activation of the endosome marker paGFP-Rab5a [65] in subapical regions of a cell of the fungus Ustilago maydis. Note the similarities in the two panels on the trajectories of motions.

situation; see density approximation (B.2) in Appendix B, we have

$$
\begin{aligned}
E_1 \quad &\leq \quad \min\{\rho(1)/\rho(0), 1\} \\
&= \quad \min\left\{\exp\left[\frac{Np_{-+}}{p_- + p_{-,u}^{l \to l+1} + p_{+,u}^{l \to l-1}} - \frac{Np_{+-}}{p_+ + p_{+,u}^{l \to l+1} + p_{+,u}^{l \to l-1}}\right], 1\right\}
\end{aligned} \tag{4.7}
$$

while considering the probability of first particle-type change occurring at the tip, we have

$$
E_1 \geq \left[1 - \frac{p_{+-}}{p_+ + p_{+,u}^{l \to l+1} + p_{+,u}^{l \to l-1} + p_{+-}}\right]^{L_{tip}} \approx 1 - \frac{Np_{+-}}{p_+ + p_{+,u}^{l \to l+1} + p_{+,u}^{l \to l-1}} \tag{4.8}
$$

as particles may change directions (or change types) several times before reaching the tip. Figure 4.7 (a) shows the upper and lower bounds for E_1 compared to the simulations. Moreover, from Table 4.5, this arrival efficiency is independent on injection rate.

The average tip delay E_2 is clearly dependent on p_{+-} for a homogeneous model as $1/p_{+-}$ is the expected delay of minus-type particles without obstruction such as in the two-lane model recalled in Section 4.2.1 (see [64] for details). We therefore consider the *delay ratio* $E_2 \times p_{+-}$, i.e., the ratio of the average tip delay to the expected delay if there are no trapped minus-type particles. This ratio is usually no less than 1, and when it is close to 1 this is the most efficient situation in terms of the delay being minimal. Simulation results in Table 4.5 and the inset to Figure 4.7 show that for both lane-change protocols in the multi-lane model, this delay ratio is larger than 1 or $E_2 > 1/p_{+-}$. This agrees with results in Table 4.4 showing the existence of certain proportion of minus-type particles being "trapped" at the tip. Comparing Figure 4.7 (a) and the inset in Figure 4.7 (b), we consider the
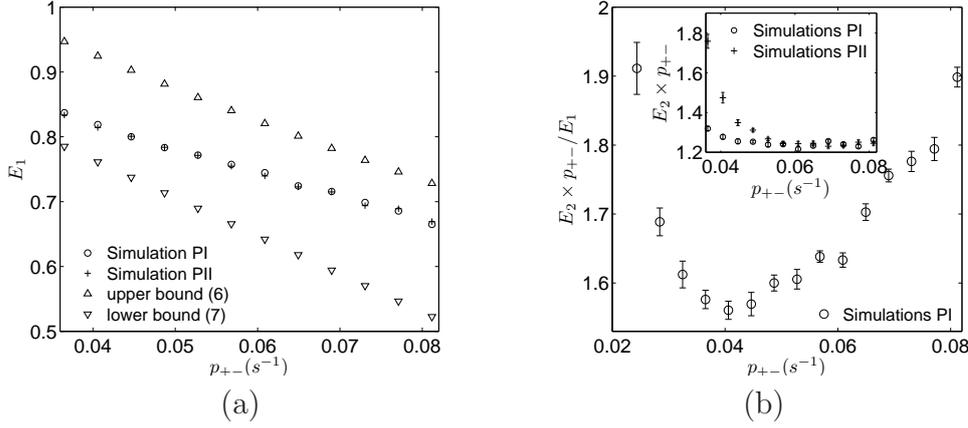
Figure 4.7: Illustration of E_1 and E_2 when varying p_{+-}. (a) shows that the arrival efficiency E_1 in both lane-change protocols PI and PII behaves similarly as varying p_{+-} with approximate upper bound from (4.7) and lower bound from (4.8). (b) shows the balance between delay ratio and arrival efficiency quantified as $E_2 \times p_{+-}/E_1$ for protocol PI; the inset shows the comparison between two protocols PI and PII of the delay ratio $E_2 \times p_{+-}$; error bars are indicated. Simulations are done by averaging over 10 runs using the Gillespie algorithm in a time interval $[T_0, T] = [500s, 3000s]$; other rates are default as in Table 4.2 and boundary conditions (4.5).

dimensionless quantity $E_2 \times p_{+-}/E_1$ to be a balance between arrival efficiency and delay ratio. As varying p_{+-} we find a minimum value where p_{+-} is closed to the experiment data of $p_{+-} = 0.0406 \ s^{-1}$; see Figure 4.7 (b). This offers an indication of *in vivo* transport rates.

Comparing the two lane-change protocols PI and PII, protocol PI is more effective in the sense that it has a relatively lower delay ratio $E_2 \times p_{+-}$ when varying α_+ (see Table 4.5) or for small p_{+-} (see the inset in Figure 4.7 (b)). Similar to the case for trapped minus-type fraction and mean tip size, the average tip delay time increases more rapidly with injection rate in protocol PII than the increase in protocol PI.

4.4 Critical behaviour and pulsing states

Results from Section 4.3.2 suggest that the mean tip size does not converge when an injection rate α_+ approaches a critical injection rate $\alpha_{c,I}$ for lane-change protocol PI ($\alpha_{c,II}$ for protocol PII) in a finite system; additionally, by simulating the efficiency defined in terms of delay ratio $E_2 \times p_{+-}$, the system will be less efficient with either a large total injection rate α_+ (see Table 4.5) or a small particle-type change rate p_{+-} (see Figure 4.7 (b)). Large mean tip size or inefficiency on $E_2 \times p_{+-}$ are expected due to high densities of plus- and minus-type particles, and in the following we discuss the dynamics of pulsing states that exist in this model.

	α_+/s	0.8	0.9	1	1.1	1.2	1.3	1.4	2
PI	E_1	81.9%	81.9%	81.5%	81.9%	81.6%	81.6%	81.9%	81.7%
	$E_2(s)$	30.71	30.87	31.1	31.1	31.8	32.6	33.5	48.8
PII	E_1	81.4%	81.8%	81.7%	81.7%	81.9%	81.8%	81.5%	≈ 0
	$E_2(s)$	31.9	33.2	34.2	37.9	44.9	48.7	61.4	$--$

Table 4.5: Comparison of E_1, E_2 between lane-change protocols PI and PII. The arrival efficiency E_1 in both protocols is relatively independent of α_+ and drops to almost zero when $\alpha_+ > \alpha_{c,I}$ for protocols PI ($\alpha_+ > \alpha_{c,II}$ for protocol PII). The average tip delay E_2 in both protocols are larger than the expected delay $1/p_{+-} \approx 24.6~s^{-1}$ when no minus-type particles are trapped, and the delay time increases more rapidly for protocol PII than for PI when increasing α_+. Note that the particle-type change rate p_{+-} is fixed here, meaning that the delay ratio $E_2 \times p_{+-}$ is a multiple of E_2. Simulations are done as in Figure 4.7 with otherwise default parameters.

4.4.1 Pulsing states in the system

For injection rate α_+ smaller than the critical value α_c discussed in Section 4.3.2, the system converges to a stationary state (*shock state*) with an accumulation of certain size at the tip, and this tip size increases as α_+ approaches α_c. For $\alpha_+ > \alpha_c$ and otherwise default parameters, a new type of behaviour that we call a *pulsing state* can appear. These are characterized by the behaviour in Figure 4.8. For finite systems, near α_c the accumulation at the tip may show large irregular oscillations including a propagating region or *pulse* of high density that moves away from the tip before dispersing.

In a *pulsing state*, the whole system density undertakes large approximately periodic oscillations. These can be split into two parts:

- A *filling phase* during which the density at the minus end is low, and a growing high density *pulse* of mixed particles moves steadily towards the minus end. During this phase there is a net flux into the system.

- An *emptying phase* during which the density at the minus-end is high, and the pulse propagates out of the system. During this phase there is a net flux out of the system.

For most of the cycle there is a low density region between the tip and the pulse. The pulsing occurs through an alternation between these phases as fronts (evident in Figure 4.8) separating low and high density regions move through the domain. At other parameters we find the system converges to a *filled state* for α_+ larger than α_c. Figure 4.9 shows examples of the pulsing and filled state. In the filled state, once the filling phase is complete the system remains approximately full.

To provide a better understanding of the behaviour of system in a pulsing state, Figure 4.10 shows successive horizontal lines as the evolution of the medium time

average of the density $\sum_{i=1}^{M}(\tau_{-,i} + \tau_{+,i})/M$ (over successive blocks of 1260 s) from a time-series and gradual changes of the local density. Figure 4.10 (a,b) shows rapid convergence to a stable accumulation at the tip, though (b) displays more fluctuations. Examples of pulsing states are illustrated in Figure 4.10 (d,e,f) for increasing values of α_+; these exhibit long approximately periodic oscillations. Figure 4.10 (c) shows an intermediate situation where the tip accumulation shows irregular large amplitude oscillations. The main behaviour in a high-density mixed region will be changes of particle types and therefore we expect the ratio of densities between minus- and plus-type particles to reach the equilibrium ratio given by the type-change rates, i.e.

$$\tilde{\rho} = \frac{p_{-+}}{p_{-+} + p_{+-}}\kappa, \quad \tilde{\sigma} = \frac{p_{+-}}{p_{-+} + p_{+-}}\kappa$$

where $\kappa = \tilde{\rho} + \tilde{\sigma} \approx 1$ represents the total local density.

For both lane-change protocols PI and PII we find pulsing states for $\alpha_+ > \alpha_c$ and otherwise default parameters - we interpret this as an existence of a negative net flux for the high-density mixed phase. Note that densities $\tilde{\rho}$ and $\tilde{\sigma}$ are primarily governed by the particle-type change rates p_{+-} and p_{-+}, if we increase p_{-+}, then the net flux may change to be positive and the pulsing state will be replaced by approaching to a high-density uniform filled state. For example, Figure 4.10 (e) shows the pulsing state for $p_{-+} = 0.0273$ s^{-1} with $\alpha_+ = 4$ s^{-1} while Figure 4.9 (b) shows a filled state for $p_{-+} = 0.14$ s^{-1} and $\alpha_+ = 4$ s^{-1} (other parameters are the default values). For the latter case, we infer that an initial pulse with $j > 0$ will saturate to $\tilde{\rho} + \tilde{\sigma} = 1$ and then $j \to 0$ as the number of vacancies in the high density state goes to zero. It will be an interesting challenge to understand the statistical properties of these high-density mixed states and, for example, to predict j from the parameters of the system, as there might be more than one particle compete for a common empty site.

Numerical simulations show that this pulsing state is robust to changes in parameters – Figure 4.11 shows phase diagrams for lane-change protocols PI and PII on varying α_+ and p_{+-} with other default parameters. The particle-type change rates that we usually use obey $\frac{p_{+-}}{p_+}, \frac{p_{-+}}{p_-} < \frac{1}{N}$ which means that a typical switching of plus-type particle occurs at the tip (see E_1 in Table 4.5). This novel pulsing state also appears when $\frac{p_{+-}}{p_+}, \frac{p_{-+}}{p_-} > \frac{1}{N}$; see Figure 4.12. A necessary condition for a pulsing state we suggest is that α_+ is beyond a critical value (i.e., not in a shock state) and there is a net negative flux in the high-density mixed region.

4.4.2 System size effects

Although the previous section focuses on a fixed system size N, the critical transition to pulsing states is invariant of N as $N \to \infty$ under certain scalings of parameters for

$t = 50000 \times h_t$

$t = 70000 \times h_t$

$t = 140000 \times h_t$

$t = 160000 \times h_t$

$t = 300000 \times h_t$

$t = 340000 \times h_t$
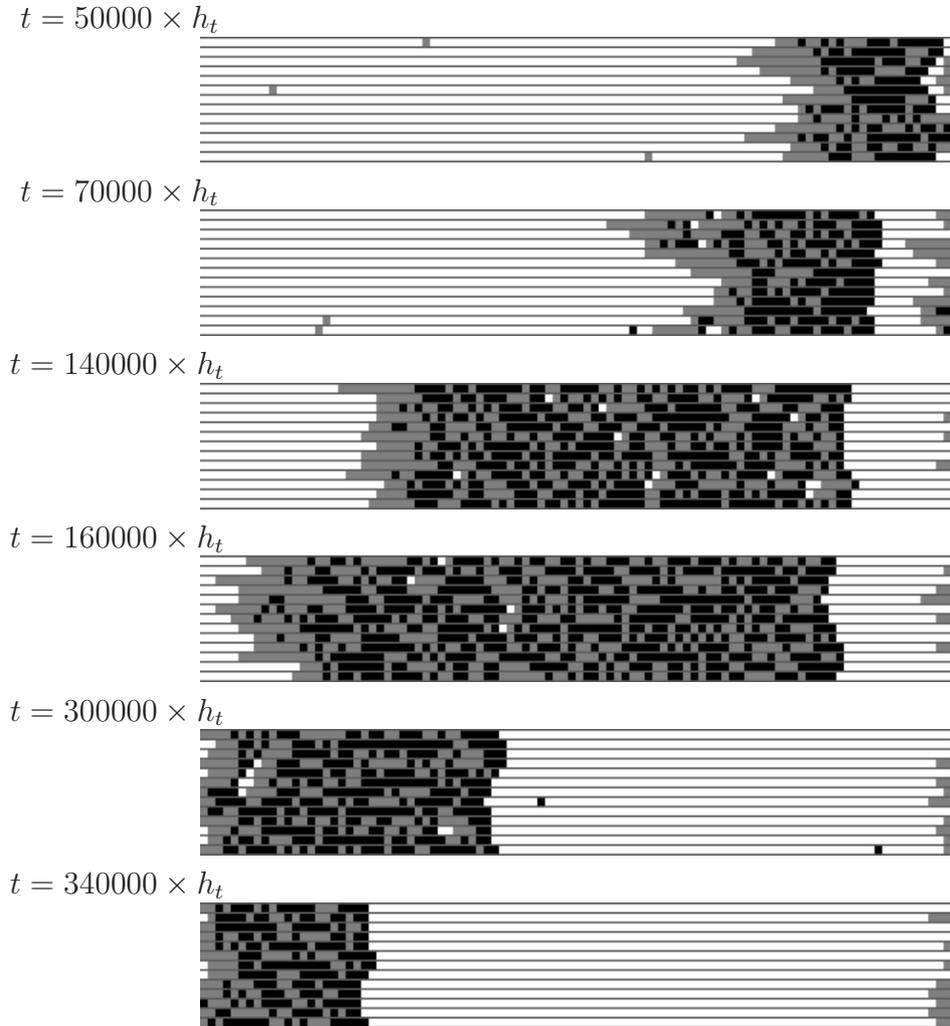
Figure 4.8: Time progress of a pulsing state for the thirteen lane model of size $N = 100$, $\alpha_+ = 4.0 \ s^{-1}$ and no flux on the plus-end; otherwise parameters as in Table 4.2 and boundary conditions as in (4.5). The sequence of filling (top three frames) and emptying (bottom three frames) repeats approximately periodically. Observe that the pulse of high-density mixed particles propagates slowly to the left via diffusion of vacancies through the pulse. Grey indicates plus-type particles (that move to the right) while black indicates minus-type particles (that move to the left). The white regions indicate vacancies.
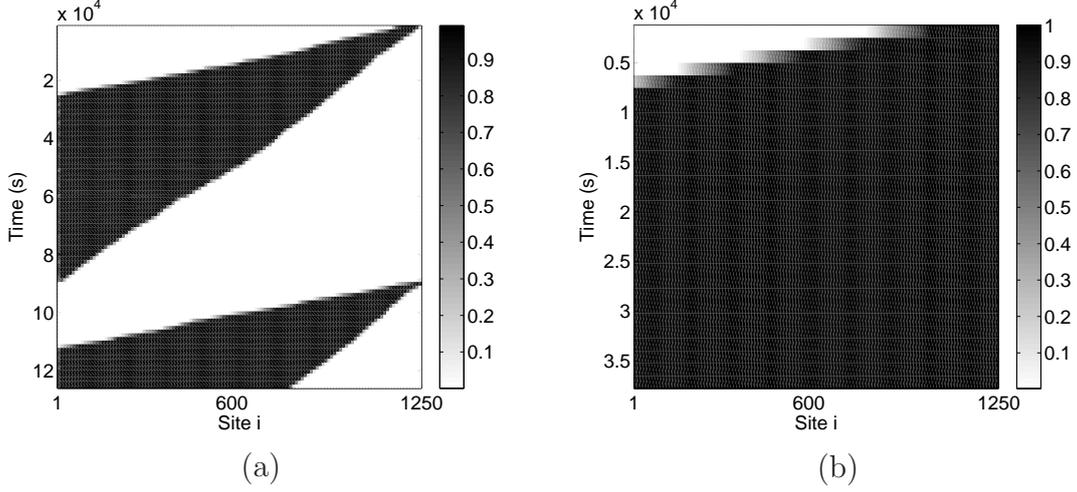
Figure 4.9: (a) shows a pulsing state for $p_{-+} = 0.05 \ s^{-1}$ and $\alpha_+ = 3 \ s^{-1}$; (b) shows a filled state for $p_{-+} = 0.14 \ s^{-1}$ and $\alpha_+ = 4 \ s^{-1}$ and this approaches a homogeneous high-density mixed equilibrium state. The other rates are default as in Table 4.2 and boundary conditions in (4.5).
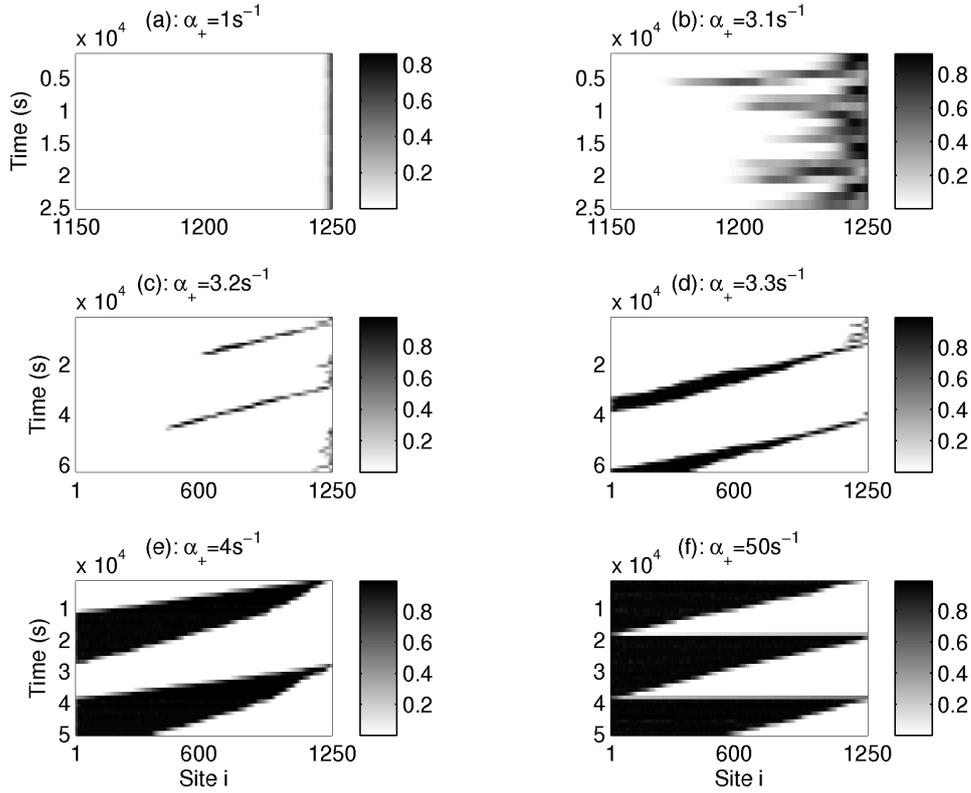
Figure 4.10: Each horizontal line represent a time-average of the occupancy $\sum_{l=1}^{M}(\tau_{-,i}^{l} + \tau_{+,i}^{l})/M$ over blocks of length 1260 s in the homogeneous thirteen-lane model ($M = 13$) with injection rate α_+ indicated (other rates as default). In (a), the model with a small total injection rate reaches its stationary state with a small number of particles accumulated in the tip. (b)-(d) show the density-time courses for injection rates near the critical value. In (d)-(f), pulsing states appear where the accumulation moves away from the plus end and simultaneously grows.
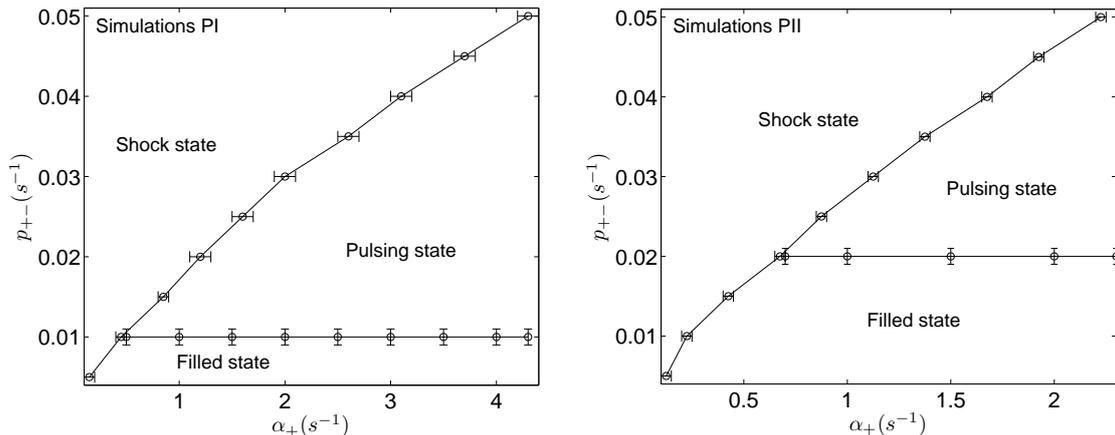
Figure 4.11: Numerically obtained phase diagrams for lane change protocol PI (left panel) and lane change protocol PII (right panel). Other default parameters are as in Table 4.2 and boundary conditions as in (4.5). Bars indicate uncertainty of the borders between different states.
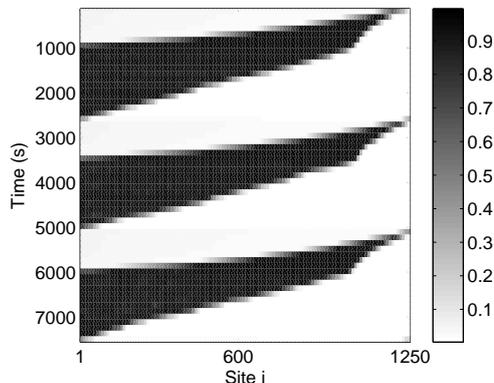
Figure 4.12: A pulsing state for $p_{-+} = 0.2 \ s^{-1}$, $p_{+-} = 0.4 \ s^{-1}$ and $\alpha_+ = 80 \ s^{-1}$; other parameters are default as in Table 4.2 and boundary conditions in (4.5).

the multi-lane model with boundary conditions (4.5). For example, if we scale the forward motion rates, keeping $p_{\pm}/N$ constant and use the lane change rates when blocked $p_+/2$ as default whilst keeping the particle-type change rates constant, we find no significant variation of mean tip size with N as illustrated in Table 4.6. This agrees with the approximation (4.4) from the two-lane model. For injection rates beyond a critical value and the same scaling we find pulsing states for arbitrarily large N.

4.4.3 A simple model with a critical injection rate

To better understand the appearance of a critical injection rate α_c that leads to a transition in the behaviour of the tip, we introduce a simpler model that computably predicts nonlinear behaviour of the mean tip size with injection rate α_+, and a singularity of the mean tip size at finite injection rate.

N	400	800	1200	1600	2000
$\langle n_{tip} \rangle \pm sem$	26.7 ± 0.278	26.9 ± 2.7	26.8 ± 2.97	26.9 ± 2.9	26.7 ± 2.9

Table 4.6: The tip size when varying the system size N for parameters in Table 4.2 and boundary conditions (4.5) except keeping $p_+/N = 0.17$, $p_-/N = 0.1631$ and $p_{-,b} = p_+/2$. There values are chosen to be consistent with rates in Table 4.2 when $N = 1250$. Mean and standard error of mean are shown.

Consider a single lane first-in, last-out queue of plus-type and minus-type particles. Plus-type particles are assumed to arrive at the left end of the queue at a rate α per time-step. Every time-step, we assume that all particles independently to be minus-type with probability p and plus-type with probability $1 - p$. A number of particles is assumed to leave the queue whenever the left-most particle is of minus-type, in which case all of the adjacent minus-type particles are assumed (instantaneously) to leave the queue. This results in a steady growth and intermittent loss of particles. At a given time-step t, if we assume the queue has size $n(t)$ then after random changes in type, the number of particles that leave the queue can be expressed as

$$\lambda(n) = \sum_{m=1}^{n} m p^m (1 - p) + n p^n = p \frac{1 - p^n}{1 - p}.$$

Hence the mean rate of net growth of the queue will be given by $\alpha_+ - \lambda(n)$. This will give zero net growth when $\alpha_+ - \lambda(n) = 0$. Therefore, with injection rate α_+, the mean size of the queue is

$$\langle n(\alpha_+) \rangle = \frac{\ln \left(1 - \alpha \frac{1-p}{p} \right)}{\ln p},$$

which predicts a critical injection rate $\alpha_c = \frac{p}{1-p}$. For $\alpha_+ < \alpha_c$, $\langle n(\alpha_+) \rangle$ grows monotonically and nonlinearly with $\lim_{\alpha_+ \to \alpha_{c-}} \langle n \rangle (\alpha) = \infty$. These are clear analogies with the observations of mean tip size in the thirteen-lane model in Figure 4.4 (a). Indeed, one can fit the data in Figure 4.4 (a) to a logarithmic function but the fit is inferior to the rational function discussed there, suggesting that the model above is too simple for an accurate quantitative explanation. This simple model reproduces the nonlinear increase for $\alpha_+ < \alpha_c$ in Figure 4.4 (a) and the singular behaviour at the critical value α_c. For $\alpha_+ > \alpha_c$ it predicts unbounded growth of the queue, analogous to convergence of the system to a "filled state".

4.5 Discussion

Motor-driven bidirectional transport of vesicles and organelles is vital for the organization and function of eukaryotic cells and intracellular motility serves various cellular processes [135]. The basic function of bidirectional vesicle transport is to deliver cargo over distances, thereby modifying gradients and ensuring communication between different regions of the cell.

By considering the process in a number of stages, starting with cargo uptake, followed by transport along the fibres of the cytoskeleton, and finally ending with cargo off-loading, the site of unloading is often also a region of cargo uptake. Transport back on the cytoskeletal track therefore not only recycles the transport vesicles, but also serves for long-distance delivery to other regions of the cell. In a fungal model system, it has recently been shown that dynein are concentrated at MT plus-ends to prevent organelles falling off the track and this concentration of dynein is done by an active retention mechanism (based on controlled protein-protein interaction) and stochastic motility of motors [65, 24].

An accumulation of motors at MT plus-ends can be seen as an inefficiency, as dynein motors are supposed to transport particles rather than wait at the MT end. Thus, the cell needs to find a compromise between (a) ensuring that organelles are captured at MT ends, which requires dynein accumulation at the plus-ends [65] and (b) keeping dynein moving along MTs to deliver the cargo to minus-ends. As discussed in Section 4.3.4, an interesting result of this study is that the parameters from [65] in a *Ustilago maydis* system (and p_{+-} in particular) do address this compromise between (a) and (b). Moreover on comparing different lane-change protocols (that is, either dynein changes lanes or both kinesin-1 and dynein change lanes), we find that it is necessary for only dynein to change lanes in order to give biologically realistic system states over a larger range of possible fluxes; see Figure 4.4 (a).

The maximum unidirectional flux in the thirteen-lane model can occur, by analogy with the so-called *maximal current state* in the ASEP model [86, 85], when $\alpha_+ \approx 13 \times p_+/2 \approx 1300 \ s^{-1}$, assuming appropriate boundary conditions and only one particle type to avoid opposite-directed collisions. Note that the maximal flux with bidirectional transport in the thirteen-lane model is about the half of that in unidirectional transport. However, the existence of a critical injection rate $\alpha_c \ll 1300/2 \ s^{-1}$ (see Figure 4.4) in the half-closed homogeneous thirteen-lane model places a much lower bound on the maximum flux. The experimentally measured $\alpha_+ \approx 1.06 \ s^{-1}$ in Table 4.2 is of the same order as α_c. To achieve bidirectional flux that is half of the maximum unidirectional flux (about $600 \ s^{-1}$) on a MT, much more organized transport with specific control of lane-change to segregate different particles into different lanes (as in Table 4.1) is therefore necessary.

For the half-closed system, we have found for $\alpha_+ > \alpha_c$ some novel "pulsing states"

of the system. It will be very interesting to further explore the region of existence of these states. There may exist other new phases for other boundary conditions and/or transition rates in the multi-lane model. An open question includes whether one can find a better understanding of the dynamics of pulsing states and/or whether there are analytic approximations that confirm the phase diagram approximated numerically in Figure 4.11.

The model can be generalized to incorporate a number of features that may be important for MT transport. This includes (a) additional species of motor with different transport properties, such as the several types of kinesin known to exist *in vivo* [21, 136]; additional motors can be expected to increase collisions along the MT length and cause high density of motors that might affect the transport efficiencies described in Section 4.3.4. (b) The detachment and reattachment of motors from the MT [113] may be important in other systems; the size of any accumulation will clearly be affected by this. (c) Non-trivial geometry of MT bundles needs consideration as motors may jump between different MTs; this might be another possibility to avoid collision between counter-moving organelle. (d) A more realistic motor and cargo size will influence the ability of lane changes to overcome blockages. Finally (e) static obstructions such as microtubule associated proteins will influence the behaviour of motors on the MT by increasing more potential blockages [134, 55, 57, 58]; a high concentration of these will clearly influence the transport efficiency. At present, quantitative data for most of these processes are not available for any living cell. With each additional process one can gain quantitatively more precise mathematical representation of the full MT-mediated transport within a cell. It remains to be seen whether new qualitative effects and better understanding will result from more accurate models.

Chapter 5

A model for motor-mediated bidirectional transport on an antipolar microtubule bundle

Long-distance bidirectional transport of organelles depends on the motor proteins kinesin and dynein. Quantitative live cell imaging in a fungal model system demonstrates that early endosomes (EEs) move along antipolar microtubule (MT) bundles. Near the cell poles these bundles become unipolar and extend their plus ends towards poles of the cell. Dynein motors move EEs from the plus end of a microtubule in the unipolar section in the bundle into the region of bipolar MTs (we refer to bipolar section) where kinesin-3 motors possibly take over. At all sections, the organelles can change direction. Using quantitative data obtained from this experimental system, we previously developed ASEP-type models of bidirectional motion on unipolar MTs. Here we extend this approach to model bidirectional motility along an antipolar microtubule bundle. In our model, particles (representing the organelles) change direction on each MT with a turning rate Ω and the MTs are linked to each other at the minus ends where particles can hop between MTs with a rate q_1 (obstacle-induced switching rate) or q_2 (end-induced switching rate). By numerical simulations and mean-field approximations, we investigate the distribution of particles along the MTs for different overall densities Θ. We find that even if Θ is low, the system can exhibit shocks in the density profiles near plus and minus ends caused by queueing of particles. We also discuss how the switching rates $q_{1,2}$ influence the type of motor that dominates the active transport in the bundle.

5.1 Introduction

Numerous theoretical studies attempt to describe motility behaviour of cargos along a single MT or a network of MTs [70, 109, 72]. One of the simplest and well

studied models is the *asymmetric simple exclusion process* (ASEP) defined on a single track [85]. Extended ASEP models for bidirectional transport have made various assumptions to avoid collisions between opposite-directed particles. One is assuming that particles are binding and unbinding to/from tracks [113, 114]. Another is assuming that the exclusion principle only applies to particles moving in the same direction and presence of a motor in the opposite direction modifies the rate at which motors enter the site [115]. Alternatively, assuming high direction-change rates can also avoid clusters due to collisions on the single lane [117]. In addition, Juhász introduces a two-lane ASEP [124] with opposite-directed particles moving in separate lanes where no collision between opposite-directed particles will occur. Moreover, we introduce a multilane model in [66] where particles can change filaments to avoid collisions, taking into account that a single MT consists of 13 protofilaments, each of which providing a potential track for motors.

Based on recent advances in live cell imaging techniques and the use of the fungal model system *Ustilago maydis*, *in vivo* observation of dynein indicates that collision between opposite-directed motors rarely occurs [65]. This allows adapting the two-lane model in [124] to investigate the bidirectional transport of dynein motors on unipolar MTs, which provides an explanation for the formation of the dynein accumulation at MT plus-ends [64, 65]. However, more recent work on *U. maydis* has shown that the unipolar MT is restricted to the cell poles, whereas MTs form antipolar bundles that extend their plus-ends towards cell poles of the hyphae [25]. EEs undergo long-distance bidirectional motility [9] and are mediated by kinesin-3 or dynein [24]. Interestingly, the long-distance motility along the bipolar MTs is mainly mediated by kinesin-3, whereas dynein is taking EEs along the unipolar MT [25]. Moreover, EEs are observed to travel across the entire bundle of MTs [25], which suggests that EEs hop between MTs in the bundle.

A similar hopping between tracks has been modelled for unidirectional traffic [104, 105, 63, 106, 107] where parallel tracks are connected to a single track via junctions. These junctions allow particles on the single track to step into either of the parallel tracks. Here we apply this junction mechanism to bidirectional transport, and introduce a simple ASEP-like lattice model for bidirectional motility of cargo along an antipolar microtubule bundle. In our model, the lattice is composed of two MTs that are coupled at microtubule minus ends and the arrangement of antipolar MT bundle gives unipolar and bipolar sections within the bundle. A detailed description of the model is given in Section 5.2. In Section 5.3, we show that the distribution of particles along the lattice can exhibit a variety of phases depending on the parameters; in Section 5.3.1 the phases in the unipolar section are analyzed while in Section 5.3.2 the phases in the entire system are considered. In particular, we show that even at a low overall density of particles, particles can accumulate at

minus ends as well as plus ends. Moreover, we find a novel and interesting phase where density profiles of one type of particles can smoothly connect between low and high density. These different phases are well approximated by mean field analysis. In Section 5.4, we consider how the MT switching affects the contribution of each type of motors in the transport of cargos. Finally, in Section 5.5 we discuss biological relevance from this model.

5.2 A lattice model with antipolar bundling

In this section, we introduce a simple discrete-lattice model with antipolar bundling of MTs (we refer to each MT as a track). The bundle is presented by a lattice of length N and contains two tracks of length $N - N_1$ and N_2 respectively. The two plus ends of MTs are located at two ends of the lattice and the other ends of two MTs - the minus ends - are in the middle; see Figure 5.1. The two tracks have a common section of length $N_2 - N_1$ (assuming $N_2 > N_1$) between two minus ends. This section is referred to *bipolar section*. The left sections in the bundle are referred to *unipolar sections* which are of a relative length x_1 and $1 - x_2$ respectively where $x_{1,2} := N_{1,2}/N$. In the following, we consider a symmetric lattice with $x_1 + x_2 = 1$.

In the bundle, each track can support bidirectional transport of particles driven by opposite-directed motors and particles are of two types: plus- and minus-type. Plus-type particles are driven by plus-directed motors moving towards the plus end of the track whereas minus-type particles move towards the minus end by minus-directed motors. Reversal of transport direction along each track can be realized by a brief "tug-of-war" event [42, 45, 43, 7] between counteracting motors on the particle. We assume no collisions between opposite-directed particles and transport on each track in a particular direction is on a separate lane as in [124, 64]. The lattice hence contains four lanes, each of which supports one direction and for a single type of particles as illustrated in Figure 5.1 (b).

When minus-end particles move from a unipolar to bipolar section, the minus end in the junction may enhance plus-directed motors on the particles to hop onto the other track, resulting changes of the track on which particles move and the type of particles. Thus the minus ends can be viewed as "obstacles" for minus-type particles when stepping forward on the same track and the bipolar section enables the particles to switch between tracks. This allows them to travel across the entire lattice from one plus end to the other. The track switching may be possible inside the bipolar section as well as at the junction between bipolar and unipolar sections. In this chapter, we only allow minus-type particles to switch tracks when stepping forward at the junctions.

In our model, we identify each location in the lattice by a pair (l, i) together
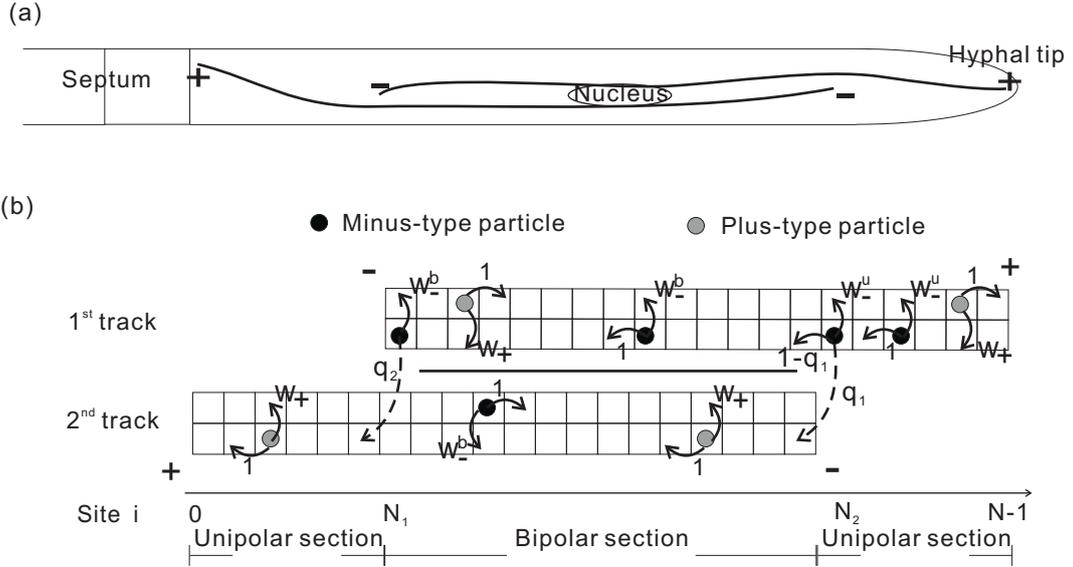
Figure 5.1: (a) shows a schematic hypha where two MTs with plus ends at cell poles (tip and septum) form an antipolar bundle. (b) shows a schematic diagram of bidirectional transport on the bundle which is presented as a discrete lattice of length N. Two tracks in the lattice represents two MTs and are of length $N - N_1$ and N_2 respectively with plus ends at two ends of the lattice. Plus- and minus-type particles on each track move on separate lanes. The *bipolar section* refers to the overlapped section of two tracks while the *unipolar sections* are for the rest sections in the bundle. The two unipolar sections are of a relative length x_1 and $1 - x_2$ where $x_{1,2} := N_{1,2}/N$. We assume that the track switching only occurs for minus-type particles at the junctions between sections and occurs with rate $q_{1,2}$. If $q_{1,2} = 0$ then the two MTs are uncoupled.

with a moving direction (corresponding to a lane in each track l) where $l \in \{1, 2\}$ and $i \in \{0, \cdots, N - 1\}$ denotes the site along the lattice. Particles hop from one location to another with a transition rate and the possible transitions we consider are given below.

Forward. Plus and minus-type particles on each location (l, i) move forward to the nearest site along the same lane with rates $p^l_{+,i}$ and $p^l_{-,i}$ respectively. We assume homogeneous forward rates on each lane which are set to be $p_\pm$ for plus- and minus-type particles except at the junctions $(1, N_2)$ and $(2, N_1 - 1)$ for minus-type particles. Furthermore, we assume $p_\pm = p$ (corresponding to same velocities which is suggested from *in vivo* transport [65, 24]). For convenience, we let $p = 1$ and other rates in units of p. For the junctions between sections, we set $p^1_{-,N_2} = p^2_{-,N_1-1} = 1 - q_1 \in [0, 1]$ where q_1 is an obstacle-induced switching rate given below.

Track switching. We allow minus-type particles at junctions $(1, N_2)$ and $(1, N_1)$ to step forward onto the second track together with a type change with rate q_1 (called obstacle-induced switching rate) and $q_2 \in [0, 1]$ (called end-induced

switching rate) respectively. Similarly, minus-type particles on the second track are allowed to switch onto the first track at the junctions with the same corresponding rate.

Direction change. Plus- and minus- type particles change directions (i.e., changes in type) at each track with rates $\omega_+^l(i)$ and $\omega_-^l(i)$ respectively. The direction change occurs at the same site and on the same track. We assume homogeneous direction-change rates for plus-type particles which denote w_+ and homogeneous rates for minus-type particles within each section which denote $w_-^{u,b}$ for unipolar and bipolar sections respectively[1]. Here, we focus on the case where all the direction-change rates on the lattice are homogeneous which denotes ω. In addition, we define $\Omega := \omega N$ which characterizes the overall direction-change rate.

The forward and obstacle-induced switching rates for minus-type particles at junctions $(1, N_2)$ and $(2, N_1 - 1)$ are chosen to preserve the overall forward rate $p = 1$. All transitions described above are subject to a simple exclusion principle, i.e., there can be at most one particle at each location of the lattice, and presence of a particle at one location prevents other particles from moving into that location. Regarding the boundary of the lattice, we assume there is no injection or exit of particles into/out of the lattice at minus and plus ends of each track, which means the total number of particles is conserved during the transport.

In the time evolution of this stochastic bidirectional transport, the occupancy at each location of the lattice for plus- and minus-type particles at time t, $\tau_{\pm,i}^l(t)$ changes according to the above transition rates (assumed to take place independently and instantaneously) from an initial state $\tau_{\pm,i}^l(0)$. The exclusion principle ensures that $\tau_{\pm,i}^l(t) \in \{0, 1\}$. A special case of the model is $q_1 = q_2 = 0$ where the transport on each of the two tracks is independent of each other. In this case the process is no longer ergodic. For the ergodic cases, the equilibrium state will be independent of initial conditions and a symmetric lattice structure gives a symmetric distribution of particles on two tracks where the total numbers of particles are equal. In order to compare transport properties with different switching rates $q_{1,2}$, including the zero track switching rates, we assume an initial condition satisfying that each track possesses an equal number of particles and assume that the system has reached statistically steady state.

In equilibrium state, densities of plus- and minus-type particles on each location

---

[1]As in general minus-type particles in the bipolar section are able to switch tracks while those in the unipolar sections are not, we assume the direction change rates for minus-type particles also differ between bipolar section and unipolar section.

(l, i) are defined as the mean occupancy of the particles:

$$\rho_i^l := \langle \tau_{i,+}^l \rangle, \ \sigma_i^l := \langle \tau_{i,-}^l \rangle$$

where the brackets $\langle \cdot \rangle$ denotes the assemble average. These densities are related with an overall density of particles expressed as [1]

$$\Theta = \Theta_+ + \Theta_- = \frac{\sum_{i=0}^{N-1}(\rho_i^1 + \rho_i^2)}{2(N - N_1 + N_2)} + \frac{\sum_{i=0}^{N-1}(\sigma_i^1 + \sigma_i^2)}{2(N - N_1 + N_2)}$$

where $\Theta_\pm$ are the overall densities of plus- and minus-type particles respectively. The overall density Θ is conserved under the time evolution whereas $\Theta_\pm$ may not be conserved. Meanwhile, the mean currents within each section in terms of the mean rate of stepping forward within unit time are given by

$$J_{\pm,i}^1 = \langle \tau_{\pm,i}^1 (1 - \tau_{\pm,i\pm1}^1) \rangle$$

in units of p on the first track; at the junctions between sections, the mean currents for minus-type particles are

$$J_{-,N_2}^1 = (1 - q_1)\langle \tau_{-,N_2}^1 (1 - \tau_{-,N_2-1}^1) \rangle + q_1 \langle \tau_{-,N_2}^1 (1 - \tau_{+,N_2-1}^2) \rangle$$

and

$$J_{-,N_1}^1 = q_2 \langle \tau_{-,N_1}^1 (1 - \tau_{+,N_1-1}^2) \rangle.$$

Similarly, we have the mean currents for the second track. The net current in the unipolar section is zero and at the junction between sections is balanced: $J_{-,N_2}^1 = J_{+,N_2-1}^1 + J_{-,N_2-1}^2$.

The standard unidirectional ASEP on a single lane and the two-lane ASEP developed by Juhász [124] share a common feature - particle-hole symmetry. This feature does not hold in the model we introduce here with homogeneous rates for plus-type particles and inhomogeneous for minus-type particles. However, by adapting the forward stepping rate of plus-type particles when crossing the junctions between sections (i.e., assuming there is inhomogeneity in stepping rates for plus-type particles at locations $(1, N_2 - 1)$ and $(2, N_1)$), the model can still exhibit an exact particle-hole symmetry as explained below. Since particles are of two types, either moving towards or away from the plus ends on each track, we also divide holes in the lattice into two types. Minus-type holes refer to the holes in lanes for plus-type particles, as holes are moving towards minus end when the corresponding plus-type particles step forward; plus-type holes refer to the holes in lanes for minus-type particles. An

---

[1]In the unipolar section, say $i < N_1$, only the location $(2, i)$ is included in the defined lattice; for convenience we set $\tau_{\pm,i}^1 = 0$, $i < N_1$ and so for another unipolar section.

(obstacle-induced) track switching of minus-type particle from the unipolar to bipolar section indicates an (end-induced) track switching of minus-type hole from the bipolar to unipolar section. Similarly, a plus-type particle steps from the bipolar to unipolar section corresponds to a minus-type hole steps from the unipolar to bipolar section. Therefore, if $p^2_{-,N_1} = p^1_{-,N_2-1} = 1 - q_2$ then the system possess particle-hole symmetry, i.e., the system is identical under symmetric exchanges:

$$q_1 \leftrightarrow q_2, \quad \tau^l_{\pm,i} \leftrightarrow 1 - \tau^l_{\mp,i}.$$

The uncoupled system with homogeneous rates for plus-type particles (i.e., $q_{1,2} = 0$ which gives $p^2_{-,N_1} = p^1_{-,N_2-1} = 1$) is a special case with particle-hole symmetry. For small q_2, the system with homogeneous rates for plus-type particles can still have some approximately "symmetric" behaviour. Thus we focus on low and intermediate overall densities and information such as the density profiles in high overall densities can be partly deduced from this "symmetry".

The exact analytical solutions of the density profiles in our model with general parameters would be very difficult to find and therefore we turn to mean-field approximations and numerical simulations. For this continuous-time discrete-state model, we use a Gillespie algorithm [126] to simulation the time evolution. For the parameters used in simulations, we use $x_1 = 1 - x_2 = 0.2$, as microtubule minus ends in *U. maydis* hyphae are shown to be approximately uniformly distributed in the middle at about 10% in hyphal length away from cell poles where the MT minus ends are "almost" absent [25]. For the parameter Ω, the *in vivo* experiments in [65, 24] suggests a range of run length $M = 10 \sim 70~\mu m$ in a hyphal length of $L = 100~\mu m$ which gives[1] $\Omega \in [1, 10]$. In addition, a lattice length of $N = 500$ is used in most of simulations unless otherwise stated.

5.3 Spatial distribution of particles and mean-field analysis

In the lattice of length N, we take a rescaled position variable defined as $x = i/N \in [0, 1]$, and in the continuum limit where $N \to \infty$, we re-express $J^l_\pm(x)$ as the mean unidirectional current to the plus/minus end on each track ($l = 1, 2$) and $J^l(x) := J^l_+(x) - J^l_-(x)$ as the net (mean) current. Moreover, we re-express the densities on each track as $\rho^l(x)$ and $\sigma^l(x)$ for plus- and minus-type particles respectively. The

---

[1]The unit p is given by $p = v/h$ where v is the velocity and h is the space step and the turning rate $\omega = v/M$. Hence the quantity Ω in unit of p is given by $\Omega = \omega N/p = L/M$.

overall density of plus- and minus-type particles can be re-expressed as

$$\Theta_+ = \frac{\int_0^1 (\rho^1(x) + \rho^2(x))dx}{2(1 - x_1 + x_2)}, \quad \Theta_- = \frac{\int_0^1 (\sigma^1(x) + \sigma^2(x))dx}{2(1 - x_1 + x_2)}.$$

In the spatial symmetric lattice with $x_1 + x_2 = 1$, we have $\rho^1(x) = \rho^2(1 - x)$ and $\sigma^1(x) = \sigma^2(1 - x)$ for these well defined regions. Hence we only need to consider the distribution of particles on one track, say the first track, and ignore the superscripts of track index without ambiguity.

As the lattice is composed of unipolar and bipolar sections, we consider these sections separately with appropriate boundary rates; see Figure 5.2. The stochastic process in each section is an ASEP similar to that discussed in [124] with symmetric boundary conditions and in [64] with a low overall density and half-closed boundary condition. In both ASEPs, the mean-field approximation predicts the density profiles well [124, 64]. By mean-field approximation, we ignore two-point correlations and the density profile in the steady state for plus- and minus-type particles in the unipolar/bipolar section of the lattice is governed by the following equations (ignoring the second derivative and second order of $1/N$) with appropriate boundary conditions (see [124, 64] for details)

$$\begin{aligned}
0 &= (2\rho - 1)\frac{d\rho}{dx} - \Omega(\rho - \sigma) \\
0 &= (1 - 2\sigma)\frac{d\sigma}{dx} + \Omega(\rho - \sigma).
\end{aligned} \tag{5.1}$$

Meanwhile, the unidirectional currents within each section are given by equations

$$J_+(x) = \rho(x)(1 - \rho(x)), \quad J_-(x) = \sigma(x)(1 - \sigma(x))$$

and the net current reads as

$$J(x) = \rho(x)(1 - \rho(x)) - \sigma(x)(1 - \sigma(x)).$$

Taking the sum of equations in (5.1) gives

$$\frac{dJ(x)}{dx} = \frac{d}{dx}\left(\rho(1 - \rho) - \sigma(1 - \sigma)\right) = 0 \tag{5.2}$$

which gives a constant net current in the mean field approximation $J(x) = J_0$ within each section in the steady state. A positive (negative) net current indicates a net current in the plus (minus) direction.

5.3.1 Spatial distribution in the unipolar section

As the system we consider is closed (no injection or exit of particles), the unipolar sections are half closed. For the first track, the unipolar section in $x_2 < x \leq 1$ is closed at the right end and this corresponds to the boundary condition

$$\rho(1) = 1, \ \sigma(1) = 0.$$

At the left end $x = x_2$ of this unipolar section, we assume the unipolar section is associated with injection/exit rates α_+^u and β_-^u. As discussed in [64], the unipolar section has a zero net current due to the closed boundary at the right end. Thus $J = \rho(x)(1 - \rho(x)) - \sigma(x)(1 - \sigma(x)) = 0$, leading to the density relation

$$\rho(x) = 1 - \sigma(x), \ \ \rho(x) = \sigma(x).$$

Together with the ODE (5.1), we have two possible solutions - "complementary" density

$$\rho(x) = 1 - \sigma(x) = 1 - \Omega + \Omega x \tag{5.3}$$

and "equal" density $\rho(x) = \sigma(x) = C$. The "equal" density may appear in the bulk of the unipolar while the "complementary" density starts from the plus end and extends toward the interior of the unipolar section.

As discussed in [64], for low injection and high exit rates, the constant in the "equal" density case reads as $C = \rho(x_2) = \alpha_+^u$; the density profile of plus-type particles experiences a shock between "equal" density and "complementary" density regimes while density of minus-type particles is continuous except near the left end. We refer this as an SL phase. The shock location x_s is determined by matching $\lim_{x \to x_s^-} \rho(x) = \lim_{x \to x_s^+} 1 - \rho(x)$. Combining the complementary solution (5.3) and the equal density α_+^u gives $x_s = 1 - \frac{\alpha_+^u}{\Omega}$. A limit $\lim_{x_s \to x_2} \alpha_+^u(x_s) = \Omega x_1$ gives a boundary of this SL phase in the space (α_+^u, β_-^u). When the shock is driven out of the unipolar section, the plus-type particles are in high density (over one half) and minus-type particles are in low density; we refer as an HL phase. The linear density profile of plus-type particles in the "complementary" density decreases from 1 at the plus end and propagates inside. When a lower bound of 1/2 for plus-type particles in density is reached before x is decreased to x_2, the density of 1/2 continues when x is further decreased and the maximum unidirectional current occurs in the unipolar section. This is referred as an MM phase and only occurs when $1 - \Omega + \Omega x_2 < 1/2$, i.e., $\Omega x_1 > 1/2$. By particle-hole symmetry, analogous to the SL phase, we have an HS phase where the "equal" density is over one half and minus-type particles experience a shock. In summary, the phase diagrams of density profiles for the unipolar section with general left boundary conditions α_+^u and β_-^u
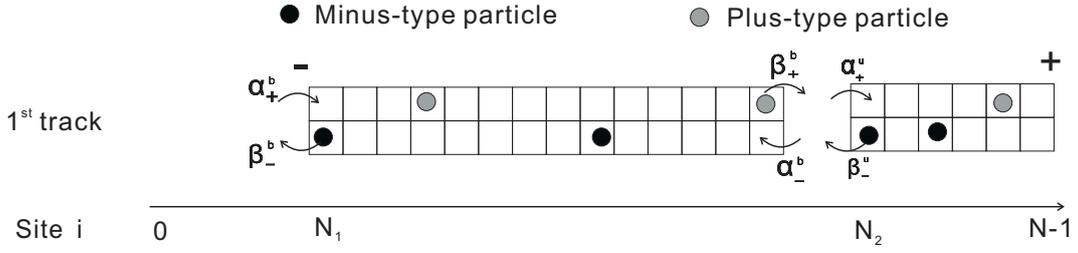
Figure 5.2: The ASEP with antipolar bundles described in Figure 5.1 is mapped onto several unbundled bidirectional ASEPs coupled by boundary conditions. This shows the sections on the first track.

are shown in Figure 5.3 for both $\Omega x_1 < 1/2$ and $\Omega x_1 > 1/2$. In the coexistence line $\alpha_+^u = \beta_-^u$, we have $\rho(x_2) = \alpha_+^u = 1 - \sigma(x_2)$ and note that $\rho(1 - \frac{\alpha_+^u}{\Omega}) = 1 - \alpha_+^u$ in the "complementary" density, thus a similar discussion as in [124] can be applied in the region $[x_2, 1 - \frac{\alpha_+^u}{\Omega}]$.

5.3.2 Spatial distribution along the entire bundle

In this subsection, we aim to analyze the density profiles in the entire symmetric bundle by considering two ASEPs on the first track with corresponding boundary rates in each section. The boundary rates in one section may depend on those in another section.

In the simplest case: $q_1 = q_2 = 0$ (uncoupled), the stochastic process on each track is exactly the same as the two-lane ASEP discussed in [124] with equal direction-change rates. Also from discussion of the unipolar section, we can see that the density profile on the first track consists of three segments in general; an equal-density segment occurs in the middle and connects with the boundaries by complementary-density segments on its left and right sides which are continuous at $x = x_1$ and 1 respectively.

For either q_1 or q_2 positive, the density profiles can exhibit a variety of phases even if the other parameters Ω and Θ are fixed. In the following, we show a mean-field approximation with appropriate boundary conditions in both unipolar and bipolar sections agrees well with numerical simulations for a variety of density profiles. In this generic case where $q_1 q_2 > 0$, the net current in the bipolar section on a single track is not necessary zero. For a general net current J, the relation $J = \rho - \rho^2 - \sigma + \sigma^2$ gives

$$\sigma = \frac{1}{2} \pm \frac{2\rho - 1}{2}\left(\sqrt{\frac{4J}{(2\rho - 1)^2} + 1} - 1\right) \pm \frac{2\rho - 1}{2}.$$

This implies the "equal" and "complementary" density solutions:

$$\sigma = \rho + \frac{2\rho - 1}{2}\left(\sqrt{\frac{4J}{(2\rho - 1)^2} + 1} - 1\right), \quad \sigma = 1 - \rho - \frac{2\rho - 1}{2}\left(\sqrt{\frac{4J}{(2\rho - 1)^2} + 1} - 1\right).$$
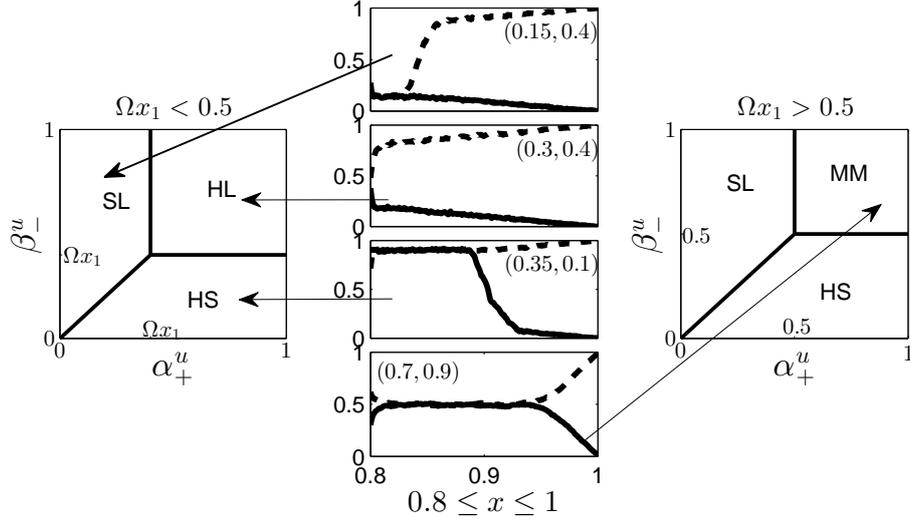
Figure 5.3: Phase diagram of the density profile in the unipolar section with general left boundary conditions α_+^u and β_-^u and closed right boundary condition for both cases $\Omega x_1 > 1/2$ (left panel) and $\Omega x_1 > 1/2$ (right panel), where $x_1 = 1 - x_2 = 0.2$. Numerical examples of density profiles in the unipolar section for each phase are illustrated with indicated boundary conditions (α_+^u, β_+^u). The top three density profiles in the middle column are using $\Omega = 1$ while the bottom density profile is using $\Omega = 10$. In the density profiles, dashed lines are for plus-type particles while solid lines are for minus-type.

Thus, the first order ODE (5.1) from the mean field approximation reads

$$0 = (2\rho - 1)\frac{d\rho}{dx} + \Omega\frac{2\rho - 1}{2}\left(\pm\sqrt{\frac{4J}{(2\rho - 1)^2} + 1} - 1\right)$$

with a general solution of "equal" or "complementary" density

$$\left(\left(1 + \frac{4J}{(2\rho - 1)^2}\right)^{3/2} \pm 1\right)(2\rho - 1)^3 = \mp 12J\Omega x + C \tag{5.4}$$

for any non-zero net current J on taking options in "$\pm$" and "$\mp$".

Particularly, when neither ρ nor σ is close to one half, we approximate the constant net current $J = \rho(1 - \rho) - \sigma(1 - \sigma)$ by $J = \text{sgn}(1 - 2\rho)(\rho - \sigma)$ and $J = \text{sgn}(1 - 2\rho)(\rho + \sigma - 1)$ for "equal" and "complementary" densities respectively. The solutions (5.4) can thus be approximated as

$$\rho = -J\Omega x + C_e, \quad \rho = \Omega x + C_c \tag{5.5}$$

for "equal" and "complementary" densities respectively and the corresponding den-

sities of minus-type particles can be approximated as

$$\sigma = \rho + \text{sgn}(2\rho - 1)J, \quad \sigma = 1 - \rho - \text{sgn}(2\rho - 1)J \tag{5.6}$$

Phases for low overall densities

For a low overall density $\Theta \ll 1/2$, the unipolar sections have a small number of particles in occupancy, thus the unipolar is in an SL phase where densities of both types of particles are equally constant away from the plus end; say $\bar{\sigma}$ which is associated with a shock location $x_s^u = 1 - \bar{\sigma}/\Omega$ in the unipolar section from (5.3). In the bipolar section, the density profiles of each type is governed by the parameters $\Omega, q_{1,2}$ as well as $\bar{\sigma}$. If the end-induced switching rate $q_2 = 0$, then queueing appears at minus ends in a similar manner to the queueing at the plus end in the unipolar section. In contrast, for a sufficiently large switching rate q_2, any queuing particles at the minus end are expected to move into the unipolar section of another track. This leads to low densities for both types of particles in the bipolar section and we refer as an LL-SL phase for the entire system (LL stands for the phase in the bipolar while SL for the unipolar section). In the following we give an explicit expression of the density profiles by the mean-field particularly using approximations (5.5) and (5.6) for "equal" density in the bipolar section in the case of low overall densities.

The transport in the bipolar section is typically dependent on the boundary rates $\alpha_\pm^b$ and $\beta_\pm^b$ as shown in Figure 5.2. These boundary rates are clearly associated with the parameters in the model. When both types of particles in the bipolar section are in low densities which are dominated by the injection rates $\alpha_\pm^b$. We note that the injection of plus-type particles on the first MT comes from the track switching of minus-type particles at the junction between unipolar and bipolar sections. Therefore by the spatial symmetry, we approximate the injection rates by

$$\alpha_+^b = \bar{\sigma}q_1 \text{ and } \alpha_-^b = \bar{\sigma}(1 - q_1). \tag{5.7}$$

where $\bar{\sigma}$ is the "equal" density solution in the unipolar section. Hence from (5.5) and (5.6), the densities on the first track in the bipolar section are approximated by

$$\rho = -J\Omega(x - x_1) + \alpha_+^b, \quad \sigma = -J\Omega(x - x_2) + \alpha_-^b. \tag{5.8}$$

Together with the approximation $J = \rho - \sigma$, we find

$$J = \frac{\alpha_+^b - \alpha_-^b}{\Omega(x_2 - x_1) + 1} = \frac{\bar{\sigma}(2q_1 - 1)}{\Omega(x_2 - x_1) + 1}, \tag{5.9}$$

which gives a zero net current if $q_1 = 1/2$. The density expressions (5.8) together

with the symmetry $\rho^1(x) = \rho^2(1-x)$ and $\sigma^1(x) = 1 - \sigma^2(1-x)$ give

$$\rho^1(x) + \sigma^2(x) = \rho^2(x) + \sigma^1(x) = \bar{\sigma}, \ x \in (x_1, x_2)$$

and so the overall density can be expressed by $\bar{\sigma}$ as

$$\Theta = \frac{\int_{x_1}^1 \rho(x) + \sigma(x)dx}{2(1-x_1)} = \frac{\bar{\sigma}/\Omega + (1 - 2\bar{\sigma}/\Omega)\bar{\sigma}}{2(1-x_1)}. \tag{5.10}$$

That is, given a low overall density Θ, a sufficiently large q_2 and assuming densities are low in the bipolar section, we have

$$\bar{\sigma} = \frac{1+\Omega}{4} - \sqrt{\frac{(1+\Omega)^2}{16} - (1-x_1)\Omega\Theta}. \tag{5.11}$$

Replacing this together with (5.9) and (5.7) into (5.8) gives an analytical approximation of the density profiles in the bipolar section in an LL-SL phase. This together with density profiles in the unipolar sections gives the density profiles in the entire bundle. Figure 5.4(a) shows an example where this approximation agrees well with numerical simulations.

In this LL-SL phase, a boundary layer may arise near the junctions and we approximate the exit rate for minus-type particles by $\beta_-^b = (1 - \bar{\sigma})q_2$. We have seen that in the uncoupled case, a shock of minus-type particles forms near the minus end. This queueing also occurs for positive track switching rates $q_{1,2}$ and is referred as an LS-SL phase; see Figure 5.4(b) as an example where mean-field approximations also agree well with numerical simulations. In the mean-field approximation, a shock for minus-type particles in the bipolar section stabilizes at $x = x_{s,-}^b$ when

$$\lim_{x \to x_{-,s}^{b+}} \sigma(x) = 1 - \lim_{x \to x_{-,x}^{b-}} \sigma(x). \tag{5.12}$$

Similar to the LL-SL phase, the density value $\bar{\sigma}$ which gives the boundary rates can in principle be worked out from the association with parameters. Hence, we have approximations using "equal" and "complementary" densities (5.5) and (5.6) for right and left sides of the shock in the bipolar section. The transition between LS-SL and LL-SL phases in a low overall density will be that the shock is driven to the junction between sections i.e., $x_{-,s}^b \to x_1$. In other words, the "equal" density of minus-type particles $\sigma(x)$ in (5.8) satisfies $\lim_{x \to x_1} \sigma(x) = 1 - \sigma(x_1) = \beta_-^b$, which gives

$$q_2(1 - \bar{\sigma}) = \bar{\sigma}q_1 - \frac{\bar{\sigma}(2q_1 - 1)}{\Omega(x_2 - x_1) + 1}. \tag{5.13}$$

Here $\bar{\sigma}$ is related to the overall density Θ by (5.11). Figure 5.4 (c,d) shows examples of this prediction on the border line between LL-SL and LS-SL phases in the space
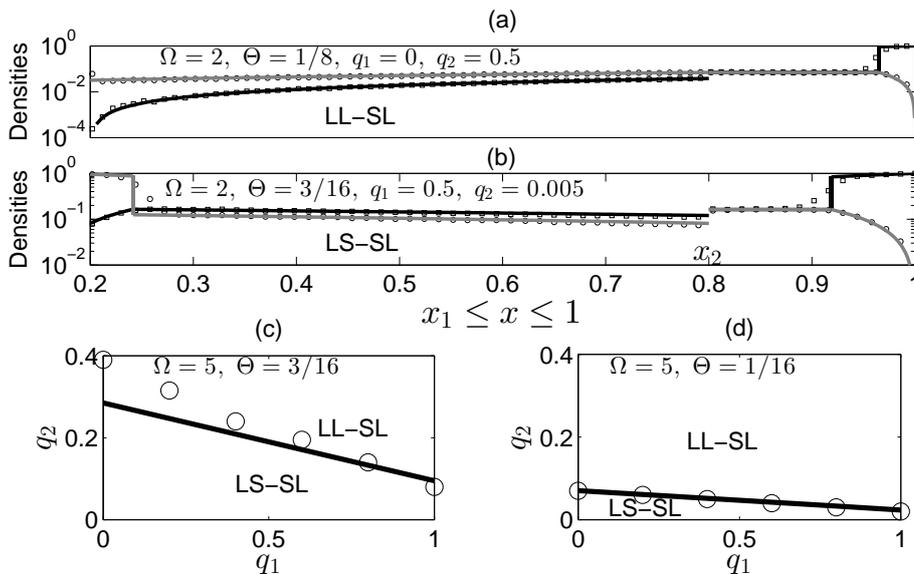
Figure 5.4: (a) and (b) show density profiles in LL-SL and LS-SL phases on the first track with $x_1 = 1 - x_2 = 0.2$ and other parameters indicated. For plus-type (minus-type) particles, black (gray) lines show the density solution from mean-field approximations and squares (circles) show the averaged densities (over $T = 60000\ s$) from Gillespie simulations. Note that low values in densities are cut for visual effects. (c) and (d) show the transition between LL-SL and LS-SL phases for indicated Ω and Θ. Lines are for mean-field approximation (5.13) while circles are from numerical simulations where the shock is identified if $\rho_{N_1+1}^1 > 0.5$.

(q_1, q_2) against numerical simulations where a shock is identified by a over one half density of minus-type particles at the last but one site to the minus end. Qualitatively, this prediction agrees well with the simulations. We suspect the deviation of the prediction can be due to size effects, or the simplification of the approximations in (5.5) and (5.6), or the definition of the shock in simulations.

More phases for intermediate overall densities

For intermediate overall densities Θ, there is more variety as well as more possible transitions between phases in the density profile along the entire system with different Ω and $q_{1,2}$. In addition to LL-SL and LS-SL phases for large Ω, small Ω could have the unipolar section in an HL phase which could give shocks for both types of particles in the bipolar section. This is referred as an SS-HL phase; see Figure 5.5 (a) for an example. In this phase, the density profiles have "equal" density in the middle separating two "complementary" density regimes in the bipolar section. If ρ and σ in the bipolar section are not close to one half, we approximate the net current by $J = \beta_+^b - \alpha_-^b = \alpha_+^b - \beta_-^b$. Together with the consideration that

$\beta^b_- = q_2\beta^b_+$, we approximate the boundary conditions in the bipolar section as

$$\alpha^b_+ = q_1\sigma(x_2), \ \alpha^b_- = (1-q_1)\sigma(x_2), \ \beta^b_+ = \frac{\sigma(x_2)}{1+q_2}, \ \beta^b_- = \frac{q_2\sigma(x_2)}{1+q_2} \qquad (5.14)$$

where $\sigma(x_2)$ is the density of minus-type particles at the left end of the unipolar section on the first track. We approximate this density by the limit of $\sigma(x)$ in (5.3) as $x \to x_2^+$, i.e., $\sigma(x_2) \approx x_1\Omega$. Thus, the net current is approximated by

$$J = \beta^b_+ - \alpha^b_- = \alpha^b_+ - \beta^b_- = \left(\frac{1}{1+q_2} - 1 + q_1\right) x_1\Omega. \qquad (5.15)$$

Similar to the discussion of the LL-SL phase, for the SS-HL phase, the relation between the shock locations in the bipolar section and the overall density can in principle be worked out and would give approximated solutions of density profiles in the bundle by using (5.5) and (5.6) again. Figure 5.5 (a) shows that the approximated solution from the mean-field also agrees well with numerical simulations.

Note that the approximation (5.15) of the net current suggests that the direction of the net current is governed by $q_{1,2}$ and $(1-q_1)(1+q_2) = 1$ gives a zero net current. Thus we are expected to have constant density in a region of the bipolar section as seen in Section 5.3.1. Particularly, when the overall density $\Theta = 1/2$, there would be a "maximum unidirectional current" region in the bulk where $\rho^1(x) = \sigma^1(x) = 1/2$. This region can be estimated by identifying degenerated shocks (with zero shock height) for both types of particles, which can be approximated as $[\frac{1}{2\Omega} + (1-q_1)x_1, 1 - \frac{1}{2\Omega} - q_1x_1]$. Note also that this "maximum unidirectional current" also appears with an MM phase in the unipolar section.

In addition to this SS-HL phase for an intermediate overall density, we found another interesting phase in the bipolar section that we call smooth connection (SC) phase where density profiles of one type of particles smoothly pass through one half while density profile of the other experiences a shock; see Figure 5.5(d) as an example with boundary conditions giving a shock for the other type (the minus-type). Density profiles in the SC phase do not necessary have shocks near minus ends in the bipolar section or have an HS phase in the unipolar section. Figure 5.5(c,d) shows examples where density profiles of plus-type particles smoothly pass through one half with boundary layers (instead of shocks) at the minus end and the unipolar section is in an SL or HL phase depending on parameters. Furthermore, the SC phase is generic seen from Figure 5.6 where each frame represents the density profiles for $\rho^1(x)$ (left panel) and $\sigma^1(x)$ (right panel) via color for fixed q_1 and changing q_2 by every 0.1 between 0 and 1. The parameter $q_1 \in \{0, 0.2, 0.5, 0.8, 1\}$ is increased from top frame to the bottom frame in both panels. In Figure 5.6, a smooth connection can be seen from a slow deviation in density of one type of particles compared to
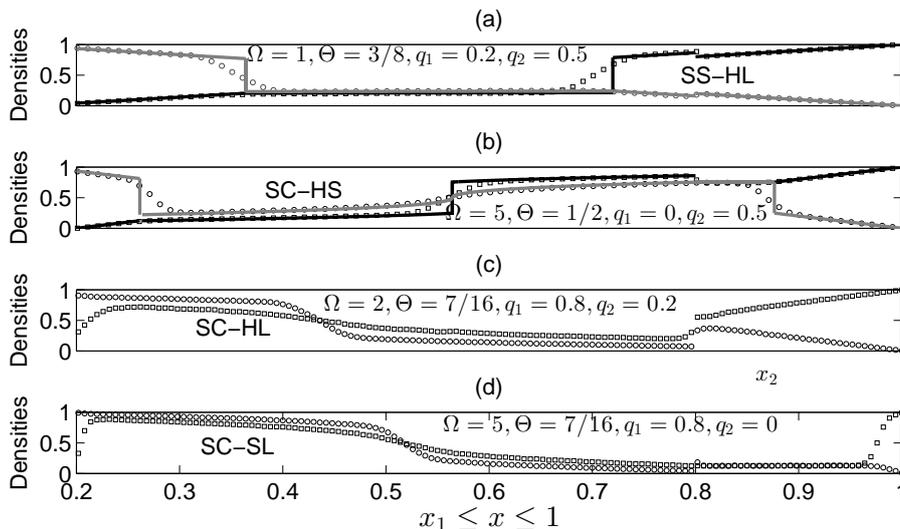
Figure 5.5: Density profiles show for four phases on the first track with parameters indicated. Simulations are compared with mean field approximation shown in black/gray lines for plus-/minus-type particles in an SS-HL (a) and SC-HS phase (b). Simulations and the markers are similar as Figure 5.4.

the other type. For instance, in the bipolar section of the bottom frames, there is a sharper deviation in ρ than that in σ; this shows a SC phase where ρ is smooth across a half while discontinuity occurs in σ in the bipolar section.

This smooth connection phenomenon can be understood from a non-zero net current which could give an increase (or decrease) in the density and eventually one half for one type of particles. As the non-zero net current J is preserved within the bipolar section, one half density for one type of particles gives two density values for the other type depending on J, which form a shock. In the following we examine the mean-field approximation for this SC phase. As the densities may close to one half, we use the mean field approximation (5.4) for the "equal" density and use the "complementary" density solutions from (5.5) and (5.6) for the bipolar section. In the example shown in Figure 5.5(b), minus-type particles form a shock in the bipolar section, and in the unipolar section densities are in an HS phase with an equal density, say $\bar{\sigma}$. Due to the non-linearity in (5.4) for the "equal" density in the bipolar section, instead of finding the relation between $J, \bar{\sigma}$ and Θ, we choose appropriate values for J and $\bar{\sigma}$ and associate them with boundary conditions $\alpha_+^b = \bar{\sigma} q_1$ and $\alpha_-^b = \bar{\sigma}(1 - q_1)$ to match the shock condition as in (5.12) and the overall density Θ. Particularly, in this example, the mean-field solution with chosen parameters $\bar{\sigma} = 0.753$ and $J = -0.065$ agrees well with the simulation seen from Figure 5.5(b).

In the intermediate overall density, we have seen that the system shows a variety of phases depending on parameters. Even for fixed Ω and Θ, Figure 5.6 shows a variety of phases on the first track: in the unipolar section, all possible phases SL,
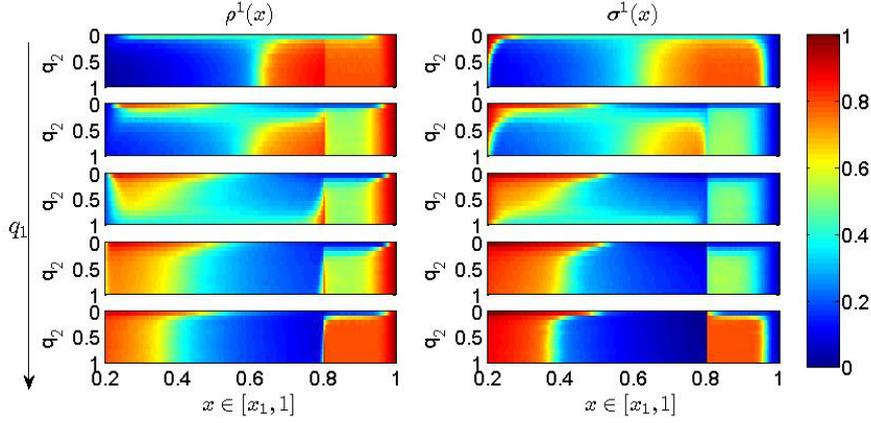
Figure 5.6: A variety of phases arise in the bundle for fixed $\Theta = 7/16$ and $\Omega = 5$ when varying the switching rates $q_{1,2}$. Each frame in the left and right panel represents densities of plus- and minus-type particles for fixed q_1 when varying q_2 by every 0.1 between 0 and 1. The fixed parameter $q_1 \in \{0, 0.2, 0.5, 0.8, 1\}$ is increased from top frame to the bottom frame in both panels.

HS and MM are realized; in the bipolar section, in addition to an LL phase, there are SC phases with different types of particles having their density profiles smoothly pass through one half. For instance, plus-type particles can experience a smooth connection for high q_1 while minus-type particles can for low q_1. Moreover, we can see from Figure 5.6 how phases change when changing q_1 or q_2. A variety of non-trivial transitions between phases are expected to occur and we have not attempted to characterize all these transitions in the parameter space.

5.4 Dominance of particles in the transport

Both types of particles are essential for bidirectional transport along the bundle of tracks in the unipolar section. However, it is possible to have only one type of particles take the bidirectional transport across the bipolar section by track switching events and indeed *in vivo* experiments of EEs suggest that kinesin-3 is the main motor for long-range EE motility across an antipolar MT bundle [25]. In the following, we discuss the contribution of each type of particles to the transport in terms of occupancy as well as current from our model.

5.4.1 Dominance in occupancy

For the transport in the entire bundle, one way to quantify the dominance in occupancy is to estimate the fraction of plus-type particles in the entire bundle, i.e.,

$$F_+ := \frac{\Theta_+}{\Theta} = \frac{\int_{x_1}^1 \rho^1(x)dx}{2\Theta(1-x_1)}$$

92

for a symmetric lattice $x_1 + x_2 = 1$. Recall that Θ is an overall density of particles in the bundle which is preserved during the transport and is considered as a parameter. It is clear that $F_+ = 1/2$ in the case $q_1 = q_2 = 0$. Note that track switching is accompanied with a change of type from minus to plus, thus increasing either q_1 or q_2 will have the potential to increase the number of plus-type particles and thus increase the fraction F_+. If F_+ is close to 1 then plus-type particles are in significant dominance in terms of occupancy in the entire bundle. For $\Omega = 0$ and $q_{1,2} > 0$ together with a sufficiently low overall density Θ, the maximum $F_+ = 1$ can be achieved.

When considering the fraction of plus-type particles within each section, it is clear that in the unipolar section there are more plus-type than minus-type particles for any parameters. In contrast, the fraction in the bipolar section

$$
F_+^b := \frac{\int_{x_1}^{x_2} \rho(x)dx}{\int_{x_1}^{x_2} \rho(x) + \sigma(x)dx}
$$

is less easy to estimate for a general overall density Θ.

For a low overall density where the system is in either LL-SL or LS-SL phase, the mean-field approximation predicts the corresponding density profiles well. Thus, for sufficiently large q_2 (i.e., larger than the critical value satisfying (5.13)) which gives low densities for both types of particles in the bipolar section, both fractions F_+ and F_+^b can be expressed using the approximated density profiles, ignoring boundary layers. The fraction in the entire bundle is

$$
F_+ \approx \frac{\bar{\sigma}\Omega(x_2 - x_1)^2/2 + \bar{\sigma}q_1(x_2 - x_1) + 1 - \bar{\sigma}^2/(2\Omega) + (x_1 - \bar{\sigma}/\Omega)\bar{\sigma}}{\bar{\sigma}/\Omega + (1 - 2\bar{\sigma}/\Omega)\bar{\sigma}} \tag{5.16}
$$

where $\bar{\sigma}$ is associated with Θ as in (5.11), and the fraction in the bipolar section is

$$
F_+^b \approx \frac{1}{2} + \frac{2q_1 - 1}{2\Omega(x_2 - x_1) + 2}. \tag{5.17}
$$

Both fractions show independence of q_2 and linear dependence on q_1. Comparatively, the latter expression for the fraction in the bipolar section is a simpler function of Ω and q_1 for fixed $x_{1,2}$. We can see that this expression agrees well with simulations from Figure 5.7. Moreover, from this approximation, $q_1 = 1/2$ gives approximately equal contribution in the bipolar section for each type of particles. This agrees with a zero net current in (5.9) which leads to equal density in an LL phase. Moreover, the sign of $q_1 - 1/2$ determines which type of particles are in dominance and by decreasing Ω, the dominance can be enhanced. Particularly,

$$
\lim_{\Omega \to 0, q_1 \to 1} F_+^b(\Omega, q_1) = 1, \quad \lim_{\Omega \to 0, q_1 \to 0} F_+^b(\Omega, q_1) = 0.
$$
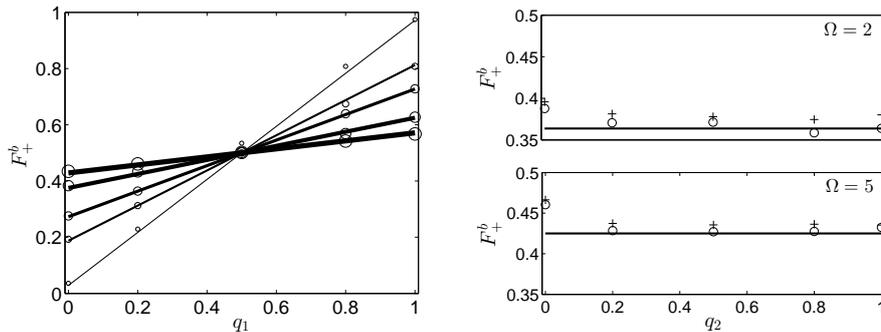
Figure 5.7: The fraction of plus-type particles in the bipolar section. Left: lines are from approximated equation (5.17) for $\Omega \in \{0.1, 1, 2, 5, 10\}$ with bolder lines for larger Ω while circles are for simulations with larger circle for larger Ω. Other parameters are using $\Theta = 1/16$, $q_2 = 1$. Right panels: to examine the independence of this fraction on the overall density Θ and switching rate q_2 if sufficiently large; cross and circle are for $\Theta = 3/16$ and $1/16$ respectively in both up and down panels. Simulated data presented are using $q_1 = 0.2$ - quantitatively similar figures can be obtained for other q_1.

That is to say, for sufficiently low Ω, plus-type particles are in significant dominance in the bipolar section for sufficiently large switching rate q_1; in contrast, minus-type particles are in significant dominance for sufficiently small q_1.

For an intermediate overall density, the plus-type and/or minus-type particles form shocks near the junctions between sections. In contrast to low overall densities where F_+^b is highly dependent on q_1 and weakly dependent on q_2, in the intermediate overall densities, the fraction in the bipolar section F_+^b shows relatively weak dependence on both switching rates $q_{1,2}$. The left panel in Figure 5.8 shows an example with an overall density $\Theta = 7/16$ of how the fraction in occupancy changes with the rates $q_{1,2}$.

5.4.2 Dominance in current

The directed currents $J_\pm$ are also quantities of importance in characterizing the transport capacity. A large current usually indicates an efficient transport. In contrast to the standard unidirectional ASEP on a single lane (where both the density and current are constant along the bulk of the lane), in our model, neither the density nor the directed current of each type of particles on a single track is constant. Here, we consider the average unidirectional current

$$\langle J_\pm \rangle_x := \frac{\int_0^1 J_\pm(x)dx}{1 - x_1}$$

and define an overall current $\langle J \rangle_x := \langle J_+ \rangle_x + \langle J_- \rangle_x$. The dominance in current of particles can be investigated by looking at the ratio of average current for plus-type
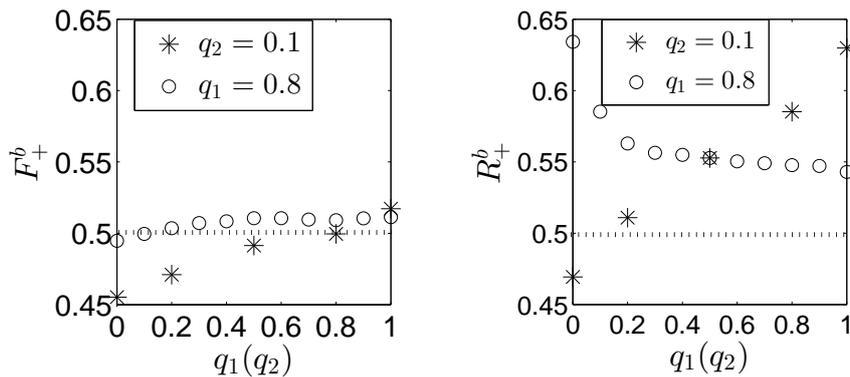
Figure 5.8: The fraction of plus-type particles F_+^b (left panel) and the ratio of average current for plus-type particles R_+^b (right panel) in the bipolar section as varying q_1 (marked as $*$) or q_2 (marked as $+$) for $\Omega = 5$ and $\Theta = 7/16$. simulated data presented are using $q_1 = 0.8$ ($q_2 = 0.1$) when varying $q_2(q_1)$ - qualitatively similar figures can be obtained for other values of $q_{1,2}$.

particles:

$$R_+ := \frac{\langle J_+ \rangle_x}{\langle J \rangle_x} = \frac{\langle J_+ \rangle_x}{\langle J_+ \rangle_x + \langle J_- \rangle_x}.$$

We simultaneously define the ratio of average currents within each section. In the unipolar sections, plus- and minus-type particles equally contribute to the average currents as the net current is zero. Thus the ratio in the entire bundle R_+ depends only on the ratio within the bipolar section,

$$R_+^b := \frac{\int_{x_1}^{x_2} J_+(x)dx}{\int_{x_1}^{x_2} (J_+(x) + J_-(x))dx}.$$

When the density profiles in the bipolar section are in the LL phase ($\rho, \sigma \ll 1/2$), the dominance in current is equivalent to that in occupancy, $R_+^b \approx F_+^b$. However, if shocks form in the bipolar section, higher densities (above a half) can give a lower current. Thus dominance in occupancy does not imply dominance in current; see Figure 5.8 as an example. Moreover, by comparing the two panels in Figure 5.8, R_+^b shows a larger range than F_+^b on changing parameters. Thus, for an intermediate overall density, one could say that current plays a more important role than occupancy. In addition, we can see that the ratio in current R_+^b shows a larger range in changing q_1 than changing q_2 in this example. This suggests that q_1 is more important than q_2 in the dominance.

Note also that the overall current $\langle J \rangle_x$ is not necessary conserved on altering switching rates $q_{1,2}$. Figure 5.9 shows an example where numerical simulations suggest that multiple local maxima of the overall current may exist as varying the rates $q_{1,2}$ and these maxima correspond to the net currents that are close to zero.
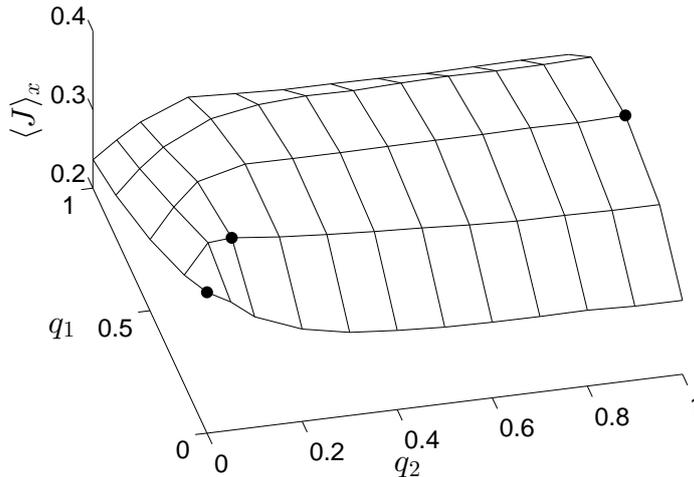
Figure 5.9: The overall current $\langle J \rangle_x$ changes in the parameter space (q_1, q_2) for fixed $\Omega = 5$ and $\Theta = 5/16$. The bold dots show the local maxima in the simulated data.

5.5 Discussions

In this chapter, we introduce a simple model to describe bidirectional motility of cellular cargoes along an antipolar MT bundle. This model includes information about particle run length (via a turning rate Ω) and ability to switching MTs at the junctions between the unipolar and bipolar sections (via the obstacle-/end-induced switching rates $q_{1,2}$). Firstly, we investigate possible density profiles in the bundle by mean-field approximations and numerical simulations. We show that the switching rates $q_{1,2}$ can dramatically influence the distribution of particles along the bundle. In particular, even under a low overall density of particles Θ, particles can accumulate at minus ends as well as plus ends formed by queueing. The critical value of end-induced switching rate q_2 in forming shocks at minus ends in a low overall density is investigated by mean-field approximation. For higher overall densities, in addition to the possible formation of shocks, we find an interesting phase where density profiles smoothly pass through one half. Secondly, we investigate the role of the switching rates $q_{1,2}$ in determining the dominant type of particles in the transport. We show that in low overall densities, the switching rate q_1 can linearly influence the fraction of plus-type particles within the bipolar section. Moreover, the linear slope is monotonically inverse to Ω. For higher overall densities, numerical simulations suggest that the ratio of average current is more important than the fraction of occupancy in considering the contribution of particles.

For the first time, we describe bidirectional transport (for early endosome organelles) on an antipolar bundle of MTs based on *in vivo* experiment observations, though the situation in living cells is far more complex. The results from the analysis

of the model can give some implications or predictions. Firstly, in dilute situation, our model suggests that there might be accumulation of organelles at minus ends of MTs for a sufficiently small end-induced switching rate q_2. In contrast, *in vivo* experiments show no obvious accumulation of EEs throughout the entire cell [25]. Therefore, one would predict that a high rate q_2 would be measured in experiments. Alternatively, a high turning rate of minus-directed organelles at minus ends (might due to an accumulation of kinesin-1 at the minus end taking dynein to plus ends) could also move the accumulation. This is a similar mechanism to the transport at plus ends where accumulation of dynein motors is suggested to increase the turning rate of EEs there and then to avoid accumulations of EEs based on the analysis in [64, 65]. Secondly, for dilute situation in the antipolar MTs, we quantify analytically the proportion of EEs carried by kinesin-3 depending on the parameters. This is accessible to test by measuring the corresponding quantities. However, measuring quantities including $q_{1,2}$ faces difficulties as it is hard to determine the the active motors on EEs when crossing minus ends. One possible method to solve this problem might be to associate the MT switching with pauses for EEs - the pauses have actually been observed [25]. Measuring these quantities will be one of the aims in the future collaborative work with experimental biologists.

In order to accurately describe the bidirectional transport of EEs, some known and measurable facts might be necessary to be included in the model. For example, hopping between MTs may not restrict at junctions between unipolar and bipolar MTs but also occur inside the antipolar MTs. The MT switching events can also be complex in real situation. Since there are more than one kinesin-3 motor attached to EEs during the transport [24], the MT switching events may keep or change the active motor type for the organelles. Moreover, there are more than two MTs involved in the EE transport from *in vivo* experiment observations [25]. In addition, each MT consists of 13 filaments [14] which offers more potential tracks for motors. It might be worth considering these scenario to see whether these details will give vital new information or qualitatively change in the transport properties. It is known that the 13-lane in model [66] would presumably exhibit a low current due to collisions/exclusions between opposition directed particles. Thus a specific question for the future is to see whether the bundling structure may reduce these collisions and hence enhance the current.

Chapter 6

Conclusion and outlook

6.1 Conclusions

This thesis is motivated by various studies of microtubule-based motor-driven bidirectional transport in a fungal system - *Ustilago maydis.* The bidirectional motility of EEs is driven by kinesin-3 to the plus end of a MT and by dynein away from the plus end. Meanwhile dynein is delivered to the plus end by kinesin-1 and forms an accumulation at the plus-ends to prevent EEs falling off the MTs [65]. The cooperation between these motors realizes the bidirectional transport on MTs. In addition, MTs form antipolar bundles that extend their plus-ends towards cell poles of the hyphae [25]. *In vivo* experiment observations show that EEs are able to travel across the entire bundle of MTs, suggesting that EEs hop between MTs in the bundle [25].

The first achievement of this thesis is to develop in Chapter 3 a ASEP-like model for the bidirectional dynein motion on a single MT at *U. maydis* hyphal tip, to investigate mechanisms of dynein accumulation at MT plus ends. In the model, we simply assume no collisions between opposite-directed motors and use a two-lane ASEP model where dynein driven by kinesin-1 and dynein carrying kinesin-1 are assigned onto two different transport lanes. By mean-field analysis, we give approximate expressions for the size and distribution of the accumulation. Using *in vivo* data on motor behaviour in *U. maydis* hyphae, this model gives one half of the measured tip size (the number of dynein in the accumulation). The deviation in tip size raises the possibility that this two-lane ASEP is oversimplified and also the possibility of other processes at work in the accumulation besides stochastic motion of motors. These possibilities and the predicted tip size were tested in the paper reproduced in Appendix A where a more sophisticated ASEP model and additional experiments are performed. The more sophisticated model includes the facts that each MT consists of 13 protofilaments [14] and dynein motors do lateral motions along MTs [29]. Surprisingly, this model gives a similar tip size as that in the two-lane ASEP model based on quantitative data from the system. Meanwhile,

the experiments in Appendix A show an approximately one-half reduction in the tip size to the normal situation by over expression of peptides that inhibit the interaction between EB1 and dynactin. Thus, the accumulation of dynein at MT plus-ends is suggested to be achieved by a combination of stochastic motions of dynein motors and a control mechanism by some specific molecules such as EB1. The tip size predicted from our two-lane ASEP model is validated for this stochastic accumulation.

An accumulation of motors at MT plus-ends can be seen as an inefficiency, as dynein motors are supposed to transport particles rather than to wait at the MT end. Thus, the cell needs to find a compromise between (a) ensuring that organelles are captured at MT ends, which requires dynein accumulation at the plus-ends [65] and (b) keeping dynein moving along MTs to deliver the cargo to minus-ends. Chapter 4 shows for the 13-lane ASEP model that the parameters from the *in vivo* experiments [65] in a *Ustilago maydis* system (and the turning rate p_{+-} in particular) are close to optimal in order to achieve these efficient motor and organelle transport and do address this compromise between (a) and (b) in a living cell. Moreover, as whether kinesin motors are doing similar lateral motion (which is described as lane changes in the model) as dynein motors do, is unclear in a living cell, we compare different lane-change protocols and find that it is necessary for only dynein to change lanes in order to give biological realistic system states over a larger range of possible flux. Chapter 4 also examines the dependence of tip size on the flux and shows a nonlinear scaling with a critical flux for the multi-lane ASEP model

Both Chapter 3 and Chapter 4 investigate models for the bidirectional transport near the hyphal tip for a single MT. In order to understand the bidirectional transport (particular of EEs) along the entire MT bundles, we introduce a simple model considering only two MTs with unipolar at two ends of the bundle in Chapter 5. Due to current lack of detailed quantitative data, we theoretically investigate the dynamical properties of this bidirectional transport, including the effects of antipolar bundling such as effects from switching of MTs. We find that even if the system is in an overall low density, the system can exhibit shocks in the density profiles near both plus and minus ends. Moreover, in the dilute situation, the switching rate can linearly influence the proportion of dynein-driven organelles in the bipolar section of bundle. We also identify a new phase where "smooth connection" can appear in the density profiles.

6.2 Future studies

6.2.1 Outlook for organelle transport in *Ustilago maydis*

Two different ASEP models are proposed in Chapter 3 and Chapter 4 to model the bidirectional motion of dynein motors on a single MT and both predict a similar tip size with the same quantitative data in *U. maydis*. One question is which model better describes the bidirectional transport. This might be answered by comparing the prediction with experiment measured tip size for different flux, seen from the difference in the scaling of tip size against flux between two ASEP models. However, to measure tip size for different parameters in living cells, we are facing difficulties in designing *in vivo* experiments to alter parameters while keeping the cell in a functional condition, as cells live only in certain limited conditions.

The antipolar bundled lattice model introduced in Chapter 5 is a first attempt to model the bidirectional transport particularly of EEs in the whole hyphae. This model simplifies the real network of MTs in hyphae which is still difficult to visualize under the limited microscopic resolutions at the moment. Fortunately, by visualizing minus ends of MTs, the distribution of minus ends is shown to be "uniform" along the middle of cells [25] and the number of minus ends can also be counted from kymographs obtained in *in vivo* experiments. Moreover, qualitative and quantitative behaviour of EEs in the bundle of MTs can be obtained. All these offer guidance in the future to model the bidirectional transport on a network of MTs.

When considering the bidirectional transport on each MT as multi-lane based which shows low current capacity in Chapter 4, we can test the hypothesis that the antipolar structure in the bundle can enhance the current capacity in the bidirectional transport. However, motors on different filaments particularly at the junctions between MTs, may behave quantitatively differently. For instance, at the minus ends, motors on the filament which is closer to another MT may be easier to switch to another MT while motors on filaments far from another MT may take longer time to switch. Therefore, appropriate assumptions of the motor behaviour on each possible filament need to be considered.

Furthermore, for a complete description of EE transport, quantitative motion behaviour of EEs and motors must be obtained. There are at least three types of motors including plus-end kinesin-1 and kinein-3 and minus-end dynein involved in the EE transport [25]. The motility of one type of motors depends on others and motors are not necessarily attached on EEs simultaneously, e.g., dynein was absent from most anterograde moving EEs [24]. Thus one feasible step to have a more realistic model of EE transport is to include more motors in the model with quantitative data of motor behaviour of each type. When modelling multiple motor mediated EE transport, particles (pair of motors or pair of motors and EE) can

be considered to be of multiple types and interact with each other in a "chemical reaction" manner. For instance, when dynein (carrying kinesin-1) meets with an EE carried by kinesin-3, the EE is able to load onto dynein [24], thus two types of particles combine together to give another type of particles.

The simulated results from a quantified model can be compared to measurable experimental data such as EE distribution, flux and run-length. This comparison can further be used to explore molecular regulation effects similar to the discovery of an active retention for the accumulation of dynein motors at MT plus ends. Eventually, we would like to understand the role of MT bundling as well as control regulation mechanisms and to identify critical parameters for efficient transport of EEs. All these efforts could give minimal design requirements for a fully functional early endosome transport system at the whole cell level.

6.2.2 Outlook for modelling intracellular transport

Intracellular transport either by diffusion or driven by motors in eukaryotic cells is important to move vesicles to be distributed appropriately throughout the cells. The whole process of transport for one vesicle can be a combination of both diffusion and motor-mediated active transport as suggested in [1]. Indeed, there is *in vivo* evidence in *U. maydis* that molecular motors - dynein and organelles fall off MTs and diffuse into the cytoplasm. These motors/organelles presumably have the ability to rebind onto MTs.

One natural question is how we can model the whole process of transport based on a combination of diffusion and active transport. The diffusion process can be modelled by Brownian motion or using (stochastic) diffusion equations. Motor-mediated transport can also be modelled by space-continuous stochastic differential equations (SDEs) (with a stochastic force term) [137]. Thus, SDEs might be a feasible approach as (stochastic) differential equations have been used to model both processes separately. In [137] the interaction between organelles is ignored and this interaction is commonly considered in space-discrete lattice models by exclusion principle. When considering the molecular interaction during transport, lattice models might also be an alternative option to model the whole process involving both diffusion and active transport. Indeed, there have already been space-discrete lattice models coupling the diffusion process with the active transport of molecular motors in theoretical works; see [114] and references therein. These lattice models are ASEP-like models as discussed in this thesis.

For the active transport alone, the lattices models also simplify the real situation such as the dynamics of MTs if the transport is MT-based and the molecular size. Possible generalizations of lattice models to include appropriate details are discussed in the discussion of Chapter 4 and Chapter 5.

When considering details of each molecule, the dynamics of molecules (or motors) which might influence the motor behaviour during the transport, need to be included in modelling the intracellular transport. In either SDEs or lattice models, particles representing organelles are identical and the detail of the dynamics of organelles is not considered. So-called molecular dynamics [138] is widely used to model the dynamics at the atomic level. Thus, coupling the dynamics of molecules together with active/diffusive transport may give a more clear picture of the transport process.

All the efforts above help to understand the intracellular transport in living cells. However, it is becoming important to understand the function of the transport, which could lead to new designs of biological systems. One plausible role of transport is signal transmission. For example, in the mitogen-activated protein kinase pathway, activated transcription factors are transported through the cell to the nucleus in order to activate the transcription [139]. This transport has been modelled as a diffusion process in [1] and references therein. By comparison between modelling and experimental analysis, the model in [1] suggests that cells utilize two distinct information transmission paradigms: fast local signalling via diffussion and long-distance signalling via the cytoskeleton transport apparatus.

This function in signal transmission addresses another question: how can we couple the diffusive/active transport in the signal transduction pathways? Signaling pathways are usually model by (ordinary) differential equations. One solution might be to use a network of (ordinary/stochastic) differential equations. Note that the transport process and the signal transduction might be in different time scales, hence a multi-scale model may be necessary in the further study.

Overall, the modelling of intracellular transport not only allows a better understanding of the transport itself but also gives biological indications for further studies.

Appendix A

Appendix: a stochastic mechanism in the formation of dynein accumulation

In this appendix, we present the results of a *in vivo* study that addresses the organization, dynamics and function of dynein accumulation in *Ustilago maydis*. We show that the dynein accumulation consists of ~ 55 dynein motors. About half of the motors are slowly turned over and they are kept at the plus-ends by an active retention mechanism which involves an interaction between dynactin and EB1. The other half is more dynamic. Our mathematical modelling suggests that the dynamic half of dynein motors concentrate at MT ends because of stochastic motor behaviour. The dual mechanism ensures that an excess of dynein motors offers sufficiently large possibility that an arriving early endosome gets captured by retrograde transport machinery.

THE
EMBO
JOURNAL

Controlled and stochastic retention concentrates dynein at microtubule ends to keep endosomes on track

Martin Schuster[1], Sreedhar Kilaru[1], Peter Ashwin[2], Congping Lin[1,2], Nicholas J Severs[3] and Gero Steinberg[1,*]

[1]School of Biosciences, University of Exeter, Exeter, UK, [2]Mathematics Research Institute, University of Exeter, Exeter, UK and [3]National Heart and Lung Institute, Imperial College London, London, UK

Bidirectional transport of early endosomes (EEs) involves microtubules (MTs) and associated motors. In fungi, the dynein/dynactin motor complex concentrates in a comet-like accumulation at MT plus-ends to receive kinesin-3-delivered EEs for retrograde transport. Here, we analyse the loading of endosomes onto dynein by combining live imaging of photoactivated endosomes and fluorescent dynein with mathematical modelling. Using nuclear pores as an internal calibration standard, we show that the dynein comet consists of ~55 dynein motors. About half of the motors are slowly turned over ($T_{1/2}$: ~98 s) and they are kept at the plus-ends by an active retention mechanism involving an interaction between dynactin and EB1. The other half is more dynamic ($T_{1/2}$: ~10 s) and mathematical modelling suggests that they concentrate at MT ends because of stochastic motor behaviour. When the active retention is impaired by inhibitory peptides, dynein numbers in the comet are reduced to half and ~10% of the EEs fall off the MT plus-ends. Thus, a combination of stochastic accumulation and active retention forms the dynein comet to ensure capturing of arriving organelles by retrograde motors.

Introduction

Bidirectional transport of organelles along microtubules (MTs) is a hallmark of eukaryotic cells, necessary for cellular organization and survival (Welte, 2004). In mammalian neurons, MT-dependent retrograde transport of early endosomes (EEs) mediates communication between the synapses and the cell nucleus, thereby preventing the cell from undergoing controlled cell death (Miaczynska *et al*, 2004; Howe and Mobley, 2005; Chevalier-Larsen and Holzbaur, 2006). Retrograde motility of EEs is mediated by dynein and the associated dynactin complex (Schroer, 2004; Vallee *et al*, 2004). It was shown that dynactin interacts with the plus-end binding protein EB1 (Ligon *et al*, 2003; Honnappa *et al*, 2006; Akhmanova and Steinmetz, 2008) thereby establishing a loading site that captures EEs (Valetti *et al*, 1999), melanophores (Lomakin *et al*, 2009) and Golgi membranes (Vaughan *et al*, 2002; Vaughan, 2005). Phosphorylation of mammalian dynactin compound p150[glued] releases the complex from MT plus-ends (Vaughan *et al*, 2002), indicating that regulatory mechanisms control the concentration and the dynamics of the transport machinery at MT ends. This is in line with numerous reports, showing active regulation of motor proteins and membrane transport (Kumar *et al*, 2000; Andersson *et al*, 2003; Deacon *et al*, 2005; Ally *et al*, 2008). However, an increasing number of reports have detailed the stochastic behaviour of motors (Klumpp and Lipowsky, 2005; Müller *et al*, 2008; Gazzola *et al*, 2009), raising the possibility that stochastic transport processes and active regulation cooperate to control cargo transport (Welte and Gross, 2008).

The genetically tractable filamentous fungus *Ustilago maydis* shares many proteins with humans that are not encoded in the model fungus *Saccharomyces cerevisiae* (Münsterkötter and Steinberg, 2007). It is therefore a good model system for the role of MTs in long-range transport (Steinberg and Perez-Martin, 2008). Similar to human cells (Hoepfner *et al*, 2005) and the ameba *Dictyostelium discoideum* (Soppina *et al*, 2009), kinesin-3 transports EEs to MT plus-ends (anterograde; Wedlich-Söldner *et al*, 2002a; Lenz *et al*, 2006), which are concentrated at the hyphal tip (Schuchardt *et al*, 2005). There, the EEs support recycling processes required for polarized growth and mating of the fungus (Wedlich-Söldner *et al*, 2000; Fuchs *et al*, 2006). It was suggested that retrograde transport of the EEs might mediate long-range communication to the nucleus (Steinberg, 2007). The motility back to the cell centre is initiated by binding of the organelles to dynein, which concentrates in a comet-like accumulation at apical MT plus-ends (Xiang, 2003; Lenz *et al*, 2006; Abenza *et al*, 2009; Zhang *et al*, 2010). How EEs are loaded onto dynein is not clear, but effective interaction of the motor and the cargo is required to ensure that the arriving organelles do not fall off the MT end. In this study, we provide evidence that dynein captures EEs in a stochastic way. In order to increase the probability of kinesin-3-delivered EEs, our study suggests that the cell raises the number of dynein motors by stochastic retention and a controlled interaction between EB1 and dynactin. This mechanism ensures efficient loading of EEs onto dynein and prevents the organelles from falling off the track at MT ends.

*Corresponding author. School of Biosciences, University of Exeter, Stocker Road, Exeter EX4 4QD, UK. Tel.: +44 139 226 3476; Fax: +44 139 226 3434; E-mail: g.steinberg@exeter.ac.uk

Appendix A
Controlled and stochastic retention concentrates dynein at MT ends
M Schuster *et al*

Results

Endosomes are rapidly loaded onto apical dynein

Hyphal cells of the filamentous fungus *U. maydis* are elongated and expand at their tip (Figure 1A, asterisk), where the MT plus-ends are concentrated (Schuchardt *et al*, 2005). To visualize the endogenous level of dynein, we integrated three tandem copies of green-fluorescent protein (GFP) into the native locus of the dynein heavy chain gene *dyn2* (for genotype of all strains see Table I). Cells expressing the fusion protein (GFP$_3$–Dyn2) were growing normally, whereas dynein mutants are morphologically defective (Supplementary Figure S1), suggesting that the fusion protein was biologically active. We next improved our microscopic setup by using solid-state lasers instead of conventional illumination in wide-field epifluorescence microscopy. In doing so, we were able to visualize strong signals of dynein concentrated at apical MT ends, labelled by the EB1-homologue Peb1 (Straube *et al*, 2003) fused to mRFP (Figure 1B, dynein intensity given in false colours; Supplementary Figure S2). In addition to the apical concentration of dynein, we observed fast moving dynein signals along the length of the hypha (Supplementary Movie 1).

It was reported that kinesin-3 takes EEs to MT plus-ends at the hyphal tip where they become loaded onto the apical dynein for retrograde motility (Lenz *et al*, 2006). To investigate this, we visualize individual EEs by fusing photoactivatable GFP (paGFP; Patterson and Lippincott-Schwartz, 2002)

to the small GTPase Rab5a that was shown to reside on EEs (Fuchs *et al*, 2006). When activated by 405 nm laser light, EEs became visible and in most cases moved to MT plus-ends before turning for retrograde motility (Supplementary Movie 2). Motility of the organelles was readily visualized in kymographs, which are graphical representation of spatial position over time (Figure 1C). We found that 0.7 ± 0.2 (sample size, $n = 151$) EEs reached the hyphal tip per second, where 88% of the organelles rapidly turned around within $<1\,s$ (Figure 1D, 'Turning'; Figure 1E). The loading of EEs onto dynein was very efficient, with only 1.74% of all EEs ($n = 800$) falling off the MT (Figure 1D, 'Detaching'), as indicated by random Brownian motion at the cell end (Supplementary Movie 3). It was suggested that arriving endosomes activate dynein at the MT plus-end for retrograde motility (Lenz *et al*, 2006). To test this, we expressed a mutant kinesin-3 protein that blocks EE motility by anchoring EEs to MTs (Kin3^{rigor}; Wedlich-Söldner *et al*, 2002a). When expressed in hyphae, EEs remained stationary and did not arrive at the apical dynein comet (Figure 2A). However, in such mutants dynein was still able to leave the MT end at normal velocity and rates (Figure 2B and C).

A large number of dyneins form the comet at MT plus-ends

The apical dynein comets showed very strong fluorescence and co-localized with the EB1-homologue Peb1 (see above),
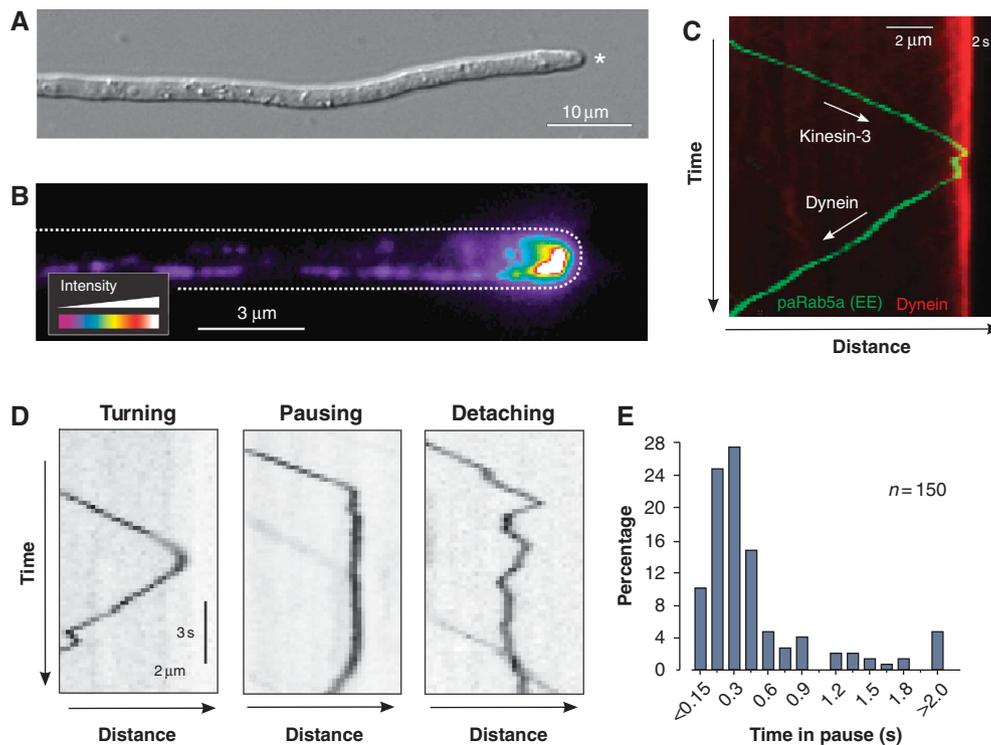
Figure 1 Loading of photoactivated EEs onto dynein at the apical MT plus-ends. (**A**) Hyphal cell of *U. maydis*. The cell elongated by polar extension at the tip (asterisk). Note that MTs in the apical region show a unipolar orientation with plus-ends directed to the cell tip (Lenz *et al*, 2006). The bar represents micrometers. (**B**) Pseudo-coloured image of dynein in the apex of a hyphal cell. The endogenous dynein heavy chain was tagged with $3 \times$ GFP (strain AB33G$_3$Dyn2, see Table I for genotypes of all strains). Most dynein accumulates at the growth region of the cell. Cell edge is indicated with a dotted line. The bar represents micrometers. (**C**) Kymograph showing anterograde delivery of an EE to the dynein comet. The organelle is labelled by paGFP-Rab5a (green), the comet is visualized by a fusion protein of the dynein heavy chain and triple tag of monomeric Cherry (red). The motors delivering the EEs is kinesin-3 (Lenz *et al*, 2006). The bars represent micrometers and seconds. (**D**) Kymographs showing the behaviour of paGFP-Rab5a-carrying EEs at an apical MT end. Detaching is characterized by irregular Brownian motion. Note that pausing and detaching are rare events. The bars represent micrometers and seconds. Inverted contrast is shown. (**E**) Bar chart showing pausing time of EEs at apical MT plus-ends. Most EEs turn within 1 s.

Table I Strains and plasmids used in this study

AB33G$_3$Dyn2	a2 Pnar-bW2 Pnar-bE1, Pdyn2-3xegfp-dyn2, ble^R, hyg^R	Lenz et al (2006)
AB33Dyn2Ch$_3$_paGRab5a	a2 PnarbW2 PnarbE1, Pdyn2-dyn2-3xmcherry, ble^R, nat^R/popaGRab5a	This study
AB33GRab5a	a2 PnarbW2 PnarbE1, ble^R/poGRab5a	This study
FB1Dyn2^{ts}	a1b1 Pdyn2-dyn2^{ts}, nat^R	Wedlich-Söldner et al (2002b)
FB2N107G_ER	a2b2 Pnup107-nup107-egfp, ble^R/pERRFP	Theisen et al (2008)
FB2N107R_N214G	a2b2 Pnup107-nup107-mrfp, Pnup214-nup214-egfp, hyg^R, ble^R	Theisen et al (2008)
FB2N214G$_3$	a2b2 Pnup214-nup214-3egfp, hyg^R	This study
FB2N107G_ N214G$_2$	a2b2 Pnup107-nup107-egfp, Pnup214-nup214-2egfp, ble^R hyg^R	This study
FB2N107G_ N214G$_3$	a2b2 Pnup107-nup107-egfp, Pnup214-nup214-3egfp, ble^R hyg^R	This study
FB2N107G_ N214G$_3$_N2G	a2b2 Pnup107-nup107-egfp, Pnup214-nup214-3egfp, Pnup2-nup2-egfp, ble^R hyg^R, nat^R	This study
AB33GRab5 _rKin3^{G105E}	a2 PnarbW2 PnarbE1/ble^R/poGRab5a/pcrgKin3^{G105E}	This study
AB33G$_3$Dyn2 _rKin3^{G105E}	a2 PnarbW2 PnarbE1 Pdyn2-3xegfp-dyn2 ble^R, hyg^R/pcrgKin3^{G105E}	This study
AB33pa$_m$G$_3$Dyn2	a2 Pnar-bW2 Pnar-bE1, Pdyn2-3xpamgfp-dyn2, ble^R, hyg^R	This study
AB33G$_3$Dyn2 _Peb1R	a2 Pnar-bW2 Pnar-bE1, Pdyn2-3xegfp-dyn2, Ppeb1-peb1-mrfp, ble^R, hyg^R, nat^R	This study
AB33G$_3$Dyn2 _cEB1	a2 PnarbW2 PnarbE1 Pdyn2-3xegfp-dyn2 ble^R, hyg^R/pcrgPeb1$^{211-268}$	This study
AB33G$_3$Dyn2 _nDya1	a2 PnarbW2 PnarbE1 Pdyn2-3xegfp-dyn2 ble^R, hyg^R/pcrgDya1$^{32-62}$	This study
AB33G$_3$Dyn2 _nDya1*	a2 PnarbW2 PnarbE1 Pdyn2-3xegfp-dyn2 ble^R, hyg^R/pcrgDya1$^{32-62,\ Q35E}$	This study
AB33pa$_m$G$_3$Dyn2 _cEB1	a2 PnarbW2 PnarbE1 Pdyn2-3xpamgfp-dyn2 ble^R, hyg^R/pcrgPeb1$^{211-268}$	This study
AB33pa$_m$GRab5a_cEB1	a2 PnarbW2 PnarbE1/popaGRab5a/pcrgPeb1$^{211-268}$	This study
popaGRab5a	Potef-pagfp-rab5a, cbx^R	This study
poGRab5a	Potef-egfp-rab5a, nat^R	This study
pERRFP	Potef-cal^S-mrfp-HDEL, cbx^R	Theisen et al (2008)
pcrgKin3^{G105E}	Pcrg-kin3^{G105E}, cbx^R	Wedlich-Söldner et al (2002a)
pcrgPeb1$^{211-268}$	Pcrg-peb1$^{211-268}$, cbx^R	This study
pcrgDya1$^{32-62}$	Pcrg-dya1$^{32-62}$, cbx^R	This study
pcrgDya1$^{32-62\ Q35E}$	Pcrg-dya1$^{32-62,\ Q35E}$, cbx^R	This study

a, b, mating type loci; P, promoter; -, fusion; hyg^R, hygromycin resistance; ble^R, phleomycin resistance; nat^R, nourseothricin resistance; cbx^R, carboxin resistance; ^{ts}, temperature-sensitive allele; /, ectopically integrated; crg, conditional arabinose-induced promoter; otef, constitutive promoter; nar, conditional nitrate reductase promoter; E1, W2, genes of the b mating type locus; nup2, nup107, nup214 nucleoporins; HDEL, ER retention signal; egfp, enhanced green-fluorescent protein; pamgfp: photoactivatable monomeric green-fluorescent protein; mrfp, monomeric red-fluorescent protein; mcherry, monomeric cherry; peb1$^{211-268}$, fragment of EB1-like plus-end binding protein; dya1$^{32-62}$, fragment of the dynactin subunit p150Glued; dya1$^{32-62Q35E}$, point mutated fragment of the dynactin subunit p150Glued; dyn2: C-terminal half of the dynein heavy chain; peb1, EB1-like plus-end binding protein; rab5a, small endosomal Rab5-like GTPase; kin3^{G105E}, rigor allele of kinesin3.

indicating that numerous motors accumulate at MT plus-ends. To determine the number of motors within the comets, we established an internal calibration standard to which our measurements could be related. Such a correlative approach was successfully used to obtain accurate numbers of GFP-labelled proteins in S. cerevisiae (Joglekar et al, 2008). We chose the nuclear pore complex because it is a highly ordered and conserved structure that contains 16 copies of the nucleoporin Nup107/84 and 8 copies of Nup214/159 (Rabut et al, 2004).

When GFP was fused to the endogenous nup107 gene, we found Nup107-GFP in spots within the nuclear envelope (Figure 3A, left panel) that showed a homogeneous fluorescence intensity (Figure 3A, right panel, intensity given in false colours) and that represent nuclear pores as confirmed by freeze-fracture electron microscopy (Figure 3A, middle panel). We next confirmed that each pore contains 16 copies of Nup107-GFP by comparing it to native levels of Nup214-GFP, a nucleoporin that is generally found in 8 copies (Rabut et al, 2004). We fused GFP to the native copy of nup214 and determined the number of GFPs by stepwise photobleaching, a method used to analyse protein numbers in the living cell (Cai et al, 2007; Ulbrich and Isacoff, 2007; Hendricks et al, 2010). We found that Nup214-GFP bleached in at most eight steps (Figure 3B) in agreement with the observation that GFP-107 signals were twice as strong as GFP-214 (Figure 3C; N107G, N214G), indicating that 16 copies of Nup107-GFP reside in a single nuclear pore.

The fluorescent intensity of GFP in the dynein comet was much stronger than that of a Nup107-GFP containing nuclear

pore, suggesting that numerous dyneins make up the comet. We therefore investigated whether an increased number of GFP tags result in a linear increase in fluorescence. To this end, we generated strains that simultaneously expressed various combinations of Nup107-GFP, Nup214 fused to double or triple GFP and GFP fused to Nup2, another nucleoporin identified in U. maydis (Theisen et al, 2008; see Supplementary data for more details). We found that the intensity of fluorescence in individual pores linear increased with the number of GFP tags (Figure 3C). This allowed us to estimate the number of GFP tags (and thereby the number of dynein motors) in the comet by determining the mean value of the Nup107-GFP intensity in single pores (= 16 GFP; distribution for single GFP shown in Figure 3D). The dynein heavy chain dimerizes and when tagged with triple GFP, a single motor is expected to carry 6 GFP tags. As no indication of proteolytic degradation of GFP$_3$–Dyn3 was found in cell extracts (Supplementary Figure S3), we used the average intensity for a single GFP derived from our internal calibration standard to estimate the dynein number in the comets. This analysis revealed that ∼ 55 dynein motors are concentrated in a dynein comet (Figure 3E).

Two different populations of dynein are found in the apical comet

Our results suggested that a large number of dynein motors accumulate at the apical MT ends. To further characterize this dynein comet, we fused a triple tag of photoactivatable GFP to the endogenous copy of the dynein heavy chain gene dyn2. Again, this modification did not affect the cell, indicating that
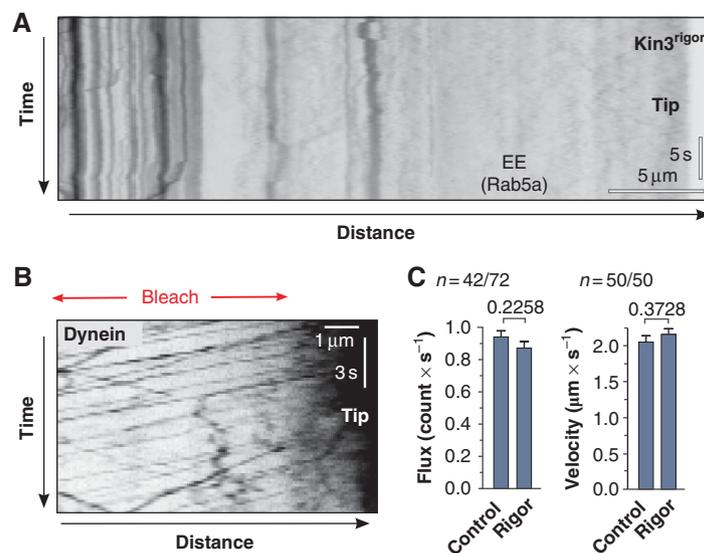
Figure 2 EE-independent retrograde motility of dynein. (**A**) Kymograph showing frozen EE motility in a hypha that overexpresses Kin3^{rigor} (strain AB33GRab5_rKin3^{G105E}). Vertical lines indicate stationary EEs and no cargo reaches the hyphal tip (Tip). The bars represent micrometers and seconds. Inverted contrast is shown. (**B**) Kymograph of a hyphal tip in cells expressing Kin3^{rigor} (strain AB33G$_3$Dyn2_rKin3^{G105E}). Despite the block in cargo motility dynein undergoes retrograde motility. This is best seen after photobleaching the subapical region of the hypha (Bleach). The bars represent micrometers and seconds. Inverted contrast is shown. (**C**) Bar charts showing a quantitative analysis of retrograde motility of dynein signals in control cells and cells that express Kin3^{rigor}. Both frequency and velocity of retrograde dynein motility are unaffected. *P*-values derived from two-tailed Student's *t*-tests are given above bars. Values are mean ± standard error of the mean; sample size *n* is given.

the fusion protein is biologically functional (Supplementary Figure S1). When activated at the apical MT plus-ends, paGFP$_3$–Dyn2 continuously left the MT end and the signal gradually decreased (Figure 4A; Supplementary Movie 4; note that in this movie photobleaching also gives this effect, and this was taken into account in the subsequent quantitative analysis). Non-linear regression of the decay curve favoured a two-phase decay over one-phase decay (Figure 4B; F-test gives $P < 0.0001$: F = 20.34; DFn = 2, DFd = 171). This suggested the existence of two populations of dynein, with about half (31–65% for 95% confidence interval) of the dynein signals rapidly leaving ($T_{1/2}$: 10.2 s; 3.7–16.7 s for 95% confidence interval) and the other half (35–69% for 95% confidence interval) staying significantly longer ($T_{1/2}$: 98.0 s; 61.4–134.6 s for 95% confidence interval). To obtain independent evidence for this result we performed fluorescent recovery after photobleaching (FRAP) experiments. When GFP$_3$–Dyn2 in the apical dynein comet was photobleached, delivery of dynein rapidly recovered the signal, again following a two-phase exponential curve (Figure 4C; F-test gives $P < 0.0001$: F = 15.36; DFn = 2, DFd = 150) with half-life times very similar to the previous experiment with $T_{1/2}$: 10.23 s (0.09061–20.37 s for 95% confidence interval) and $T_{1/2}$: 89.97 s (57.65–122.3 s for 95% confidence interval).

An interaction between dynactin and EB1 retains half of the dynein in the comet

We next consider the mechanism by which dynein is held at MT plus-ends. In mammalian cells, the dynactin complex, which binds dynein, is anchored to MT plus-ends by an interaction with the plus-end binding protein EB1 (Ligon *et al*, 2003), and the interaction site is well characterized in humans (Honnappa *et al*, 2006). In *U. maydis*, the EB1-

homologue Peb1 also co-localizes with dynein (see above), and the p150^{glued} dynactin compound Dya1 also concentrate at MT plus-ends (Lenz *et al*, 2006). Furthermore, the primary amino-acid sequence of the interaction site is highly conserved (Figure 4D). This suggested that dynein might be anchored to MT plus-ends by an interaction of Peb1 and Dya1. To test this, we generated two peptides, Peb1c and Dya1n, which covered the predicted interacting amino acids in both proteins (Figure 4D). Indeed, high expression of both peptides led to a significant decrease of the amount of dynein at MT plus-ends (Figure 4E and F). This reduction was not found when a Dya1 peptide was expressed that contained a point mutation known to inhibit the binding to EB1 (Figure 4D and F; Dya1n*; Honnappa *et al*, 2006). This suggests that the inhibitory effect of Peb1c and Dya1n is due to a specific blockage of the interaction of the EB1 homologue and dynactin. Surprisingly, the inhibitory peptides were only able to remove ∼60% of the dynein from MT ends (Figure 4F). This result was in agreement with the finding of two populations of dynein that differ in their turnover at MT ends. These data suggested that anchorage of dynein impairs its release and, consequently, the remaining ∼40% of dynein represent the more dynamic population. To test this, we expressed the inhibitory peptide Peb1c in cells containing paGFP$_3$–Dyn2 and analysed the decay of the remaining comet. We found that under these conditions, the photoactivatable dynein is released in one-phase decay reaching a plateau of 4.5% (favoured over a two-phase decay; F-test at $P = 0.9276$; F = 0.07515; DFn = 2, DFd = 141), with a rapid half-life time of 20.88 s (18.15–23.65 s for 95% confidence interval; Figure 4G), suggesting that it indeed represents the dynamic population. In summary, these results suggest that a dynein comet builds up by active retention via an interaction of dynactin and EB1. However, a second, EB1/dynactin-
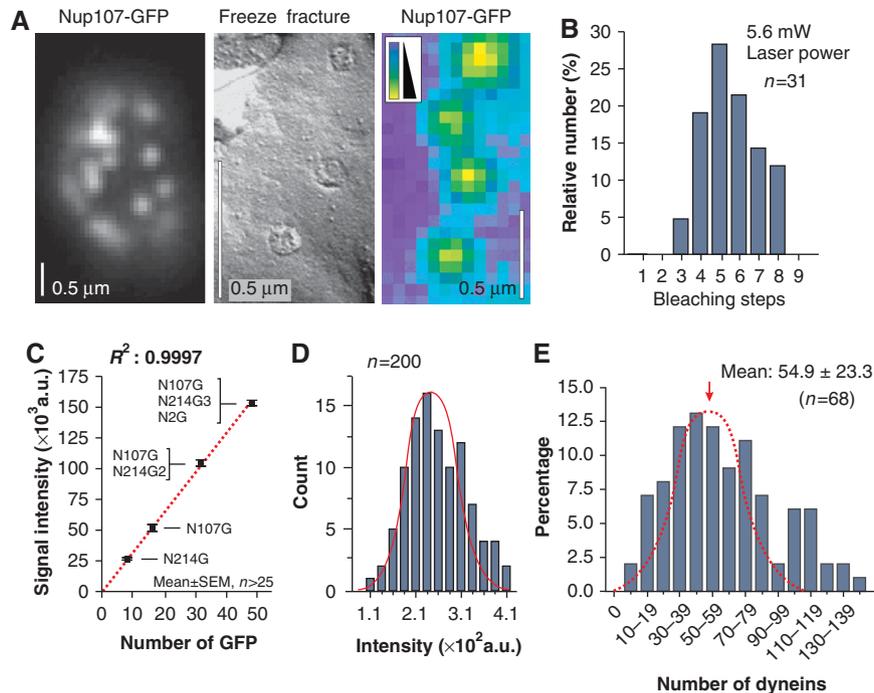
Figure 3 Nuclear pores as internal calibration standard for quantitative fluorescence intensity measurements. (**A**) The endogenous copy of the nucleoporin Nup107 was fused to GFP and the fusion protein labels nuclear pores (left panel, Nup107-GFP). Freeze-fracture electron microscopy confirms that these signals represent single pores (middle panel, freeze fracture), which often show uniform signal intensity (right panel, Nup107-GFP, false-coloured image). The bars represent 0.5 μm. (**B**) Bleaching-step analysis of Nup214-GFP in nuclear pores. Note that the endogenous *nup214* gene was fused to GFP. Bleaching steps from 3 to maximal 8 was found. This demonstrates that 8 copies of Nup214 reside in single nuclear pores. (**C**) Fluorescence intensity of nuclear pores containing Nup214-GFP (N214G), Nup107-GFP (N107G), Nup107-GFP + Nup214-GFP$_2$ (N107G/N214G2) and Nup107-GFP + Nup214-GFP$_3$ + Nup2-GFP (N107G/N214G3/N2G). The increase in fluorescent intensity is linear. The regression coefficient R^2 is given. Values are mean ± standard error of the mean, sample size n is given. Note that all GFP tags were fused to the endogenous genes. (**D**) Bar chart showing the signal intensity distribution of Nup107-GFP in nuclear pores. The measurements fit a Gaussian distribution (red line). Note that absolute values differ from those in C due to different experimental conditions used in these particular experiments (e.g. laser power and exposure time). (**E**) Bar chart showing the estimated number of dynein motors in comets at MT plus-ends. Note that most of the population follows a Gaussian distribution (red dotted line). Larger numbers might reflect two adjacent comets and were therefore excluded from the calculation of the mean.

independent mechanism helps to increase the number of dyneins at apical MT ends.

Transport properties of antergrade and retrograde dynein motility

It was previously shown that *in vitro* molecular motors can accumulate at MT ends thereby forming 'comet-like' structures (Okada and Hirokawa, 1999). This phenomenon does not involve any active regulation but can be understood as a consequence of queuing of motors, and we considered it possible that dynein concentrates at the MT plus-end in a similar stochastic way. We aimed to analyse this possibility by developing a mathematical model to describe the formation of the dynein comet. To generate a robust model, we set out to raise quantitative data about dynein motility in our cell system. We analysed GFP$_3$–Dyn2 movements in greater detail near the hyphal tip, where MTs have a unipolar orientation (Lenz *et al*, 2006). After photobleaching this region, anterograde and retrograde motility of GFP$_3$–Dyn2 signals became easily visible (Figure 5A). Individual signals moved in both directions at similar velocities ($V_{anterograde} = 1.66 \pm 0.37$ μm/s, $n = 202$; $V_{retrograde} = 1.76 \pm 0.55$ μm/s, $n = 209$), and signals sometimes turned direction (Figure 5A; arrowhead, lower panel), with 2.39% of the motors ($n = 300$) turning from anterograde to retrograde motility and 1.60% ($n = 300$) turning from retrograde to anterograde motility per 1 μm travelled

(see Supplementary data). To analyse the frequencies of transport towards and away from the MT plus-ends, we set out to determine the number of dynein motors per moving signal. Motor numbers were previously determined by step-wise photobleaching (Cai *et al*, 2007; Hammond *et al*, 2009; Hendricks *et al*, 2010). To apply this method to moving dynein signals, we reduced interference by photobleaching large parts of the hyphal cell. In addition, we treated the cells with cyanide 3-chlorophenyl-hydrazone (CCCP), a drug that reversibly inhibits cell respiration resulting in reduced ATP levels. This treatment gradually immobilized the dynein and allowed accurate bleaching-step analysis. In a typical experiment, GFP$_3$–Dyn2 was photobleached in the subapical regions. From unbleached parts at the cell tip dynein moved retrograde into the darkened area before it got immobilized by the depletion of ATP (Figure 5B, yellow arrows). Thus, the signals could be recognized as retrograde dynein and were analysed for stepwise bleaching. We found that the majority of the retrograde, as well as the anterograde GFP$_3$–Dyn2 signals bleached in up to six steps (Figure 5C and D), suggesting that they represent a single dynein motor. This was confirmed by comparison of their fluorescence intensity with our nuclear pore calibration standard, again showing that most signals are single dynein motors (Figure 5E). Statistical analysis using the bleaching-step curves revealed that the proportion of single-to-double

108

Appendix A
Controlled and stochastic retention concentrates dynein at MT ends
M Schuster *et al*
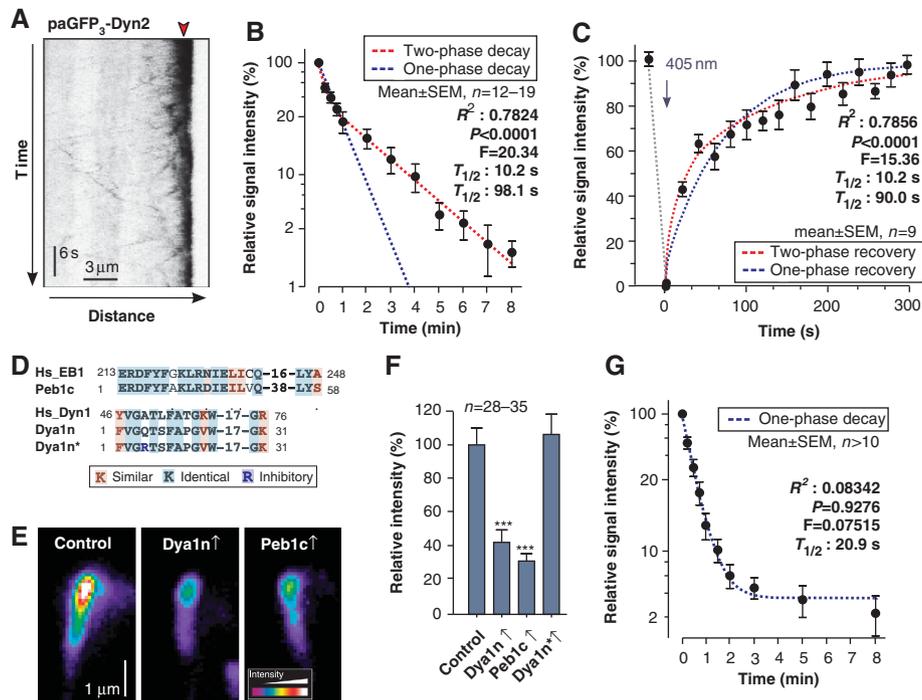
Figure 4 Experimental evidence for two populations of dynein at MT plus-ends. (**A**) Kymograph showing the decay of photoactivatable dynein at the hyphal tip (strain AB33pa$_m$G$_3$Dyn2). Note that the endogenous dynein heavy chain was tagged with a triple tandem repeat of photoactivatable GFP. Point of activation by a 405-nm laser is indicated with red arrowhead. Note that under continuous observation, photobleaching also reduces the apical dynein signals. (**B**) Decay of photoactivatable dynein after activation at MT plus-ends. The decay follows a two-phase decay curve (red dotted line) that strongly favoured over one-phase decay (blue dotted line; F-test, $P<0.0001$). R^2 for two-phase exponential decay, F-test results and predicted half-life times are given. The Y-axis is given in log-scale. Values are mean ± standard error of the mean; sample size n is given. The decrease of fluorescent intensity that was due to release from the MT plus-ends was measured in intervals to account for bleaching effects. (**C**) Fluorescence recovery of GFP$_3$-dynein heavy chain at MT plus-ends after photobleaching. The recovery follows a two-phase curve (red dotted line) that is strongly favoured over one-phase recovery (blue dotted line; F-test, $P<0.0001$). R^2 for two-phase exponential recovery, F-test results and predicted half-life times are given. Values are mean ± standard error of the mean; sample size n is given. The 405-nm bleaching laser pulse is indicated with an arrow. The increase of fluorescent intensity was measured in intervals to account for bleaching effects. (**D**) Sequence comparison of EB1 and the dynactin compound p150^{glued} from human (Hs_EB1, Hs_Dyn1) with the inhibitory peptides Peb1c and Dya1n, which reflect the sequence of the EB1- and p150^{glued} counterparts in *U. maydis* (Peb1c, Dya1n). The peptide Dya1n* contains a point mutation (blue) that was shown to inhibit binding of dynactin to EB1 (Honnappa *et al*, 2006). (**E**) Pseudo-coloured images of dynein signals at MT plus-ends of control cells (control) and cells that express the inhibitory peptides Peb1c (strain AB33G$_3$Dyn2_rEB1$^{211-268}$) and Dya1n (strain AB33G$_3$Dyn2_rDya1$^{32-62}$). Expression of peptides covering the interface between EB1 (Peb1c) and p150^{glued} (Dya1n) results in a significant reduction of the amount of dynein at MT ends. (**F**) Bar chart showing the effect of high expression of the peptides Dya1n, Peb1c and the mutant peptide Dya1n* on the amount of dynein at apical MT plus-ends. Triple asterisks indicate significant difference to control at $P<0.0001$. All bars are given as mean ± standard error of the mean. Note that the control peptide Dya1n* contains an inhibitory point mutation that should prevent its binding to EB1 and therefore was expected to have no effect of dynein numbers at the MT plus-ends. (**G**) Decay of photoactivatable dynein after activation at MT plus-ends in cells that express Peb1c, which interferes with dynein anchorage. The decay follows a one-phase decay curve to a plateau of 4.5% (blue dotted line) that is strongly favoured over a two-phase decay. R^2 coefficient, F-test results and predicted half-life times are given for the one-phase exponential decay to a plateau. The Y-axis is given in log-scale. Values are mean ± standard error of the mean; a sample size n is given. The decrease of fluorescent intensity that was due to release from the MT plus-ends was measured in intervals to account for bleaching effects.

dyneins was found to be 3.998:1 ($n=77$) for retrograde and 8.492:1 ($n=56$) for anterograde moving GFP$_3$–Dyn2 signals. These ratios were used, along with the frequency of signal movement to estimate that the flux at which dynein enters (Flux$_{anterograde}$) and leaves (Flux$_{retrograde}$) the apical region. We estimated a rate 1.06 dynein/second for both directions, which further was included in the mathematical modelling (see below; see Materials and methods for further details).

Mathematical modelling suggests that dynein accumulates stochastically

Having determined the motility parameters and motors numbers, we constructed a stochastic model for the bidirectional motility behaviour of dynein based on asymmetric simple exclusion process (ASEP) models of biological transport processes (Chowdhury *et al*, 2005). We simulated dynein motility using a published two-lane model that assumes that motors move on two lanes (Supplementary Figure S4; Ashwin *et al*, 2010). Using our experimental rates and velocities, this model produced kymographs that show remarkable similarities to our experimental results (Figure 6A) and predicted an accumulation of dynein at the MT end (Supplementary Movie 5). However, the simple two-lane model did not take into account that MTs consist of 13 protofilaments (Tilney *et al*, 1973), or that dynein changes lanes frequently (Wang *et al*, 1995), whereas kinesin-1 does not change lanes (Ray *et al*, 1993). Furthermore, we recognized that the cytoplasmic background of GFP$_3$–Dyn2 in the apex is higher than in the subapical cytoplasm
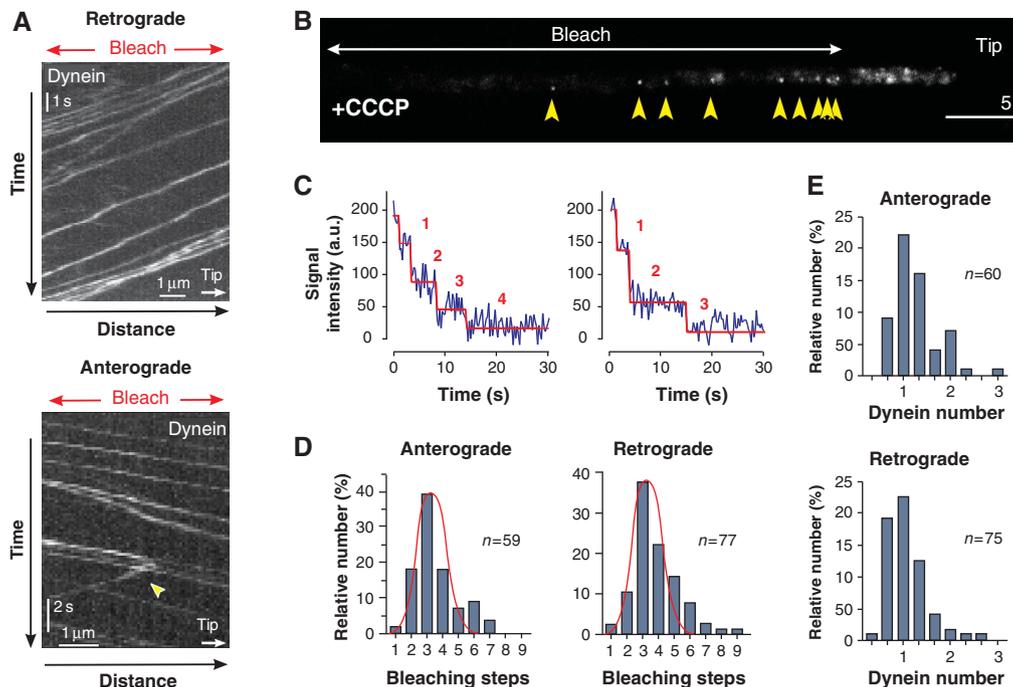
Figure 5 Motility behaviour and quantitative analysis of motor numbers in moving dynein signals. (**A**) Kymograph showing anterograde and retrograde motility of GFP$_3$–Dyn2. The analysis was restricted to the apical 10 µm, where MTs are unipolar oriented (Lenz *et al*, 2006). To avoid interference, the apical region was photobleached (Bleach) and the velocity, frequency and turning (arrowhead) of signals that moved into the darkened part of the cell was analysed. The bars represent micrometers and seconds. (**B**) GFP$_3$–Dyn2 signals in a photobleached cell that was placed on 100 µM CCCP for 15 min. Motors entered the darkened region from the unbleached hyphal tip at the right (Tip). CCCP inhibits the respiration chain and quickly leads to a drop in ATP levels, which in turn immobilized GFP$_3$–Dyn2 within the bleached part of the hypha (yellow arrowheads). The number of GFP tags in these signals was investigated by quantitative bleaching-step analysis. The bars represent micrometers and seconds. (**C**) Bleaching curves showing bleaching steps of GFP$_3$–Dyn2 signals after immobilization with CCCP. Step analysis was done with the algorithm STEPFINDER (Kerssemakers *et al*, 2006). Predicted bleaching steps are indicated with red numbers. (**D**) Bar chart showing the distribution of bleaching steps for anterograde and retrograde signals. In both cases, the majority fits to a normal distribution with a maximum at 3–4 bleaching steps (red curve in bar charts), indicating that they are single dynein motors, containing 6 GFP in a dimer of GFP$_3$–Dyn2. (**E**) Bar charts showing an estimation of dynein numbers in fluorescent signals derived from comparison with Nup107-GFP as internal calibration standard. Again, most anterograde and retrograde GFP$_3$–Dyn2 signals are predicted to represent single dynein motors.

(Supplementary Figure S5), suggesting some dynein detachment at MT plus-ends, again a possibility that is excluded in the two-lane model (Ashwin *et al*, 2010). We therefore extended the two-lane model to a more realistic 13-lane scenario that took these observations and conditions into account. It assumes that motors undertake 8 nm steps (Schnitzer and Block, 1997; Reck-Peterson *et al*, 2006) at certain probabilities (Figure 6B) and that the behaviour of motors is homogeneous along the MT (e.g. no change of turning rates at the MT tip). Finally, we included a 2% loss of arriving dynein, which reflects the escape rate for EEs at plus-ends (see above; for further details see Supplementary data). In this model, motor collisions are resolved by dynein changing lanes (Supplementary Figure S6). We assume that the probability for this side stepping (P_6; Figure 6B) is the same as the measured probability of dynein changing lanes without running into an obstacle (Wang *et al*, 1995; P_5; Figure 6B). Under these conditions, the 13-lane model predicted the accumulation of 25.4 ± 0.2 (mean $\pm$ s.e.m., $n = 400$) dyneins at MT plus-ends ($P_6 = P_5$; Figure 6D; Supplementary Movie 6). We realized that P_6 is an estimate that is not supported by experimental data. We therefore investigated the degree to which alterations in P_6 influence the comet size. First, we considered the possibility that motor collision increases P_6, allowing dynein moving forward without any

delay ($P_6 = \frac{1}{2}P_1$). Second, we considered the possibility that collisions decrease P_6 but blockages clear faster than we can resolve in the experiments ($P_6 = P_7$). Simulations based on these P_6 values showed very little difference in the comet size (Figure 6C). Thus, the 13-lane model predicts that homogeneous stochastic transport processes could account for the dynamic accumulation of dynein in the comet. However, breaking the homogeneity, for example by setting a different turning probability P_2(tip) within the first 500 nm of the MT, affects the dynein number at plus-ends (Figure 6D). This reinforces the observation that local conditions at the plus-end, such as the reported interaction with EB1, can have a strong influence on the comet size.

The high number in the dynein comet is required to keep EEs on the track

In contrast to our previous model of dynein loading, EEs seem not to activate dynein, which suggests that loading of the organelles onto dynein is a stochastic process. Such a concept would imply that a higher amount of dynein at the tip should result in an increase in EE turning from antero-grade to retrograde motility. Indeed, the results described so far indicated that the cell actively increases the number of dynein motors at MT plus-ends. Assuming a stochastic loading process, we considered it possible that the high dynein
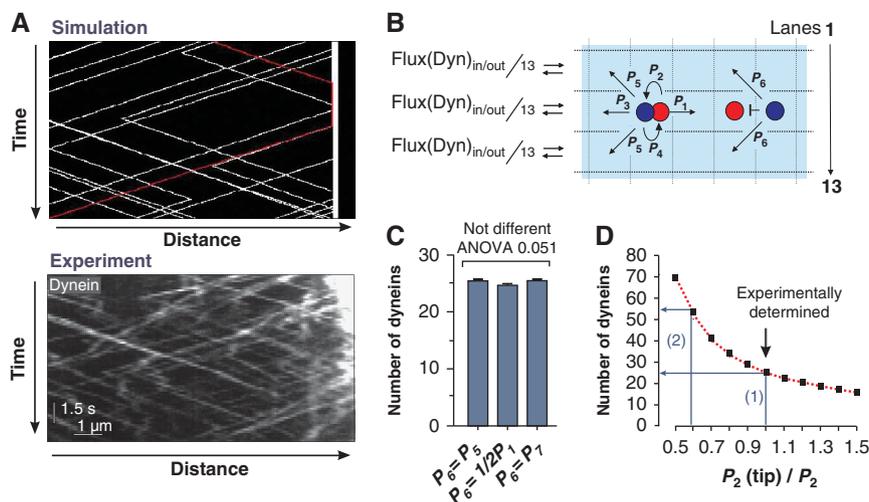
Figure 6 A stochastic model for dynein dynamics at MT plus-ends. (**A**) Comparison of kymographs of dynein motility derived from the two-lane model (Ashwin *et al*, 2010) showing computer simulations (Simulation) and experimental observation (Experiment). The bars represent micrometers and seconds. (**B**) The stochastic 13-lane model for dynein motility near a MT plus-end. At each time step, each motor has the illustrated probabilities (P_1–P_6) of moving in various directions. The model includes collisions between motors and detachment at the MT plus-end. For further conditions see main text and Supplementary data. (**C**) Model prediction of the dynein comet size at the MT plus-end for three different values of P_6. Variations in the probability of dynein changing lanes when meeting kinesin-1 on the same lane (P_6) are (1) meeting the obstacle has no influence on dynein changing lanes ($P_6 = P_5$); (2) dynein changes lane with higher probability ($P_6 = \frac{1}{2}P_2$); and (3) the probability P_6 is reduced, but blockage of motility is still too fast to be recognized in kymographs ($P_6 = P_7$). All simulations predict ~25 dynein motors in the comet. All bars are given as mean ± standard error of the mean; the sample size is 400 simulations. (**D**) Model prediction of the dynein comet size at the MT plus-end breaking homogeneity by setting $P_2(\text{tip})$ different from P_2 on the last 500 nm of the MT. Using the measured value of P_2 and an assumption of homogeneity predicts ~25 motors in the comet (blue arrow 1). For a lower value $P_2(\text{tip}) \approx 0.55 P_2$ the comet size is ~55 dynein motors (blue arrow 2).

density in the comet serves as a 'buffer stop' for arriving EEs. We carefully analysed the distribution of dynein within comets of various intensities and always found a steady increase of the motor density towards the MT plus-ends (Figure 7A and B). Consistent with the idea that EEs get loaded onto dynein in a stochastic way, they often turned before they have reached the highest dynein density in the comet (Figure 7C, red line represents dynein in the comet, green lines are moving EEs). However, the turning rate increased with an increase in dynein numbers (Figure 7D), suggesting that the probability that EEs get captured by dynein rises within the comet. These results supported the idea that the cell maintains a high number of dynein in order to reduce the risk that EEs detach from or 'fall off' the end of their track. To test this possibility, we reduced the comet size by expressing Peb1c in hyphal cells that also contained GFPRab5a-labelled EEs. Indeed, when only the stochastic dynein population was left, the number of EEs that detached at the end of the MT significantly increased (9.22%; Figure 7E). These results are consistent with a function of the dynein comet being the capture EEs through a stochastic loading process.

Discussion

Bidirectional transport along MTs is an important process that underlies the function and survival of animal cells (Gross, 2004; Welte, 2004; Chevalier-Larsen and Holzbaur, 2006). In this study, we have used a fungal model system to address the question how organelles are kept on track when they reach the end of a MT? It was previously suggested that dynein accumulates at the MT plus-end in an inactive state to receive

arriving EEs for retrograde transport (Lenz *et al*, 2006; Abenza *et al*, 2009). We show here that this simple concept needs to be revised. We provide evidence that dynein does not need to be activated but leaves the MT end randomly, suggesting that EEs get loaded onto dynein motors via a stochastic mechanism. In order to increase the probability that arriving organelles meet a dynein motor, the cell accumulates a large number of dynein motors. This is done in two ways (1) an active retention of dynein motors via an interaction between dynein/dynactin and the plus-end binding protein EB1 (=Peb1) and (2) a stochastic process that appears to require no active control but is a consequence of the motility behaviour of motors (Figure 8). This mechanism avoids the cargo from falling off and ensures high fidelity of the transport process.

Dynein is anchored at MT plus-ends by an interaction of dynactin and EB1
In the elongated hyphal cells of fungi, dynein forms comet-like accumulations at the plus-ends of MTs (Han *et al*, 2001; Lenz *et al*, 2006). In this study, we have established nuclear pores as an internal calibration standard and found that an average of 55 motors concentrate in the comet. Dynein is a huge protein complex (King, 2000), making it unlikely that such a large number of motors concentrates at the MT plus-end without serving a cellular function. In mammalian cells, dynactin interacts with the plus-end binding protein EB1 (Ligon *et al*, 2003) and the interaction site is well characterized (Honnappa *et al*, 2006). It was shown that phosphorylation of p150[glued] releases the complex from MT plus-ends and allows retrograde organelle motility (Vaughan *et al*, 2002). Our results described here argue that a similar mechanism is
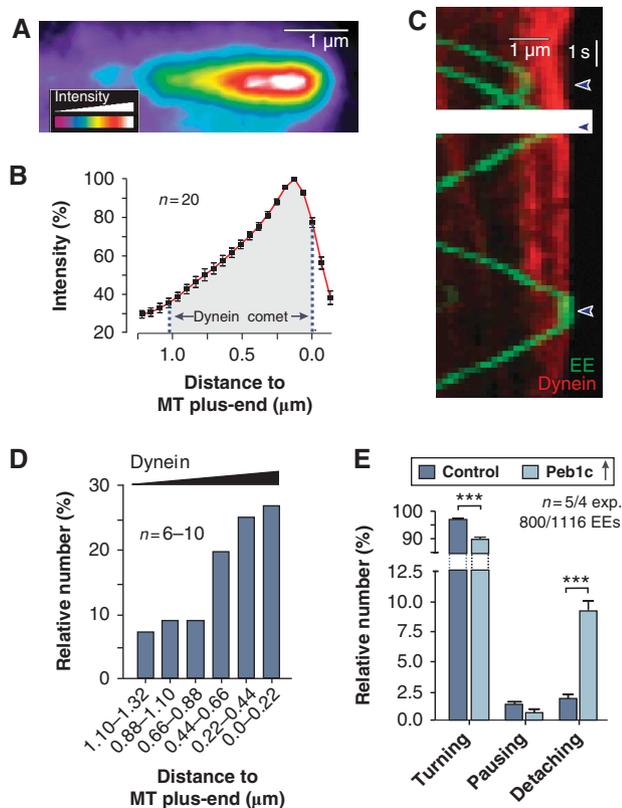
Figure 7 Dynein numbers and EE escape rate at MT plus-ends. (**A**) Pseudo-coloured image of an apical dynein comet (strain AB33G$_3$Dyn2). The bar represents one micrometer. (**B**) Graph showing intensity profile along the length of the dynein comet. Values are mean ± standard error of the mean of linescan analysis of 20 apical dynein comets. Note that the distribution of the dynein along the length of the MT is independent of the overall intensity of the comet. (**C**) Kymograph showing the arrival and turning of photoactivated paRab5a-carrying EEs (green lines) and dynein heavy chain fused to a triple mCherry tag (red). Note that only one of the EEs arrived at the very end of the MT, where dynein concentration is highest. (**D**) Turning of arriving EEs within the dynein comet. Note that the MT plus-end was defined by the maximum intensity of the dynein signal in the comet. (**E**) Bar chart showing the behaviour of EEs in control and cells expressing the peptide Peb1c. Note that Peb1c reduces the average number of dyneins to ~20, which results in 9.22% loss of EEs at the MT end. Triple asterisks indicate significant difference to control at $P < 0.0001$.

conserved in fungi, although the dynactin/dynein complex is already assembled at the plus-ends. In addition, we found evidence for a population of more dynamic dynein that is rapidly turned over at the MT plus-end. We assumed that these dynein motors are not anchored at plus-ends, but instead are accumulating as a 'traffic jam' of arriving motors. A similar stochastic accumulation was shown for recombinant kinesin motors *in vitro* (Okada and Hirokawa, 1999), which was argued could be due to local ATP depletion (Chowdhury *et al*, 2005).

A mathematical model suggests that a stochastic mechanism accounts for about one-half of the dynein comet

Recent theoretical approaches have strongly suggested that stochastic properties of motor behaviour may be sufficient to
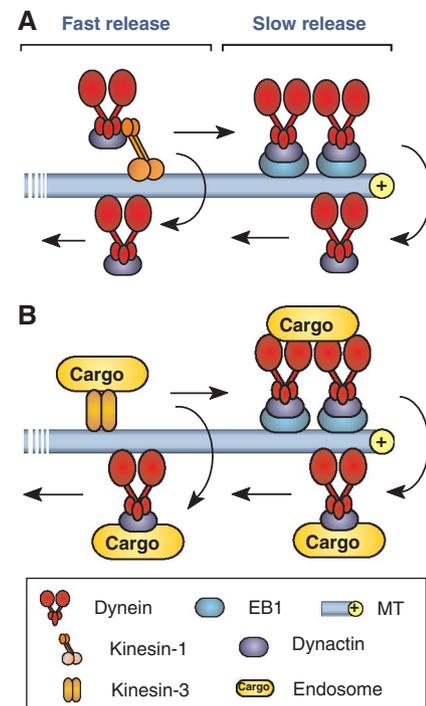
Figure 8 Model of the formation and function of the apical dynein comet. (**A**) Dynein is targeted to plus-ends by kinesin-1. About half of the motors are rapidly turned over (fast release) whereas the other half gets trapped at the MT plus-ends. This involves an interaction between dynactin and the plus-end binding EB1 (=Peb1). This active retention is implicated in the observed slow release of dynein. (**B**) EEs get delivered by kinesin-3. Loading of the cargo onto dynein is a stochastic process that is most likely when the dynein density reaches its maximum.

explain bidirectional motility in living cells (Klumpp and Lipowsky, 2005; Gazzola *et al*, 2009; Soppina *et al*, 2009; Hendricks *et al*, 2010; Müller *et al*, 2008, 2010). Based on a previous stochastic two-lane model (Ashwin *et al*, 2010), we developed a more realistic 13-lane model to help us understand how dynein accumulates at the MT plus-end simply as a result of the observed stochastic traffic properties on the MT. Most previous mathematical models have exclusively relied on data from *in vitro* experiments and/or used motility parameters from different motors and different organisms. While the lack of consistent data has made this necessary, one should recognize that motors from different organisms or cell types may have very different features. An illustrating example is the difference in the *in vitro* transport velocity of kinesin-1 from animals (~0.4–0.8 μm/s; Vale *et al*, 1985; Porter *et al*, 1987; Bloom *et al*, 1988; Ingold *et al*, 1988) and from fungi (~2–2.5 μm/s; Steinberg and Schliwa, 1996; Steinberg, 1997; Steinberg *et al*, 1998). In our model we also included *in vitro* results from other systems and assume that motors move in multiples of 8 nm steps (Schnitzer and Block, 1997; Reck-Peterson *et al*, 2006) along the 13 protofilaments of the MT (Tilney *et al*, 1973). In contrast to Ashwin *et al* (2010), we consider that dynein is able to change lanes (Wang *et al*, 1995), whereas kinesin-1, which is thought to be the motor for dynein delivery (Zhang *et al*, 2003; Lenz *et al*, 2006), keeps on its protofilament with high fidelity (Ray *et al*, 1993). The remaining parameters in our 13-lane model are based on a quantitative analysis of dynein numbers and

112

Appendix A
Controlled and stochastic retention concentrates dynein at MT ends
M Schuster *et al*

motility behaviour in the living cell. Indeed, the 13-lane model nicely predicts that about one-half of the dynein motors in the comet can be found, simply by assuming stochastic transport processes. This number is in good agreement with the amount of dynein that is left at plus-ends when the Dynactin/EB1 interaction is blocked by inhibitory peptides. However, the model assumes homogeneity of motor behaviour along the length of the MT, that is it assumes that turning rates along the track are the same as turning rates at the end of the MT. This is clearly an oversimplification, as the MT plus-end binds numerous proteins (Akhmanova and Steinmetz, 2008) that may occupy sites or influence the tug-of-war between dynein-delivering kinesin-1 and opposing dynein. The assumed presence of additional plus-end binding proteins is also indicated by the fact that the comet stretches over ∼700 nm (see above, Figure 7A), which is larger than the comet length predicted by our model, and which might reflect that motors and plus-end binding proteins compete for binding at MT ends. Such competition could influence the probability for turning from anterograde to retrograde motility, which in our model is described by the probability P_2 per simulation time step. Our data show that varying this P_2 near the tip has a very significant influence on the comet size and can result in much higher numbers of motors at the plus-end. A change in P_2 would also be the consequence of active retention of dynein/dynactin by interaction with EB1. Thus, local conditions at the MT end also influence the comet size in our model. Nevertheless, our model demonstrates that such local conditions are not necessary to predict an accumulation of motors at the plus-end.

The comet serves as a 'buffer stop' for arriving endosomes

Our experiments clearly show that the cell actively concentrates dynein at MT plus-ends to form a comet, which argues for a biological function of the comet. It was previously suggested that the dynein comet serves as a 'dynein loading zone' for arriving endosomes (Lenz *et al*, 2006) that mediate recycling processes to support tip growth of the hyphal cell (Abenza *et al*, 2009; Wedlich-Söldner *et al*, 2000; reviewed in Peñalva, 2010). Indeed, apical recycling makes it necessary that EEs reach the hyphal tip, which increases the risk of EEs falling off the track and requires an efficient capture mechanism. Our results suggest that the dynein comet is part of such a MT-end capture mechanism. We show that dynein is stochastically released from the comet and that EEs have a higher probability to turn around in regions of high dynein numbers. This suggests that the EEs get loaded onto dynein in a stochastic way with the comet serving as a dynamic 'buffer stop'. While our result argue for a function of the comet in capturing arriving organelles, it need to be considered that the apical dynein might also support other functions, such as control of MT length (Adamikova *et al*, 2004) or the retrograde transport of other cargo, such as RNA-binding particles (Becht *et al*, 2006).

Conclusions

Long-range organelle transport is important for numerous aspect of eukaryotic cell function. How motors cooperate in endosome motility is currently under intensive investigation (Soppina *et al*, 2009), but what happens to organelles and motors at the end of the track is not well understood. We

show here that the cell uses the stochastic behaviour of the motors on the track and active retention to increase the number of dynein at the tip. Given a stochastic loading process, this ensures that an arriving organelle ultimately finds a dynein to which it can bind for retrograde transport. Recent work has started to highlight the importance of the stochastic behaviour of motor in bidirectional transport processes (Klumpp and Lipowsky, 2005; Müller *et al*, 2008; Gazzola *et al*, 2009) or in controlling MT length (Hough *et al*, 2009). In combination with higher-order regulation, the stochastic transport properties of motors might underlie the complexity of cargo movement in the cell (Müller *et al*, 2008; Welte and Gross, 2008). Our results add to this emerging picture and in particular expand our understanding of motor cooperation in EE motility. However, the biological reason for the bidirectional long-range EE transport is still elusive. Addressing this question is a fascinating challenge for future research.

Materials and methods

Strains and plasmids
The strains AB33G₃Dyn2, FB2N107G_ER, FB2N107R-N214G and FB1Dyn2ᵗˢ were described previously (Wedlich-Söldner *et al*, 2002b; Lenz *et al*, 2006; Theisen *et al*, 2008). To visualize EEs either GFP, paGFP or mCherry were individually fused to the endosome-specific Rab5a (Fuchs *et al*, 2006) under the control of the constitutive *otef* promoter (Spellig *et al*, 1996) and the resulting plasmids were integrated ectopically into the genome of *U. maydis*. Dynein was visualized by labelling the endogenous copy of *dyn*2 with 3GFP, 3paGFP or 3mCherry. The rigor alleles of kinesin-3 as well as the short fragments of the EB1-like plus-end binding protein (Peb1) and the Dynactin subunit p150Glued were expressed as an additional copy under the conditional arabinose-induced *crg* promoter (Bottin *et al*, 1996). Monomeric RFP was fused to the endogenous copy of Peb1 to visualize the plus-ends of MTs. Nuclear pores were visualized by homologous integration of single, double or triple GFP into the native locus of Nup107, Nup214 or Nup2. Various GFP-tagged nucleoporins were combined in single strains to achieve stronger fluorescent signals that could be related to defined numbers of GFP tags. The genotypes of all strains used in this work are summarized in Table I.

Growth conditions
All *U. maydis* cultures were grown overnight at 28°C in complete medium (CM) (Holliday, 1974) containing 1% (w/v) glucose, shaking at 200 revolutions per minute (r.p.m.). Hyphal growth was induced by shifting in NM liquid medium supplemented with 1% (w/v) glucose. Colony growth of strains AB33, a temperature sensitive mutant strain FB1Dyn2ᵗˢ, AB33G₃Dyn2 and AB33paₘG₃₋Dyn2 was analysed on CM-G plates at 32°C. The expression of genes under the control of the *crg* promoter was introduced by changing the carbon source form glucose to 1% (w/v) arabinose.

Freeze-fracture electron microscopy and Laser-based epifluorescence microscopy
Ultrastructural analysis of nuclear pores were done as described (Severs, 2007; see Supplementary data for details). For light microscopy, cells were placed on a thin layer of 2% agarose, covered with a cover slip, and immediately observed using a IX81 motorized inverted microscope (Olympus, Hamburg, Germany) and a VS-LMS4 Laser-Merge-System solid-state lasers using a 50 or 75 mW observation lasers at 488 and 561 nm. Photoactivation and photobleaching experiments were performed using a Visitron 2D FRAP system. Images were captured using a charged-coupled device camera (Photometric CoolSNAP HQ2, Roper Scientific, Germany). All parts of the system were under the control of the software package MetaMorph (Molecular Devices, Downingtown), which was also used for fluorescence measurements and image processing. For quantitative analysis, images were taken below light

saturation and corrected for the adjacent background. See Supplementary data for further details.

Quantitative analysis of fluorescent intensities

For intensity measurements of Nup107-GFP and other GFP-nucleoporins, images were taken at 50 or 250 ms exposure time, focusing on the upper area of the nucleus. Only those signals were analysed for their integrated intensity that (1) were far enough apart from other pores to be measured and (2) were located in the central one square micrometer of the observation field. All measurements were corrected for the background in the nuclear envelope. All corrected values were plotted and the average integrated intensity value for a single Nup107-GFP was calculated. The number of motors was estimated by comparing the corrected integrated intensity values for GFP$_6$-dynein with the average value of the background-corrected integrated intensity values of a single Nup107-GFP. For each motor measurement, nuclear pore intensities were measured at the same day under the same conditions. To analyse the signal intensity in cells overexpressing the inhibitory peptides Peb1c or Dya1n, the integrated intensity of a single loading zone was recorded. The measured values were background corrected as described above.

Protein extraction and immunodetection

Protein extraction and immunodetection was performed as described (Straube *et al*, 2001). For detection of GFP$_3$–Dyn2, a monoclonal anti-GFP antibody was used (Roche Diagnostic GmbH, Mannheim, Germany). As secondary antibody, an anti-mouse peroxidase-conjugated antibody was used (Promega, Southampton, UK). Chemiluminescence was detected using the ECL Plus Western Blot detection reagent, following the manufacture's instructions (GE Healthcare, Uppsala, Sweden).

Activation of photoactivatable dynein and photoactivatable Rab5a

For experiments that monitored the decay of pa$_m$G$_3$Dyn2, the hyphal tip was irradiated for 25 ms using 2% output power of a solid state 60 mW 405 nm laser, followed by observation using the 488-nm laser at 15% power. A reference image was taken immediately after activation. After 15, 30, 45, 60 s and then every minute a Z-stack with 3 plains and a Z-distance of 0.25 μm was taken. In a maximum projection, the integrated intensity of the apical accumulation was measured and corrected by the background that was measured in a neighbouring area within the cell. The intensity of the signal at time zero was set to 100% and the intensity of the following time points were correlated to this. Photoactivatable Rab5a was activated like pa$_m$G$_3$Dyn2 (see above) and movies with 100 plains at 150 ms exposure time at 20% of the 488-nm laser were taken.

Fluorescent recovery after photobleaching experiments and photobleaching analysis

Dynein motility was analysed after photobleaching using a Visitron 2D FRAP system (Visitron Systems, Munich, Germany) with a solid state 60 mW 405 nm laser. This was followed by observation using the 488-nm observation laser. Velocity, frequency and turning rates/mean run lengths were analysed in kymographs that were generated from these image series using MetaMorph. For stepwise photobleaching experiments, dynein signals (and the internal calibration standard GFP-Nup107) were immobilized using 100 μM CCCP (carbonyl cyanide *m*-chlorophenyl-hydrazone; Sigma-Aldrich Ltd, Gillingham, UK) and bleaching was recorded using the 488-nm observation laser at 5.6 mW laser power were taken. The average intensity of signals was corrected for the background and the number of bleaching steps were determined by a step-find algorithm (Kerssemakers *et al*, 2006) kindly provided by Dr Jacob Kerssemakers, Delft, The Netherlands) in the program MatLab (The MathWorks, Natick). For a more detailed description of both models, see Supplementary data.

Determination of the dynein flux from bleaching-step analysis

Bleaching-step distributions were fit to a sum of normal distributions using the software Prism (GraphPad, San Diego). From this the ratio of 1 dynein:2 dyneins was determined and the measured fluxes of GFP$_3$–Dyn2 signals were corrected. The mean value of anterograde and retrograde fluxes was used in the mathematical modelling. For a more detailed description of both models, see Supplementary data.

Mathematical modelling

The mathematical model represents an ASEP-type model, extended from a two-lane model for bidirectional motor motion (Ashwin *et al*, 2010). The model makes the following assumptions: (1) motors take multiples of 8 nm steps forward at fixed rate per time step, unless the site to be moved into is already occupied; (2) motion takes place in both directions over 13 lanes corresponding to protofilaments of an MT; (3) motors do not fall off along the track but a minor loss of 2% of the delivered dynein occurs at the tip; (3) dynein changes lanes on average 5.1-times per micrometer (corresponding to experimental data of Wang *et al* (1995)); and (4) kinesin-1 delivering dynein to the plus-end does not change lanes (Ray *et al*, 1993). These assumptions and the experimental measurements were used to determine all rates in the model. Simulations were done using C++ (http://sourceforge.net/projects/dev-cpp/). For a more detailed description of both models, see Supplementary data.

Non-linear regression and statistical analysis

Non-linear regression and all statistical tests were done using the software Prism (GraphPad). Comparison of one-phase decay and two-phase decay models in Figure 4 was done using an F-test ($\alpha = 0.05$). The half-lives of the decay and the proportions in each population are the fitting parameters for a signal that is normalized to lie between 0 and 100%. For further details see Supplementary data.

Supplementary data

Supplementary data are available at *The EMBO Journal* Online (http://www.embojournal.org).

Conflict of interest

The authors declare that they have no conflict of interest.

References

Abenza JF, Pantazopoulou A, Rodriguez JM, Galindo A, Penalva MA (2009) Long-distance movement of *Aspergillus nidulans* early endosomes on microtubule tracks. *Traffic* **10:** 57–75

Adamikova L, Straube A, Schulz I, Steinberg G (2004) Calcium signaling is involved in dynein-dependent microtubule organization. *Mol Biol Cell* **15:** 1969–1980

Appendix A
Controlled and stochastic retention concentrates dynein at MT ends
M Schuster *et al*

Akhmanova A, Steinmetz MO (2008) Tracking the ends: a dynamic protein network controls the fate of microtubule tips. *Nature Rev* **9:** 309–322

Ally S, Jolly AL, Gelfand VI (2008) Motor-cargo release: CaMKII as a traffic cop. *Nat Cell Biol* **10:** 3–5

Andersson TP, Svensson SP, Karlsson AM (2003) Regulation of melanosome movement by MAP kinase. *Pigment Cell Res* **16:** 215–221

Ashwin P, Lin C, Steinberg G (2010) Queueing induced by bidirectional motor motion near the end of a microtubule. *Phys Rev E* **82:** 051907

Becht P, Konig J, Feldbrugge M (2006) The RNA-binding protein Rrm4 is essential for polarity in *Ustilago maydis* and shuttles along microtubules. *J Cell Sci* **119:** 4964–4973

Bloom GS, Wagner MC, Pfister KK, Brady ST (1988) Native structure and physical properties of bovine brain kinesin and identification of the ATP-binding subunit polypeptide. *Biochemistry* **27:** 3409–3416

Bottin A, Kämper J, Kahmann R (1996) Isolation of a carbon source-regulated gene from *Ustilago maydis*. *Mol Gen Genet* **253:** 342–352

Cai D, Verhey KJ, Meyhöfer E (2007) Tracking single kinesin molecules in the cytoplasm of mammalian cells. *Biophys J* **92:** 4137–4144

Chevalier-Larsen E, Holzbaur EL (2006) Axonal transport and neurodegenerative disease. *Biochim Biophys Acta* **1762:** 1094–1108

Chowdhury D, Schadschneider A, Nishinari K (2005) Physics of transport and traffic phenomena in biology: from molecular motors and cells to organisms. *Phy Life Rev* **2:** 318–352

Deacon SW, Nascimento A, Serpinskaya AS, Gelfand VI (2005) Regulation of bidirectional melanosome transport by organelle bound MAP kinase. *Curr Biol* **15:** 459–463

Fuchs U, Hause G, Schuchardt I, Steinberg G (2006) Endocytosis is essential for pathogenic development in the corn smut fungus *Ustilago maydis*. *Plant Cell* **18:** 2066–2081

Gazzola M, Burckhardt CJ, Bayati B, Engelke M, Greber UF, Koumoutsakos P (2009) A stochastic model for microtubule motors describes the *in vivo* cytoplasmic transport of human adenovirus. *PLoS Comput Biol* **5:** e1000623

Gross SP (2004) Hither and yon: a review of bi-directional microtubule-based transport. *Phys Biol* **1:** R1–R11

Hammond JW, Cai D, Blasius TL, Li Z, Jiang Y, Jih GT, Meyhofer E, Verhey KJ (2009) Mammalian Kinesin-3 motors are dimeric *in vivo* and move by processive motility upon release of autoinhibition. *PLoS Biol* **7:** e72

Han G, Liu B, Zhang J, Zuo W, Morris NR, Xiang X (2001) The *Aspergillus* cytoplasmic dynein heavy chain and NUDF localize to microtubule ends and affect microtubule dynamics. *Curr Biol* **11:** 719–724

Hendricks AG, Perlson E, Ross JL, Schroeder III HW, Tokito M, Holzbaur EL (2010) Motor coordination via a tug-of-war mechanism drives bidirectional vesicle transport. *Curr Biol* **20:** 697–702

Hoepfner S, Severin F, Cabezas A, Habermann B, Runge A, Gillooly D, Stenmark H, Zerial M (2005) Modulation of receptor recycling and degradation by the endosomal kinesin KIF16B. *Cell* **121:** 437–450

Holliday R (1974) *Ustilago maydis*. In *Handbook of Genetics*, King RC (ed) Vol. 1, pp 575–595. New York: Plenum Press

Honnappa S, Okhrimenko O, Jaussi R, Jawhari H, Jelesarov I, Winkler FK, Steinmetz MO (2006) Key interaction modes of dynamic +TIP networks. *Mol Cell* **23:** 663–671

Hough LE, Schwabe A, Glaser MA, McIntosh JR, Betterton MD (2009) Microtubule depolymerization by the Kinesin-8 motor Kip3p: a mathematical model. *Biophys J* **96:** 3050–3064

Howe CL, Mobley WC (2005) Long-distance retrograde neurotrophic signaling. *Curr Opin Neurobiol* **15:** 40–48

Ingold AL, Cohn SA, Scholey JM (1988) Inhibition of kinesin-driven microtubule motility by monoclonal antibodies to kinesin heavy chains. *J Cell Biol* **107:** 2657–2667

Joglekar AP, Salmon ED, Bloom KS (2008) Counting kinetochore protein numbers in budding yeast using genetically encoded fluorescent proteins. *Methods Cell Biol* **85:** 127–151

Kerssemakers JW, Munteanu EL, Laan L, Noetzel TL, Janson ME, Dogterom M (2006) Assembly dynamics of microtubules at molecular resolution. *Nature* **442:** 709–712

King SM (2000) The dynein microtubule motor. *Biochim Biophys Acta* **1496:** 60–75

Klumpp S, Lipowsky R (2005) Cooperative cargo transport by several molecular motors. *Proc Natl Acad Sci USA* **102:** 17284–17289

Kumar S, Lee IH, Plamann M (2000) Cytoplasmic dynein ATPase activity is regulated by dynactin-dependent phosphorylation. *J Biol Chem* **275:** 31798–31804

Lenz JH, Schuchardt I, Straube A, Steinberg G (2006) A dynein loading zone for retrograde endosome motility at microtubule plus-ends. *EMBO J* **25:** 2275–2286

Ligon LA, Shelly SS, Tokito M, Holzbaur EL (2003) The microtubule plus-end proteins EB1 and dynactin have differential effects on microtubule polymerization. *Mol Biol Cell* **14:** 1405–1417

Lomakin AJ, Semenova I, Zaliapin I, Kraikivski P, Nadezhdina E, Slepchenko BM, Akhmanova A, Rodionov V (2009) CLIP-170-dependent capture of membrane organelles by microtubules initiates minus-end directed transport. *Dev Cell* **17:** 323–333

Miaczynska M, Pelkmans L, Zerial M (2004) Not just a sink: endosomes in control of signal transduction. *Curr Opin Cell Biol* **16:** 400–406

Müller MJ, Klumpp S, Lipowsky R (2008) Tug-of-war as a cooperative mechanism for bidirectional cargo transport by molecular motors. *Proc Natl Acad Sci USA* **105:** 4609–4614

Müller MJ, Klumpp S, Lipowsky R (2010) Bidirectional transport by molecular motors: enhanced processivity and response to external forces. *Biophysical J* **98:** 2610–2618

Münsterkötter M, Steinberg G (2007) The fungus *Ustilago maydis* and humans share disease-related proteins that are not found in *Saccharomyces cerevisiae*. *BMC Genomics* **8:** 473

Okada Y, Hirokawa N (1999) A processive single-headed motor: kinesin superfamily protein KIF1A. *Science* **283:** 1152–1157

Patterson GH, Lippincott-Schwartz J (2002) A photoactivatable GFP for selective photolabeling of proteins and cells. *Science* **297:** 1873–1877

Peñalva MA (2010) Endocytosis in filamentous fungi: Cinderella gets her reward. *Curr Opin Microbiol* **13:** 1–9

Porter ME, Scholey JM, Stemple DL, Vigers GP, Vale RD, Sheetz MP, McIntosh JR (1987) Characterization of the microtubule movement produced by sea urchin egg kinesin. *J Biol Chem* **262:** 2794–2802

Rabut G, Doye V, Ellenberg J (2004) Mapping the dynamic organization of the nuclear pore complex inside single living cells. *Nat Cell Biol* **6:** 1114–1121

Ray S, Meyhöfer E, Milligan RA, Howard J (1993) Kinesin follows the microtubule's protofilament axis. *J Cell Biol* **121:** 1083–1093

Reck-Peterson SL, Yildiz A, Carter AP, Gennerich A, Zhang N, Vale RD (2006) Single-molecule analysis of dynein processivity and stepping behavior. *Cell* **126:** 335–348

Schnitzer MJ, Block SM (1997) Kinesin hydrolyses one ATP per 8-nm step. *Nature* **388:** 386–390

Schroer TA (2004) Dynactin. *Annu Rev Cell Dev Biol* **20:** 759–779

Schuchardt I, Assmann D, Thines E, Schuberth C, Steinberg G (2005) Myosin-V, Kinesin-1, and Kinesin-3 cooperate in hyphal growth of the fungus *Ustilago maydis*. *Mol Biol Cell* **16:** 5191–5201

Severs NJ (2007) Freeze-fracture electron microscopy. *Nat Protoc* **2:** 547–576

Soppina V, Rai AK, Ramaiya AJ, Barak P, Mallik R (2009) Tug-of-war between dissimilar teams of microtubule motors regulates transport and fission of endosomes. *Proc Natl Acad Sci USA* **106:** 19381–19386

Spellig T, Bottin A, Kahmann R (1996) Green fluorescent protein (GFP) as a new vital marker in the phytopathogenic fungus *Ustilago maydis*. *Mol Gen Genet* **252:** 503–509

Steinberg G (1997) A kinesin-like mechanoenzyme from the zygomycete *Syncephalastrum racemosum* shares biochemical similarities with conventional kinesin from *Neurospora crassa*. *Eur J Cell Biol* **73:** 124–131

Steinberg G (2007) On the move: endosomes in fungal growth and pathogenicity. *Nat Rev Microbiol* **5:** 309–316

Steinberg G, Perez-Martin J (2008) *Ustilago maydis*, a new fungal model system for cell biology. *Trends Cell Biol* **18:** 61–67

Steinberg G, Schliwa M (1996) Characterization of the biophysical and motility properties of kinesin from the fungus *Neurospora crassa*. *J Biol Chem* **271:** 7516–7521

Steinberg G, Schliwa M, Lehmler C, Bölker M, Kahmann R, McIntosh JR (1998) Kinesin from the plant pathogenic fungus *Ustilago maydis* is involved in vacuole formation and cytoplasmic migration. *J Cell Sci* **111:** 2235–2246

Straube A, Brill M, Oakley BR, Horio T, Steinberg G (2003) Microtubule organization requires cell cycle-dependent nucleation at dispersed cytoplasmic sites: polar and perinuclear microtubule organizing centers in the plant pathogen *Ustilago maydis*. *Mol Biol Cell* **14:** 642–657

Straube A, Enard W, Berner A, Wedlich-Söldner R, Kahmann R, Steinberg G (2001) A split motor domain in a cytoplasmic dynein. *EMBO J* **20:** 5091–5100

Theisen U, Straube A, Steinberg G (2008) Dynamic rearrangement of nucleoporins during fungal 'open' Mitosis. *Mol Biol Cell* **19:** 1230–1240

Tilney LG, Bryan J, Bush DJ, Fujiwara K, Mooseker MS, Murphy DB, Snyder DH (1973) Microtubules: evidence for 13 protofilaments. *J Cell Biol* **59:** 267–275

Ulbrich MH, Isacoff EY (2007) Subunit counting in membrane-bound proteins. *Nat Methods* **4:** 319–321

Vale RD, Reese TS, Sheetz M (1985) Identification of a novel force-generating protein, kinesin, involved in microtubule-based motility. *Cell* **42:** 39–50

Valetti C, Wetzel DM, Schrader M, Hasbani MJ, Gill SR, Kreis TE, Schroer TA (1999) Role of dynactin in endocytic traffic: effects of dynamitin overexpression and colocalization with CLIP-170. *Mol Biol Cell* **10:** 4107–4120

Vallee RB, Williams JC, Varma D, Barnhart LE (2004) Dynein: an ancient motor protein involved in multiple modes of transport. *J Neurobiol* **58:** 189–200

Vaughan KT (2005) Microtubule plus ends, motors, and traffic of Golgi membranes. *Biochim Biophys Acta* **1744:** 316–324

Vaughan PS, Miura P, Henderson M, Byrne B, Vaughan KT (2002) A role for regulated binding of p150(Glued) to microtubule plus ends in organelle transport. *J Cell Biol* **158:** 305–319

Wang Z, Khan S, Sheetz MP (1995) Single cytoplasmic dynein molecule movements: characterization and comparison with kinesin. *Biophys J* **69:** 2011–2023

Wedlich-Söldner R, Bölker M, Kahmann R, Steinberg G (2000) A putative endosomal t-SNARE links exo- and endocytosis in the phytopathogenic fungus *Ustilago maydis. EMBO J* **19:** 1974–1986

Wedlich-Söldner R, Schulz I, Straube A, Steinberg G (2002b) Dynein supports motility of endoplasmic reticulum in the fungus *Ustilago maydis. Mol Biol Cell* **13:** 965–977

Wedlich-Söldner R, Straube A, Friedrich MW, Steinberg G (2002a) A balance of KIF1A-like kinesin and dynein organizes early endosomes in the fungus *Ustilago maydis. EMBO J* **21:** 2946–2957

Welte MA (2004) Bidirectional transport along microtubules. *Curr Biol* **14:** R525–R537

Welte MA, Gross SP (2008) Molecular motors: a traffic cop within? *HFSP J* **2:** 178–182

Xiang X (2003) LIS1 at the microtubule plus end and its role in dynein-mediated nuclear migration. *J Cell Biol* **160:** 289–290

Zhang J, Li S, Fischer R, Xiang X (2003) Accumulation of cytoplasmic dynein and dynactin at microtubule plus ends in *Aspergillus nidulans* is kinesin dependent. *Mol Biol Cell* **14:** 1479–1488

Zhang J, Zhuang L, Lee Y, Abenza JF, Peñalva MA, Xiang X (2010) The microtubule plus-end localization of Aspergillus dynein is important for dynein-early-endosome interaction but not for dynein ATPase activation. *J Cell Sci* **123:** 3596–3604

Supplementary Methods

Strains

The *Ustilago maydis* strains AB33G$_3$Dyn2, FB2N107G_ER, FB2N107R_N214G and

FB1Dyn2^{ts} were described previously (Lenz et al, 2006; Theisen et al, 2008 Wedlich-

Söldner et al, 2002b). Strains expressing single and double GFP-tagged dynein were

constructed by homologous integration of the plasmids pGFPDyn2 and pGFP$_2$Dyn2

in AB33. For photo-activation studies of Rab5a the plasmid popaGFPRab5a was

integrated into the succinate dehydrogenase locus of the strains AB33Dyn2Ch$_3$, and

AB5Dyn2^{ts}. The strain Ab33GRab5a was generated by ectopic integration of plasmid

poGRab5a in AB33. Strains AB33GRab5_rKin3^{G105E} and AB33G3Dyn2 _rKin3^{G105E},

expressing the previously described rigor allele *kin3*^{G105E} (Wedlich-Söldner et al,

2002a) under control of the strong and inducible *crg*-promoter (Bottin et al, 1996) in

the succinate dehydrogenase locus were generated by transforming plasmid

prKin3^{G105E} in the strains AB33GRab5a and AB33G$_3$Dyn2. The plus-end dynamics

of dynein was studied in strain AB33pamG$_3$Dyn2. For Strain AB33pamG$_3$Dyn2 a

triple tag of monomeric photo-activatable GFP (Patterson and Lippincott-Schwartz,

2002), kindly provided by Dr. J. Lippincott-Schwartz) was fused to the 5′-end of the

endogenous dynein heavy gene *dyn2*. The plasmids pcrgPeb1$^{211-268}$, pcrgDya1$^{32-62}$ and

pcrgDya1$^{32-62\ Q35E}$ were transformed into strain AB33G$_3$Dyn2 to obtain AB33

G$_3$Dyn2_rEB1$^{211-268}$, AB33 G$_3$Dyn2_rDya1$^{32-62}$ and AB33 G$_3$Dyn2_rDya1$^{32-62\ Q35E}$.

The strain AB33G$_3$Dyn2 _Peb1R was obtained by homologous integration of plasmid

pPeb1R_N (Lenz et al, 2006) in AB33G$_3$Dyn2. The genotypes of all strains used in

this work are summarized in Table 1.

Plasmid construction

popaGRab5a. Plasmid popaGRab5a was constructed as follow: a 708bp fragment (cut by *Nco*I and *Nde*I) containing the photo-activatable GFP was cloned into plasmid p123 (Aichinger et al, 2003), downstream of the constitutive *otef* promoter, resulting in plasmid p123-paGFP. The full-length *rab5a* gene (Fuchs et al, 2006) and its terminator sequence were amplified by PCR, cut by *Nde*I and *Eco*RI and subsequently fused in frame with paGFP in plasmid p123-paGFP, cut by the same restriction enzymes, generating an N-terminal fusion. The resulting plasmid was linearized with *Ssp*I before fungal transformation to direct its homologous integration at the *sdh2* succinate dehydrogenase locus.

poGRab5a. The plasmid poGRab5a was generated by cloning a 700bp fragment (cut by *Nco*I and *Nde*I) containing the GFP gene downstream of the constitutive *otef* promoter carried by plasmid p123. The GFP gene was then N-terminally fused to the full-length *rab5a* followed by its terminator obtained as described above. The nourseothricin resistance cassette (cut by *Not*I) was cloned upstream of the *otef* promoter. The resulting plasmid was linearized with *Sap*I before fungal transformation, leading to ectopic integration in the genome.

ppa$_m$G$_3$Dyn2. For generating plasmid ppa$_m$G$_3$Dyn2, a plasmid containing single photoactivatable $_m$GFP (Patterson and Lippincott-Schwartz, 2002) was used as a template to generate the triple tandem repeat tag. In a first step, the pa$_m$GFP gene was amplified from the obtained vector. After blunt-end ligation of three pa$_m$GFP amplicons, the complete triple tandem repeat tag was amplified in a second PCR, using primers generating *Nco*I and *Nde*I restriction sites. The obtained 2176 bp DNA fragment was digested with *Nco*I and *Nde*I. The resulting 2166 bp fragment was cloned downstream of a 1724 bp fragment of the endogenous promoter of *dyn2* (Straube et al, 2001)) followed by the first 1762 bp of the coding sequence of *dyn2*

using *Nde*I and *Eco*RI restriction sites. The hygromycin phosphotransferease

resistance cassette and a 1261 bp fragment of the *dyn2* promoter were fused upstream

of the *dyn2* promoter in order to trigger homologous recombination. The resulting

plasmid was digested with *Sph*I and *Eco*RV for homologous integration into the

native *dyn2* locus of strain AB33, resulting in AB33pa$_m$G3Dyn2.

pcrgDya1$^{32-62}$, *pcrgDya1$^{32-62Q35E}$* and *pcrgPeb1$^{211-268}$* . The plasmids pcrgDya1$^{32-62}$,

pcrgDya1$^{32-62\ Q35E}$ and pcrgPeb1$^{211-268}$ were generated through *in vivo* recombination

in the *Saccharomyces cerevisiae* strain DS94 (MATα, *ura3-52*, *trp1-1*, *leu2-3*, *his3-*

111, and *lys2-801* (Tang et al, 1996) following published procedures (Raymond et al,

1999). For all the recombination events, the fragments were amplified with 30 bp

homologous sequences to the upstream and downstream of the fragments to be cloned.

In order to obtain the yeast - *E. coli* shuttle vector, 2680 bp fragment containing the

yeast URA3 marker and 2μm *ori* amplified from plasmid pEYA2 was cloned in to

linearized (cut by *Nde*I) plasmid pNEBcbx containing the ampicilin resistance

cassette, *E. coli* origin of replication, and the carboxin resistance cassette resulting the

plasmid pNEBcbx-yeast. 174 bp fragment of C-terminus Peb1 gene, 93 bp fragment

of N-terminus Dya1 gene and 93 bp fragment of N-terminus Dya1 gene (Q35E) were

individually cloned in to linearized plasmid pNEBcbx-yeast (cut by *Bam*HI) along

with the 3508 bp *crg* promoter and 307 bp Tnos terminator. The resulting plasmids

were linearized with *Age*I before fungal transformation to direct its homologous

integration at the succinate dehydrogenase locus. Molecular cloning followed

standard procedures and transformation of *U. maydis* was carried out as previously

described (Lenz et al, 2006).

pNup214-2G, *pNup214-3G*, *pNup2-G*. To measure the intensity of fluorescence in

individual pores we expressed several fusion proteins introducing various amounts of

GFPs into a single pore (Nup214-GFP= 8GFP), (Nup107-GFP= 16 GFP), (Nup107-GFP+ Nup214-GFP$_2$= 32 GFP), and (Nup107-GFP+Nup214-GFP$_3$+Nup2-GFP= 48 GFP). To generate the required plasmids pNup214-2G and pNup214-3G, plasmid pNup214-G (Theisen et al, 2008) was digested with BsrGI and additional copies of gfp genes were introduced as BsrGI fragments. The resulting plasmids were digested with PvuII and integrated homologously into the $Nup214$ locus of strains FB2, and FB2N107G resulting in FB2N214G$_3$, FB2N107G_N214G$_2$ and FB2N107G_N214G$_3$ respectively. The hygromycin phosphor-transferase resistance cassette in the plasmid pNup2-G (Theisen et al, 2008) was exchanged with nourseothricin gene resistance cassette and the resulting plasmid was digested with PvuII and integrated homologously in to the locus of strain FB2N107G_N214G$_3$ resulting in FB2N107G_N214G$_3$_N2G.

Laser-based epifluorescence-microscopy

Cells were placed on a thin layer of 2% agarose, covered with a cover slip, and immediately observed using a IX81 motorized inverted microscope (Olympus, Hamburg, Germany), equipped with a PlanApo 100X/1.45 Oil TIRF objective (Olympus, Hamburg, Germany). Excitation of fluorescently-labeled proteins was carried out using a VS-LMS4 Laser-Merge-System with solid state lasers (488 nm/50 mW or 75mW and 561 nm/50 mW or 75mW, Visitron System, Munich, Germany). Photo-activation and photo-bleaching experiments were performed using a Visitron 2D FRAP system, consisting of a 405 nm/ 60 mW diode laser which was attenuated by a ND 0.6 Filter, resulting in 15mW output power. The FRAP laser was controlled by UGA-40 controller (Rapp OptoElectronic GmbH, Hamburg, Germany) and a VisiFRAP 2D FRAP control software for Meta Series 7.5.x (Visitron System, Munich,

Germany). Images were captured using a Charged-Coupled Device camera (Photometric CoolSNAP HQ2, Roper Scientific, Germany). All parts of the system were under the control of the software package MetaMorph (Molecular Devices, Downingtown, USA). Fluorescence measurements and image processing were carried out with MetaMorph (Molecular Devices, Downingtown, USA).

Quantitative photo-bleaching analysis

Cells of strain FB2N107R_N214G and AB33G$_3$Dyn2 were treated with 100μM CCCP (Carbonyl cyanide m-chlorophenyl-hydrazone, Sigma-Aldrich Ltd, Gillingham, UK) for 10 minutes and then placed on a thin layer of 2% agarose containing 100μM CCCP as well. For strain FB2N107R_N214G movies of 150 to 250 frames at an exposure time of 250ms were taken and further analyzed using MetaMorph. In the case of AB33G$_3$Dyn2 the first 10 to 15 μm of the hyphae or most of the hyphae but not the first 5 μm were photo bleached. After 5 minutes incubation in the dark movies of 200 frames at an exposure time of 250ms and 5.6 mW laser power were taken. The average intensity of signals was measured in each frame and values were corrected for the neighboring background. The number of bleaching steps was determined by a step-finding algorithm (Kerssemakers et al, 2006) kindly provided by Dr. Jacob Kerssemakers, Delft, the Netherlands) in the program MatLab (The MathWorks, Natick, USA).

Fluorescent recovery after photo-bleaching (FRAP) experiments and photo-bleaching analysis

5 pre-bleach images of hyphal cells of strain AB33G$_3$Dyn2 with 50ms and 50% of a 50mW 488nm laser were taken. The hyphal tip was irradiated for 300 ms using 22.5%

output power of a solid state 60 mW 405 nm laser. Every 15 s an image with 50ms

and 50% of a 50mW 488nm laser was taken. The average intensity of the apical

accumulation was measured. The measured intensity was corrected by subtracting the

background and for bleaching. The photo-bleaching experiments were done using

strains AB33G$_3$Dyn2, AB33G$_3$Dyn2_rKin3^{G105E} and AB33GRab5a. A region of 10

μm in length at 5 μm behind the tip was irradiated for 300 ms with a beam diameter of

30 pixels using 22.5% output power of a solid state 60 mW 405 nm laser. This was

followed by observation using an exposure time of 150 ms and the 488 nm laser at

100% for dynein and 10% for GFP-Rab5a. 75 frames were taken for each experiment.

Velocity, frequency and turning rates were analyzed in kymographs which were

generated from these images series using MetaMorph.

Freeze-fracture transmission electron microscopy

 Samples of *U. maydis* were concentrated by brief centrifugation and sandwich-

mounted between cleaned copper holders coated with a thin smear of polyvinyl

alcohol mounting medium. The mounted specimens were rapidly frozen by plunging

into liquid nitrogen slush and inserted into a Balzers "double-replica" device for

tensile fracturing. Freeze-fracture and platinum/carbon replication were carried out at

-120ºC at a vacuum of more than 10^{-6} mbar in a Balzers BAF 400T freeze-fracture

unit, as previously described (Severs, 2007). The replicated specimens were floated

off their holders into sodium hypochlorite cleaning solution for 2-6 hours to remove

biological material from the replica. After washing in distilled water, replicas were

mounted on hexagonal thin-bar grids for examination and recording of images using a

Hitachi H7000 transmission electron microscope.

Determination of the dynein flux from bleaching step analysis

Bleaching of GFP fused to Dyn2 followed a normal distribution for the number of steps. To determine the ratio of single to double dynein motors, the bleaching step distributions were fit to a sum of normal distributions with means 3 and 6 (corresponding to one and two dynein, respectively) using the software Prism (GraphPad, San Diego, USA). The degrees of freedom available are the standard deviation and area under each of the normal curves. This analysis was done for retrograde dynein signals and gave a good fit (R^2=0.9143) to the sum of normal curves, giving a ratio of 1 dynein: 2 dynein that was 3.998:1 (*n*=77). This ratio was used to scaling of the measured retrograde flux of GFP_3-Dyn2 signals (0.941±0.237 particles/s) by a factor of 1.20, implying a mean retrograde flux of 1.128 dynein/s. The anterograde dynein signals were found to display a very good fit (R^2=0.9977) to the sum of normal curves, giving a ratio of 1 dynein: 2 dynein that was 8.492:1 (*n*=56). This implies a scaling of the measured anterogade flux (0.894±0.318 particles/s) by a factor of 1.10, resulting in a mean anterograde flux of 0.983 dynein/s. Taking an assumption of equal fluxes in both directions, the mean value of 1.06 dynein/s was used in the simulations.

Estimation of mean run-lengths/turning rates

The mean run-lengths M_a and M_r were estimated by examining (in data similar to Fig. 5A) the proportion F(x) of motors that turned within a distance x μm after entering a 3 μm window of MT away from any obvious defects. We assume an exponential association $F(x)=1-\exp(-x/M_a)$ where M_a represents mean anterograde run-length before turning. For x/M_a small, this is close to linear with slope given by $1/M_a$. Measuring this by linear regression gives $1/M_a$=0.0160 μm^{-1} (n=300) and similarly

$1/M_r = 0.0239$ μm^{-1} (n=300) for retrograde moving motos. These estimates give the

values $M_a = 41.89$ μm and $M_r = 62.37$ μm, and hence the turning rates P_2 and P_4 used in

the modeling (see below).

Non-linear regression and statistical analysis

Non-linear regression and all statistical tests were done using the software Prism

(GraphPad, San Diego, USA). Comparison of one phase decay and two phase decay

models was done using an F-test ($\alpha = 0.05$). The half-lives of the decay and the

proportions in each population are the fitting parameters for a signal that is

normalized to lie between 0% and 100%. The one phase decay assumes the

dependence on time t is of the form $100\% \times 2^{-t/K1}$ while the two phase decay assumes a

the dependence is $(100\%-S) \times 2^{-t/K1} + S \times 2^{-t/K2}$. The fitting constants K_1 and K_2 are half-

lives (constrained to be ≥ 0), while S (constrained to be between 0% and 100%) gives

the percentage in the second population. Similarly, Figure 4C compares a fit to

$100\% \times (1-2^{-t/K1})$ with a fit to $(100\%-S) \times (1-2^{-t/K1}) + S \times (1-2^{-t/K2})$ while Figure 4G

compares a fit to $100\% \times 2^{-t/K1}$ with a fit to $(100\%-S) \times 2^{-t/K1} + S$.

Mathematical modelling

We develop here a more geometrically realistic 13-lane model from a recently

published 2-lane model (Ashwin et al, 2010), using comparable assumptions. We

assume the spatial domain is a cylinder on which there are 13 lanes corresponding to

MT protofilaments. Left and right-moving motors can be on any of the filaments, and

while the kinesin-3 is assumed to remain on the same lane (Ray et al 1993), the

dynein is assumed the "dance" between lanes at a rate of $\delta = 5.1$ changes per $1\mu m$

moved (Wang et al, 1995). Probabilities are assumed to be homogeneous in space and time and the obvious exclusion principles apply: motors cannot enter a site that is occupied. Anterograde motors are injected into every lane at a rate of $1/13^{th}$ of the total flux rate $Flux_{in}(Dyn)$. We discretize using a space-step of $h_s=24$ nm (corresponding roughly 3 times the size of the motor heads) and use a sequential-update Monte-Carlo method with time-step $h_t=0.01$ s. The transition probabilities are as follows:

$P_1= v_{mean}h_t/h_s=0.7083$: the probability of kinesin stepping towards the tip gives the correct mean velocity.

$P_2= v_{mean}h_t/M_a=0.000406$: the probability of kinesin propulsion changing to dynein propulsion gives the correct measured rate for anterograde-to-retrograde turns.

$P_3=P_1-2P_5=0.6216$: the probability of dynein stepping away from the tip (whether it changes lane or not) gives the same mean speed as kinesin, i.e. $P_3+2P_5 = v_{mean}h_t/h_s= P_1$.

$P_4=v_{mean}h_t/M_r =0.000273$: the probability of dynein propulsion changing to kinesin propulsion gives the correct measured rate for retrograde-to-anterograde turns.

$P_5= P_1h_s\delta/2= 0.04335$: the probability of dynein changing lanes while progressing gives the correct mean rate of lane changes, i.e. a mean of δ changes per micrometer travelled.

$P_6=$ between 0.03 and 0.3542, default value $P_6=P_5=0.04335$: We assume that dynein will change lanes to resolve head-on collisions of counter-moving motors, as our experiments have found no evidence of collision on the MT within the time-resolution of the image capture. Hence any head-on collisions should resolve within 0.15 s implying that $P_6 \geq (h_t/150 \text{ ms})/2=0.03$. Note also that P_6 is unlikely exceed $(P_3+2P_5)/2$ $=0.3542$. Assuming $P_6=P_5=0.04335$ gives an intermediate value. Note that P_5 reflects the experimentally measured probability found for dynein motility in vitro (Wang et al., 1995).

$P_7= 0.03$: the estimated reduced probability that dynein changes lanes when facing an anterograde moving dynein on the same lane. This is chosen to ensure that motility blocks caused by individual collisions are not greater than 0.15 s in mean duration. Delays of more than 0.15 s would have been recognised in the kymographs of actual experiments, but such delays were not found.

$P_{in}= \text{Flux}_{in}(\text{Dyn})h_t/13=0.000815$: the injection probability assumes equal injection rate to each lane.

$P_{out}=1.9\times10^{-5}$: the probability of detachment at the MT plus-end is chosen to ensure that approximately 2% of the dynein delivered to the MT plus-end are lost, corresponding to the observed rate of loss of kinesin-3 transported EE at the tip and assuming a similar fidelity between the kinesin-3 and kinesin-1 delivery mechanisms.

Supplementary Figures
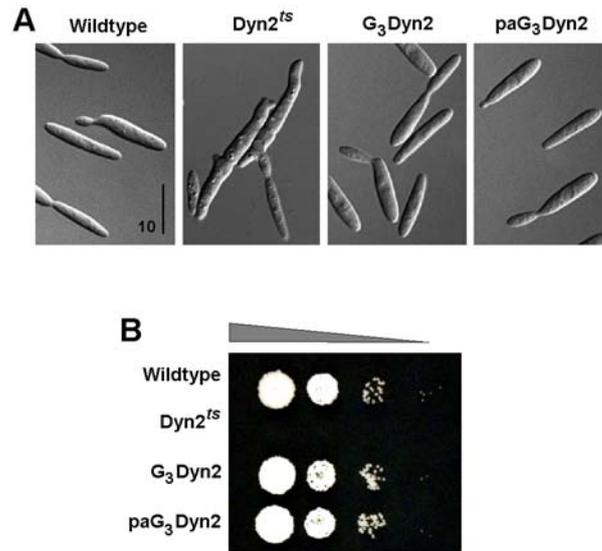
Supplementary Figure 1 Growth of wildtype, a conditional dynein mutant (Dyn2^{ts}) and strains expressing the fusion proteins GFP$_3$-Dyn2 (G$_3$Dyn2) and paGFP$_3$-Dyn2 (paG$_3$Dyn2). In contrast to the dynein mutant, the fusion proteins cause no morphological defect (**A**) or growth defect on plates (**B**), indicating that they are biologically functional.
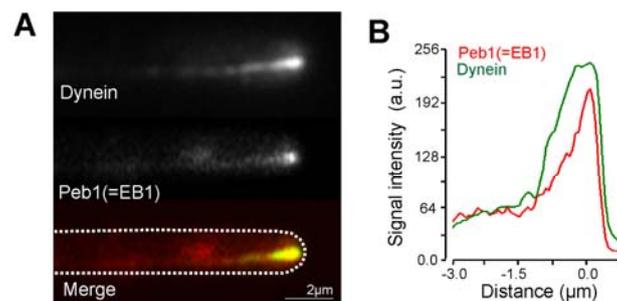
Supplementary Figure 2 Double labeling of GFP$_3$-Dyn2 and the EB1-homolouge Peb1 fused to monomeric RFP. Both signals co-localize at the MT end (**A, B).** Bar represents micrometer.
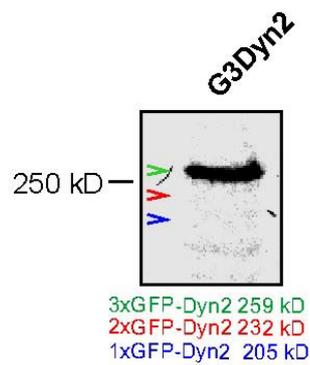
Supplementary Figure 3 Immunoblot showing expression of GFP$_3$-Dyn2. Note that no degradation products of GFP were found in extracts of cells expressing GFP$_3$-Dyn2 and that the fusion protein appears at the expected height, indicating that GFP$_3$-Dyn2 is stable and no proteolysis occurs. The position of potential breakdown products of GFP$_3$-Dyn2 is indicated by open arrowheads.
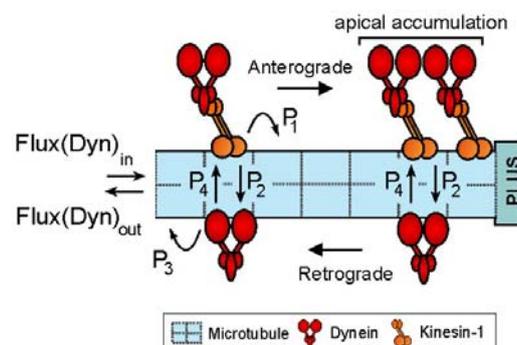
Supplementary Figure 4 A stochastic 2-lane model for dynein dynamics at MT plus-ends. At each time-step along the MT motors have different choices that are taken at certain probabilities (P_1-P_4). Note that the model does not consider any regulatory control, but it does assume that motors are not falling off at the end of the MT. See main text and (Ashwin et al 2010) for further details.
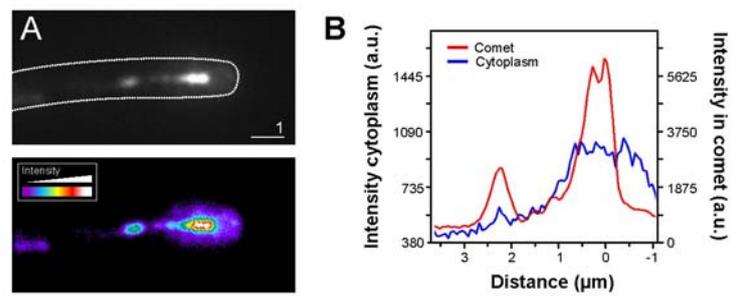
Supplementary Figure 5 Cytoplasmic background within the apex of a hypha expressing GFP$_3$-Dyn2. False colored images (A) and linescan analysis (B) demonstrate that the cytoplasmic background near the apical dynein comet is increased, indicating some loss of dynein from the comet into the cytoplasm. Bar represents 1 micrometer.
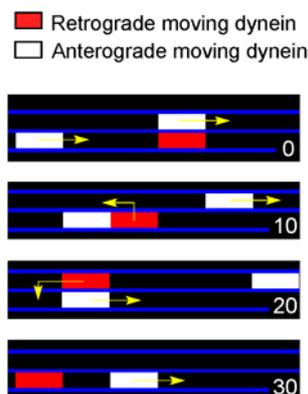
Supplementary Figure 6 Image series from a 13-lane simulation showing collision between retrograde dynein (red) and anterograde dynein delivered by kinesin-1 (white). Note that block of motility is avoided by dynein changing lanes. Time is given in lower left corner in milliseconds. Transport direction indicated by yellow arrows.

Supplementary movie legends

Supplementary Movie 1 Motility of GFP$_3$-labelled dynein heavy chain.

A fusion protein of a triple-GFP tag N-terminally fused to the endogenous dynein heavy chain gene *dyn2* displays bi-directional motility. Most of the dynein concentrates at the MT plus-ends near the hyphal tip. Time is given in seconds : milliseconds, the bar is given in micrometers.

Supplementary Movie 2 Loading of an endosome onto apical dynein.

A photo-activatable GFP-Rab5a was activated near the cell center. An EE moves towards the hyphal tip, reaches the dynein accumulation and turns for retrograde motility. Time is given in seconds : milliseconds, the bar is given in micrometers

Supplementary Movie 3 Behavior of EEs at the apical end of the MT tracks.

A photo-activatable GFP-Rab5a was activated near the cell center. EEs move along MTs towards the hyphal tip (blue arrowheads) where the plus-ends are located (yellow arrowheads). Most arriving EEs turn around (turning) or stay immobile for a short period (Pausing). Less than 2% of the EEs appear to lose contact and show Brownian motion (Falling off). Time is given in seconds : milliseconds, the bar is given in micrometers.

Supplementary Movie 4 Release of photo-activated dynein from apical MT plus-ends. A triple-tag of photo-activatable GFP was fused to the endogenous copy of the dynein heavy chain. After activation by a 405 nm pulse, apical dynein becomes visible that leaves the tip for retrograde movement. Time is given in seconds : milliseconds, the bar is given in micrometers.

Supplementary Movie 5 Simulation of the formation of an apical dynein accumulation in a 2-lane model**.**

The simulation uses the simple 2-lane model and experimentally measured parameters (see main text). The number of dynein motors accumulating at the tip (vertical line on the right side) is indicated by a color code and a running counter (upper middle).

Supplementary Movie 6 Simulation of dynein motility at the apical 2 micrometers near the MT plus-end in a 13-lane model.

The simulation is based on a more realistic 13-lane model that, as for to the 2-lane model, uses probabilities for back- and forward motility that are derived from experimental data. In addition, retrograde moving dynein (red) can change lanes and thereby avoid traffic jams with anterograde moving dynein that is delivered by kinesin-1 (white). Again, an apical accumulation of dynein is generated (yellow). Time is given in seconds : milliseconds.

References "Supplementary Information"

Aichinger C, Hansson K, Eichhorn H, Lessing F, Mannhaupt G, Mewes W, Kahmann R (2003) Identification of plant-regulated genes in *Ustilago maydis* by enhancer-trapping mutagenesis. *Mol Genet Genomics* **270:** 303-314

Ashwin P, Lin C, Steinberg G (2010) Queueing induced by bidirectional motor motion near the end of a microtubule. *Phys Rev E* (in press).

Becht P, Konig J, Feldbrügge M (2006) The RNA-binding protein Rrm4 is essential for polarity in *Ustilago maydis* and shuttles along microtubules. *J Cell Sci* **119:** 4964-4973

Bottin A, Kämper J, Kahmann R (1996) Isolation of a carbon source-regulated gene from *Ustilago maydis*. *Mol Gen Genet* **253:** 342-352

Fuchs U, Hause G, Schuchardt I, Steinberg G (2006) Endocytosis is essential for pathogenic development in the corn smut fungus *Ustilago maydis*. *Plant Cell* **18:** 2066-2081

Kerssemakers JW, Munteanu EL, Laan L, Noetzel TL, Janson ME, Dogterom M (2006) Assembly dynamics of microtubules at molecular resolution. *Nature* **442:** 709-712

Lenz JH, Schuchardt I, Straube A, Steinberg G (2006) A dynein loading zone for retrograde endosome motility at microtubule plus-ends. *EMBO J* **25:** 2275-2286

Patterson GH, Lippincott-Schwartz J (2002) A photoactivatable GFP for selective photolabeling of proteins and cells. *Science* **297:** 1873-1877

Ray S, Meyhöfer E, Milligan RA, Howard J (1993) Kinesin follows the microtubule's protofilament axis. *J Cell Biol* **121**:1083-1093.

Raymond CK, Pownder TA, Sexson SL (1999) A general method for plasmid construction using homologous recombination. *Biotechniques* **26:** 134-141

Severs NJ (2007) Freeze-fracture electron microscopy. *Nat Protoc* **2:** 547-576

Straube A, Enard W, Berner A, Wedlich-Söldner R, Kahmann R, Steinberg G (2001) A split motor domain in a cytoplasmic dynein. *EMBO J* **20:** 5091-5100

Tang X, Halleck MS, Schlegel RA, Williamson P (1996) A subfamily of P-type ATPases with aminophospholipid transporting activity. *Science* **272:** 1495-1497

Theisen U, Straube A, Steinberg G (2008) Dynamic rearrangement of nucleoporins during fungal "open" Mitosis. *Mol Biol Cell* **19:** 1230-1240

Wang Z, Khan S, Sheetz MP (1995) Single cytoplasmic dynein molecule movements: characterization and comparison with kinesin. *Biophys J* **69**:2011-2023.

Wedlich-Söldner R, Straube A, Friedrich MW, Steinberg G (2002a) A balance of KIF1A-like kinesin and dynein organizes early endosomes in the fungus *Ustilago maydis*. *EMBO J* **21:** 2946-2957

Wedlich-Söldner R, Schulz I, Straube A, Steinberg G. (2002b) Dynein supports motility of endoplasmic reticulum in the fungus *Ustilago maydis*. *Mol Biol Cell* **13**:965-977

Appendix B

Appendix: mean field approximation for the multi-lane model

We use a mean field approximation to give an equation for evolution of the densities ρ_i^l and σ_i^l for the multi-lane model with lane-homogeneous rates (but not necessarily boundary conditions). Examining the balance of incoming and outgoing particles to a given site, the mean field approximation gives the following, where on the right hand side we write ρ_i to mean ρ_i^l, etc.

$$
\begin{aligned}
\frac{d\rho_i^l}{dt} &= p_+ \rho_{i-1}(1 - \rho_i - \sigma_i) + p_{-+}\sigma_i - p_+\rho_i(1 - \rho_{i+1} - \sigma_{i+1}) - p_{+-}\rho_i \\
&+ p_{+,u}^\uparrow \rho_{i-1}^{l-1}(1 - \rho_i^{l-1} - \sigma_i^{l-1})(1 - \rho_i - \sigma_i) \\
&+ p_{+,u}^\downarrow \rho_{i-1}^{l+1}(1 - \rho_i^{l+1} - \sigma_i^{l+1})(1 - \rho_i - \sigma_i) \\
&+ \left(p_{+,b}^\uparrow \rho_{i-1}^{l-1}(\rho_i^{l-1} + \sigma_i^{l-1}) + p_{+,b}^\downarrow \rho_{i-1}^{l+1}(\rho_i^{l+1} + \sigma_i^{l+1}) \right)(1 - \rho_i - \sigma_i) \\
&- \left(p_{+,u}^\uparrow (1 - \rho_{i+1}^{l-1} - \sigma_{i+1}^{l-1}) + p_{+,u}^\downarrow (1 - \rho_{i+1}^{l+1} - \sigma_{i+1}^{l+1}) \right)\rho_i(1 - \rho_{i+1} - \sigma_{i+1}) \\
&- \left(p_{+,b}^\uparrow (1 - \rho_{i+1}^{l-1} - \sigma_{i+1}^{l-1}) + p_{+,b}^\downarrow (1 - \rho_{i+1}^{l-1} - \sigma_{i-1}^{l-1}) \right)\rho_i(\rho_{i+1} + \sigma_{i+1})
\end{aligned}
$$

There is a similar expression for $\frac{d\sigma^l}{dt}$, but for reasons of space we do not give this here. As the general mean field equations are not easy to solve, we consider below two special cases of these mean field equations.

Dilute lane-inhomogeneous densities

Let us assume that

- $\rho_i^l(t) = \rho^l(x, t)$ with $x = i\delta$ (where $\delta = 1/N = h_s/L$ is small) and the spatial

dimension is parametrized by $x \in [0, 1]$,

- ρ and σ are small (i.e. dilute limit);

- the lane changes rates are lane homogeneous and symmetric (i.e., $p_{\pm,u} = p_{\pm,u}^{\downarrow(\uparrow)}$);

On expanding $\rho_{i+1}^l = \rho^l(x) + \delta \frac{\partial \rho^l}{\partial x} + O(\delta^2)$ and discarding any terms that are quadratic in δ, the mean field equations above simplify to

$$
\frac{\partial \rho^l}{\partial t} = -\delta p_+ \frac{\partial \rho^l}{\partial x} + p_{+,u} \left(\rho^{l+1} + \rho^{l-1} - 2\rho^l - \delta \frac{\partial \rho^{l-1}}{\partial x} - \delta \frac{\partial \rho^{l+1}}{\partial x} \right)
$$
$$
+ p_{-+}\sigma^l - p_{+-}\rho^l
$$
$$
\frac{\partial \sigma^l}{\partial t} = \delta p_- \frac{\partial \sigma^l}{\partial x} + p_{-,u} \left(\sigma^{l+1} + \sigma^{l-1} - 2\sigma^l + \delta \frac{\partial \sigma^{l-1}}{\partial x} + \delta \frac{\partial \sigma^{l+1}}{\partial x} \right)
$$
$$
+ p_{+-}\rho^l - p_{-+}\sigma^l
$$

which can be used to characterize the combination of bidirectional transport $(p_\pm)$, change in direction $(p_{+-}$ and $p_{-+})$ and cross-lane diffusion $(p_{\pm,u})$ as regards the effect on the density. Considering a region of the domain where the dilute approximation holds, the stationary state distribution will therefore satisfy

$$
\delta p_+ \frac{d\rho^l}{dx} = p_{+,u} \left(\rho^{l+1} + \rho^{l-1} - 2\rho^l - \delta \frac{d\rho^{l-1}}{dx} - \delta \frac{d\rho^{l+1}}{dx} \right) + p_{-+}\sigma^l - p_{+-}\rho^l
$$
$$
-\delta p_- \frac{d\sigma^l}{dx} = p_{-,u} \left(\sigma^{l+1} + \sigma^{l-1} - 2\sigma^l + \delta \frac{d\sigma^{l-1}}{dx} + \delta \frac{d\sigma^{l+1}}{dx} \right) + p_{+-}\rho^l - p_{-+}\sigma^l.
$$

If $p_{\pm,u} = 0$, adding the above two equations gives $p_+ \frac{d\rho^l}{dx} = p_- \frac{d\sigma^l}{dx}$, meaning that in dilute situation, ρ^l and σ^l have a linear relationship. This gives a solution to the above ODEs:

$$
\begin{cases}
\rho^l(x) = C \exp\left[\left(\frac{p_{-+}N}{p_-} - \frac{p_{+-}N}{p_+} \right) x \right] + D \\
\sigma^l(x) = \frac{p_+ C}{p_-} \exp\left[\left(\frac{p_{-+}N}{p_-} - \frac{p_{+-}N}{p_+} \right) x \right] + \frac{p_{+-}D}{p_{-+}}
\end{cases}
\tag{B.1}
$$

where C, D can be determined by the densities at $\rho^l(x_0)$ and $\sigma^l(x_0)$ and are associated with l.

If $p_{\pm,u}$ are large $(p_{+-}, p_{-+} \ll p_{\pm,u})$, ignoring the turning rates, the above ODEs lead to

$$
\delta p_+ \frac{d\rho^l}{dx} = p_{+,u} \left(\rho^{l+1} + \rho^{l-1} - 2\rho^l - \delta \frac{d\rho^{l-1}}{dx} - \delta \frac{d\rho^{l+1}}{dx} \right)
$$
$$
-\delta p_- \frac{d\sigma^l}{dx} = p_{-,u} \left(\sigma^{l+1} + \sigma^{l-1} - 2\sigma^l + \delta \frac{d\sigma^{l-1}}{dx} + \delta \frac{d\sigma^{l+1}}{dx} \right).
$$

Lane-homogeneous densities

Now consider homogeneous model which gives lane-homogeneous densities $\rho(x) = \rho_i^l$ due to the symmetric structure of the cylinder and as before $x = i\delta$. In this case we have, ignoring second and higher order terms in $\delta = 1/N$, that the stationary state in the dilute case satisfies

$$
\begin{aligned}
0 &= p_{-+}\sigma - p_{+-}\rho + \delta\left[-p_+ - p_{+,u}^{l\to l+1} - p_{+,u}^{l\to l-1}\right]\frac{d\rho}{dx} \\
0 &= -p_{-+}\sigma + p_{+-}\rho + \delta\left[p_- + p_{-,u}^{l\to l+1} + p_{-,u}^{l\to l-1}\right]\frac{d\rho}{dx}
\end{aligned}
$$

Assuming zero net flux, this implies that $v_+\rho - v_-\sigma = 0$ where $v_\pm/h_s = p_\pm + p_{\pm,u}^{l\to l+1} + p_{\pm,u}^{l\to l-1}$. Applying the boundary conditions $\rho(0) = \frac{\alpha_+}{p_+ M}$ gives

$$
\rho(x) = \frac{\alpha_+}{p_+ M}\exp\left[\left(\frac{Np_{-+}}{p_- + p_{-,u}^{l\to l-1} + p_{-,u}^{l\to l+1}} - \frac{Np_{+-}}{p_+ + p_{+,u}^{l\to l-1} + p_{+,u}^{l\to l+1}}\right)x\right] \tag{B.2}
$$

analogous to the expression found for the two lane model in [64] but spread over all M lanes. This mean field approximation of density works well for low densities. However, near the tip plus-type and minus-type particles do not have complementary density as in [64]; in fact they can be at the same order near the tip for typical turning rates; for this reason it does not appear to be easy to obtain the mean tip size from a mean field approximation.

Appendix C

Appendix: an example of program codes

In this appendix, I attach an example of C++ codes which is used to simulate the multilane ASEP model discussed in Chapter 4.

```cpp
#include <iostream>
#include <stdio.h>
#include <string.h>
#include <math.h>
#include <stdlib.h>
#include <time.h>


// for generate ran2()
#define IM1 2147483563
#define IM2 2147483399
#define AM (1.0/IM1)
#define IMM1 (IM1-1)
#define IA1 40014
#define IA2 40692
#define IQ1 53668
#define IQ2 52774
#define IR1 12211
#define IR2 3791
#define NTAB 32
#define NDIV (1+IMM1/NTAB)
#define EPS 1.2e-7
#define RNMX (1.0-EPS)




#define NCLRS  255  //Number of CoLoRS
#define CUT_OFF_GIF_OUTPUT 1 // change to 0 to invoke..
#define CUT_OFF_SCREEN_PRINTING  0 // change to 0 to invoke..
//run information


bool flagoutden=false;//true;// save the output of sumk and sumd;
bool flagoutden_ave=true;
bool flagoutinitial=false;//true;//
bool flagleavetime=false;  // record the leaving time
bool flaglump=false;//true;   //10 sites lump into one;
bool flagtip=false;//true;// calculate the tip number
bool flagtiprecord=true;//false;
bool flagmovie=false;//true;
bool flagdecay=false;//true;//
bool flagcovering=false;//true;
bool flagtipsum=false;//true;//
bool flagtipsum_indep=false;//true;
bool flagcrossing=false;//true;
bool flagobstaifx=false;//true; // true mean obstacles are fixed in each run
bool flagdecrecstart=false;
bool flagfall=false;//true;//;// to count the  percentage of falling off.
bool flagtipdynamics=false;//true;
//others
const int M=13;
const double hs=0.008;
const double ht=0.0042;
const double Length=10;
const int L=600;
const int densteps=300000;// average in every densteps steps
const int ttrans=densteps;
const int rsteps=densteps*20;//
const int runtime=1;
const int repete=2;
const int Tip=L;
const int Tstep=100; //the steps between tips recorder
```

```cpp
//rate listing
const double vmean=1.7;
const double vplus=vmean;
const double vminus=vmean;
const double Ma=41.89;
const double Mr=62.37;
const double fluxin=50;
const double delta=5.1;
const double pk=vplus*ht/hs;
const double pk_d=50.0/double(L)*ht;
const double pd_k=34.0/double(L)*ht;
const double  pkb_up=0;//pro. of kenisin turn upload when blocked
const double  pkb_do=0;// kenisin turn downpload when blocked
const double  pku_up=0; // chane lane when unblocked
const double  pku_do=0;
const double  pdb_up=pk/2; // dynein turn uppload when blocked
const double  pdb_do=pk/2; // dynein turn downpload when blocked
const double  pdu_up=pk*delta*hs/2; //chane lane when unblocked
const double  pdu_do=pk*delta*hs/2;
const double  pd=pk-2*pdu_up;
const double  pink=fluxin*ht/M;
const double  fallpercentage=0;
const double  poutk=0;
const double  poutd=pk;
double tipsize[runtime];
double tipsize_mean=0,tipsize_std=0;
double rr,g,b;  //colorname
bool flagslow=false;
double ratiok,ratiod=1;
double movietime=0;
int fall;
int comein;

int tiptemp2=0;    // record the tip number
char file_name[56];
int lattice[M][L], tempstate[M][L];;
int sumk[M][L],sumd[M][L];
double r;
int k; //update steps
long idum;
int dect,st,ststep,leftno,num,num1;
int cro[L];
int obsta=10, obsta_num=10;

//subfunctions
void MCS();
double ran2(long *idum);
void sum(int K[][L],int D[][L],int A[][L],int M);
int sumdec(int A[][L],int M);

//movie parameters
char pathname[256];
char pathname1[256];
char filename_3[256];
char dosline[256];
int yenlarge=4,xenlarge=yenlarge*3,up=60,down=25;//image
int y,x,Lre=int(9*L/10);
int lanch=0;
char fname[256],*dummy;
int main()
{
    using namespace std;
```

```c
    FILE *denk;
    FILE *dend;
    FILE *denk_ave;
    FILE *dend_ave;
    FILE *tip;
    FILE *f_tipfluc;    //record the tip number with steps;
    FILE *tips;
    FILE *tips_indep;
    FILE *f_tipsize;
    FILE *wrong;
    FILE *leave;
    FILE *INI;
    FILE* fout3;
    FILE *crossing;
    FILE *fallper;
    FILE *tipdynamics;

    double ntip2;
    double tipsum;
    double dk[M][L],dd[M][L];//density for kensin and dynein

    int Initial[M][L];
    int i,j;
    double t;
    bool flagtimechange=true;
    idum=-(long)time(NULL);
    if (flagslow) {ratiok=1;}//ratiod=0.5}
    else ratiok=1;
    if ((pdu_up+pdu_do+pd+pd_k)>=1 || (pdb_up+pdb_do+pd_k+pd_k*ratiok)>=1){
        wrong=fopen("Important.txt","w");
        fprintf(wrong,"parameters over exceed");
        fclose(wrong);
    }

    sprintf(pathname1,"fluxin_%2f.txt",fluxin);
    if (flagtipsum_indep) {
        sprintf(pathname,"m_std_%s",pathname1);
        tips_indep=fopen(pathname,"w");
    }
   if (flagfall)fallper=fopen("c_fallper_2per_test_4_11.txt","w");
   if (flagtip) tip=fopen("c_tip_0.1_flux2.txt","w");
   if (flagtipsum) tips=fopen("c_tips_kins_19_10.txt","w");
   if(flagtiprecord)  {
      sprintf(pathname,"tipflu_%s",pathname1);
     f_tipfluc=fopen(pathname,"w");
   }
   if (flagdecay || flagcovering) leave=fopen("leftmotors.txt","w");
   if (flagtipdynamics)
 tipdynamics=fopen("tipdyna_noinver_kno_dboth_1.4_Tip125.txt","w");
    if (flagoutden_ave) {

        denk_ave=fopen("c_denk_ave.txt", "w");
        dend_ave=fopen("c_dend_ave.txt", "w");
    }
   if (flagoutden)  {
        denk=fopen("c_denk_p6003.txt", "w");
        dend=fopen("c_dend_p6003.txt", "w");
    }
    if (flagmovie) {
    sprintf(pathname,"movie_color_%d",rsteps);
    sprintf(dosline,"mkdir %s_dat",pathname);
    system(dosline);
```

```cpp
    }

    for (int repe=0;repe<repete;repe++)  {
    for(int rep=0; rep<runtime; rep++)   {
        ntip2=0;
        tiptemp2=0;
        tipsum=0;
        fall=0;
        comein=0;
        flagdecrecstart=false;
        if (flagtip)  {
            for(i=0;i<M;i++){
                for(j=0;j<L;j++) {
                sumk[i][j]=0;
                sumd[i][j]=0;
                }
            }
        }
    // initialization
    if (!flagobstaifx) {
        for(i=0;i<M;i++) {
            for(j=0;j<L;j++)  {
                lattice[i][j]=0;
                tempstate[i][j]=lattice[i][j];
                if (flagoutinitial) cout<< lattice[i][j]<<" ";
            }
            if (flagoutinitial) cout<<endl;
        }
    }

    // update one site/partical if possible
    for(k=0;k<ttrans+rsteps;k++) {
            MCS();
            if(k>=ttrans){
                if(flagoutden_ave || flagoutden) {
                    sum(sumk,sumd,lattice,M);
                    if ((k-ttrans)%densteps ==densteps-1) {
                        for(int i=0;i<M;i++) {
                            for(int j=0;j<L;j++) {

dk[i][j]=double(sumk[i][j])/double(densteps-1);

dd[i][j]=double(sumd[i][j])/double(densteps-1);
                                if (flagoutden) {
                                fprintf(denk,"%fl ", dk[i][j]);
                                fprintf(dend,"%fl ", dd[i][j]);
                                }
                                if (flagtip &&
(dk[i][j]>=0.06||dd[i][j]>=0.06)) {

ntip2=ntip2+dk[i][j]*(dk[i][j]>=0.06)+dd[i][j]*(dd[i][j]>=0.06);
                                }
                                sumk[i][j]=0;
                                sumd[i][j]=0;
                            }
                            if (flagoutden) {
                            fprintf(denk, "\n");
                            fprintf(dend, "\n");
                            }
                        }
                        if (flagoutden_ave){
                        for (int j=0;j<L;j++){
```

```
                                    double mk=0;
                                    double md=0;
                                   for (int i=0;i<M;i++) {
                                      mk=mk+dk[i][j];
                                      md=md+dd[i][j];
                                   }
                                    mk=mk/double(M);
                                    md=md/double(M);
                                    fprintf(denk_ave,"%fl ", mk);
                                    fprintf(dend_ave,"%fl ", md);

                                 }
                                 fprintf(denk_ave, "\n");
                                 fprintf(dend_ave, "\n");
                            }
                          }
                       }

                if (((flagtipsum || flagtipsum_indep || flagtiprecord) && (k-
ttrans)%Tstep==Tstep-1) || flagmovie) {
                        tiptemp2=0;
                        for (i=0;i<M;i++){
                            for (int s=L-Tip;s<L;s++)

tiptemp2=tiptemp2+((lattice[i][s]==1)||(lattice[i][s]==2));
                        }
                        if (flagtiprecord) fprintf(f_tipfluc, "%d ", tiptemp2);

                        if (flagtipsum_indep && (k==ttrans+rsteps-1))
tipsize[rep]=tiptemp2;
                        if (flagtipsum) tipsum=tipsum+double(tiptemp2);
                    }
                        if(flagmovie)// &&   ((k-ttrans) % 10 ==0) )//&& ((k-
ttrans)<M*L)  )
                        {
                            sprintf(filename_3, "%s_dat/im_%09u.ppm",pathname,k);
                            fout3 = fopen(filename_3, "w");

                            fprintf(fout3, "P3\n  %d %d\n 255\n", int (L-
Lre)*xenlarge, down+up+M*(yenlarge+1));

                            for (int i=0;i<M+up+down;i++){
                                if (i<up) {
                                    for (int j=Lre;j<L;j++){
                                        rr=1;g=1;b=1;
                                        for (x=0;x<xenlarge;x++)
                                        fprintf(fout3,"%d %d %d\n",(int)(rr*NCLRS),
(int)(g*NCLRS),(int)(b*NCLRS));
                                    }
                                }
                                else if (i<up+M) {
                                    for (y=0;y<yenlarge;y++) {
                                        for (int j=Lre;j<L;j++)  {
                                            rr=(lattice[i-up][j]>0);//1-
(lattice[i][j]==0);//
                                            g=(lattice[i-
up][j]==1);//(lattice[i][j]==0);//
                                            b=(lattice[i-
up][j]==1);//(lattice[i][j]==0);//
                                            for (x=0;x<xenlarge;x++)
                                            fprintf(fout3,"%d %d %d\n",(int)(rr*NCLRS),
(int)(g*NCLRS),(int)(b*NCLRS));
```

```
                                      }
                                  }
                              for (int j=Lre;j<L;j++) // color for MT
                                  for (x=0;x<xenlarge;x++)
                                      fprintf(fout3,"0 0 %d\n",(int)(NCLRS));
                          }
                          else{
                              for (int j=Lre;j<L;j++) {
                                  rr=1;g=1;b=1;
                                  for (x=0;x<xenlarge;x++)
                                  fprintf(fout3,"%d %d %d\n",(int)(rr*NCLRS),
(int)(g*NCLRS),(int)(b*NCLRS));
                              }
                          }
                      }
                      fclose(fout3);
#if CUT_OFF_GIF_OUTPUT
    sprintf(dosline,"convert %s_dat/im_%09u.ppm %s_dat/im_%09u.gif",pathname,k,
pathname,k);
    system(dosline);
    sprintf(dosline, "convert -fill black -pointsize 12 -draw  \" text 476,55
\'%d\'\" %s_dat/im_%09u.gif  %s_dat/im_%09u.gif", tiptemp2,pathname,k,pathname,
k);
    system(dosline);
    sprintf(dosline,"rm %s_dat/im_%09u.ppm",pathname,k);
    system(dosline);
#endif
movietime=movietime+ht;
                  }//movie over
              }// if k>ttrans over
          }// k<ttrans+rsteps over
      if (flagtipdynamics) {
              for (int i=0;i<M;i++) {
                      for (int j=L-Tip;j<L;j++)
                          fprintf(tipdynamics,"%d ",lattice[i][j]);

                      fprintf(tipdynamics,"\n");
              }
      }
    if (flagcrossing)  {
            crossing=fopen("c_cros.txt","w");
            for (int i=Lre;i<L-Tip;i++) fprintf(crossing,"%f\n",
double(cro[i])/double(rsteps));
            fclose(crossing);
      }
     if (flagtipsum)    {
            tipsum=tipsum/double(rsteps);
            fprintf(tips,"%fl ", tipsum);
      }
    if (flagtiprecord) fprintf(f_tipfluc, "\n");
    if(flagmovie)  fclose(fout3);
    if (flagtip) fprintf(tip,"%fl ", ntip2);
    if (flagdecay || flagcovering) {
        flagdecrecstart=true;
        st=10;
        leftno=0;
        flagtimechange=true;
        if (flagcovering) st=1;//20;
        ststep=0;
        INI=fopen("ini.txt","w");
              for (int i=0;i<M;i++) {
                      for (int j=L-Tip;j<L;j++){
```

```
                              fprintf(INI,"%d ", lattice[i][j]);
                              if (!(lattice[i][j]==10)&&(lattice[i][j]>0)){
                                  lattice[i][j]=lattice[i][j]+2;
                                  tempstate[i][j]=lattice[i][j];
                              }
                          }
                      fprintf(INI,"\n");
                      }
               double t=0;   // leaving time start at 0;
               num=sumdec(lattice,M);
             fprintf(leave,"%fl %d \n",t, num);
              MCS();
                    while((t<480 && flagdecay)|| (flagcovering && t<300)){
                          t=t+ht;//.0042;
                          num=sumdec(lattice,M);
                          if (flagdecay && t>60 && flagtimechange) {
                                  ststep=1;st=60;flagtimechange=false;
                          }
                          if (t<(ststep+1)*st && t>ststep*st) {
                              ststep=ststep+1;
                              fprintf(leave, "%fl %d \n", t,num);
                          }
                          MCS();
                      }
               fprintf(leave,"\n");
               for (int i=0;i<M;i++)   {
                       for (int j=L-Tip;j<L;j++)    fprintf(INI,"%d ", lattice[i][j]);
                       fprintf(INI,"\n");
               }
             }//decay or recovering end
             if (flagfall)  {
                     fprintf(fallper,"%f ",double(fall)/double(comein));
             }
       }//one run end;
       if (flagtipsum) fprintf(tips,"%fl ", pink/ht*M);
       if (flagtipsum && !(repe==repete)) fprintf(tips,"\n");
       if (flagtipsum_indep){
           tipsize_mean=0;
           tipsize_std=0;
           for (int rep=0;rep<runtime;rep++)  {
               tipsize_mean=tipsize_mean+tipsize[rep];
           }
           tipsize_mean=tipsize_mean/double(runtime);
           for (int rep=0;rep<runtime;rep++){
               tipsize_std=tipsize_std+(tipsize[rep]-tipsize_mean)*(tipsize[rep]-
tipsize_mean);
           }
           tipsize_std=tipsize_std/double(runtime);//tipsize_std/double(runtime-
1);
           fprintf(tips_indep,"%fl %fl %fl %fl %d \n",pink*M/ht,tipsize_mean,
tipsize_std,sqrt(tipsize_std)/sqrt(runtime),runtime);
       }
       }//one repe end
       if (flagfall)fclose(fallper);
       if (flagtipsum_indep) {
          fclose(tips_indep);
          // fclose(f_tipsize);
       }

if (flagmovie)
{
#if CUT_OFF_GIF_OUTPUT
```

```
    sprintf(dosline,"convert -delay 10 %s_dat/im*.gif -adjoin
%s_dat/output.gif",pathname,pathname);
    printf("Executing %s\n",dosline);
    printf("(animated gif in output.gif\n)");
    system(dosline);
#endif
}
    if(flagtiprecord) fclose(f_tipfluc);
    if (flagtip) fprintf(tip,"\n");
    if(flagtip) fclose(tip);
    if(flagdecay || flagcovering) {
        fclose(leave);
        fclose(INI);
    }
    if (flagtipdynamics) fclose(tipdynamics);
    if(flagtipsum) fclose(tips);
    if(flagoutden){
                fclose(denk);
                fclose(dend);
    }
    if (flagoutden_ave) {
        fclose(denk_ave);
        fclose(dend_ave);
    }
system("pause");
return 0;
}
void MCS(){
    using namespace std;
    int i,j;
        for (i=0;i<M;i++){// lane loop start
            if (tempstate[i][0]==0){// && (i%2)==1)//injuection
                r=ran2(&idum);
                if (r<pink){
                    tempstate[i][0]=1;
                }
            }
            else if (lattice[i][0]==1 || lattice[i][0]==3){// first site
                if (tempstate[i][1]==0) {//unblocked
                    r=ran2(&idum);
                    if (r<pk){  //forward
                        tempstate[i][1]=lattice[i][0];
                        tempstate[i][0]=0;
                    }
                    else if (r>=pk && r<pk+pk_d) //turning
                        tempstate[i][0]=lattice[i][0]+1;
                    else if (r<pk+pk_d+pku_up&& tempstate[(i+M-1)%M][1]==0) {
                        tempstate[(i+M-1)%M][1]=lattice[i][0];   //up lane
                        tempstate[i][0]=0;
                    }
                    else if (r>=pk+pk_d+pku_up && r<pk+pk_d+pku_up+pku_do &&
tempstate[(i+1)%M][1]==0) {
                        tempstate[(i+1)%M][1]=lattice[i][0];   //down lane
                        tempstate[i][0]=0;
                    }
                }
                else  {
                    r=ran2(&idum);
                    if (r<pk_d) //turning to be dynein
                        tempstate[i][0]=lattice[i][0]+1;
                    else if (r<pk_d+pkb_up && tempstate[(i+M-1)%M][1]==0) {
                        tempstate[(i+M-1)%M][1]=lattice[i][0];   //up lane
```

```
                    tempstate[i][0]=0;


                }
                else if (r>=pk_d+pkb_up && r<pk_d+pkb_up+pkb_do &&
tempstate[(i+1)%M][1]==0){
                    tempstate[(i+1)%M][1]=lattice[i][0];   //down lane
                    tempstate[i][0]=0;
                }
            }
        }
        else if ((lattice[i][0]==2) || (lattice[i][0]==4))  {
          r=ran2(&idum);
                if (r<poutd)  {
                    tempstate[i][0]=0;// exit
                }
                else if (r<poutd+pd_k) // turn
                    tempstate[i][0]=lattice[i][0]-1;


            }
        for (j=1;j<L-1;j++) {
            if (lattice[i][j]==1 || lattice[i][j]==3){//kenisin
                r=ran2(&idum);
                if (tempstate[i][j+1]==0){ //unblocked
                    if (r<pk){  //forward
                        tempstate[i][j+1]=lattice[i][j];
                        tempstate[i][j]=0;
                        if (k>=ttrans && j==L-Tip-1 && flagfall &&
lattice[i][j]==1) comein=comein+1;
                    }
                    else if (r>=pk && r<pk+pk_d) //turning
                        tempstate[i][j]=lattice[i][j]+1;
                    else if (r<pk+pk_d+pku_up && tempstate[(i+M-
1)%M][j+1]==0) {

                        tempstate[(i+M-1)%M][j+1]=lattice[i][j];   //up lane
                        tempstate[i][j]=0;
                    }
                    else if (r>=pk+pk_d+pku_up && r<pk+pk_d+pku_up+pku_do &&
tempstate[(i+1)%M][j+1]==0)
                    {
                        tempstate[(i+1)%M][j+1]=lattice[i][j];   //down lane
                        tempstate[i][j]=0;
                    }
                    //else cout<<"stay ";
                }
                else {// blocked
                    if (flagcrossing)    {
                        if (k>ttrans && j>Lre && j<L-Tip )   cro[j]=cro[j]+1;
                    }
                    if (r<pk_d && j<L-Tip) //turning
                        tempstate[i][j]=lattice[i][j]+1;
                    else if (r>=pk_d && r<pk_d+pk_d*ratiok && j>=L-Tip)//turn
                        tempstate[i][j]=lattice[i][j]+1;
                    else if (r>=pk_d+pk_d*ratiok && r<pk_d*ratiok+pkb_up+pk_d
&& tempstate[(i+M-1)%M][j+1]==0) {
                        tempstate[(i+M-1)%M][j+1]=lattice[i][j];   //up lane
                        tempstate[i][j]=0;


                    }
                    else if (r>=pk_d*ratiok+pkb_up+pk_d&&
r<pk_d*ratiok+pkb_up+pkb_do+pk_d && tempstate[(i+1)%M][j+1]==0){
                        tempstate[(i+1)%M][j+1]=lattice[i][j];   //down lane
                        tempstate[i][j]=0;
```

```
                }
              }
            }//kenisin ends
            else if ((lattice[i][j]==2) || (lattice[i][j]==4)){//dynein
                if (tempstate[i][j-1]==0){    // unblocked
                      r=ran2(&idum);
                      if (r<pd){//backward
                         tempstate[i][j-1]=lattice[i][j];
                         tempstate[i][j]=0;
                      }
                      else if (r<pd+pdu_up && tempstate[(i+M-1)%M][j-1]==0){
// uplane

                          tempstate[(i+M-1)%M][j-1]=lattice[i][j];

                          tempstate[i][j]=0;
                          if (k>=ttrans && j>Lre ) lanch=lanch+1;
                      }
                      else if (r<pd+pdu_up+pdu_do && tempstate[(i+1)%M][j-
1]==0 && r>=pd+pdu_up){ //down lane
                             tempstate[(i+1)%M][j-1]=lattice[i][j];

                             tempstate[i][j]=0;
                             if (k>=ttrans && j>Lre) lanch=lanch+1;
                      }
                      else if (r<pd+pdu_up+pdu_do+pd_k &&
r>=pd+pdu_up+pdu_do) // turn
                             tempstate[i][j]=lattice[i][j]-1;
                }
                else {   //blocked
                      if (flagcrossing)    {
                         if (k>ttrans && j>Lre && j<L-Tip)
cro[j]=cro[j]+1;
                      }
                        r=ran2(&idum);
                      if (r<pdb_up &&  tempstate[(i+M-1)%M][j-1]==0){ //
uplane

                          tempstate[(i+M-1)%M][j-1]=lattice[i][j];

                          tempstate[i][j]=0;
                      }
                      else if (r<pdb_up+pdb_do && tempstate[(i+1)%M][j-1]==0
&& r>=pdb_up) {//down lane
                             tempstate[(i+1)%M][j-1]=lattice[i][j];

                             tempstate[i][j]=0;
                      }
                      else if (r<pdb_up+pdb_do+pd_k && r>=pdb_up+pdb_do &&
j<L-Tip) // turn
                             tempstate[i][j]=lattice[i][j]-1;
                      else if (r>=pdb_up+pdb_do+pd_k &&
r<pdb_up+pdb_do+pd_k+pd_k*ratiod && j>=L-Tip) // turn
                             tempstate[i][j]=lattice[i][j]-1;
                   }
            }//dynein ends
        }// bulk update before Tip ends
  // last site
           j=L-1;
           if (lattice[i][j]==1 || lattice[i][j]==3) {//kenisin
             r=ran2(&idum);
                 if (r<poutk) { //forward
                       tempstate[i][j]=0;
                       if (k>=ttrans && flagfall && lattice[i][j]==1)
fall=fall+1;
```

```
                    }
                else  if (r>=poutk && r<poutk+pk_d*ratiok) //turning
                        tempstate[i][j]=lattice[i][j]+1;
            }//kenisin ends
            else if ((lattice[i][j]==2) || (lattice[i][j]==4)) {//dynein
                if (tempstate[i][j-1]==0) {  // unblocked
                    r=ran2(&idum);
                    if (r<pd){//backward
                        tempstate[i][j-1]=lattice[i][j];
                        tempstate[i][j]=0;
                    }
                    else if (r<pd+pdu_up && tempstate[(i+M-1)%M][j-1]==0){
// uplane
                        tempstate[(i+M-1)%M][j-1]=lattice[i][j];

                        tempstate[i][j]=0;
                        if (k>=ttrans && j>Lre ) lanch=lanch+1;
                    }
                    else if (r<pd+pdu_up+pdu_do && tempstate[(i+1)%M][j-
1]==0 && r>=pd+pdu_up) {//down lane
                        tempstate[(i+1)%M][j-1]=lattice[i][j];

                        tempstate[i][j]=0;
                        if (k>=ttrans && j>Lre) lanch=lanch+1;
                    }
                    else if (r<pd+pdu_up+pdu_do+pd_k &&
r>=pd+pdu_up+pdu_do) // turn
                        tempstate[i][j]=lattice[i][j]-1;
                }
                else {//blocked
                    if (flagcrossing)     {
                        if (k>ttrans && j>Lre && j<L-5)   cro[j]=cro[j]+1;
                    }
                     r=ran2(&idum);
                    if (r<pdb_up && tempstate[(i+M-1)%M][j-1]==0){ //
uplane
                        tempstate[(i+M-1)%M][j-1]=lattice[i][j];

                        tempstate[i][j]=0;
                    }
                    else if (r<pdb_up+pdb_do && tempstate[(i+1)%M][j-1]==0
&& r>=pdb_up) {//down lane
                        tempstate[(i+1)%M][j-1]=lattice[i][j];

                        tempstate[i][j]=0;
                    }
                    else if (r<pdb_up+pdb_do+pd_k*ratiod &&
r>=pdb_up+pdb_do) // turn
                        tempstate[i][j]=lattice[i][j]-1;
                }
            }//dynein ends
        }// one lane loop ends
        for(i=0;i<M;i++){ // copy back to lattice
            for(j=0;j<L;j++) {
                lattice[i][j]=tempstate[i][j];//*(!tempstate[i][j]==obsta);
            }
        }
    }
}
void sum(int K[][L],int D[][L],int A[][L],int M){
    for(int i=0;i<M;i++)  {
        for(int j=0;j<L;j++) {
            K[i][j]=K[i][j]+(A[i][j]==1 ||A[i][j]==3);
```

```
                D[i][j]=D[i][j]+(A[i][j]==2 ||A[i][j]==4);
            }
        }
}
int sumdec(int A[][L],int M){
    int s=0;
     for(int i=0;i<M;i++) {
          for(int j=L-Tip;j<L;j++) {
            if (flagcovering) s=s+((A[i][j]==1) ||(A[i][j]==2));
            else if (flagdecay) s=s+((A[i][j]==3) ||(A[i][j]==4));
          }
      }
      return s;
}
double ran2(long *idum){
    int j;
    long k;
    static long idum2=123456789;
    static long iy=0;
    static long iv[NTAB];
    double temp;
    if (*idum <= 0) {
        if (-(*idum) < 1) *idum=1;
        else *idum = -(*idum);
        idum2=(*idum);
        for (j=NTAB+7;j>=0;j--) {
            k=(*idum)/IQ1;
            *idum=IA1*(*idum-k*IQ1)-k*IR1;
            if (*idum < 0) *idum += IM1;
            if (j < NTAB) iv[j] = *idum;
        }
        iy=iv[0];
    }
    k=(*idum)/IQ1;
    *idum=IA1*(*idum-k*IQ1)-k*IR1;
    if (*idum < 0) *idum += IM1;
    k=idum2/IQ2;
    idum2=IA2*(idum2-k*IQ2)-k*IR2;
    if (idum2 < 0) idum2 += IM2;
    j=iy/NDIV;
    iy=iv[j]-idum2;
    iv[j] = *idum;
    if (iy < 1) iy += IMM1;
    if ((temp=AM*iy) > RNMX) return RNMX;
    else return temp;
}
#undef IM1
#undef IM2
#undef AM
#undef IMM1
#undef IA1
#undef IA2
#undef IQ1
#undef IQ2
#undef IR1
#undef IR2
#undef NTAB
#undef NDIV
#undef EPS
#undef RNMX
```

References

[1] C. Howe. Modeling the signaling endosome hypothesis: Why a drive to the nucleus is better than a (random) walk. *Theor. Biol. Med. Model.*, 2(1):43–57, 2005.

[2] J. E. Duncan and L. S. B. Goldstein. The genetics of axonal transport and axonal transport disorders. *PLoS Genet.*, 2(9):e124, 2006.

[3] Erica Chevalier-Larsen and Erika L.F. Holzbaur. Axonal transport and neurodegenerative disease. *Biochimica et Biophysica Acta (BBA) - Molecular Basis of Disease*, 1762:1094 – 1108, 2006.

[4] M. A. Welte, S. P. Gross, M. Postner, S. M. Block, and E. F. Wieschaus. Developmental regulation of vesicle transport in drosophila embryos: Forces and kinetics. *Cell*, 92(4):547 – 557, 1998.

[5] C. Valetti, D. M. Wetzel, M. Schrader, M. J. Hasbani, S. R. Gill, T. E. Kreis, and T. A. Schroer. Role of dynactin in endocytic traffic: Effects of dynamitin overexpression and colocalization with clip-170. *Mol. Biol. Cell*, 10(12):4107–4120, 1999.

[6] M. Suomalainen, M. Y. Nakano, S. Keller, K. Boucke, R. P. Stidwill, and U. F. Greber. Microtubule-dependent plus- and minus end-directed motilities are competing processes for nuclear targeting of adenovirus. *J. Cell. Biol.*, 144 (4):657–672, 1999.

[7] V. Soppina, A. K. Rai, A. J. Ramaiya, P. Barak, and R. Mallik. Tug-of-war between dissimilar teams of microtubule motors regulates transport and fission of endosomes. *Proc. Nat. Acad. Sci. USA*, 106(46):19381–19386, 2009.

[8] R. Wedlich-Söldner and G. Steinberg. A kinesin responsible for movement of early endosomes in the fungus ustilago maydis. *Mol. Biol. Cell*, 11:408, 2000.

[9] J. H. Lenz, I. Schuchardt, A. Straube, and G. Steinberg. A dynein loading zone for retrograde endosome motility at microtubule plus-ends. *EMBO J.*, 25(11):2275–2286, 2006.

[10] M. A. Welte. Bidirectional transport along microtubules. *Curr. Biol.*, 14(13): R525–R537, 2004.

[11] S. Ally, A. G. Larson, K. Barlan, S. E. Rice, and V. I. Gelfand. Opposite-polarity motors activate one another to trigger cargo transport in live cells. *J. Cell. Biol.*, 187(7):1071–1082, 2009.

[12] S. J. Atkinson, S. K. Doberstein, and T. D. Pollard. Moving off the beaten track. *Curr. Biol.*, 2(6):326 – 328, 1992.

[13] A. Desai and T. J. Mitchison. Microtubule polymerization dynamics. *Annu. Rev. Cell Dev. Biol.*, 13:83–117, 1997.

[14] L. G. Tilney, J. Bryan, D. J. Bush, K. Fujiwara, M. S. Mooseker, D. B. Murphy, and D. H. Snyder. Microtubules: evidence for 13 protofilaments. *J. Cell Biol.*, 59(2):267–275, 1973.

[15] T. Mitchison and M. Kirschner. Dynamic instability of microtubule growth. *Nature*, 312(5991):237–242, 1984.

[16] G. Steinberg, R. Wedlich-Söldner, M. Brill, and I. Schulz. Microtubules in the fungal pathogen ustilago maydis are highly dynamic and determine cell polarity. *J. Cell Sci.*, 114(3):609–622, 2001.

[17] A. Akhmanova and M. O. Steinmetz. Tracking the ends: a dynamic protein network controls the fate of microtubule tips. *Nat. Rev. Mol. Cell Bio.*, 9(4): 309–322, 2008.

[18] K. Svoboda, C. F. Schmidt, B. J. Schnapp, and S. M. Block. Direct observation of kinesin stepping by optical trapping interferometry. *Nature*, 365(6448):721–727, 1993.

[19] R. Mallik, B. C. Carter, S. A. Lex, S. J. King, and S. P. Gross. Cytoplasmic dynein functions as a gear in response to load. *Nature*, 427(6975):649–652, 2004.

[20] C. Kural, H. Kim, S. Syed, G. Goshima, V. I. Gelfand, and P. R. Selvin. Kinesin and dynein move a peroxisome in vivo: A tug-of-war or coordinated movement? *Science*, 308(5727):1469–1472, 2005.

[21] R. D. Vale. The molecular motor toolbox for intracellular transport. *Cell*, 112 (4):467–480, 2003.

[22] S. A. Endow, F. J. Kull, and H. Liu. Kinesins at a glance. *J. Cell Sci.*, 123 (20):3420–3424, 2010.

[23] P. Höök and R. B. Vallee. The dynein family at a glance. *J. Cell Sci.*, 119 (21):4369–4371, 2006.

[24] M. Schuster, R. Lipowsky, M.-A. Assmann, P. Lenz, and G. Steinberg. Transient binding of dynein controls bidirectional long-range motility of early endosomes. *Proc. Nat. Acad. Sci. USA*, 2011.

[25] M. Schuster, S. Kilaru, G. Fink, J. Collemare, Y. Roger, and G. Steinberg. Kinesin-3 and dynein cooperate in long-range retrograde endosome motility along a nonuniform microtubule array. *Mol. Biol. Cell*, 22(19):3645–3657, 2011.

[26] R. D. Vale and R. A. Milligan. The way things move: Looking under the hood of molecular motor proteins. *Science*, 288(5463):88–95, 2000.

[27] S. L. Reck-Peterson, A. Yildiz, A. P. Carter, A. Gennerich, N. Zhang, and R. D. Vale. Single-molecule analysis of dynein processivity and stepping behavior. *Cell*, 126(2):335–348, 2006.

[28] N. Mizuno, S. Toba, M. Edamatsu, J. Watai-Nishii, N. Hirokawa, Y. Y. Toyoshima, and M. Kikkawa. Dynein and kinesin share an overlapping microtubule-binding site. *EMBO J.*, 23(13):2459–2467, 2004.

[29] Z. H. Wang, S Khan, and M. P. Sheetz. Single cytoplasmic dynein molecule movements: Characterization and comparison with kinesin. *Biophys. J.*, 69 (5):2011–2023, 1995.

[30] S. J. King and T. A. Schroer. Dynactin increases the processivity of the cytoplasmic dynein motor. *Nat Cell Biol*, 2(1):20–24, 2000.

[31] M. Nishiura, T. Kon, K. Shiroguchi, R. Ohkura, T. Shima, Y. Y. Toyoshima, and K. Sutoh. A single-headed recombinant fragment of dictyostelium cytoplasmic dynein can drive the robust sliding of microtubules. *J. Biol. Chem.*, 279(22):22799–22802, 2004.

[32] S. Toba, T. M. Watanabe, L. Yamaguchi-Okimoto, Y. Y. Toyoshima, and H. Higuchi. Overlapping hand-over-hand mechanism of single molecular motility of cytoplasmic dynein. *Proc. Nat. Acad. Sci. USA*, 103(15):5741–5745, 2006.

[33] R. D. Vale, T. S. Reese, and M. P. Sheetz. Identification of a novel force-generating protein, kinesin, involved in microtubule-based motility. *Cell*, 42 (1):39 – 50, 1985.

[34] K. Svoboda and S. M. Block. Force and velocity measured for single kinesin molecules. *Cell*, 77(5):773 – 784, 1994.

[35] G. Steinberg and M. Schliwa. Characterization of the biophysical and motility properties of kinesin from the fungus neurospora crassa. *J. Biol. Chem.*, 271 (13):7516–7521, 1996.

[36] J. Beeg, S. Klumpp, R. Dimova, R. S. Gracià, E. Unger, and R. Lipowsky. Transport of beads by several kinesin motors. *Biophys J.*, 94(2):532–541, 2008.

[37] A. Seitz and T. Surrey. Processive movement of single kinesins on crowded microtubules visualized using quantum dots. *EMBO J.*, 25(2):267–277, 2006.

[38] Y. Okada, H. Higuchi, and N. Hirokawa. Processivity of the single-headed kinesin kif1a through biased binding to tubulin. *Nature*, 424(6948):574–577, 2003.

[39] G. T. Shubeita, S. L. Tran, J. Xu, M. Vershinin, S. Cermelli, S. L. Cotton, M. A. Welte, and S. P. Gross. Consequences of motor copy number on the intracellular transport of kinesin-1-driven lipid droplets. *Cell*, 135(6):1098–1107, 2008.

[40] M. P. Dodding and M. Way. Coupling viruses to dynein and kinesin-1. *EMBO J.*, 30(17):3527–3539, 2011.

[41] S. P. Gross. Hither and yon: a review of bi-directional microtubule-based transport. *Physical Biology*, 1(2):R1–, 2004.

[42] M. J. I. Müller, S. Klumpp, and R. Lipowsky. Tug-of-war as a cooperative mechanism for bidirectional cargo transport by molecular motors. *Proc. Nat. Acad. Sci. USA*, 105(12):4609–4614, 2008.

[43] A. G. Hendricks, E. Perlson, J. L. Ross, H. W. Schroeder, M. Tokito, and E. L.F. Holzbaur. Motor coordination via a tug-of-war mechanism drives bidirectional vesicle transport. *Curr. Biol.*, 20(8):697–702, 2010.

[44] S. P. Gross, M. A. Welte, S. M. Block, and E. F. Wieschaus. Coordination of opposite-polarity microtubule motors. *J. Cell. Biol.*, 156(4):715–724, 2002.

[45] M. J. I. Müller, S. Klumpp, and R. Lipowsky. Bidirectional transport by molecular motors: Enhanced processivity and response to external forces. *Biophys J.*, 98(11):2610–2618, 2010.

[46] G. Steinberg. On the move: endosomes in fungal growth and pathogenicity. *Nat. Rev. Micro.*, 5(4):309–316, 2007.

[47] R. Kahmann and J. Kämper. Ustilago maydis: how its biology relates to pathogenic development. *New Phytol.*, 164(1):31–42, 2004.

[48] M. Bölker. Ustilago maydis: a valuable model system for the study of fungal dimorphism and virulence. *Microbiology*, 147(6):1395–1401, 2001.

[49] T. Brefort, G. Doehlemann, A. Mendoza-Mendoza, S. Reissmann, A. Djamei, and R. Kahmann. Ustilago maydis as a pathogen. *Annu. Rev. Phytopathol.*, 47:423–445, 2009.

[50] G. Steinberg. Tracks for traffic: microtubules in the plant pathogen ustilago maydis. *New Phytol.*, 174(4):721–733, 2007.

[51] G. Steinberg and J. Perez-Martin. Ustilago maydis, a new fungal model system for cell biology. *Trends in Cell Biology*, 18(2):61–67, 2008.

[52] M. Müensterkötter and G. Steinberg. The fungus ustilago maydis and humans share disease-related proteins that are not found in saccharomyces cerevisiae. *Bmc Genomics*, 8:473, 2007.

[53] I. Schuchardt, D. Aßmann, E. Thines, C. Schuberth, and G. Steinberg. Myosin-v, kinesin-1, and kinesin-3 cooperate in hyphal growth of the fungus ustilago maydis. *Mol. Biol. Cell*, 16(11):5191–5201, 2005.

[54] A. Straube, W. Enard, A. Berner, R. Wedlich-Söldner, R. Kahmann, and G. Steinberg. A split motor domain in a cytoplasmic dynein. *EMBO J.*, 20 (18):5091–5100, 2001.

[55] A. Seitz, H. Kojima, K. Oiwa, E.-M. Mandelkow, Y.-H. Song, and E. Mandelkow. Single-molecule investigation of the interference between kinesin, tau and map2c. *EMBO J.*, 21(18):4896–4905, 2002.

[56] R. J. McKenney, M. Vershinin, A. Kunwar, R. B. Vallee, and S. P. Gross. Lis1 and nude induce a persistent dynein force-producing state. *Cell*, 141(2): 304–314, 2010.

[57] Y. Chai, R. Lipowsky, and S. Klumpp. Transport by molecular motors in the presence of static defects. *J. Stat. Phys.*, 135(2):241–260, 2009.

[58] I. A. Telley, P. Bieling, and T. Surrey. Obstacles on the microtubule reduce the processivity of kinesin-1 in a minimal in vitro system and in cell extract. *Biophys J*, 96(8):3341–3353, 2009.

[59] J. R. Kardon, S. L. Reck-Peterson, and R. D. Vale. Regulation of the processivity and intracellular localization of saccharomyces cerevisiae dynein by dynactin. *Proc. Nat. Acad. Sci. USA*, 106:5669–5674, 2009.

[60] H. M. Zhou, I. Brust-Mascher, and J. M. Scholey. Direct visualization of the movement of the monomeric axonal transport motor unc-104 along neuronal processes in living caenorhabditis elegans. *J. Neurosci.*, 21(11):3749–3755, 2001.

[61] S. Ma and R. L. Chisholm. Cytoplasmic dynein-associated structures move bidirectionally in. *J. Cell Sci.*, 115(7):1453–1460, 2002.

[62] D. Cai, K. J. Verhey, and E. Meyhöfer. Tracking single kinesin molecules in the cytoplasm of mammalian cells. *Biophys J*, 92(12):4137–4144, 2007.

[63] R. Wang, M. Liu, and R. Jiang. Theoretical investigation of synchronous totally asymmetric exclusion processes on lattices with multiple-inputsingle-output junctions. *Phys. Rev. E*, 77(5):051108–, 2008.

[64] P. Ashwin, C. Lin, and G. Steinberg. Queueing induced by bidirectional motor motion near the end of a microtubule. *Phys. Rev. E*, 82(5):051907–, 2010.

[65] M. Schuster, S. Kilaru, P. Ashwin, C. Lin, N. J. Severs, and G. Steinberg. Controlled and stochastic retention concentrates dynein at microtubule ends to keep endosomes on track. *EMBO J.*, 30(4):652–664, 2011.

[66] C. Lin, G. Steinberg, and P. Ashwin. Bidirectional transport and pulsing states in a multi-lane asep model. *J. Stat. Mech.*, 2011(09):P09027, 2011.

[67] C. Lin, P. Ashwin, and G. Steinberg. A model for motor-mediated bidirectional transport on an antipolar microtubule bundle. *submitted*, 2012.

[68] J. R. Norris. *Markov Chains*. Cambridge University Press, 1997.

[69] C. T. MacDonald and J. H. Gibbs. Concerning the kinetics of polypeptide synthesis on polyribosomes. *Biopolymers*, 7(5):707–725, 1969.

[70] K. Nishinari, Y. Okada, A. Schadschneider, and D. Chowdhury. Intracellular transport of single-headed molecular motors kif1a. *Phys. Rev. Lett.*, 95(11):118101–, 2005.

[71] D. Chowdhury, A. Schadschneider, and K. Nishinari. Physics of transport and traffic phenomena in biology: from molecular motors and cells to organisms. *Phys. Life Rev.*, 2(4):318–352, 2005.

[72] O. Campás, C. Leduc, P. Bassereau, J. Casademunt, J.-F. Joanny, and J. Prost. Coordination of kinesin motors pulling on fluid membranes. *Biophys. J.*, 94(12):5009–5017, 2008.

[73] T. Chou, K. Mallick, and R. K. P. Zia. Non-equilibrium statistical mechanics: from a paradigmatic model to biological transport. *Rep. Prog. Phys.*, 74(11): 116601, 2011.

[74] C. Leduc, K. Padberg-Gehle, V. Varga, D. Helbing, S. Diez, and J. Howard. Molecular crowding creates traffic jams of kinesin motors on microtubules. *Proc. Nat. Acad. Sci. USA*, 109(16):6100–6105, 2012.

[75] A. Schadschneider. Traffic flow: a statistical physics point of view. *Physica A.*, 313(1-2):153–187, 2002.

[76] D. Chowdhury, L. Santen, and A. Schadschneider. Statistical physics of vehicular traffic and some related systems. *Physics Reports*, 329(4-6):199–329, 2000.

[77] C. Appert-Rolland, H. J. Hilhorst, and G. Schehr. Spontaneous symmetry breaking in a two-lane model for bidirectional overtaking traffic. *J. Stat. Mech.*, 2010(08):P08024, 2010.

[78] N. G. van Kampen. *Stochastic processes in physics and chemistry.* Elsevier, 3rd edition, 2007.

[79] F. Spitzer. Interaction of markov processes. *Adv. Math.*, 5:246–290, 1970.

[80] T. M. Liggett. *Interacting particle system.* Springer, New York, 1985.

[81] T. M. Liggett. *Stochastic interacting systems: contact, voter, and exclusion processes.* Springer, Berlin, 1999.

[82] C. T. MacDonald, J. H. Gibbs, and A. C. Pipkin. Kinetics of biopolymerization on nucleic acid templates. *Biopolymers*, 6(1):1–25, 1968.

[83] T. Chou. Ribosome recycling, diffusion, and mrna loop formation in translational regulation. *Biophys. J.*, 85(2):755–773, 2003.

[84] C. A. Brackley, M. C. Romano, and M. Thiel. The dynamics of supply and demand in mrna translation. *PLoS Comput. Biol.*, 7(10):e1002203–, 2011.

[85] R. A. Blythe and M. R. Evans. Nonequilibrium steady states of matrix-product form: a solver's guide. *J. Phys. A: Math. Theor.*, 40(46):R333, 2007.

[86] B. Derrida, M. R. Evans, V. Hakim, and V. Pasquier. Exact solution of a id asymmetric exclusion model using a matrix formulation. *J. Phys A: Math. Gen.*, 26(7):1493–1517, 1993.

[87] J. Krug. Boundary-induced phase transitions in driven diffusive systems. *Phys. Rev. Lett.*, 67(14):1882–1885, 1991.

[88] V. Popkov and G. M. Schütz. Steady-state selection in driven diffusive systems with open boundaries. *EPL*, 48(3):257, 1999.

[89] J. S. Hager, J. Krug, V. Popkov, and G. M. Schütz. Minimal current phase and universal boundary layers in driven diffusive systems. *Phys. Rev. E*, 63 (5):056110, 2001.

[90] A. B. Kolomeisky, G. M. Schütz, E. B. Kolomeisky, and J. P. Straley. Phase diagram of one-dimensional driven lattice gases with open boundaries. *J. Phys A: Math. Gen.*, 31(33):6911, 1998.

[91] G. M. Schütz. Critical phenomena and universal dynamics in one-dimensional driven diffusive systems with two species of particles. *J. Phys A: Math. Gen.*, 36(36):R339, 2003.

[92] L. Santen and C. Appert. The asymmetric exclusion process revisited: Fluctuations and dynamics in the domain wall picture. *J. Stat. Phys.*, 106(1): 187–199, 2002.

[93] V. Popkov, A. Rákos, R. D. Willmann, A. B. Kolomeisky, and G. M. Schütz. Localization of shocks in driven diffusive systems without particle number conservation. *Phys. Rev. E*, 67(6):066117, 2003.

[94] R. Juhász, L. Santen, and F. Iglói. Partially asymmetric exclusion models with quenched disorder. *Phys. Rev. Lett.*, 94(1):010601–, 2005.

[95] F. M. Ebrahim, S. Chaaboki, and M. Saalehi. Characteristics of the asymmetric simple exclusion process in the presence of quenched spatial disorder. *Phys. Rev. E*, 75(1):011127, 2007.

[96] F. Turci, A. Parmeggiani, E. Pitard, M. C. Romano, and L. Ciandriniy. Exclusion process on a lattice with dynamical defects. arXiv:1207.1804.

[97] D. A. Adams, B. Schmittmann, and R. K. P. Zia. Far-from-equilibrium transport with constrained resources. *J. Stat. Mech.*, 2008(06):P06009, 2008.

[98] C. A. Brackley, M. C. Romano, C. Grebogi, and M. Thiel. Limited resources in a driven diffusion process. *Phys. Rev. Lett.*, 105(7):078102–, 2010.

[99] C. A. Brackley, L. Ciandrini, and M. C. Romano. Multiple phase transitions in a system of exclusion processes with limited reservoirs of particles and fuel carriers. *J. Stat. Mech. Theor. Exp.*, 2012(03):P03002, 2012.

[100] A. Parmeggiani, T. Franosch, and E. Frey. Phase coexistence in driven one-dimensional transport. *Phys. Rev. Lett.*, 90(8):086601, 2003.

[101] R. Lipowsky, S. Klumpp, and T. M. Nieuwenhuizen. Random walks of cytoskeletal motors in open and closed compartments. *Phys. Rev. Lett.*, 87(10): 108101, 2001.

[102] S. Klumpp and R. Lipowsky. Traffic of molecular motors through tube-like compartments. *J. Stat. Phys.*, 113(1):233–268, 2003.

[103] K. E. P. Sugden and M. R. Evans. A dynamically extending exclusion process. *J. Stat. Mech.*, 2007(11):P11013, 2007.

[104] J. Brankov, N. Pesheva, and N. Bunzarova. Totally asymmetric exclusion process on chains with a double-chain section in the middle: Computer simulations and a simple theory. *Phys. Rev. E*, 69(6):066128–, 2004.

[105] E. Pronina and A. B. Kolomeisky. Theoretical investigation of totally asymmetric exclusion processes on lattices with junctions. *J. Stat. Mech.*, 2005(07): P07010, 2005.

[106] B. Embley, A. Parmeggiani, and N. Kern. Understanding totally asymmetric simple-exclusion-process transport on networks: Generic analysis via effective rates and explicit vertices. *Phys. Rev. E*, 80(4):041128–, 2009.

[107] I. Neri, N. Kern, and A. Parmeggiani. Totally asymmetric simple exclusion process on networks. *Phys. Rev. Lett.*, 107(6):068702–, 2011.

[108] S. A. Nowak, P.-W. Fok, and T. Chou. Dynamic boundaries in asymmetric exclusion processes. *Phys. Rev. E*, 76(3):031135–, 2007.

[109] L. E. Hough, A. Schwabe, M. A. Glaser, J. R. McIntosh, and M. D. Betterton. Microtubule depolymerization by the kinesin-8 motor kip3p: A mathematical model. *Biophys J*, 96(8):3050–3064, 2009.

[110] P. Greulich and A. Schadschneider. Disordered driven lattice gases with boundary reservoirs and langmuir kinetics. *Phys. Rev. E*, 79(3):031107, 2009.

[111] C. A. Brackley, M. C. Romano, and M. Thiel. Slow sites in an exclusion process with limited resources. *Phys. Rev. E*, 82(5):051920–, 2010.

[112] S. Klumpp and R. Lipowsky. Phase transitions in systems with two species of molecular motors. *EPL*, 66(1):90, 2004.

[113] M. Ebbinghaus and L. Santen. A model for bidirectional traffic of cytoskeletal motors. *J. Stat. Mech.*, 2009(03):P03030, 2009.

[114] M. Ebbinghaus, C. Appert-Rolland, and L. Santen. Bidirectional transport on a dynamic lattice. *Phys. Rev. E*, 82(4):040901, 2010.

[115] M. Liu, K. Hawick, and S. Marsland. Asymmetric exclusion processes with site sharing in a one-channel transport system. *Phys. Lett. A*, 374(4):516–521, 2010.

[116] S. Muhuri and I. Pagonabarraga. Collective vesicle transport on biofilaments carried by competing molecular motors. *EPL*, 84(5):58009, 2008.

[117] S. Muhuri, L. Shagolsem, and M. Rao. Bidirectional transport in a multispecies totally asymmetric exclusion-process model. *Phys. Rev. E*, 84(3):031921–, 2011.

[118] M. R. Evans, D. P. Foster, C. Godrèche, and D. Mukamel. Spontaneous symmetry breaking in a one dimensional driven diffusive system. *Phys. Rev. Lett.*, 74:208–211, 1995.

[119] D. W. Erickson, G. Pruessner, B. Schmittmann, and R. K. P. Zia. Spurious phase in a model for traffic on a bridge. *J. Phys A: Math. Gen.*, 38(41):L659, 2005.

[120] S. Großkinsky, G. Schütz, and R. Willmann. Rigorous results on spontaneous symmetry breaking in a one-dimensional driven particle system. *J. Stat. Phys.*, 128:587–606, 2007.

[121] V. Popkov, M. R. Evans, and D. Mukamel. Spontaneous symmetry breaking in a bridge model fed by junctions. *J. Phys A: Math. Gen.*, 41(43):432002, 2008.

[122] S. Gupta, D. Mukamel, and G. M. Schütz. The robustness of spontaneous symmetry breaking in a bridge model. *J. Phys. A: Math. Theor.*, 42(48): 485002, 2009.

[123] A. Jelić, C. Appert-Rolland, and L. Santen. A bottleneck model for bidirectional transport controlled by fluctuations. *EPL (Europhysics Letters)*, 98(4): 40009, 2012.

[124] R. Juhász. Weakly coupled, antiparallel, totally asymmetric simple exclusion processes. *Phys. Rev. E*, 76(2):021117–, 2007.

[125] R. Juhász. Dynamics at barriers in bidirectional two-lane exclusion processes. *J. Stat. Mech.*, 2010(03):P03010–, 2010.

[126] D. T. Gillespie. Exact stochastic simulation of coupled chemical reactions. *J. Phys. Chem.*, 81(25):2340–2361, 1977.

[127] D. T. Gillespie. Stochastic simulation of chemical kinetics. *Annu. Rev. Phys. Chem.*, 58:35–55, 2007.

[128] C. Arita. Queueing process with excluded-volume effect. *Phys. Rev. E*, 80(5): 051119, 2009.

[129] A. Gennerich, A. P. Carter, S. L. Reck-Peterson, and R. D. Vale. Force-induced bidirectional stepping of cytoplasmic dynein. *Cell*, 131(5):952–965, 2007.

[130] M. J. I. Müeller, S. Klumpp, and R. Lipowsky. Molecular motor traffic in a half-open tub. *J. Phys.: Condens. Matter*, 17(47):S3839–S3850, 2005.

[131] D. Gross and C. M. Harris. *Fundamentals of queueing theory (2nd edition).* NY Chichester Wiley, 1985.

[132] P. Brémaud. *An Introduction to Probabilistic Modeling.* New York, Springer, 1988.

[133] S. Ray, E. Meyhöfer, R. A. Milligan, and J. Howard. Kinesin follows the microtubule's protofilament axis. *J. Cell Biol.*, 121(5):1083–1093, 1993.

[134] K. Dreblow, N. Kalchishkova, and K. J. Böhm. Kinesin passing permanent blockages along its protofilament track. *Biochem. Biophys. Res. Commun.*, 395(4):490 – 495, 2010.

[135] M. A. Welte and S. P. Gross. Molecular motors: a traffic cop within? *HFSP J.*, 2(4):178–182, 2008.

[136] R. Wedlich-Söldner, I. Schulz, A. Straube, and G. Steinberg. Dynein supports motility of endoplasmic reticulum in the fungus ustilago maydis. *Mol. Biol. Cell*, 13(3):965–977, 2002.

[137] S. A. McKinley, A. Athreya, J. Fricks, and P. R. Kramer. Asymptotic analysis of microtubule-based transport by multiple identical molecular motors. *J. Theor. Biol.*, 305(21):54–69, 2012.

[138] B. J. Alder and T. E. Wainwright. Studies in molecular dynamics. i. general method. *J. Chem. Phys.*, 31:459–476, 1959.

[139] B. N. Kholodenko. Map kinase cascade signaling and endocytic trafficking: a marriage of convenience? *Trends in Cell Biology*, 12(4):173 – 177, 2002.